University of Southampton

FACULTY OF ENVIRONMENTAL AND LIFE SCIENCE

Ocean and Earth Science

Hydrothermal alteration in the lower oceanic crust

by

Barbara Zihlmann

Thesis for the degree of Doctor of Philosophy

September 2018

University of Southampton

Abstract

FACULTY OF ENVIRONMENTAL AND LIFE SCIENCE

Ocean and Earth Science

Thesis for the degree of Doctor of Philosophy

Hydrothermal alteration in the lower oceanic crust

by

Barbara Zihlmann

Hydrothermal circulation is a fundamental process for chemical and isotopic exchange between the solid Earth and oceans and for the extraction of heat from newly accreted crust at mid-ocean ridges. However, due to a dearth of samples from modern oceanic crust and ophiolites, there remain major short-comings in our understanding of hydrothermal circulation in the oceanic crust, especially in the lower plutonic crust. In particular, it is not known whether fluid recharge and discharge occurs pervasively or if it is mainly channelled in discrete zones such as faults.
This thesis integrates field observations with petrographic descriptions, mineral chemistry and Sr-isotope compositions of whole rock and mineral separates of variably altered gabbro samples collected throughout the lower ocean crust. The data are used to (i) constrain cross-cutting relationships of hydrothermal alteration from high to low temperatures, (ii) characterise observed zones of channelled fluid-flow, such as faults, and (iii) calculate elemental mass-changes related to intensive hydrothermal fluid-rock exchange in one lower crustal fault and extrapolate them to global hydrothermal fluxes.
The Samail ophiolite in Oman offers a unique exposure of the lower ocean crust. Cross-cutting relationships of hydrothermal veins indicate a clear and continuous alteration sequence from temperatures of ~800 °C down to temperatures < 100-200 °C. Decimetres to metres-wide zones, fully re-equilibrated under greenschist facies conditions, are observed throughout the lower ocean crust and indicate that there was pathway for focussed hydrothermal discharge. Whole rock and epidote mineral separates sampled from these discharge zones yield Sr-isotope compositions ($^{87}Sr/^{86}Sr$=0.7043-0.7049) that are distinctly elevated relative to fresh layered gabbro and similar to compositions observed in epidosites of the sheeted dyke complex. No systematic decrease of the $^{87}Sr/^{86}Sr$ composition with depth was observed, therefore a channelled recharge, transporting hydrothermal fluids quickly and efficiently down to the base of the crust, is regarded as likely. Mass-change calculations from one chlorite-rich fault zone indicate that most elements were mobilised during intensive hydrothermal fluid-rock interaction and were either transported away by the passage of the hydrothermal fluid or were partially incorporated into secondary mineral phases. Chlorite thermometry indicate alteration temperatures of 300-350 °C at high fluid/rock ratios of up to 450:1-900:1, calculated from silica solubility. Elemental mass-changes extrapolated to global hydrothermal fluxes result in significant, previously undocumented fluxes in- and out of the lower crust of most major elements as well as Sr, Cu, Zn and Cs. These results evidently highlight the importance of lower crustal fault zones for the global geochemical cycles.

Table of Contents

Table of Tables

Table of Figures

Research Thesis: Declaration of Authorship

Print name: Barbara Zihlmann

Title of thesis: Hydrothermal alteration of the lower ocean crust

I declare that this thesis and the work presented in it are my own and has been generated by me as the result of my own original research.

I confirm that:

1. This work was done wholly or mainly while in candidature for a research degree at this University;
2. Where any part of this thesis has previously been submitted for a degree or any other qualification at this University or any other institution, this has been clearly stated;
3. Where I have consulted the published work of others, this is always clearly attributed;
4. Where I have quoted from the work of others, the source is always given. With the exception of such quotations, this thesis is entirely my own work;
5. I have acknowledged all main sources of help;
6. Where the thesis is based on work done by myself jointly with others, I have made clear exactly what was done by others and what I have contributed myself;
7. Parts of this work have been published as:

Zihlmann, B., Muller, S., Coggon, R.M., Koepke, J., Garbe-Schoenberg, D., Teagle, D.A.H. Hydrothermal fault zones in the lower oceanic crust: An example from Wadi Gideah, Samail ophiolite, Oman. Lithos, 2018

Signature: Date:

Acknowledgements

This thesis would not have been possible without the invaluable help of a large number of people, to whom I would like to say a special “thank you”.

First of all, a big thanks goes to my supervisor Damon Teagle for his support over the last four years and for providing all the opportunities to go to amazing places and meet scientists all over the world. I will always remember great fieldwork in Oman and especially our “very British” afternoon tea-breaks out in the field.
Secondly, there are many people in Southampton who helped me in various ways throughout this PhD. First of all, a massive thanks to Matt Cooper who introduced me to the world of geochemistry and who taught me everything I needed to know in the lab. Thanks Matt for your patience! Agnes and Andy are thanked for answering many questions either in the clean lab or the instrument lab. John, Dan and Matt are thanked for letting me use the saw for that many hours, making all these amazing thin sections and providing chats and laughter when spirits were low. Ross Williams is thanked for XRD analysis. Jürg Matter is sincerely thanked for introducing me to fieldwork practise in Oman and for answering my many questions related to Oman. Andy Barker is thanked for many fruitful and inspiring thin section discussions. Catriona and Michelle are thanked for introducing me into working in the labs at the start of my PhD, for answering many questions related to geochemistry (Catriona) and ocean crust in particular (Michelle). Thank you both, your help is greatly appreciated! Roz Coggon is thanked for introducing me into the world of global fluid fluxes.

Within the framework of this PhD I had the possibility to go and work on the Microprobe in Hannover. This would not have been possible without the help of Jürgen Koepke. Thank you Jürgen for welcoming me to Hannover, for thin section discussion and letting me work on the microprobe.

Samuel Müller and Dieter Garbe-Schönberg from Kiel are greatly thanked for fruitful collaboration both in the field and later on while working on the paper. Thank you Samuel for the numerous Skype meetings discussing hydrothermal alteration.

Peter Kelemen is thanked for introducing me to the geology in Oman and for providing sheeted dyke samples of the area I'm working in.

Margot Godard and all the senior scientists of the ABYSS ITN are thanked for putting together this amazing project and for organising the numerous great meetings, short courses and field trips. And of course a massive thanks to the whole ABYSS group! Carlotta, Aurélien, Sofia, Val, Zeudia,

Manuel, Adriana, Rachael, Karin, Kristina, Tom, Pavel and Olivier. It hast been great to spend so much time with you all!

In Southampton I would like thank to all my friends from the office and the coffee break crew (Melanie, Luca, Najeeb, Chen, Sahoo, Giuseppe) for the amazing time at NOCS. Anna, Gaye, Kévin, Chen, Aurélien, Anita… thank you all for many great evenings, wonderful food and pints at the Guide dog. Jude and Catriona, thank you both for great climbing and other adventures in Calshot, it was always a pleasure and Esther, Veerle, Marc and Anna for letting me join you at Bouldershack!

A massive thanks goes to my family for always encouraging me to follow my dreams and for mental support all over these years! Merci för alles.

And finally, I'm thanking Marc, for always being there, for your understanding when times were stressful and all your support. It made everything easier and without you I wouldn't be where I am now. And of course, thank you for your enormous help during my second field work and for providing the fault zone photo of figure 5.3. It was a privilege to have you at my side for fieldwork!

I acknowledge the European Commission for funding this PhD Project as part of the ABYSS Initial Training Research network (project number 608001).

Chapter 1 Introduction

1.1 Rationale

Oceanic crust formed at mid-ocean ridges covers almost two thirds of our planet. Nearly 50% of todays ocean floor has been formed at fast spreading rates (> 80 mm/y, half-spreading rate) (e.g., Bird, 2003; Müller et al., 2008; Teagle et al., 2012). The formation of new oceanic crust is a fundamental process in the global plate tectonic cycle. Hydrothermal circulation occurring close to mid-ocean ridges and on the vast ridge flanks, driven by the available heat of crystallising magma and the cooling of the lithosphere (e.g., Morton and Sleep, 1985; Sleep, 1991), results in the exchange of chemical elements between the oceans and the solid Earth and ultimately changes the chemical composition of the oceans, the crust and the mantle (Palmer and Edmond, 1989).

To date, there remain major short-comings in our understanding of the formation of oceanic crust at fast-spreading mid-ocean ridges and in particular, the accretion of the deeper plutonic portion of the ocean crust. There are two long-standing end-member models of how oceanic crust is accreted: the gabbro glacier model where magma crystallises in a shallow melt lens and the lower crust is formed via the subsidence of crystal mush (Henstock et al., 1993; Morgan and Chen, 1993; Quick and Denlinger, 1993), and the sheeted sills model where the lower crust is formed by in-situ crystallisation of magma in sills distributed throughout the lower crust (Kelemen et al., 1997; MacLeod and Yaouancq, 2000). To be thermally feasible, both models require hydrothermal circulation as a heat sink to remove the latent heat released during the crystallisation of magma (e.g., Chen, 2001; Maclennan et al., 2004; Theissen-Krah et al., 2016). In the gabbro glacier model this hydrothermal circulation is restricted to the upper crust, whereas in a sheeted sills model circulation is required down to the base of the crust to remove heat. Whether such vigorous hydrothermal circulation occurs in the deep crust is still under debate principally because of a dearth of samples from modern fast-spreading ocean crust (e.g., Teagle et al., 2012).

Hydrothermal alteration throughout the oceanic crust is a key evidence of ancient hydrothermal circulation. Hydrothermal veins are the fossil traces of former hydrothermal fluids and allow the reconstruction of the geochemical properties of the fluid and to the estimation of alteration conditions. During intense hydrothermal fluid-rock exchange, some elements are leached from one part of the crust and transported and deposited at different locations. However, the extent and the conditions of hydrothermal alteration in the lower oceanic crust remains poorly constrained. The aim of this thesis is to geochemically and structurally characterise hydrothermal

alteration of the lower oceanic crust in the Samail ophiolite in Oman in greater detail. The Samail ophiolite in the Sultanate of Oman is the largest obducted piece of ancient ocean crust on the continent and serves as a unique model to study processes related to the formation and alteration of ocean crust.

1.2 Mid-ocean ridge processes and ocean crust formed at fast spreading ridges

The formation of oceanic crust at mid-ocean ridges plays a fundamental role in the global plate tectonic cycle. With a total length of about 60,000 km, mid-ocean ridges represent the largest volcanic system on Earth. Mid-ocean ridges can be classified into four main groups, according to their spreading rate (half-spreading rate givien throughout the text): fast spreading (> 80 mm/y; e.g. East Pacific Rise), intermediate spreading (40-80 mm/y; e.g. Juan de Fuca ridge), slow spreading (< 40 mm/y; e.g. Mid-Atlantic ridge) and ultraslow spreading ridges (< 20 mm/y; Gakkel ridge, Southwest Indian ridge) (Müller et al., 2008; Figure 1.1). The spreading rate at which oceanic crust is formed, directly influences the structure of the ridge and the crust itself. Fast spreading ridges are characterised by a narrow axial high, overlapping spreading centres and a layered, homogenous structure. These characteristics are mainly the result of spreading being accommodated by magmatism (e.g., Detrick et al., 1987; Kent et al., 1993; White et al., 2002).

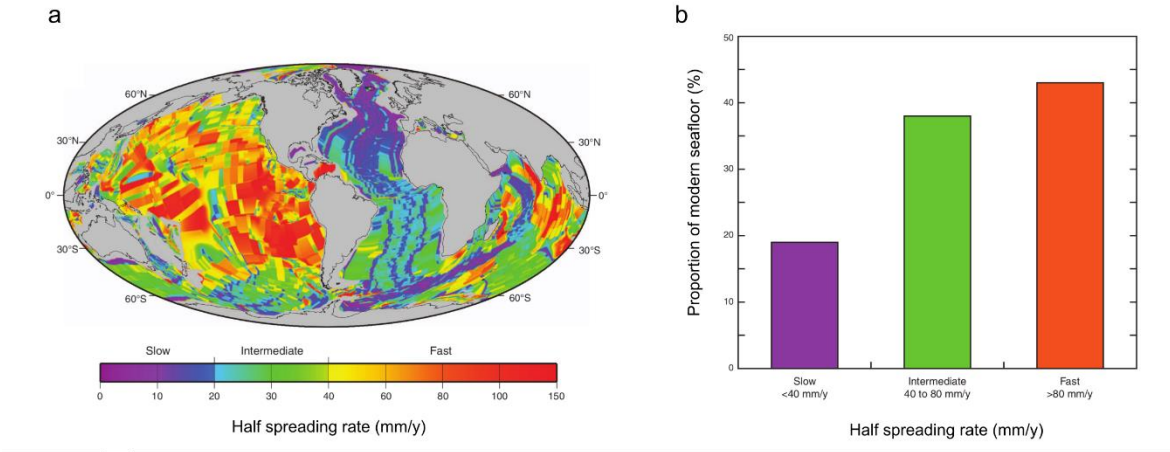

Figure 1.1: Distribution of oceanic crust formed at different spreading rates. (a) Global view showing oceanic crust colour coded according to half-spreading rates and (b) Histogram of proportion of modern seafloor (%) formed at corresponding half-spreading rates. Oceanic crust formed at fast spreading rates accounts for more than 40% of modern oceanic crust. Map from Müller et al. (2008) and histogram from Teagle et al.(2012).

In contrast, ocean crust formed at slow-spreading rates typically shows a wide axial valley and a more heterogeneous and variable structure due to much lower magma fluxes and dominant ductile to brittle deformation.

This layered structure of the ocean crust has been confirmed by direct sampling of modern in-situ oceanic crust via deep ocean drilling and dredging samples during numerous expeditions. To this day, there are two ODP/IODP holes that penetrating through the entire extrusive lavas and into the sheeted dyke complex: Holes 504B and 1256D. Hole 504B is located on 6.9 Ma ocean crust formed at intermediate spreading rates at the Costa Rica Rift. It was drilled to 1836 metres below seafloor (mbsf) and is the deepest hole into hard rocks of the oceanic basement accomplished so far. It includes more than 1000 m of sheeted dykes (Alt et al., 1993). Hole 1256D was drilled and deepened during four expeditions and reaches a depth of 1257 metres sub-basement (msb), and is the only penetrating the dyke/gabbro transition and the upper gabbros (Teagle et al., 2006; Wilson et al., 2006, 2003). This hole is located on 15 Ma ocean crust formed at super-fast spreading rates at the East Pacific Rise. Further knowledge on the structure and petrology of crust formed at fast-spreading rates was gained from dredging and drilling expeditions to tectonic windows such as Hess Deep at the junction of the East Pacific Rise (EPR) and Cocos-Nazca ridge east Pacific (Lonsdale, 1988) and Pito Deep on the Easter microplate (Party et al., 1988).

The thickness of the crust has been determined by seismic methods on modern and in-situ oceanic crust and is on average ~ 6-7.5 km (e.g., Dunn, 2015; Canales et al., 2003; White et al., 1992). The geophysical structure of the oceanic crust is characterised by four layers, displaying characteristic seismic velocities. Layer 1 corresponds to the sediments on top of the ocean crust and is underlain by a low density Layer 2, which can be further sub-divided into layer 2A (V_p < 3 km/s) and 2B (V_p > 4.5-5.0 km/s). Layer 3 shows the highest velocities with V_p = 6-7 km/s (Detrick et al., 1994). The seismic boundary beneath Layer 3 is the Mohorovicic Discontinuity (Moho) and represent the transition from Layer 3 into seismic velocities of approximately V_p = 8-8.5 km/s characteristic of mantle peridotites (Miller and Christensen, 1997). The Moho has been interpreted to be the transition from crustal to upper mantle rocks. Generally, it is not straightforward to link the geophysical layers with the observed geology, as the changes in layers does not coincide with the observed petrological changes between lavas and sheeted dykes and the dyke-gabbro transition. The boundary between Layer 2A/B is usually found within the lavas but was also found at the lava-dyke transition (Christeson et al., 2007). It was proposed that this boundary might reflect an alteration front below which porosity is filled by secondary hydrothermal minerals, resulting in an increase in seismic velocity (Christeson et al., 2007). The boundary between Layer 2 and 3 does not correspond to the boundary between sheeted dyke complex and the gabbroic section but has only been observed and sampled within the sheeted

dykes at ODP Hole 504B (Detrick et al., 1994). In contrast, upper gabbros of Hole 1256D show characteristics of Layer 2B (Gilbert and Salisbury, 2011; Teagle et al., 2006).

Initial geophysical studies on fast-spreading oceanic crust at the East Pacific Rise documented the existence of a high amplitude reflector with a low velocity at the top of the lower crust, which was interpreted to be a small and shallow melt lens (Detrick et al., 1987). Below this melt lens a zone of low velocity extending for 1-2 km from the axis was interpreted as a mostly solidified zone, possibly a crystal mush with less than 3% of melt remaining (Detrick et al., 1987; Sinton and Detrick, 1992). In addition to a shallow axial melt lens, small lenses at the base of the crust, near the Moho (Canales et al., 2009; Dunn et al., 2000) as well as in the Moho transition zone (Singh et al., 2006) were imaged by multi-channel seismic experiments. More recent 3D seismic experiments further confirm the existence of melt lenses at the base of the crust (Aghaei et al., 2014; Arnulf et al., 2014) but also reveal that the nature of the Moho transition zone is highly variable, potentially indicating variations in the accretion style (Aghaei et al., 2014). A stack of multiple melt lenses over roughly 900 m could be shown by 3D seismic at an overlapping spreading centre on the East Pacific Rise (Arnulf et al., 2014), Off-axis melt lenses (2-10 km off-axis) mostly at depths of the sheeted dyke-gabbro transition zone but also down to 4.5 km depth were imaged by 3D seismic experiments at the East-Pacific-Rise (Han et al., 2014). Although such off-axis melt lenses are abundant, estimates show that they are likely to contribute only little to the overall crustal volume. However, they might affect the thermal structure, the mineralogy and composition of the surrounding country rock significantly and may facilitate high temperature off-axis hydrothermal circulation (Han et al., 2014).

1.3 Accretion of the lower oceanic crust

On the basis of petrological observation from ophiolites and geophysical studies on modern oceanic crust two end-member models on the accretion of the lower oceanic crust at fast spreading rates have been proposed (Figure 1.2): the gabbro glacier model (e.g., Henstock et al., 1993; Morgan and Chen, 1993; Quick and Denlinger, 1993) and the sheeted sills model (e.g., Bédard et al., 1988; Kelemen et al., 1997; Korenaga and Kelemen, 1997; MacLeod and Yaouancq, 2000). The gabbro glacier model proposes a formation of the lower crust by crystallisation of magma in one single shallow melt lens and the subsequent outwards and downwards flow of the crystal mush, leading to the formation of the lower crust. This model was established mainly on geophysical observations of the East-Pacific Rise (EPR) and was then further developed by observation from the magmatic layering observed in the lower crust of the Samail ophiolite (e.g., Morgan and Chen, 1993; Quick and Denlinger, 1993). To be thermally feasible, the gabbro glacier model requires extensive hydrothermal cooling in the upper oceanic crust in order to remove

latent heat from the crystallisation process but a conductive cooling for the lower crust would be possible. Several studies on cooling rates estimated from Ca diffusion in olivine throughout the lower crust of the Samail ophiolite (Coogan et al., 2002b), Mg diffusion in plagioclase from the upper plutonic section of the East Pacific Rise (Faak et al., 2015) and from a combined Mg in plagioclase and Ca in olivine cooling rate study of gabbros from Hess Deep (Faak and Gillis, 2016) favour near conductive cooling of the lower crust.

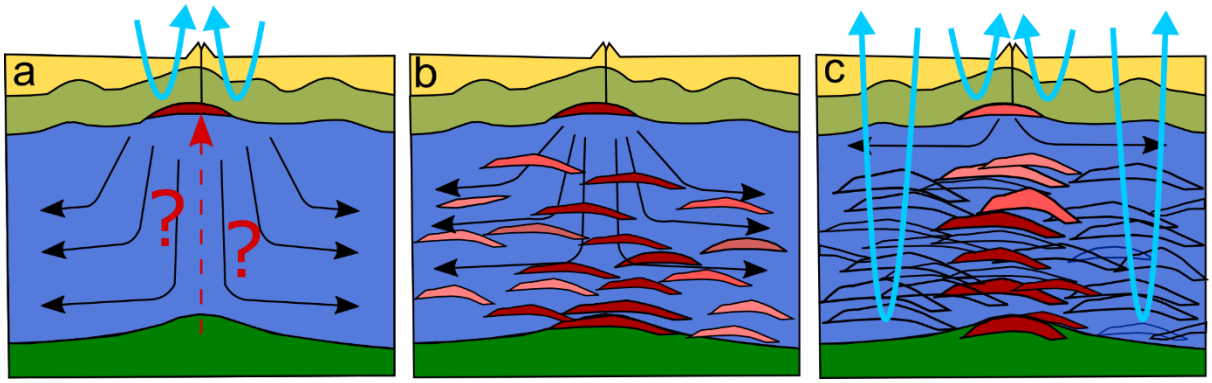

Figure 1.2: Schematic illustration of the two end-member models of the formation of oceanic crust, modified after Teagle et al. (2010). (a) Gabbro glacier model, where melt ponds in a shallow axial melt lens and lower crust is formed by subsidence and outward flow of crystal mush (e.g., Henstock et al., 1993; Morgan and Chen, 1993; Quick and Denlinger, 1993). (b) A hybrid model where crust is formed from both, a shallow melt lens including ductile flow and in-situ crystallisation in sills (e.g., Boudier et al., 1996). (c) Sheeted sills model where the lower crust is formed in-situ by the intrusion and crystallisation of melt at all levels in the lower crust (e.g., Bédard et al., 1988; Kelemen et al., 1997; Korenaga and Kelemen, 1997; MacLeod and Yaouancq, 2000).

The sheeted sills model proposes the crystallisation of magma in-situ in multiple small melt lenses distributed throughout the lower crust. This model was first proposed on the basis of observations of gabbroic sill intrusions at the crust-mantle boundary in the Samail ophiolite, which were interpreted as in-situ crystallisation products (Kelemen et al., 1997). Later on it was further confirmed by studies showing chemical changes with depth in the plutonic section on different scales and thicknesses of metres to hundreds of metres have been calculated for such melt lenses (Korenaga and Kelemen, 1997; MacLeod and Yaouancq, 2000). A crystallisation of magma throughout the lower oceanic crust requires an efficient heat extraction via hydrothermal circulation deep in the plutonic section (Chen, 2001). Such a convective cooling of the lower crust was further inferred from cooling rate studies derived from diffusion of Ca in olivine from the Samail ophiolite from VanTongeren et al. (2008), contrasting the results of Coogan et al. (2002a)

and from a Mg and REE bulk diffusion study between co-existing plagioclase and pyroxene in the gabbros from the East Pacific Rise and Hess Deep (Sun and Lissenberg, 2018).

A mixed model between both end-member accretion styles may be more likely in reality and has been proposed earlier (e.g., Boudier et al., 1996); where the upper oceanic crust predominantly forms at gabbro glacier style and the lower crust by multiple sill intrusions.
Whether a sheeted sills model or a hybrid model is considered, the critical point is the requirement for the removal of the heat released during crystallisation to allow the cooling of the lower crust. The total amount of heat in the lower crust is the sum of the latent heat being released during crystallisation and the sensible heat, which is the heat being released when the crust cools down to a lower temperature. Depending on the temperature the crust is cooled down to, the total amount of heat is considerable and has to be removed in order to solidify the lower crust. Geophysical observations show that the crust is completely solidified within 2 km from the ridge axis (Vera et al., 1990), hence there must be a significant heat-sink like hydrothermal circulation. Results obtained from thermal models calculating the proportion of lower crust which may be formed in-situ vary considerably. An early model by Chen (2001) suggests that less than 10% of the lower crust could crystallise in-situ to fit the thermal structure. A more advanced model, taking both the geophysical and geochemical structure into account favours a hybrid model in which 25-75% of the lower crust is formed in a shallow melt lens and the rest crystallises in-situ (Maclennan et al., 2004). Numerical models simulating coupled crustal accretion and hydrothermal circulation at fast-spreading ridges infer that the majority of the lower crust is formed in a shallow melt lens with less than 50% crystallising in-situ within sheeted sills (Theissen-Krah et al., 2016, 2011). Theissen-Krah et al. (2016) further implies that deep hydrothermal circulation must occur as otherwise the thermal structure of the oceanic crust is inconsistent with seismic tomography data.

Even though new and more precise geophysical studies were carried out in recent years, imaging the ocean crust to a higher resolution (e.g., Aghaei et al., 2014; Arnulf et al., 2014; Canales et al., 2009; Han et al., 2014; Singh et al., 2006) and detailed numerical models integrating geophysical and geochemical constraints have been developed (e.g., Hasenclever et al., 2014; Maclennan et al., 2004; Theissen-Krah et al., 2016, 2011), there are still many unresolved questions concerning the thermal structure and the accretion process of fast-spreading oceanic crust. This is principally due to a dearth of samples from deep intact ocean crust that can be used to test competing hypotheses outlined above.

1.4 Ophiolites versus modern in-situ ocean crust

The relatively ease of access of ophiolites compared to in situ ocean crust means that ancient ocean crust can be studied, mapped and sampled in three dimensions. Consequently ophiolites provide invaluable sources of information on the structure and the evolution of oceanic crust. However, many ophiolites show geochemical indications that they might not have formed entirely by spreading along mid-ocean ridges in a large ocean basin. In addition to conventional mid-ocean ridge basalt (MORB) rocks found at mid-ocean ridges, the many ophiolites include abundant differentiated rocks and basalts with a different geochemical trace element signature, suggesting formation in some form of supra-subduction zone setting (e.g., Miyashiro, 1973; Pearce et al., 1984). Moreover, some ophiolites display a complex and disrupted structure due to their obduction history. This makes a reconstruction of the initial stratigraphy more complex. Moreover, the estimated time integrated hydrothermal fluid-fluxes through ophiolitic ocean crust are about an order of magnitude greater than estimated hydrothermal fluid fluxes through modern in-situ crust (Bickle and Teagle, 1992; Davis, 2004; Gillis et al., 2005; Teagle et al., 2003). For these reasons, although ophiolites are good analogues of intact and modern ocean crust they are not perfect, and may not be fully representative of crust formed at the mid-ocean ridges in large oceanic basins. This has to be considered and kept in mind when doing research on ocean crust sampled from ophiolites and extrapolating findings to the modern plate tectonic cycle. Nevertheless, the gabbroic lower crustal rocks that crop out in the Samail ophiolite of the Sultanate of Oman remain some of our best, and to some extent only, sources of information on the structural, petrological, hydrothermal and geochemical properties of lower oceanic crust.

1.5 Hydrothermal circulation

Hydrothermal circulation in the oceanic crust is an important process; not only for the extraction of heat during crustal accretion but also for the chemical and isotopic exchange between the crust and the oceans (Elderfield and Schultz, 1996; Palmer and Edmond, 1989a). Throughout the oceanic crust hydrothermal circulation is recorded and preserved by secondary minerals that fill fractures, porosity and replace primary minerals in altered rocks. Secondary minerals formed at different temperatures and therefore under different conditions can provide a time-integrated record of all stages of hydrothermal circulation as the crust cools and ages. There has been substantial work on the alteration present in the upper part of intact ocean crust, including the lavas and the sheeted dyke complex. There, the progressive downward transition from low temperature alteration to higher temperature, mainly under greenschist facies conditions, is well documented from sampling both, in-situ ocean crust by deep drilling as well as ophiolites (e.g.,

Alt, 1995; Alt et al., 2010; Bickle and Teagle, 1992; Gillis et al., 2001; Harris et al., 2015; Heft et al., 2008; Nehlig and Juteau, 1988a; Teagle et al., 1996).

1.5.1 Hydrothermal circulation and alteration in the lower oceanic crust

There are relatively few existing studies on hydrothermal alteration of the deeper, gabbroic section of the crust. This is primarily due to the dearth of samples from in-situ ocean crust but also because hydrothermal circulation traditionally has been considered to be restricted to the upper crust. Lower crust from the Samail ophiolite and Hess Deep provide the most detailed insights into lower crustal hydrothermal alteration so far. In the early 1980`s oxygen- and strontium isotope studies from layered gabbros samples in the Samail ophiolite as well as lower crust exhumed at the Macquarie Island ophiolite suggested the existence of a deep hydrothermal system (Cocker et al., 1982; Gregory and Taylor, 1981; Lanphere et al., 1981; McCulloch et al., 1981). This was confirmed by the documentation of an early- and high temperature amphibole vein system from both, Hess Deep and the Samail ophiolite gabbros (Bosch et al., 2004; Früh-Green et al., 1996; Manning et al., 1996; Manning and MacLeod, 1996; Nehlig et al., 1994; Nehlig and Juteau, 1988b; Nicolas et al., 2003). These amphibole veins may be the fossil trace of a cracking front at the interface between the hydrothermal and the magmatic system, with estimated temperatures for amphibole formation of 700 °C at the dyke-gabbro transition and 825 °C at the crust-mantle boundary (Manning et al., 2000). Similarly, hydrothermal alteration at even higher temperatures (700-1000 °C; (Nicolas et al., 2003) is suspected (Bosch et al., 2004; Nicolas et al., 2003), where recharge occurs via a regularly spaced network of micro-cracks, now preserved as the previously described amphibole veins, and a discharge system manifested in a network of pargasite-bearing gabbroic dykes which are the product of hydrous partial melting. Thermodynamic reaction-path models support the formation of anhydrous alteration at temperatures > 750 °C resulting in an alteration assemblage of plagioclase ± clinopyroxene ± olivine ± magnetite and suggests that hydrothermal alteration in the lower crust may take place with little petrological evidence (Gregory and Taylor, 1981; McCollom and Shock, 1998). Hydrous partial melting has been further suspected in samples showing typical microstructures and mineral paragenesis of orthopyroxene and pargasite rimming olivine and clinopyroxene in contact with neoblastic, An-enriched plagioclase (Koepke et al., 2014, 2005).

On the basis of structural observations, Nicolas et al. (2003) proposed that gabbroic dykes formed as the result of hydrous partial melting grade into lower temperature hydrothermal veins formed at greenschist facies conditions up-section (400-500 °C). Such discrete vein systems comprise zoisite and zoisite-epidote veins cross-cutting the earlier and higher-temperature amphibole veins

throughout the lower crustal section in Oman and are interpreted to be formed off-axis (Nehlig and Juteau, 1988b).

In contrast to isolated veins distributed through the lower crust, Coogan et al. (2006) showed the presence of discrete and widely spaced zones, that are up to tens of metres wide, of intense mainly greenschist facies hydrothermal alteration. Fluid flow within these zones is suspected to have started at around 800 °C and continued down to < 300 °C indicated by amphibole microthermometry and other secondary mineral paragenesis. Based on strontium isotope and preliminary oxygen isotope data, Coogan et al. (2006) demonstrated an intense interaction with a seawater derived hydrothermal fluid within these zones. High fluid fluxes through these channels are suspected to reset the Sr-isotopic composition of the crust to equal that of the fluid and enhanced cooling rates in the surrounding crust have been inferred. From observations on aerial photos, Coogan et al. (2006) estimates that these zones occur approximately every kilometre.

1.5.2 Elemental mass changes during hydrothermal alteration and global elemental fluxes

From upper crustal hydrothermal and black smoker systems chemical changes occurring during intensive hydrothermal fluid-rock interactions at high temperatures are well documented, from both ophiolites (Alt, 1994; Coggon et al., 2016; Gillis, 2002; Gillis and Robinson, 1990; Harper et al., 1988; Nehlig et al., 1994) and in-situ oceanic crust (Alt and Teagle, 2000; Hart and Staudigel, 1982; Humphris et al., 1998; Teagle et al., 1996; Teagle and Alt, 2004). The reaction of the rock with a 350-440 °C hydrothermal fluid leads to a depletion in metals (mainly Cu and Zn) and sulphur (Alt, 1995; Bednarz and Schmincke, 1989; Harper et al., 1988; Nehlig et al., 1994; Seewald and Seyfried, 1990; Teagle and Alt, 2004), as well as alkali elements, namely Li, K, Rb, Cs and B (e.g., Alt, 1995; Gillis et al., 1993; Humphris and Thompson, 1978), which are carried away with the hydrothermal fluid. Cu and Zn can then be precipitated with pyrite in stockwork zones or in seafloor massive sulphides forming metal deposits and the loss of alkalis leads to the observed enrichment of Li, K, Rb, Cs and B in high-temperature mid-ocean ridge axial vent fluids (Von Damm, 1995). However, only little is known about elemental movements during hydrothermal circulation in the lower crust. Preliminary studies indicate that, similar to the upper crustal system, metals such as Cu and Zn are being leached from the rock during alteration with a hydrothermal fluid at greenschist facies conditions (Alt et al., 2010; Coogan et al., 2006).

There are few studies extrapolating chemical mass changes to global hydrothermal fluxes to quantify the contribution of hydrothermal circulation to the global chemical budget (e.g., Bach et al., 2003; Bednarz and Schmincke, 1989; Coggon et al., 2016; Coogan and Dosso, 2012; Staudigel, 2014). These studies vary in several ways as they quantify different sections of the crust, at

various ages and consider crust altered at different conditions. Overall, there are two studies quantifying the contribution of pervasive background alteration through the whole crustal section to the global elemental cycle: (i) a full section of 10 Ma ocean crust sub-aerially exposed in the sub-Antarctic Macquarie Island ophiolite (Coggon et al., 2016); and (ii) samples of ocean crust recovered from several sites by scientific ocean drilling, that were combined to yield a composite full-crustal section (Staudigel, 2014). Even though both studies were done on ocean crust formed at similar, relatively slow spreading rate, there are significant discrepancies between the results of these two studies, which most likely reflect both global variations in the nature of hydrothermal circulation but also the differing approaches used to calculate the fluxes. This shows the real need for a better constraint of global hydrothermal elemental fluxes. Consequently, hydrothermal elemental fluxes need to be determined for ocean crust produced at different spreading rates and not only background alteration but also veins, fault zones and regions of focussed fluid flow need to be taken into account in order to define global hydrothermal flux estimates.

1.6 Geology of the Samail ophiolite, Sultanate of Oman

1.6.1 Geological history

The Samail ophiolite is generally regarded as the best analogue of fast-spreading oceanic crust preserved on land (e.g., Nicolas et al., 2000). It stretches approximately 550 km in length and 50 km in width along the coast of the Sultanate of Oman and the United Arab Emirates (UAE) (Figure 1.3). The ophiolite was formed in a spreading centre in the Neotethyan ocean during the Late Cretaceous (Searle and Cox, 1999). Zircons from gabbros and late stage intrusive bodies such as tonalites and trondhjemites from all over the ophiolite were dated by U-Pb and yield ages between 97 to 93 Ma (e.g., Rioux et al., 2013, 2012; Tilton et al., 1981; Warren et al., 2005) with most ages in between 96.44 to 95.48 Ma (Rioux et al., 2013). This age span marks the formation age of the crustal rocks and suggests that most of the ophiolitic crust was formed by ridge axis magmatism within a very short period of < 1 Ma (Rioux et al., 2013). Neodymium isotopes show similar compositions to modern MORB, supporting a formation from a MOR-type mantle source (Rioux et al., 2013). Westward thrusting onto the eastern margin of the Arabian Shield is likely to have started at ~ 95 Ma (e.g., Hacker et al., 1996; Warren et al., 2007, 2005) and peak metamorphic conditions of the metamorphic sole were reached at ~87-79 Ma (e.g., Gnos and Peters, 1993; Hacker et al., 1996; Searle and Cox, 2002; Warren et al., 2005, 2003). Despite numerous studies into the paleo-tectonic setting of the ophiolite, it is not entirely clear and remains debated. Originally, the ophiolite was considered to have formed purely in a normal mid-ocean ridge magmatic environment (Coleman, 1981). But the discovery of a second, locally

intruding and more hydrous magmatic stage and makes the influence of a subduction zone likely (e.g., Alabaster et al., 1982; Godard et al., 2003; Lippard et al., 1986; Pearce et al., 1981; Searle and Cox, 1999b, 2002; Searle, 1980; Searle and Malpas, 1982; Warren et al., 2005). This younger, second stage magmatism comprises pyroxenites, gabbronorites, olivine gabbros and wehrlites intruding the crust in all levels (e.g., Alabaster et al., 1982; Goodenough et al., 2013; Juteau et al., 1988; Koepke et al., 2009; Python and Ceuleneer, 2003). Within the extrusive sequence, lavas with compositions attributed to subduction related volcanism cross-cut earlier, more MORB-like lavas and are generally summarised under the term "V2 lavas" (e.g., Alabaster et al., 1982; Ernewein et al., 1988; Godard et al., 2003; Pallister and Knight, 1981). U/Pb ages of intruding dykes, sill and stocks from the crust and mantle reveal ages between 95.41-95.07 (Rioux et al., 2013), younger than rocks formed during the main accretion stage. Neodymium isotopic compositions of intruding sills, dykes and stocks are slightly lower than on-axis rocks and more similar compositions to the V2 volcanic series (Rioux et al., 2013).

Many authors propose that the main accretion stage of the ophiolite happened at a spreading centre in a marginal basin above an infant subduction zone and second stage magmas were emplaced as the subduction zone developed (e.g., Boudier et al., 1988; Koepke et al., 2009; Rioux et al., 2013). The influence of the subduction zone is more pronounced in the northern part of the ophiolite and the proportion of second stage magmatic rocks decreases southwards. In the two most southern massifs (Samail and Wadi Tayin) the second stage magmatic intrusions are limited to minor intrusions in the mantle and V2 lavas are mostly absent (e.g., Godard et al., 2003; MacLeod et al., 2013), although primary water contents are still elevated compared to primary MORB (MacLeod et al., 2013). This makes the lower crustal rocks exposed in the Wadi Tayin block of the ophiolite an ideal location to investigate the deep processes that occur during the accretion of the lower crust at fast spreading mid-ocean ridges.

Generally, the Samail ophiolite is regarded to have formed at a relatively fast spreading mid-ocean ridge. This is based on the following observations: (i) the ophiolite shows a typical layered structure with lavas, followed by a sheeted dyke complex and a gabbroic lower crust and a crust-mantle transition zone (Moho transition zone) (Lippard et al., 1986); (ii) there are no observations of large transform faults which would indicate a formation in a slow-spreading environment (MacLeod and Rothery, 1992; Nicolas et al., 2000); (iii) the narrow crystallisation range inferred from U/Pb ages in zircons (Rioux et al., 2013, 2012; Tilton et al., 1981; Warren et al., 2005); and (iv) the orientation of a well-developed sheeted dyke complex perpendicular to the Moho (MacLeod and Rothery, 1992).

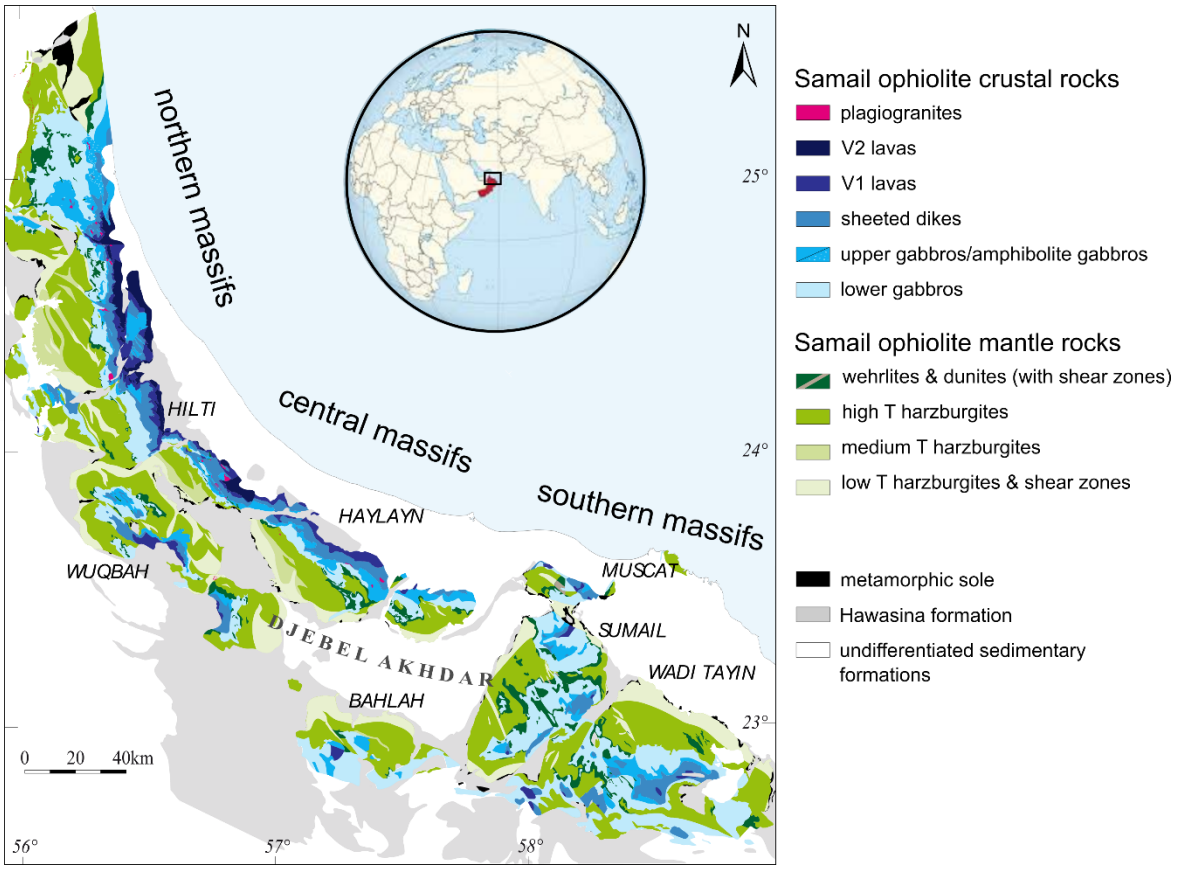

Figure 1.3: Overview map of the whole Samail ophiolite. Mantle rock are shown in green and crustal rocks are displayed in various shades of blue. Map modified after Nicolas et al. (2000). Map courtesy of Jude Coggon (Oman Drilling Project).

Nowadays, the ophiolite is divided into 12 individual thrust-bound blocks (Nicolas et al., 2000) and shows the complete “Penrose” sequence of rock types (as defined by Penrose Conference participants in 1972) expected to be formed at a fast spreading mid-ocean ridge. This sequence is made of the following rock types from top to the bottom of the crust (thicknesses after Coogan et al. 2002; Nicolas et al., 1996):

- Extrusive suite comprising (predominantly pillowed) lava flows which are partially overlain by metalliferous sediments (umber) and /or pelagic sediments. Typically, the lava sequences in the Samail ophiolite are about 0.5 km thick (Nicolas et al., 2000).
- Well-developed sheeted dyke complex with dykes trending parallel to the paleo-ridge axis and perpendicular to the Moho (MacLeod and Rothery, 1992). The thickness of the sheeted dyke complex varies throughout the ophiolite from 1 to 1.5 km, with greater thicknesses generally in the northern part of the ophiolite.
- The plutonic lower crust consists of high-level varitextured gabbros (0.1-1 km) beneath the sheeted dyke complex, underlain by cumulate planar-foliated gabbros (0.3-1 km) and cumulate layered gabbros (1-4 km) (Nicolas et al., 2000).

- The Moho transition zone is dominated by the increasing abundance of ultramafic rocks with depth. Its thickness varies from tens of metress to hundreds of metress.
- The mantle sequence, 8-12 km thick, comprising harzburgite and minor but locally major proportions of dunite.
- The ophiolite is separated from the underlying metasedimentary and metavolcanic rocks by a several hundreds of metres thick metamorphic sole (Hacker, 1990) with peak metamorphic conditions at amphibolite facies, formed during the obduction of the ophiolite on to the Arabian margin.

1.6.2 Wadi Tayin massif and the Ibra area

As discussed in the previous section, the Wadi Tayin massif is the southernmost of all the different blocks of the Samail ophiolite (Figure 1.3; Figure 1.4) and shows only very few indications of late-stage, subduction zone-related magmatism. It is therefore well suited for studies related to processes occurring during the accretion at the mid-ocean ridge. Mantle rocks (harzburgite and subordinate dunite) are the dominant rock type of the massif but the lower crustal section including the layered gabbros are well exposed in many areas. Classical work including structural, petrographic and isotope geochemical observations on the accretion of the lower crustal section of the ophiolite were carried out in several valleys (e.g Wadi Qafifah, Wadi Khadir, Wadi Gideah, Wadi Saq) of the Wadi Tayin, most of them in the Ibra area (e.g., Hopson et al., 1981; Lanphere et al., 1981a; McCulloch et al., 1980; Pallister, 1981; Pallister and Knight, 1981).

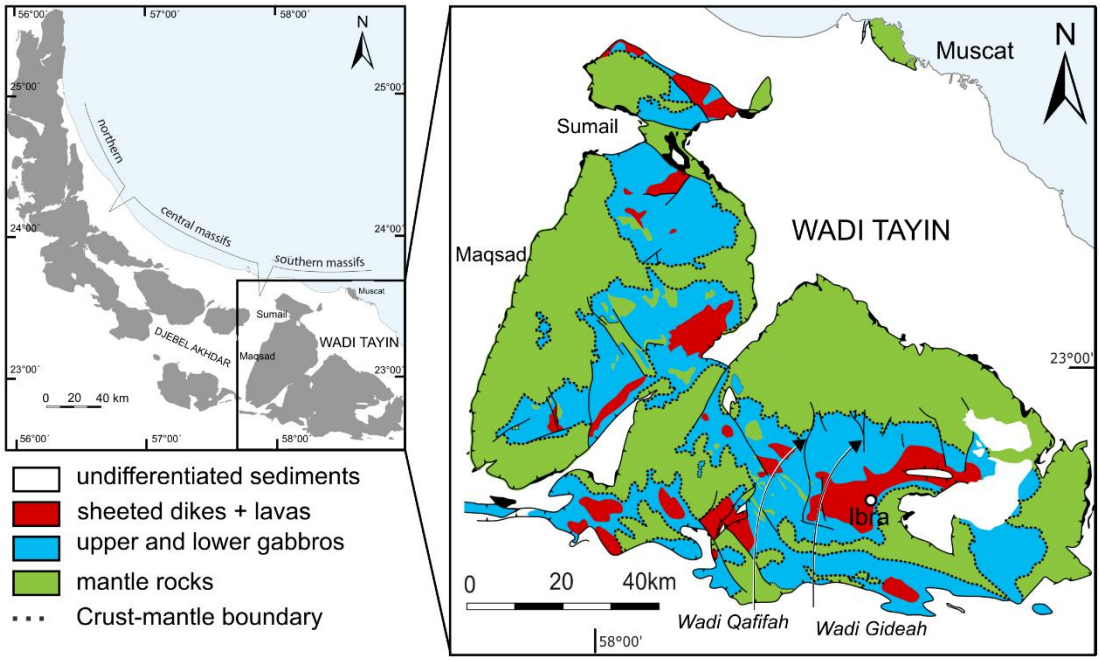

Figure 1.4: Overview of the Wadi Tayin massif. Map modified after Nicolas et al. (2000).

The Ibra area is structurally defined by a large syncline with the Ibra valley in its core (Hopson et al., 1981; Pallister, 1981). This synclinal structure is suggested because the sequence from lower crustal rock up to dykes is repeated in both the northern and the southern flank of the Ibra valley. Lavas and dykes are in the core of the syncline. Whereas the ophiolitic section along the northern limb is well developed and shows mainly undisturbed sequences, it is greatly thinned out along the southern limb.

1.7 Aims of this thesis

This thesis was undertaken to investigate hydrothermal alteration in the lower oceanic crust in the Samail ophiolite and to addresses the following aims:

- To determine a sequence of hydrothermal alteration in the lower oceanic crust and to provide a detailed description of vein and alteration mineralogy including major element characterisation of primary and secondary minerals.

- To provide estimations on formation temperatures of different observed hydrothermal alteration stages.

- To estimate how far hydrothermal alteration extends away from veins into the host rocks and to explore the relationship between vein aperture versus the width of alteration haloes.

- To document zones of channelled hydrothermal fluid-flow, such as faults throughout the lower oceanic crust and to provide mineralogical and Sr-isotopic description of these zones.

- To estimate formation conditions of such as temperature of zones indicating channelled hydrothermal fluid-flow

- To discuss the structural formation conditions of hydrothermal veins and discuss hydrothermal vein formation in a wider tectonic context.

- To characterise a chlorite-rich and mineralised fault zone in the lower layered gabbros Wadi Gideah in terms of major- and trace elements and to discuss possible formation mechanisms.

- To calculate chemical mass-changes occurring during intensive hydrothermal fluid-rock interactions in a lower crustal fault and to extrapolate calculated mass-changes to global elemental fluxes and discuss the importance of a lower crustal fault zones to the global elemental cycle.

1.8 Thesis outline

This thesis consists of an extensive methods chapter, three main results chapters and a conclusions chapter which summarises the main outcomes and provides ideas for future research.

Chapter 2: "Methods". This chapter details the methodologies and analytical techniques used to acquire the data presented in this thesis. It further includes discussions of precision and accuracy of each analytical technique.

Chapter 3: "Cross-cutting hydrothermal alteration observed in the lower ocean crust in Wadi Qafifah, Samail ophiolite, Oman". This chapter presents a detailed study on cross-cutting relationships of high to low temperature alteration of gabboic rocks from the Wadi Qafifah area of the ophiolite. This includes detailed petrographic descriptions of veins and observed background alteration accompanied by mineral composition analysis of primary and secondary minerals by electron microprobe. Building on these observations, an alteration sequence is presented and formation conditions of different alteration stages are estimated. In addition, Sr-isotope composition of fresh layered gabbro, altered whole rock and mineral separates of hydrothermal vein are presented and possible fluid evolution over time and the nature of the hydrothermal fluid is discussed.

Chapter 4: "Fossil hydrothermal discharge zones in the lower oceanic crust, Samail ophiolite Oman". This chapter presents the results of a survey of intensly altered outcrops throughout the lower oceanic crust. All of these outcrops show hydrothermal alteration along discrete fluid-flow and fault zones. Alteration patterns within these zones are described and characterised in terms of secondary mineralogy and strontium isotope composition. The combination of field- and geochemical indications are used to demonstrate that these zones served as discharge zones of hot, upwelling hydrothermal fluids in the lower oceanic crust.

Chapter 5: "A deep hydrothermal fault zone in the lower oceanic crust, Wadi Gideah, Samail ophiolite, Oman". Within this chapter, a deep hydrothermal fault zone that crops out in the Wadi Gideah is characterised by secondary minerals, major- and trace elements and Sr-isotope compositions. Mass changes due to hydrothermal alteration were calculated and indicate which elements were either locally re-distributed, lost to the hydrothermal fluid or carried into the system with hydrothermal fluids. These changes are extrapolated to global elemental fluxes, giving a first estimate of how much a lower crustal fault can contribute to global hydrothermal fluxes. This chapter has been published in the Lithos Special Issue entitled: "*Reactive Geological Systems from the Mantle to abyssal-seafloor*". This chapter is co-authored by Barbara Zihlmann, Samuel Müller, Rosalind Coggon, Jürgen Koepke, Dieter Garbe-Schönberg and Damon Teagle, but

the research has been principally led by Zihlmann. Author contributions: Barbara Zihlmann sampled and analysed major- and trace elements eight of the twelve samples, measured chlorite and epidote composition of two fault rock samples with the electron microprobe, analysed the Sr-isotope composition of all twelve samples, processed the data, calculated mass-changes and global hydrothermal fluxes, wrote the manuscript and made Figures 5.1-5.3, 5.6-5.9 and 5.11-5.12 as well as all the Tables. Samuel Müller analysed major- and trace elements of four of the twelve samples and performed electron microprobe analysis on primary and secondary minerals from the fault rock as well as the wall rocks and provided Figure 5.4 and 5.5. Figure 5.10 was co-produced by Samuel Müller and Barbara Zihlmann. Rosalind Coggon assisted with global fluid-flux calculation and interpretation, and contributed to the written part of the global flux section. Juergen Koepke provided Sr-isotope data from eight fresh layered gabbro samples and commented on an early version of the manuscript. Dieter Garbe-Schönberg provided major- and trace element data of the eight fresh layered gabbro samples around the outcrop and commented on an advanced version of the manuscript. Damon Teagle helped develop this study with the lead author and commented on all versions of the manuscript.

Chapter 6: "Conclusions and outlook". This last chapter summarises the main finding of this study and discusses further ideas and potentials for following research.

Chapter 2 Methods

2.1 Field work

Field work was carried out in January-February 2015 and February-March 2016. At the beginning of the 2015 field work season a range of different outcrops (see Figure2.1) were visited, to establish (i) a general overview of how hydrothermal alteration is developed in outcrops of the lower crustal section of the Samail ophiolite; (ii) to see how variable and/or representative the hydrothermal patterns are, and (iii) to select the most appropriate outcrops for detailed field- and geochemical studies. For a list of all outcrops visited during both field seasons see Table 2.1.

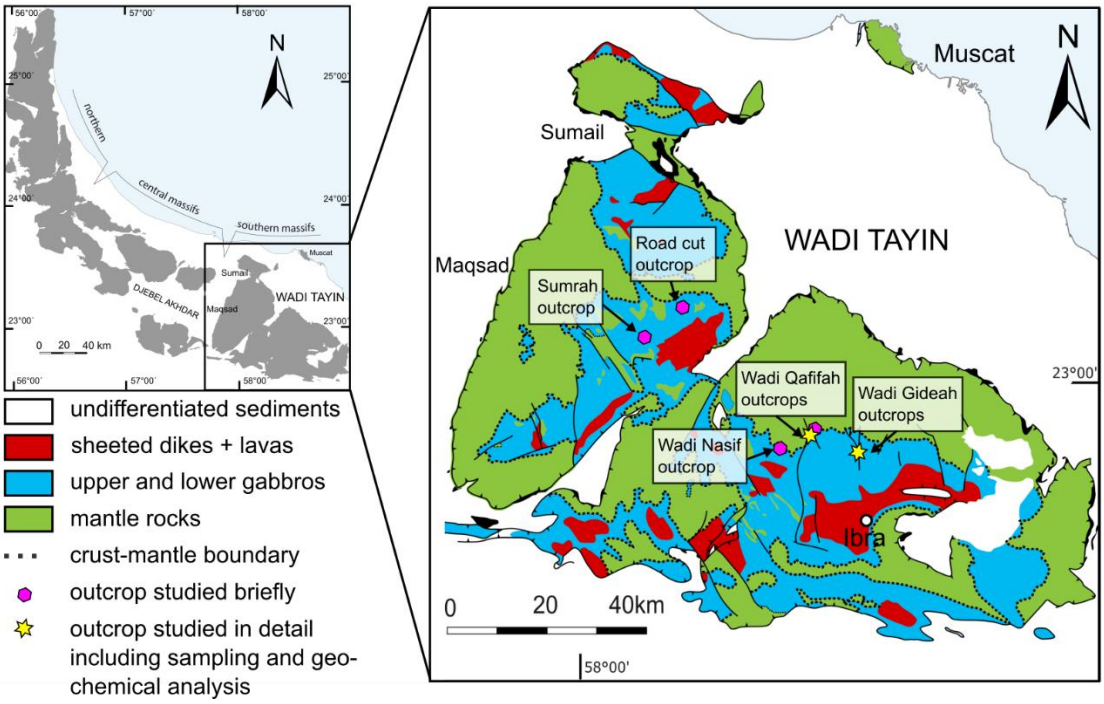

Figure 2.1: Overview of outcrops studied during fieldwork in 2015 and 2016. Outcrops studied only briefly in the beginning of fieldwork season 2015 are marked in pink whereas outcrops studied in more detail, including extensive sampling and geochemical analysis are marked with a yellow star. Map modified after Nicolas et al. (2000).

All outcrops showed similar hydrothermal vein patterns (Table 2.1). However, the overall intensity of alteration as well as the occurrence of cross-cutting relationships are different between individual outcrops. After visiting several outcrops in 2015, outcrop OM1521 in Wadi Qafifah was selected for a detailed study because of the occurrence of all hydrothermal vein types, excellent cross-cutting relationships as well as the existence of fresh and hydrothermally altered gabbro in close proximity. Moreover, Wadi Qafifah has been studied relatively well in terms of evolution and geochemistry of the primary igneous rocks in the early 1980's (e.g., Hopson et al., 1981;

McCulloch et al., 1980; Pallister, 1981; Pallister and Hopson, 1981; Pallister and Knight, 1981), which provided a solid background for a hydrothermal study.

Outcrop OM1523 in Wadi Gideah was discovered together with co-workers from Germany. It was the first outcrop where a sulphide-bearing and chlorite-rich hydrothermal fault zone was discovered. The first field notes, sketches and samples were taken during fieldwork in 2015, but these were supplemented by additional observations and sampling in future visits.

Table 2.1: List with studied outcrop during fieldwork in 2015 and 2016.

	Year	Coordinates	Observed hydrothermal alteration	Observed cross-cutting relationships	Studied in detail
Road cut outcrop along newly built motorway OM1502	2015	23.11015°N/58.16891°E	Amphibole veins and amphibole background alteration, laumontite veinlets	Very few cross-cutting relationships observed	No
Sumrah outcrop OM1505	2015	23.09304°N/58.10387°E	Amphibole veins, few epidote veins, prehnite and laumontite veins, halo alteration	Few cross-cutting relationships observed	No
Sumrah outcrop OM1506	2015	23.08922°N/58.11658°E	Amphibole veins, few epidote and prehnite veins, laumontite veinlets	Few cross-cutting relationships observed	No
Wadi Nasif OM1509	2015	22.89601°N/58.36579°E	Amphibole veins, few epidote veins, laumontite veinlets, amphibole background alteration	Few cross-cutting relationships observed	No
Wadi Qafifah OM1518	2015	22.91170°N/58.43341°E	Amphibole veins, epidote-clinozoisite veins, prehnite veins, laumontite veins; pronounced alteration haloes, fault zones	Yes, cross-cutting relationships observed	No
Wadi Qafifah OM1521	2015	22.89446°N/58.42697°E	Amphibole veins, epidote-clinozoisite veins, prehnite veins, sulphide mineralisation, laumontite and calcite veinlets, pronounced alteration haloes	Yes, excellent cross-cutting relationships observed	Yes, see Chapter 3
Wadi Gideah OM1523	2015/2016	22.89411°N/58.51602°E	Chlorite-rich fault zone, sulphide mineralisation, epidote veins, amphibole veins, prehnite and laumontite veins, calcite veins, pronounced alteration halo	Yes, cross-cutting relationships observed	Yes, see Chapter 4 and 5
Wadi Gideah OM1606	2016	22.90071°N/58.52316°E	Amphibole veinlets, epidote-prehnite veins, laumontite and calcite veinlets	Few cross-cutting relationships observed	No but few samples collected and analysed
Wadi Gideah OM1602	2016	22.84710°N/58.51892°E	Amphibole veins, epidote-clinozoisite veins, prehnite veins, alteration haloes	Few cross-cutting relationships observed	No but few samples collected and analysed
Wadi Gideah OM1605	2016	22.86475°N/58.52312°E	Chlorite-rich fault zone, epidote-clinozoisite veins, amphibole veins, pronounced alteration haloes, laumontite veins	Yes, cross-cutting relationships observed	Yes, see Capter 4
Wadi Gideah OM1609	2016	22.84597°N/58.52522°E	Chlorite-rich fault zone, abundant sulphide mineralisation, epidote veins, amphibole veins, laumontite and calcite veinlets, pronounced halo alteration	Yes, cross-cutting relationships observed	Yes, see Chapter 4
Wadi Gideah OM1616	2016	22.91025°N/58.50533°E	Epidote-prehnite veins, prehnite veins, amphibole veins, laumontite veins, sulphide mineralisation, some halo alteration	Yes, cross-cutting relationships observed	Yes, see Chapter 4

The two main goals of fieldwork season 2016 were to study hydrothermal fault zones and to establish a hydrothermal profile through the lower oceanic crust in the Samail ophiolite. To do so, Wadi Gideah was chosen as this valley cuts across the whole lower crustal section, from the Moho transition zone up to the sheeted dyke complex. Furthermore, the Moho transition zone appears undisturbed showing only minor faulting unlike in many other parts of the Wadi Tayin massif.

Other reasons to choose the valley of Gideah were good knowledge of the geochemistry and evolution of the igneous crustal rocks (Mueller et al., 2017; Müller, 2016) as well as the perspective of the upcoming Oman Drilling Project in 2017 with two boreholes (Hole GT1A and Hole GT2A) planned in the gabbroic section of Wadi Gideah.

Each outcrop studied in detailed was described, sketched and photographed. The orientations of hydrothermal veins and other structural features such as dyke margins or igneous layering were measured. The abundances of hydrothermal veins were accounted and the extent of alteration haloes measured and described. The following geological maps were used: Sheet NF40-7C Samad (De Gramon et al., 1986) mapped in a scale of 1:100,000 and sheet Al Hadmah NF40-8A1 (Peters et al., 2008), mapped in a scale of 1:50,000. To record sample and outcrop locations, a Garmin GPSmap64s was used and the declination for the compass was set to +1°, according to the World Magnetic Model provided by NOAA.

2.2 Sampling and analytical strategy

The overall analytical strategy for this thesis was to work at different scales, from outcrop scale down to the microscopic and atomic scale and to link all results in the end. Therefore, outcrops that were studied in detail were sampled to cover (i) the full range of hydrothermal vein types observed; (ii) altered gabbro in alteration haloes around hydrothermal veins as well as in isolated patches; and (iii) unaltered layered gabbros. Whenever possible, veins showing cross-cutting relationships were sampled or sketched and photographed before taking samples. Each whole rock sample was at least the size of a fist, in order to be representative. After returning from the field, samples were cleaned with a tooth brush and Milli-Q water, sketched, photographed and macroscopically described. A range of suitable and representative samples were chosen for thin section petrography. After detailed petrographic descriptions, samples were selected for further geochemical analysis including major- and trace elemental composition and Sr-isotope composition.

2.3 Petrography

After returning from the field representative samples of fresh gabbro, veins and hydrothermally altered gabbro were cut into thin section billet using a water lubricated diamond saw. Polished thin sections were made to a standard thickness of 30 µm at the University of Southampton. Before performing any bulk rock or mineral geochemical analysis, detailed descriptions of mineral parageneses were made and, mineral abundances and the degree of alteration were estimated

for each sample. On the basis of those descriptions, samples for electron probre micro analysis as well as all geochemical analysis were chosen.

2.4 Scanning Electron Microscope (SEM)

Unknown mineral phases in several thin section were identified using a Carl Zeiss Leo1450VP electron scanning microscope (SEM), at the University of Southampton, equipped with an Oxford Instruments EDS detector coupled to the Aztec Energy software system. Operating conditions were 20 kV at a working distance of 19 mm. Semi-quantitative elemental microanalysis were determined with an Oxford Instrument X-Act-10mm2 area Silicon Drift Detector, coupled with the Aztec Energy software systems. The calculated data have been acquired using standard less analysis and all result are normalised to 100%. Minimum detection limits are 0.195% for Na Kα and decreasing to 0.085% for Ca Kα (Goldstein et al., 2003).

2.5 Mineral chemistry – Electron Probe Micro-Analysis (EPMA)

Major element compositions of minerals were analysed by electron microprobe at the Leibniz University in Hannover, Germany. Analysis were performed on standard polished thin sections with a thickness of 30 µm using a Cameca SX100 equipped with five spectrometers and the Peak Sight software. All data were obtained operating at 15 kV accelerating voltage. For all analysis a focussed and static beam of 15 nA current was applied, with spot sizes of 2 µm except for plagioclase where the beam was defocused to 5 µm. Calibration was done against natural and synthetic standard materials. Counting times are dependent on the element and range from 10 s to 60 s (Cl and F). The international standard materials USNM 111356 Kakanui Hornblende, San Carlos Olivine and Lake County Plagioclase were measured in the beginning and the end of each analytical session to monitor analytical precision. Calculated mean values, precision (%RSD) and reference values for all three standards are listed in Table 2.2.

Major element composition of chlorite in sample OM15-3C and of amphibole, plagioclase, prehnite, laumontite of sample OM15-3A and OM15-3E (Chapter 5) were analysed by electron probe microanalysis (EPMA) at the University of Kiel operating a Joel JXA 8900 R EMP with a 15kV accelerating voltage and a focused and static 15nA beam current with, 15 s counting times. Typical spot sizes were 2 µm except for plagioclase where the beam was defocused to ~5 µm.

Table 2.2**:** Precision of standard material analysed during EPMA analysis at the Cameca SX100 at the University of Hannover. Accepted values from Jarosewich et al. (1980).

	Kakanui hornblende									
	SiO_2	TiO_2	Al_2O_3	FeO	MnO	NiO	MgO	CaO	Na_2O	K_2O
Jarosewich et al., 1980	**40.37**	**4.72**	**14.90**	**11.25**	**0.09**		**12.80**	**10.30**	**2.60**	**2.05**
Koepke, 1995	**40.4**	**4.96**	**14.3**	**10.8**	**0.09**		**12.5**	**10.3**	**2.71**	**2.12**
ean (n=8)	40.61	4.93	14.57	10.25	0.08		12.38	9.96	2.61	2.04
sd	0.19	0.04	0.08	0.11	0.03		0.26	0.06	0.04	0.02
%RSD	0.48	0.85	0.53	1.10	30.94		2.07	0.60	1.72	1.05
	San Carlos olivine									
	SiO_2	TiO_2	Al_2O_3	FeO	MnO	NiO	MgO	CaO	Na_2O	K_2O
Jarosewich et al., 1980	**40.81**			**9.55**	**0.15**		**49.42**	**0.05**		
Koepke, 1995	**41.00**			**10.00**	**0.16**	**0.38**	**49.20**	**0.09**		
mean (n=8)	40.98			9.39	0.14	0.37	49.11	0.08		
sd	0.14			0.12	0.01	0.03	0.67	0.00		
%RSD	0.34			1.32	8.06	6.92	1.37	5.22		
	Lake County plagioclase									
	SiO_2	TiO_2	Al_2O_3	FeO	MnO	NiO	MgO	CaO	Na_2O	K_2O
Jarosewich et al., 1980	**51.25**		**30.91**	**0.46**			**0.14**	**13.64**	**3.45**	**0.18**
Koepke, 1995	**51.90**		**30.60**	**0.50**				**13.90**	**3.78**	**0.12**
mean (n=8)	50.98		30.44	0.40			0.12	13.30	3.74	0.13
sd	0.25		0.12	0.03			0.04	0.08	0.06	0.00
%RSD	0.49		0.38	6.98			32.58	0.64	1.54	3.14

2.6 Sample preparation for geochemical analysis

For whole rock geochemical analysis samples were cut into several cubes using a water lubricated diamond saw. Any saw mark were ground off on a high speed diamond grinding lap in first place and a silicon carbide high speed grinding belt during a second stage. Each sample was thoroughly cleaned with Milli-Q water (>18 MΩ) and ultra-sonicated until there was no turbidity left. Samples were dried at 50-60 °C in an oven overnight. Before milling, each sample was crushed into < 5mm sized pieces using a fly press. In order to prevent any metal contamination from the fly press each sample was wrapped into plastic a bag and a chopping board and a piece of cardboard were placed beneath and on top of the sample. The fly press was cleaned after each sample to prevent any cross-contamination between different samples. Rock chips were milled for about 1-3 min in

hardened chrome-steel heads using a Rocklabs^{TM} top-bench mill until the powder had the consistency of cornflower with no grittiness. Chrome-steel heads were cleaned with Milli-Q and methanol after each run. Additionally, the mills were cleaned with pure quartz sand before milling started and at the end of each session. When milling highly altered or sulphide-bearing samples this procedure was repeated after each samples. After using quartz sand the chrome steel pot were pre-contaminated by milling rock chips of a sheeted dyke sample collected during the first field season in 2015. Powdered samples were finally transferred into cleaned, labelled glass bottles and sub-sampled for major-and trace element and Sr-isotope analysis.

Mineral separates of epidote-clinozoisite, amphibole, prehnite, chlorite, laumontite and calcite veins were obtained by picking individual grains from veins. Veins were cut out of a rock sample with a diamond saw, dried and then crushed in an agate pestle and mortar. Crushed samples were sieved, washed in Milli-Q water and dried overnight. Depending on the mineral, the fraction 150 – 250 µm or 100- 150 µm were picked manually under a binocular microscope. After picking, minerals separates were ultra-sonicated for about 10 min, dried overnight and powdered using an agate pestle and mortar. Picked laumontite mineral separates were further decarbonated with 10 % acetic acid in order to remove any calcite crystals which were too small to be picked out. After decarbonation the mineral separates were washed three times with Milli-Q water and dried in an oven at 40-50 °C overnight.

2.7 X-ray Powder Diffraction (XRD)

X-ray powder diffraction (XRF) was carried out at the University of Southampton, on both selected mineral separates samples and selected whole rock samples in order to qualitatively determine their mineralogical composition. Samples were powdered and measured with a Panaltytical X`Pert Pro Diffractometer equipped with a Cu-tube. Measurements were taken from 2-76 °2θ and for the Panalytical software “Highscore Plus” was used for mineral identification.

2.8 Dissolution of rock powders and picked mineral phases for trace element and Sr-isotope analysis

Standard HF-HNO3 digestions

Samples analysed for trace elements by Inductively-Coupled Plasma Mass Spectrometry (ICP-MS) and strontium isotopes by Thermal Ionization Mass Spectrometry (TIMS) were digested with the following HF-HNO_3 method:

a. Weight in 50 mg of sample powder into a clean Savillex pot

b. Add sufficient concentrated sub-boiled (SB) HNO_3 to form a slurry
c. In a scrubbed fume cupboard add 1 drop of HF per each mg of sample powder
d. Put lid back on and leave Savillex pot on the hot plate at 130 °C overnight
e. Remove sample from the hot plate and leave to cool.
f. Turn scrubber on and remove lid. Check there are no black specks of undissolved sample powder remaining. White or pale colour solids may be present. Dry the sample to incipient dryness on the hotplate at 130 °C.
g. Once the sample is dry, remove it carefully from the hot plate and add approximately 2 mL of SB 6M HCl to dissolve the sample.
h. Place the sample pot back on to the hot plate and leave and allow to reflux until sample as dissolved.
i. Remove the sample from the hot plate and allow to cool. If the sample has failed to completely dissolve add additional SB 6M HCl and repeat reflux.
j. Dry down sample to incipient dryness but do not over dry as this may result in the formation of insoluble oxides. Add sufficient SB 6M HCl to dissolve the sample and leave to dissolve.
k. Transfer the sample into an acid clean and weighted HDPE bottle and make up the sample to an appropriate volume with SB HCl and Milli-Q and weight again. This is the mother solution.

Dilution factors for mother solutions were calculated, generally on the basis of 400. At least one laboratory blank accompanied each batch of digests. The blank sample underwent exactly the same digestion procedure but without any rock powder. International rock Standard Reference Materials JA-2 and PM-S and internal standards BRR-1 and BAS206 were prepared using the same procedure.

Ammonium fluoride (NH_4F) Digestion

Fresh layered gabbro from the Wadi Qafifah outcrop, presented in Chapter 2 were digested using a NH_4F method, adapted from Hu et al. (2013), following the procedure outlined here:

a. Weight out 50 mg of powdered rock sample into a 7 mL screw-top Teflon vial and add a few drops of Milli-Q water.
b. In a scrubbed fume hood 300 mg trace element grade NH_4F are weighted into the 7 mL Teflon vial and vials are tightly closed.
c. All vials are placed inside an oven bag into an electric oven inside a fume hood and were heated at 235 °C for about 5 hours.

d. After cooling down, Teflon vials are opened in a scrubbed fume hood and 1.5 mL of sub-boiled (SB) conc HNO_3 was added and samples were put onto a hotplate at 130 °C for approximately 1.5 hours in order to let sample reflux.
e. Samples are then cooled down, lid removed and dried down to incipient dryness at 150 °C. Once dry, 1.5 mL conc HNO_3 (SB) is added and left to reflux.
f. Sample are dried down to incipient dryness at 150 °C and as a final step are re-dissolved in 6M HCl (SB), let on a 130 °C hotplate overnight to reflux and then made up with Milli-Q to mother solutions in 30 mL HDPE bottles.

2.9 Major- and trace elements by X-ray Fluorescence (XRF)

Major and trace element (V, Cr, Co, Ni, Cu, Zn, Rb, Sr, Y, Zr, Nb, Cs, Ba, La and Ce) concentrations were analysed by X-ray fluorescence (XRF) using a Spectro XEPOS_HE Energy Dispersive Polarised X-ray Fluorescence (EDPXRF) Analyser at the University of St. Andrews, following the procedure outlined in Toy et al. (2017). For major element analysis powdered samples were first dried at 105 °C and then 0.5000 g of sample was accurately weighed and mixed with either 5.0000 g of Lithium Metaborate or Lithium Tetraborate. The mixture was fused at 1080 °C for 15 min and cast into a 32 mm diametres Glass “Bead”. Loss on ignition (LOI) is calculated on a separate portion of powdered sample. For trace element analysis approximately 10 g of sample powder was mixed with Polyvinylalcohol binder (Movial 1%) and pressed at 20 T using tungsten-carbide anvils to produce a 32 mm pressed powder pellet.
Precision and accuracy were better than ±2.5 % RSD and ± 5% RMSD for most major elements (except for P_2O_5) and ± 5% RSD, ± 4 % RMSD for most trace elements respectively (except for Co, Cs, Y, Th and U; Table 2.3).

Table 2.3: Precision and accuracy of standard reference material OU-6 and BE-N measured by XRF. Accepted values from Jochum et al. (2016) and Potts and Kane (2005).

	OU-6				BE-N			
	Preferred value[1)]	*Average (n=5)*	*Precision (%RSD)*	*Accuracy (%RMSD)*	Preferred value[2)]	*Average (n=12)*	*Precision (%RSD)*	*Accuracy (%RMSD)*
	µg/g	*µg/g*			µg/g	*µg/g*		
Na_2O	1.78	1.8	*1.15*	*2.3*	-	-	-	-
MgO	2.42	2.4	*1.08*	*2.2*	-	-	-	-
Al_2O_3	20.47	20.5	*0.37*	*0.7*	-	-	-	-
SiO_2	57.41	57.4	*0.17*	*0.3*	-	-	-	-
P_2O_5	0.12	0.1	*4.14*	*8.4*	-	-	-	-
K_2O	3.03	3.0	*0.67*	*1.3*	-	-	-	-
CaO	0.74	0.7	*2.03*	*4.1*	-	-	-	-
TiO_2	0.99	1.0	*1.27*	*2.5*	-	-	-	-
MnO	0.28	0.3	*2.48*	*5.0*	-	-	-	-
Fe_2O_3	8.94	8.9	*0.44*	*0.9*	-	-	-	-
V	131.07	131.1	*0.88*	*1.8*	231.9	241.0	*0.74*	*1.5*
Cr	70.59	70.6	*0.74*	*1.5*	353.1	381.3	*0.78*	*1.7*
Co	30.23	30.2	*7.64*	*15.9*	59.0	62.9	*1.89*	*4.0*
Ni	40.95	41.0	*2.92*	*6.0*	269.7	265.0	*1.09*	*2.2*
Cu	41.02	41.0	*1.83*	*3.7*	68.8	73.3	*1.84*	*3.9*
Zn	111.28	111.3	*1.59*	*3.2*	122.9	120.7	*1.83*	*3.6*
Ga	24.07	24.1	*3.10*	*6.2*	17.2	14.8	*3.67*	*6.3*
Rb	122.67	122.7	*1.25*	*2.5*	47.6	50.5	*3.11*	*6.6*
Sr	131.70	131.7	*0.61*	*1.2*	1392.0	1375.1	*0.42*	*0.8*
Y	28.34	28.3	*5.51*	*11.2*	29.4	31.6	*2.87*	*6.2*
Zr	175.56	175.6	*2.70*	*5.5*	272.9	272.0	*1.65*	*3.3*
Nb	15.19	15.2	*2.43*	*4.9*	113.2	108.7	*1.53*	*2.9*
Cs	8.49	8.5	*11.50*	*24.4*				
Ba	485.31	485.3	*3.20*	*6.5*	1039.0	1026.8	*1.39*	*2.7*
La	33.84	33.8	*4.70*	*9.6*	82.6	76.1	*2.79*	*5.1*
Ce	78.81	78.8	*5.24*	*10.7*	153.0	142.7	*2.91*	*5.4*
Pb	29.55	29.5	*3.75*	*7.7*	4.1	5.3	*5.65*	*14.7*
Th	10.90	10.9	*8.47*	*16.8*	10.6	13.6	*5.87*	*15.1*
U	1.78	1.78	*15.39*	*27.4*	2.4	2.3	*21.10*	*40.4*

[1)](Potts and Kane, 2005), [2)](Jochum et al., 2016)

2.10 Trace element analysis by Inductively Coupled Plasma Mass Spectrometry (ICP-MS)

Trace elements in whole rock and mineral separate samples were analysed in solution mode on the Thermo X-series II ICP-MS at the University of Southampton. Analysis were performed with a general dilution factor of 4000. For this the mother solution was sub-sampled and dried down on the 130 °C hot plate to incipient dryness. The sample was re-dissolved in 3% HNO_3 (SB) containing 5 ppm In and Re and 20 ppb Be as internal standards to monitor internal drift during measurements. At the beginning of each analysis cycle the instrument was tuned using a multi-element solution in order to obtain the optimum sensitivity and stability of the instrument. Samples were run in random orders and five rock international calibration standard reference materials JB-1a, JB-3, BHV02, BIR-1 and JGb-1 and an additional blank standard C.Blk were run at the beginning and the end of each measurement cycle. Several blank acids (3% HNO_3 (SB) containing 5 ppm In and Re and 20 ppb Be) were run at the very end of each cycle to constrain detection limits. To monitor precision of measurements, international standard JA-2 and internal standard material BAS206 and BRR-1 were used (Table 2.4) and precision is expressed as the relative standard deviation (%RSD). Internal precision was monitored by measuring each sample four times. Accuracy was monitored by international standard JA-2 and PM-S (Table 2.5) and is expressed as the relative root-mean square deviation (%RMSD) compared to the preferred reference value.

Table 2.4: Precision for international reference materials JA-2 and PM-S and internal standards BRR-1 and BAS206 during the analytical period of 35 months.

	JA-2	*PM-S*	*BRR-1*	*BAS206*	Average
	RSD%	*RSD%*	*RSD%*	*RSD%*	*RSD%*
Li	*1.24*	*3.76*	*1.30*	*1.62*	***1.98***
Sc	*2.34*	*3.74*	*2.26*	*1.94*	***2.57***
Ti	*3.70*	*4.32*	*2.02*	*1.83*	***2.97***
V	*6.55*	*6.42*	*3.25*	*1.87*	***4.52***
Cr	*1.65*	*4.81*	*2.50*	*3.19*	***3.04***
Co	*1.84*	*3.56*	*1.79*	*1.91*	***2.27***
Ni	*1.19*	*3.69*	*1.90*	*1.88*	***2.17***
Cu	*2.27*	*4.14*	*1.99*	*2.18*	***2.65***
Zn	*4.69*	*3.72*	*2.49*	*3.53*	***3.61***
Rb	*2.60*	*4.83*	*3.00*	*2.80*	***3.31***
Sr	*0.97*	*3.49*	*1.00*	*2.71*	***2.04***
Y	*2.09*	*3.82*	*1.98*	*1.58*	***2.37***
Zr	*2.01*	*7.30*	*3.62*	*2.55*	***3.87***
Nb	*2.37*	*4.75*	*6.34*	*2.95*	***4.10***
Sn	*3.24*	*17.50*	*5.14*	*2.21*	***7.02***
Cs	*0.81*	*2.81*	*6.18*	*3.18*	***3.24***
Ba	*1.37*	*3.44*	*2.19*	*3.35*	***2.59***
La	*0.99*	*3.18*	*1.51*	*1.94*	***1.91***
Ce	*0.96*	*2.06*	*1.02*	*1.38*	***1.35***
Pr	*0.67*	*3.60*	*0.73*	*1.43*	***1.61***
Nd	*0.70*	*3.56*	*0.99*	*1.49*	***1.68***
Sm	*0.83*	*3.07*	*0.99*	*1.43*	***1.58***
Eu	*1.27*	*3.74*	*2.58*	*2.41*	***2.50***
Gd	*2.82*	*3.76*	*2.89*	*2.82*	***3.07***
Tb	*0.64*	*3.36*	*1.35*	*1.94*	***1.82***
Dy	*0.65*	*3.37*	*0.53*	*1.53*	***1.52***
Ho	*0.88*	*3.85*	*0.71*	*1.60*	***1.76***
Er	*0.63*	*3.24*	*0.90*	*1.66*	***1.61***
Tm	*0.77*	*3.01*	*0.71*	*1.51*	***1.50***
Yb	*0.92*	*3.71*	*0.90*	*1.74*	***1.82***
Lu	*1.13*	*3.44*	*0.74*	*1.86*	***1.79***
Hf	*2.78*	*5.24*	*2.32*	*2.06*	***3.10***
Ta	*4.93*	*10.25*	*6.77*	*10.17*	***8.03***
Pb	*3.06*	*4.84*	*7.68*	*17.79*	***8.34***
Th	*1.46*	*7.98*	*14.53*	*6.88*	***7.71***
U	*1.64*	*9.53*	*6.42*	*2.86*	***5.11***

Table 2.5: Accuracy of standard material JA-2 and PM-S during the analytical period of 35 months. Accepted reference values from Jochum et al. (2016).

	JA-2	JA-2	JA-2	PM-S	PM-S	PM-S	Average
	reference value[1)]	mean	Accuracy	reference value[1)]	mean	Accuracy	Accuracy
	µg/g	µg/g	%RMSD	µg/g	µg/g	%RMSD	**%RMSD**
Li	29.2	29.2	0.0	*7.6*	7.4	2.3	**1.1**
Sc	18.9	17.9	5.7	*34.0*	33.8	0.6	**3.1**
Ti	4012.6	3953.1	1.5	-	6772.4	-	**1.5**
V	119.7	111.9	6.5	*186.4*	185.8	0.3	**3.4**
Cr	424.8	395.2	7.0	*319.0*	320.7	0.5	**3.7**
Co	28.3	27.1	4.2	*49.0*	49.1	0.3	**2.3**
Ni	136.0	125.4	7.8	*117.8*	118.1	0.2	**4.0**
Cu	29.0	29.7	2.5	*57.2*	59.1	3.4	**3.0**
Zn	64.5	63.7	1.3	*60.0*	58.6	2.3	**1.8**
Rb	69.8	76.2	9.2	*1.0*	0.9	5.5	**7.3**
Sr	245.8	243.4	1.0	*279.2*	272.7	2.3	**1.6**
Y	16.9	17.4	3.3	*11.3*	11.2	1.1	**2.2**
Zr	108.5	115.3	6.3	*38.2*	36.3	5.1	**5.7**
Nb	9.3	9.0	3.6	*2.4*	2.3	6.8	**5.2**
Sn	1.7	1.6	8.1	*3.0*	2.6	14.5	**11.3**
Cs	4.8	5.1	7.5	*0.4*	0.3	7.5	**7.5**
Ba	308.4	320.5	3.9	*148.1*	144.5	2.4	**3.2**
La	15.5	16.0	3.3	*2.7*	2.5	5.7	**4.5**
Ce	32.9	33.5	1.9	*6.9*	6.5	5.8	**3.9**
Pr	3.7	3.8	3.4	*1.1*	1.0	2.0	**2.7**
Nd	14.0	14.5	3.2	*5.5*	5.4	1.4	**2.3**
Sm	3.0	3.1	2.4	*1.8*	1.7	2.2	**2.3**
Eu	0.9	0.9	1.9	*1.1*	1.0	1.8	**1.8**
Gd	3.0	3.1	2.5	*2.0*	2.0	0.0	**1.2**
Tb	0.5	0.5	0.6	*0.3*	0.3	0.8	**0.7**
Dv	2.9	2.9	2.0	*2.1*	2.1	2.0	**2.0**
Ho	0.6	0.6	1.7	*0.4*	0.4	3.4	**2.6**
Er	1.7	1.7	2.0	*1.1*	1.1	2.0	**2.0**
Tm	0.3	0.3	0.8	*0.2*	0.2	6.7	**3.8**
Yb	1.6	1.7	3.0	*1.0*	1.0	0.0	**1.5**
Lu	0.3	0.3	0.4	*0.2*	0.1	3.0	**1.7**
Hf	2.8	2.9	1.3	*1.1*	1.0	4.9	**3.1**
Ta	0.7	0.7	12.6	*0.2*	0.2	-2.5	**5.0**
Pb	18.9	22.2	17.4	*2.5*	2.0	17.9	**17.7**
Th	4.8	5.0	3.2	*0.1*	0.0	13.6	**8.4**
U	2.2	2.3	5.5	*0.0*	0.0	28.6	**17.0**

[1)] (Jochum et al., 2016)

2.11 Comparison of XRF and ICP-MS analysis of trace elements

Nine elements have been analysed by both, XRF and ICP-MS for whole rock of Wadi Gideah fault zone samples and international standard material PM-S (Figure 2.2). For most elements there is a good correlation between the results obtained by ICP-MS and XRF. However, there are three elements where the correlation is not strong: Cobalt shows higher values measured by XRF. This is most likely due to a standardisation problem during ICP-MS analysis. Most of these samples are relatively rich in Co compared to common rock types.

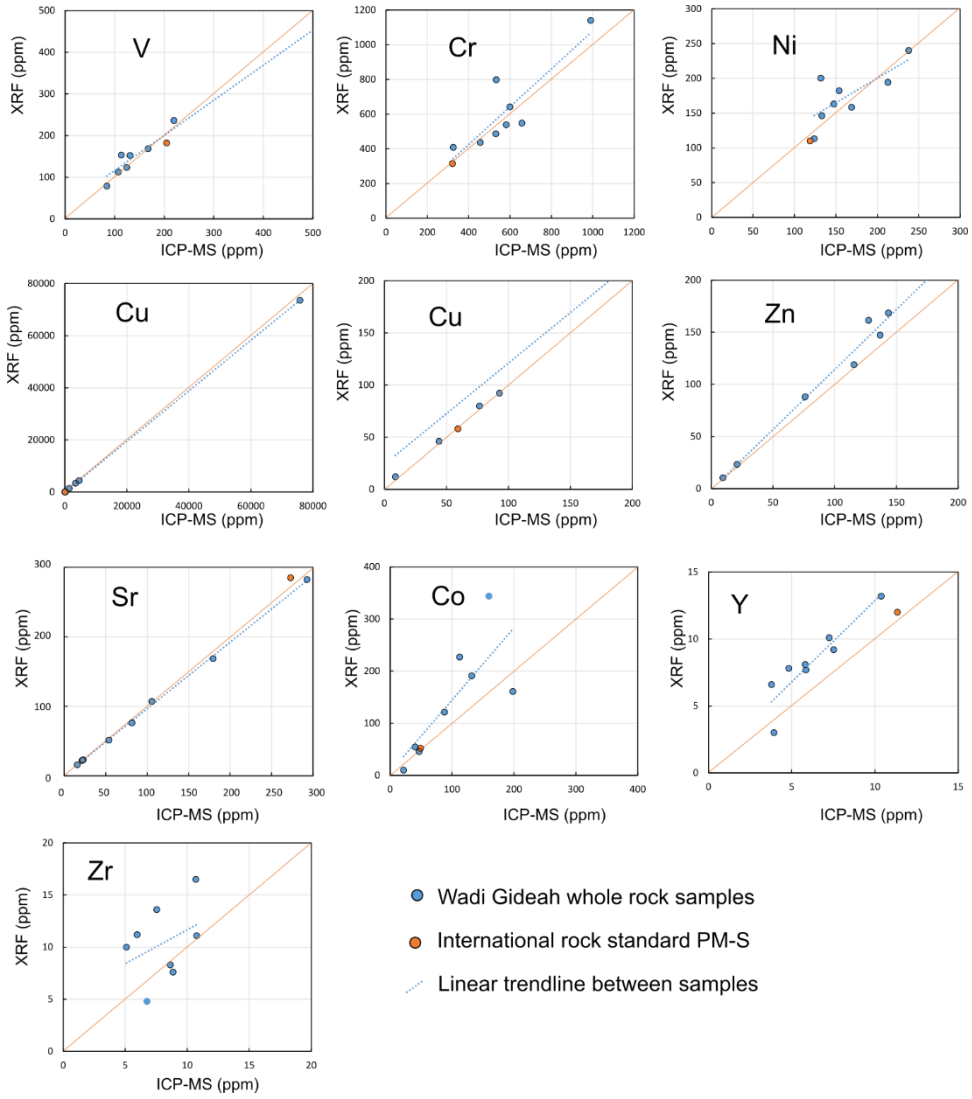

Figure 2.2: Whole rock XRF vs ICP-MS data of Wadi Gideah fault zone samples. The orange line represents the 1:1 line.

All international standard material used for calibration during ICP-MS analysis show considerably less Co-concentrations than analysed here. A good correlation between XRF and ICP-MS data could only be obtained for reference sample PM-S and two samples containing less than 150 µg/g of Co. Therefore, only the results obtained by XRF measurements were used. Both, Y and Zr show

a relatively good correlation between the two methods however, the concentration measured by XRF are higher than those measured by ICP-MS for Y and partially also for Zr. This can be either due to incomplete dissolution during digestion or a reaction between the element and the acid during the digestion process (personal comment from S. Müller, University of Kiel).

2.12 Major- and trace element analysis by Inductively Coupled Plasma - Optical Emission Spectrometry (ICP-OES) and by Laser Ablation – Inductively Coupled Plasma – Mass Spectrometry (LA-ICP-MS) at the University of Kiel

Four fault zone samples (OM15-3A, OM15-3C, OM15-3E, OM15-3F) and eight background gabbros (Table C2; Chapter 5) were analysed at Kiel University. For liquid analysis 250mg of dried powder (105°C) was dissolved in perfluoralkoxy (PFA) vials applying a multi-acid digestion protocol. All acids were sub-boiled and, all work was carried out under Class 100 clean laboratory conditions. Procedural blanks, duplicates, and international reference materials were processed the same way. Reproducibility of this digestion procedure is typically better than 1 %RSD (1SD) (see Garbe-Schönberg (1993) for details).

Major elements were analysed using a Spectro CIROS SOP ICP-OES. SiO_2 cannot be analysed after digestion procedures including hydrofluoric acid and was therefore calculated to 100% oxides with due regard to loss on ignition. Analytical precision was better than 0.5-1 %. Matrix-matched calibration was done by correcting against solutions of certified reference materials basalt BHVO-2, basalt BE-N, and granite AC-E processed the same way as the samples. Accuracy was monitored with running digest solutions of basalt BIR-1 and gabbro JGb-2. For liquid-based minor and trace element determination solutions where analysed using an AGILENT 7500cs, applying a standard addition (Be, In, Re) protocol. The analytical precision is typically better than 0.5-2 %RSD (1SD) for all elements analysed. Results for reference materials BHVO-2 and JGb-1 are reported in Table 2.6.

Most trace element of these four fault zone samples (OM15-3A, OM15-3C, OM15-3E, OM15-3F) were analysed by Laser Ablation – Inductively Coupled Plasma – Mass Spectrometry (LA-ICP-MS) on nano-particulate pressed powder pellets (NPP). operating a 193 nm ArF excimer laser ablation system (GeoLasPro, Coherent) coupled to an Agilent 7500s ICP-MS. Details of this procedure can be found in Garbe-Schönberg and Müller (2014). The advantage of this approach is the full recovery of HFSE composition from gabbros containing accessory minerals (zircon, spinel). Initial calibration was done against NIST SRM612 using Ca as internal standard. For applying a matrix

matched correction BHVO-2, BIR-1 and JGb-1 were prepared the same way as the samples and analysed in the same batch. Analytical precision is typically better than 1-5 %RSD (1SD) for all elements analysed at concentrations > 10x LOD (Table 2.6).

2.13 Radiogenic Strontium isotopes by Thermal Ionisation Mass Spectrometry (TIMS)

Strontium was separated from dissolved samples using Strontium Spec^{TM} columns. An appropriate amount of mother solution was sub-sampled to give approximately 0.5 - 1 µg of Sr and dried down. Columns were filled with Sr-spec resin up to the neck of the column and washed using the following procedure: 1.5 mL of milli-Q followed by 1.5 mL of 3M HNO_3 (sb), followed by 1.5 mL of milli-Q and 1.5 mL of 3M HNO_3 (sb). The sample was then dissolved in 200 µL 3M HNO_3 (sb) and loaded carefully onto the resin. This was followed by a wash-in step of 200 µL of 3M HNO_3 (sb) and an elution step of 2 mL of 3M HNO_3 (sb). Finally, the Strontium was collected with 1.5 mL of H_2O in clean Savillex Teflon pots to be dried down.

Prior to loading on the filament for isotopic analysis, the strontium concentrate was re-dissolved in 1.5 µL HCl (SB). Outgassed tantalum filaments were attached to a power supply and the current was increased up to 1.8 A. With parafilm two small barriers were placed on both sides of the filament and the current was reduced to 0.8 A. 1 µL of tantalum activator was added in two steps of 0.5 µL each. The sample was then loaded onto the filament in several small volumes and the current was subsequently turned up to 2 A to dry the sample. Once 2 A was reached the current was increased until the filament glowed and was left for 10 s.

Loaded filaments were then analysed by a ThermoFisher Scientific TritonPlus TIMS. The international strontium standard NBS987 was measured as an external standard at the beginning and in the middle of each measurement cycle to monitor analytical precision and accuracy. Throughout the analytical period of 34 months, NBS987 was analysed 36 times, giving an average of $^{87}Sr/^{86}Sr=0.710242 \pm 0.000023$ (2σ). Measured Sr-spec coloumn blanks contained less than 1 ng of strontium.

Strontium isotope compositions of the eigh background gabbros (Chapter 5; Appendix C.2) were determined at the Institute of Mineralogy at the University of Hannover following the procedure of Pin et al. (1994). The analyses were carried out with a ThermoFinnigan Neptune MC-ICP-MS. International standards, used for precision monitoring, were AMES, BIR-1, JGB-2, JMC, and NIST SRM 987. ^{86}Sr and ^{87}Sr were corrected for ^{86}Kr and ^{87}Rb interferences and $^{87}Sr/^{86}Sr$ corrected for mass fractionation. The mean value for $^{87}Sr/^{86}Sr$ in the external standard NBS987 was 0.710276

±0.000012 (2SD). All $^{87}Sr/^{86}Sr$ ratios presented in Chapter 5 were corrected to a NBS987 value of $^{87}Sr/^{86}Sr=0.710248$.

Throughout the thesis $^{87}Sr/^{86}Sr$ ratios are age corrected to initial ratios at 95 Ma, using analysed Sr and Rb concentrations as well as all measured isotopes of Sr. This correction is done to account for the ^{87}Sr resulting from the decay of ^{87}Rb. In making this correction it is assumed that the alteration occurred at the time of the formation of the crust. However, the formation of laumontite and calcite may have been later and therefore, the corrected and uncorrected $^{87}Sr/^{86}Sr$ ratios provide minimum and maximum limits.

Table 2.6: Precision and accuracy of trace elements measured at the University in Kiel. Analysis were performed in solution mode (ICP-MS) and on nano-particulate pressed powder pellets (LA-ICP-MS). Preferred values of standard material from Govindaraju (1994); Imai et al. (1995); Jochum et al. (2016); Potts and Kane (2005).

Lab	Kiel																			
Sample[1)]	BHVO-2 (AD)				JGb-1 (AD)				Average (AD)		BHVO-2 (NPP)				JGb-1 (NPP)				Average (NPP)	
	Preferred value[2)]	*Median (n=4)*	*Precision (%RSD)*	***Accuracy (%RMSD)***	Preferred value[3)]	*Median (n=5)*	*Precision (%RSD)*	*Accuracy (%RMSD)*	*Precision (%RSD)*	*Accuracy (%RMSD)*	Preferred value[2)]	*Median (n=6)*	*Precision (%RSD)*	*Accuracy (%RMSD)*	Preferred value[3)]	*Average (n=6)*	*Precision (%RSD)*	*Accuracy (%RMSD)*	*Precision (%RSD)*	***Accuracy (%RMSD)***
Element	µg/g	*µg/g*			µg/g	*µg/g*					µg/g	*µg/g*			µg/g	*µg/g*				
Li	4.50	*4.44*	*0.88*	***1.7***	4.59	*5.00*	*1.41*	*7.6*	*1.1*	*4.7*	4.50	*4.43*	*1.21*	*1.6*	4.59	*4.60*	*0.39*	*0.3*	*0.8*	***1.0***
Sc	31.83	*31.68*	*1.50*	***1.3***	36.60	*33.11*	*4.78*	*9.3*	*3.1*	*5.3*	31.83	*33.00*	*1.12*	*3.9*	36.60	*35.79*	*1.46*	*2.7*	*1.3*	***3.3***
V	318.20	*315.98*	*1.05*	***1.0***	640.00	*462.55*	*19.47*	*2.3*	*10.3*	*1.6*	318.20	*318.20*	*0.62*	*0.6*	640.00	*657.32*	*0.46*	*2.6*	*0.5*	***1.6***
Cr	287.20	*290.37*	*1.33*	***1.6***	59.30	*42.88*	*25.19*	*6.9*	*13.3*	*4.3*	287.20	*287.20*	*1.63*	*1.6*	59.30	*66.78*	*7.84*	*13.3*	*4.7*	***7.4***
Co	44.89	*44.20*	*1.68*	***2.0***	61.60	*58.29*	*2.45*	*5.3*	*2.1*	*3.6*	44.89	*44.76*	*0.91*	*0.8*	61.60	*60.69*	*2.58*	*2.7*	*1.7*	***1.7***
Ni	119.80	*119.15*	*1.25*	***1.2***	25.40	*23.20*	*5.44*	*10.2*	*3.3*	*5.7*	119.80	*119.66*	*1.16*	*1.0*	25.40	*25.29*	*0.20*	*0.5*	*0.7*	***0.8***
Cu	129.30	*126.19*	*1.33*	***2.7***	86.80	*85.48*	*2.68*	*3.8*	*2.0*	*3.3*	129.30	*131.42*	*0.98*	*1.4*	86.80	*80.13*	*2.34*	*7.8*	*1.7*	***4.6***
Zn	103.90	*103.35*	*1.39*	***1.3***	111.00	*102.72*	*1.71*	*7.7*	*1.6*	*4.5*	103.90	*103.90*	*3.96*	*3.8*	111.00	*112.20*	*3.72*	*3.4*	*3.8*	***3.6***
Rb	9.26	*9.11*	*1.21*	***2.0***	5.60	*5.86*	*1.14*	*4.1*	*1.2*	*3.0*	9.26	*9.27*	*1.26*	*1.4*	5.60	*5.47*	*1.79*	*2.5*	*1.5*	***1.9***
Sr	394.10	*393.94*	*1.22*	***1.1***	327.00	*324.24*	*1.60*	*2.1*	*1.4*	*1.6*	394.10	*392.86*	*0.61*	*0.7*	327.00	*328.74*	*0.47*	*0.7*	*0.5*	***0.7***
Y	25.91	*25.45*	*1.40*	***2.1***	10.40	*9.61*	*1.27*	*9.0*	*1.3*	*5.5*	25.91	*25.92*	*2.29*	*2.2*	10.40	*9.97*	*0.72*	*4.1*	*1.5*	***3.2***
Zr	171.20	*172.91*	*1.68*	***1.6***	28.40	*26.31*	*2.08*	*9.0*	*1.9*	*5.3*	171.20	*171.63*	*0.73*	*0.6*	28.40	*27.53*	*0.82*	*3.2*	*0.8*	***1.9***
Cs	0.10	*0.10*	*4.39*	***7.3***	0.27	*0.22*	*2.68*	*19.7*	*3.5*	*13.5*	0.10	*0.10*	*1.92*	*1.8*	0.27	*0.19*	*1.72*	*40.1*	*1.8*	***20.9***
Ba	130.90	*132.08*	*1.37*	***1.4***	63.00	*64.84*	*1.02*	*2.7*	*1.2*	*2.0*	130.90	*130.90*	*0.21*	*0.2*	63.00	*62.94*	*0.22*	*0.3*	*0.2*	***0.2***
La	15.20	*15.22*	*1.45*	***1.3***	3.74	*3.50*	*1.15*	*7.2*	*1.3*	*4.2*	15.20	*15.51*	*1.67*	*2.5*	3.74	*3.64*	*1.62*	*2.9*	*1.6*	***2.7***
Ce	37.53	*37.65*	*1.52*	***1.4***	7.86	*8.13*	*0.86*	*3.8*	*1.2*	*2.6*	37.53	*36.88*	*1.18*	*1.8*	7.86	*8.36*	*1.01*	*6.2*	*1.1*	***4.0***
Pr	5.34	*5.39*	*1.53*	***1.7***	1.14	*1.16*	*0.80*	*2.2*	*1.2*	*1.9*	5.34	*5.22*	*0.73*	*2.3*	1.14	*1.15*	*0.39*	*0.7*	*0.6*	***1.5***
Nd	24.27	*24.90*	*1.66*	***2.8***	5.65	*5.43*	*0.76*	*4.4*	*1.2*	*3.6*	24.27	*24.47*	*0.85*	*1.0*	5.65	*5.33*	*0.60*	*6.1*	*0.7*	***3.6***
Sm	6.02	*6.21*	*1.43*	***3.2***	1.49	*1.48*	*0.50*	*1.1*	*1.0*	*2.1*	6.02	*6.18*	*0.64*	*2.5*	1.49	*1.47*	*0.45*	*1.5*	*0.5*	***2.0***

Eu	2.04	*2.08*	*1.35*	***2.2***	0.63	*0.62*	*0.63*	*1.0*	*1.0*	*1.6*	2.04	*2.04*	*1.44*	*1.3*	0.63	*0.63*	*2.34*	*2.1*	*1.9*	***1.7***
Gd	6.21	*6.23*	*1.46*	***1.3***	1.63	*1.67*	*0.81*	*2.5*	*1.1*	*1.9*	6.21	*6.10*	*0.63*	*1.6*	1.63	*1.65*	*0.59*	*1.5*	*0.6*	***1.6***
Tb	0.94	*0.95*	*1.47*	***2.0***	0.30	*0.28*	*0.81*	*7.7*	*1.1*	*4.8*	0.94	*0.94*	*2.40*	*2.2*	0.30	*0.28*	*1.69*	*6.7*	*2.0*	***4.4***
Dy	5.28	*5.38*	*1.26*	***2.4***	1.53	*1.77*	*0.56*	*13.8*	*0.9*	*8.1*	5.28	*5.23*	*1.15*	*1.2*	1.53	*1.80*	*1.25*	*15.0*	*1.2*	***8.1***
Ho	0.99	*0.99*	*1.19*	***1.1***	0.32	*0.36*	*0.57*	*11.7*	*0.9*	*6.4*	0.99	*0.99*	*0.90*	*0.8*	0.32	*0.37*	*2.18*	*14.4*	*1.5*	***7.6***
Er	2.51	*2.46*	*1.50*	***2.3***	1.07	*0.99*	*0.49*	*8.2*	*1.0*	*5.3*	2.51	*2.52*	*1.32*	*1.3*	1.07	*1.04*	*0.98*	*2.5*	*1.2*	***1.9***
Tm	0.33	*0.33*	*1.17*	***1.4***	0.15	*0.15*	*0.24*	*2.7*	*0.7*	*2.1*	0.33	*0.34*	*0.74*	*0.8*	0.15	*0.15*	*2.35*	*2.1*	*1.5*	***1.5***
Yb	1.99	*2.01*	*1.90*	***2.2***	0.97	*0.95*	*0.87*	*2.0*	*1.4*	*2.1*	1.99	*1.99*	*1.71*	*1.6*	0.97	*0.97*	*0.55*	*0.5*	*1.1*	***1.0***
Lu	0.28	*0.28*	*1.63*	***2.3***	0.15	*0.14*	*0.68*	*5.9*	*1.2*	*4.1*	0.28	*0.28*	*2.72*	*3.6*	0.15	*0.15*	*1.48*	*2.5*	*2.1*	***3.0***
Hf	4.47	*4.31*	*1.51*	***4.1***	0.88	*0.82*	*1.45*	*7.6*	*1.5*	*5.8*	4.47	*4.47*	*1.51*	*1.4*	0.88	*0.83*	*0.22*	*5.6*	*0.9*	***3.5***
Pb	1.65	*1.79*	*15.58*	***17.5***	1.90	*1.56*	*1.22*	*21.2*	*8.4*	*19.4*	1.65	*1.87*	*0.92*	*11.8*	1.90	*1.66*	*3.09*	*14.7*	*2.0*	***13.3***
Th	1.22	*1.19*	*3.74*	***4.9***	0.53	*0.42*	*2.41*	*26.8*	*3.1*	*15.9*	1.22	*1.32*	*1.28*	*7.5*	0.53	*0.47*	*5.82*	*12.8*	*3.5*	***10.2***
U	0.41	*0.42*	*1.80*	***2.9***	0.15	*0.10*	*2.75*	*52.8*	*2.3*	*27.9*	0.41	*0.41*	*0.48*	*0.4*	0.15	*0.15*	*6.29*	*6.0*	*3.4*	***3.2***

[1)]AD: acid digestion, analysed by liquid ICP-MS; NPP: nano-particulate pressed powder pellet, analysed by LA-ICP-MS

[2)]preferred values Jochum et al. (2016)

[3)]preferred values Govindarju (1994); Imai et al. (1995)

[4)]Potts and Kane (2005)

Chapter 3 Cross-cutting relationships of hydrothermal alteration observed in the lower oceanic crust of Wadi Qafifah, Samail ophiolite, Oman

3.1 Introduction

Traditionally, intense hydrothermal circulation near fast spreading oceanic ridges has been thought to be largely confined to the upper crust, operating down to the base of the sheeted dyke complex. This has been shown and discussed by numerous studies from ophiolites and modern fast-spreading oceanic crust (e.g., Alt, 1995; Alt et al., 2010; Bickle and Teagle, 1992; Gillis et al., 2001; Harris et al., 2015; Heft et al., 2008; Nehlig and Juteau, 1988a; Teagle et al., 2003). However, the existence of a similar, but lower crustal hydrothermal system has been suspected on the basis of oxygen (Cocker et al., 1982; Gregory and Taylor, 1981) and strontium isotope (Lanphere et al., 1981; McCulloch et al., 1981; Spooner et al., 1977) studies carried out in the lower oceanic crust in the Samail ophiolite. This has been confirmed by detailed studies on hydrothermal vein systems in the Samail ophiolite (e.g., Bosch et al., 2004; Manning et al., 2000; Nehlig, 1994; Nehlig et al., 1994; Nehlig and Juteau, 1988b, 1988a). Amphibole veins in gabbroic rocks may be the fossil trace of a cracking front at the interface between the hydrothermal and the magmatic system (Bosch et al., 2004; Nicolas et al., 2003) with estimated formation temperatures for early and discrete amphibole veins ranging between 700 °C at the dyke-gabbro interface and 825°C right at the crust-mantle boundary (Manning et al., 2000). Strontium and oxygen isotope studies on such high-temperature and regularly spaced amphibole veins indicate interactions with a seawater derived hydrothermal fluid at low fluid-rock ratios (e.g., Bosch et al., 2004; Nicolas et al., 2003). They are interpreted to represent the fossil record of a hydrothermal recharge system, where seawater derived hydrothermal fluids circulated through the oceanic crust (e.g., Bosch et al., 2004; Nicolas, 2003). In addition to amphibole veins, Nehlig and Juteau (1988b) observed and describe a zoisite and zoisite-epidote vein system cross-cutting earlier and high-temperature amphibole veins throughout the lower crustal section in the Samail ophiolite, Oman. Together with a third and younger vein system of prehnite veins, off-axis with fluid circulation down to the base of the crust is suspected. In addition to isolated veins distributed through out the lower crust, Coogan et al. (2006) reported the presence of discrete and widely spaced zones of intense hydrothermal alteration that are up to 10's of metres wide that are proposed to record zones of concentrated hydrothermal fluid flow. Fluid flow within these zones is suspected to have started at around 800 °C and continued down to < 300 °C indicated by

amphibole microthermometry and other greenschist mineral parageneses. Based on strontiumisotope and preliminary oxygen isotope data, Coogan et al. (2006) demonstrated an intense interaction with a seawater-derived hydrothermal fluid within these zones. High fluid fluxes through these channels are suspected to reset the Sr-isotopic composition of the crust to equal that of the fluid. Enhanced cooling rates in the surrounding crust have been observed. From observations on aerial photos, Coogan et al. (2006) estimated that similar zones occur approximately every kilometre.

In this chapter, results are presented from a detailed study of one outcrop situated in the layered gabbros in Wadi Qafifah, of the Wadi Tayin block of the Samail ophiolite Oman. This outcrop comprises multiple vein systems and is therefore well suited to study cross-cutting relationships of hydrothermal veins and alteration. Along this outcrop, the relatively fresh host rocks were described and hydrothermal veins and corresponding alteration haloes mapped and sampled. The detailed petrographic observations from outcrop and thin sections are supplemented with geochemical data, obtained from a dense sampling along the whole outcrop. The primary aims of this study are (i) to determine cross-cutting relationships of hydrothermal alteration in order to establish an alteration sequence; (ii) estimate alteration temperatures for the different alteration stages; (iii) determine hydrothermal fluid compositions, constrain fluid-rock interactions and estimate how far alteration extends from features such as veins and faults.

3.2 Wadi Qafifah and the mapped outcrop

Wadi Qafifah is a north to south trending valley, approximately 15 km NW of the town of Ibra (Figure3.1) in the central part of the Wadi Tayin massif of the Samail ophiolite. The wadi has its source in mantle rocks but cuts mainly through the layered gabbro section. Foliated and high level gabbros crop out at the valley entrance and are partially eroded. The dyke and volcanic sequence are eroded and overlain by alluvium. There are a few localities where late stage intrusives such as trondhjemites and diorites crop out at the top of the high-level gabbros. Unlike in other valleys of this area (e.g. Wadi Nasif to the west and Wadi Gideah to the east of Wadi Qafifah) the transition from mantle to crustal rock is faulted and has relatively uplifted residual harzburgites or the upper mantle and juxtaposed them adjacent to layered gabbros of the lower oceanic crust (Figure3.2).

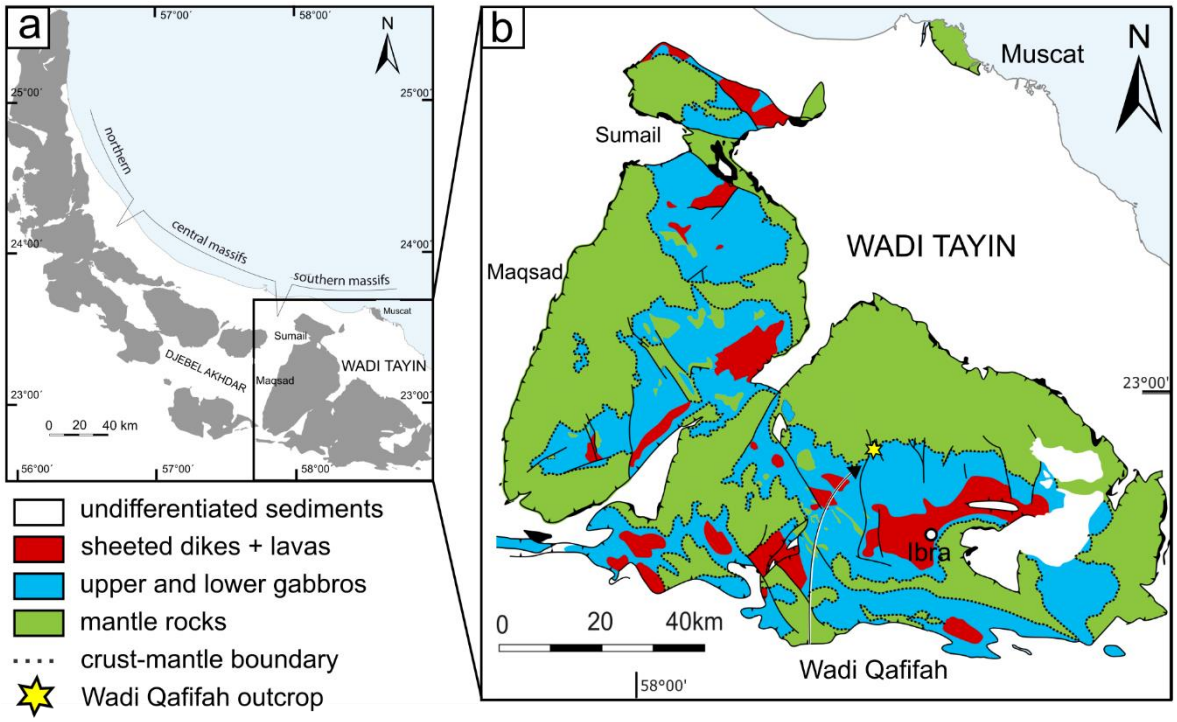

Figure 3.1: Overveiw of the Samail ophiolite (a) and the Wadi Tayin block (b) with the mapped outcrop. Wadi Qafifah is located NW of the town of Ibra and the mapped outcrop is marked with a yellow star.

Wadi Qafifah is one of localities in the Ibra area where initial structural, petrographic and geochemical observations on the accretion and the formation of the crustal section of the Samail ophiolite were made (Hopson et al., 1981; Pallister, 1981; Pallister and Hopson, 1981; Pallister and Knight, 1981) and the area was mapped in the early 1980's by French researchers and is covered by the Samad sheet of the 1:100,000 geological map of the Sultanate of Oman (De Grarmon et al., 1986).

The outcrop (22.895 °N, 58.426 °E, Figure3.2) studied here is located along a small path, about 80 m away from the main road and ~10 m above the wadi bed. It has recently been exposed due to road construction providing relatively fresh exposure. The locality is within the layered gabbro section, approximately 1.5 km above the mantle transition zone. Due to faulting, mantle rocks including harzbugites and locally dunites crop out on the western part of the main wadi valley. The mapped part of the outcrop is about 60 m long and oriented east-west. At its highest point it reaches 10 m above the road.

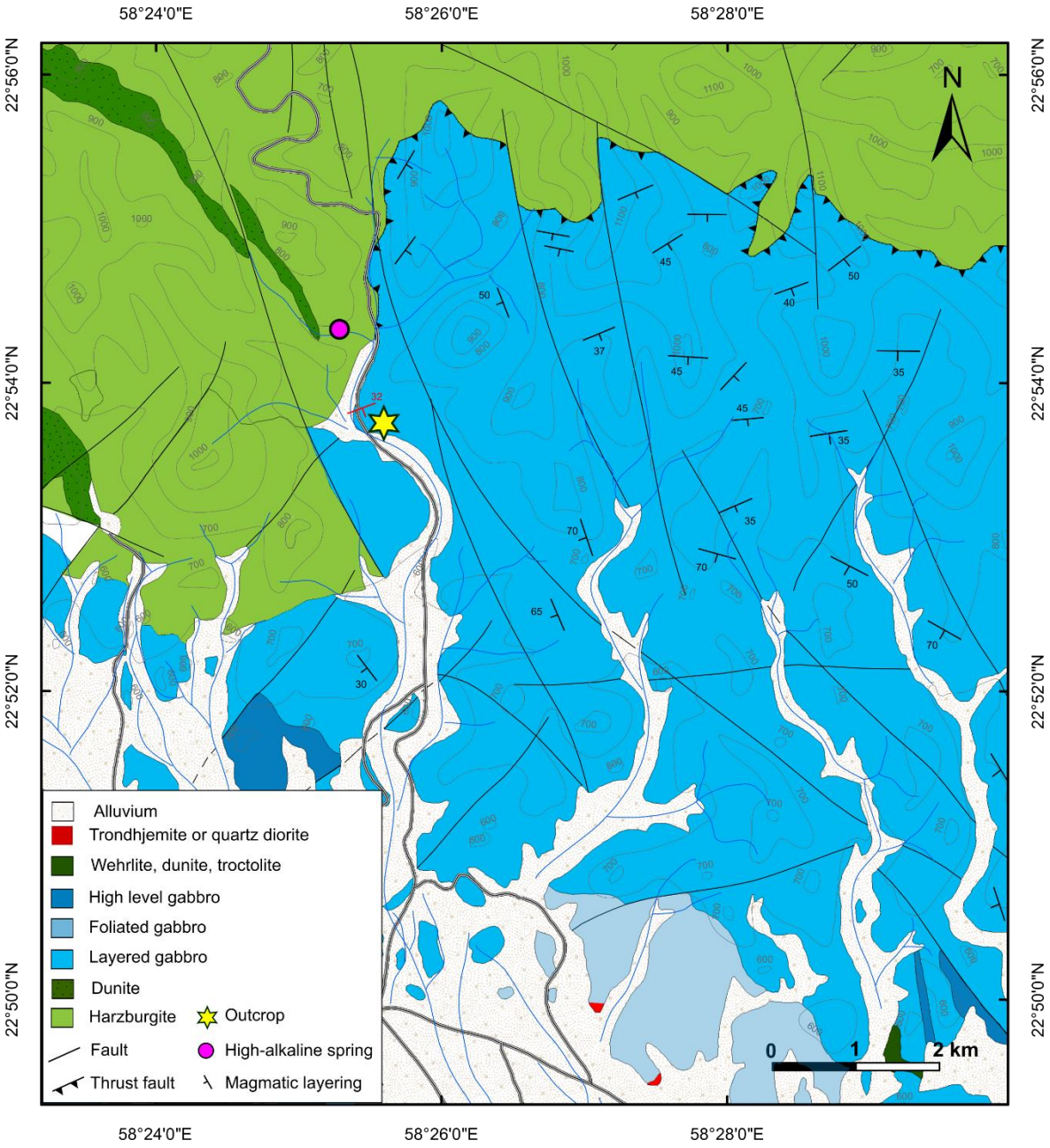

Figure 3.2: Overview map of Wadi Quafifah. Wadi Qafifah is a N-S trending valley to the NE of the town Ibra. The studied outcrop is located close to the crust-mantle boundary. The red symbol close to the outcrop represents the mean (n=5) value of the dip direction and dip of the magmatic layering close by the outcrop measured during fieldwork season 2015 (see Figure3.5). Map modified after De Gramon et al. (1986).

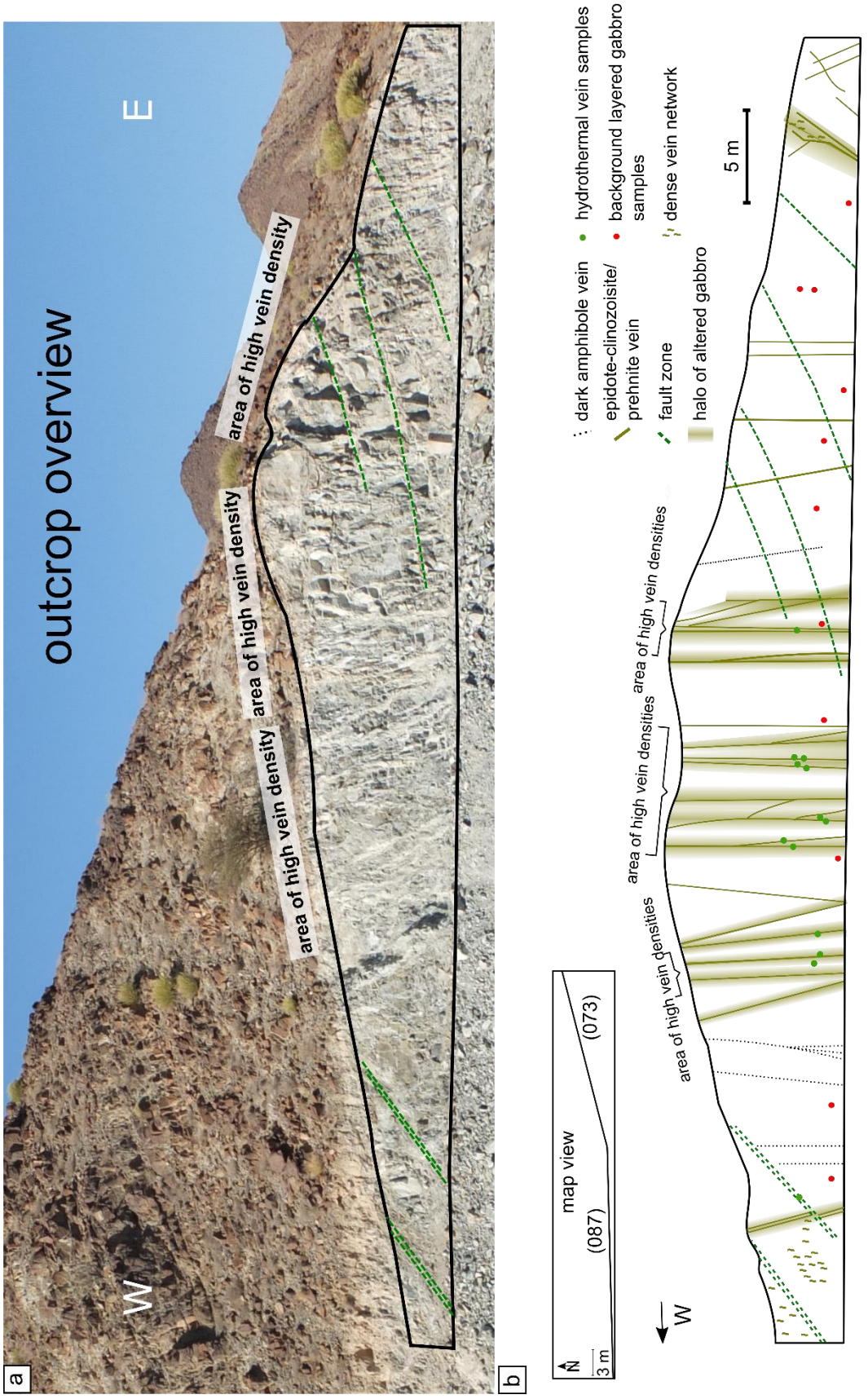

Figure 3.3: Overview of the mapped Wadi Qafifah outcrop. (a) Photograph of the outcrop, (b) Schematic sketch of the mapped outcrop showing major hydrothermal veins (epidote-clinozoisite and prehnite veins, both shown in pale-green) including halo with highly altered gabbro, fault zones and sample location. Vein and haloes are not to scale.

The magmatic layering is only weakly visible due to the fresh cut nature of the outcrop and was therefore measured approximately 150 m further away, along the main road. It strikes NE-SW, dipping about 32° SSE (average measured value of 164/32° dip direction and dip), which is approximately orthogonal to the mean orientation of the sheeted dyke in the area and in good agreement with what has been measured and mapped previously for the whole Qafifah area by Pallister and Hopson (1981) and French scientist from BRGM (De Gramon et al., 1986) and the Wadi Tayin in general (Pallister, 1981).

A dense network of hydrothermal veins and small fault zone (Figure 3.3) can be observed along the whole outcrop. There are three main areas with a high density of hydrothermal veins and a strikingly high degree of alteration. Fourteen hydrothermal vein samples and 12 layered gabbro samples were collected.

3.3 Field descriptions

3.3.1 Host rock and vein systems

Host-rock gabbro is olivine-bearing and relatively fine grained with crystal sizes between 0.5-2 mm. Olivine grains are predominantly weathered and are visible as dark spots. Hydrothermal veins occur across the outcrop. Based on field observations they can be divided into the following sub-groups:

Dark amphibole veins

Dark brown, almost black amphibole veinlets have been identified and mapped in the outcrop. These thin veins are typically about 1-2 mm wide, are continuous with subvertical orientations and do not have a macroscopically visible halo. Their contact to the surrounding gabbro is sharp and they are best displayed on fresh surfaces.

Epidote-clinozoisite veins

Green to yellowish and white to pale pink epidote-clinozoisite veins are the most common type of veins observed and mapped in this outcrop (Figure 3.4b, c). Their orientation is parallel to sub-parallel to those of the dark amphibole veinlets. Generally, they are continuous, although variable in width. Typically, their thickness varies over a scale of decimetres (dm) from a few millimetres (mm) up to several centimetres (cm). On average they show thicknesses between 0.5-2 cm. In many cases veins bifurcate into several branches. In most cases, epidote and clinozoisite co-exist in a single vein, although mono-mineralic veins are also present. Commonly, epidote-clinozoisite veins are rimmed by a selvage up to several millimetres wide of dark-green amphiboles (Figure

3.4f). Gabbro around epidote-clinozoisite veins are altered up to cm to several dm around the vein. Such alteration haloes are symmetric, typically pale green and have a "spotty" appearance due to mm-sized chlorite patches. In several locations the whole-rock surrounding epidote-clinozoisite veins is brecciated and mm- to cm-sized whole rock clasts occur within the veins (Figure 3.4e).

Prehnite ± clinozoisite veins

White to slightly pinkish veins, up to several cm wide and sub-parallel to epidote-clinozoisite veins are the second most abundant type of veins (Figure 3.4d). Massive prehnite is their major component, although many of them are clinozoisite or calcite bearing. Several prehnite veins are sulphide (chalcopyprite ± pyrite) bearing (Figure 3.4a) but no quartz was observed. Sulphides are disseminated throughout the vein and range in size of up to several millimetres. Commonly, sulphides are partially weathered to Fe-oxyhydroxides and malachite giving the surrounding minerals a typical dark brownish to blue-greenish staining. Alteration haloes are also well developed around the prehnite veins and range in size from cm up to several dm, depending on the size of the vein aperture and the spacing between neighbouring veins. These haloes range from whitish-bleached near the vein itself to whitish-greenish further away of the vein. Typically, the whole rock around prehnite veins is brecciated and in many cases it is difficult to distinguish what belongs to the vein itself and what is part of the surrounding alteration.
A second set of 1-4 mm-wide monomineralic prehnite veins clearly cross-cuts epidote-clinozoisite veins and corresponding alteration haloes.

iii) Laumontite-calcite veinlets

White, fibrous laumontite ± calcite veinlets with a wide variety of orientations, cross-cut all previously described vein systems. Typically, they are < 1-2 mm wide and continuous for metres across the outcrop. These veins are most common in fault zones and alteration haloes.

In addition to the described vein systems, there are several cm-wide fault zones, formed of greenish, chlorite- and carbonate-rich, crumbly fault gauge cross-cutting previously described vein systems. Their structural relationship to the laumontite vein system is unclear. In several localities it could be observed that laumontite-calcite veins cross-cut these fault zones but in one locality, the fault zone clearly cross-cut earlier laumontite veinlet. Shear sense indications are rare and poorly developed. Consequently, no clear sense of shear could be determined.

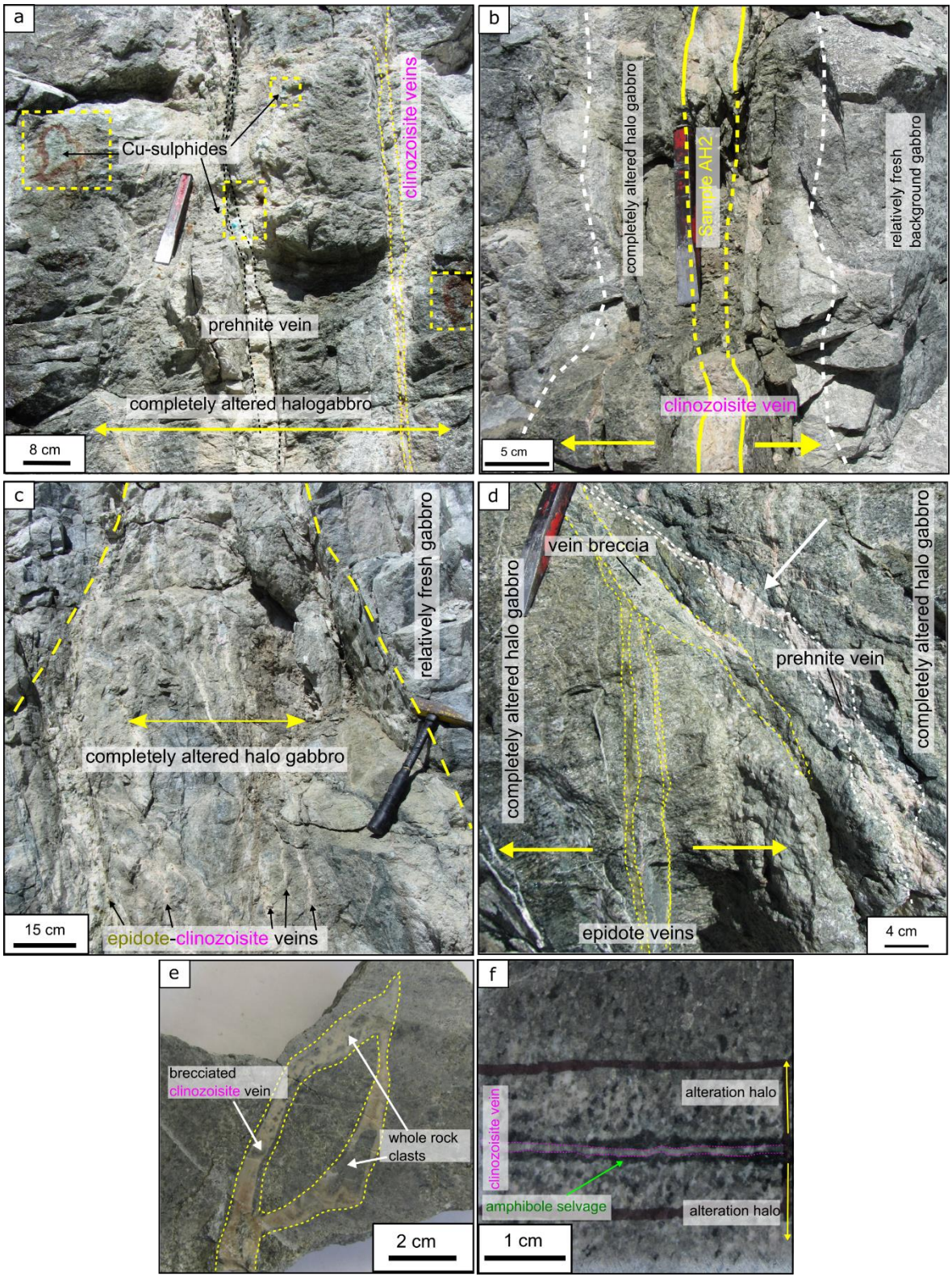

Figure 3.4: Overview photos showing the appearance of hydrothermal veins in the outcrop and in hand specimen. (a) Prehnite ± clinozoisite vein (~ 3-4 cm) parallel to two (< 1 cm) clinozoisite veins. Prehnite vein is partially brecciated and Cu-sulphide bearing. Cu-sulphides are weathered to Fe-oxyhydroxides and malachite and can also be found in the well-developed alteration halo around the vein. (b) Brecciated (3-4 cm wide clinozoisite vein with alteration halo around. Dashed lines indicate where sample

AH2 (e) has been taken. (c) Area with densely spaced epidote and clinozoisite veins (~1 cm in size). Area around and in between these veins is highly altered with initial magmatic texture and mineralogy completely replaced by secondary minerals. (d) Several parallel epidote veins with greenish-patchy alteration halo are cross-cut by branched epidote-clinozoisite veins, partially brecciating the epidote veins. Prehnite veins show strongly variable thicknesses and a dark-green, almost bluish alteration halo. Note the alteration halo around the epidote vein has its patchy appearance due to chlorite replacing plagioclase. (e) Cut sample AH2 showing brecciated clinozoisite vein/whole rock. Small (mm-sized) altered whole rock clasts are imbedded in the vein. (f) Millimetre-sized clinozoisite vein rimmed by a symmetric dark-green amphibole selvage. Microprobe data show a predominant composition of Mg-hornblende. (e) 2 mm sized clinozoisite vein rimmed by dark green Mg-hornblende. Note the cm-wide alteration halo, mainly consisting of albite +hornblende + clinozoisite + chlorite + actinolite.

3.3.2 Vein orientations

Measured amphibole veins are sub-parallel to each other and have a mean orientation of 253/80° (dip direction/dip), sub-orthogonal to the magmatic layering measured nearby (164/32°) and parallel to the mean strike of the sheeted dykes in the area (261/71°; Pallister, 1981), although amphibole veins generally dip slightly more steeply than the sheeted dykes (Figure 3.5). The mean orientation of epidote-clinozoisite and prehnite veins is 230/82°, sub-parallel to the mean orientation of the sheeted dykes and sub-orthogonal to the magmatic layering. The orientation of late fault zones, cross-cutting earlier hydrothermal veins is 318/72°, sub-orthogonal to amphibole, epidote-clinozoisite and prehnite veins.

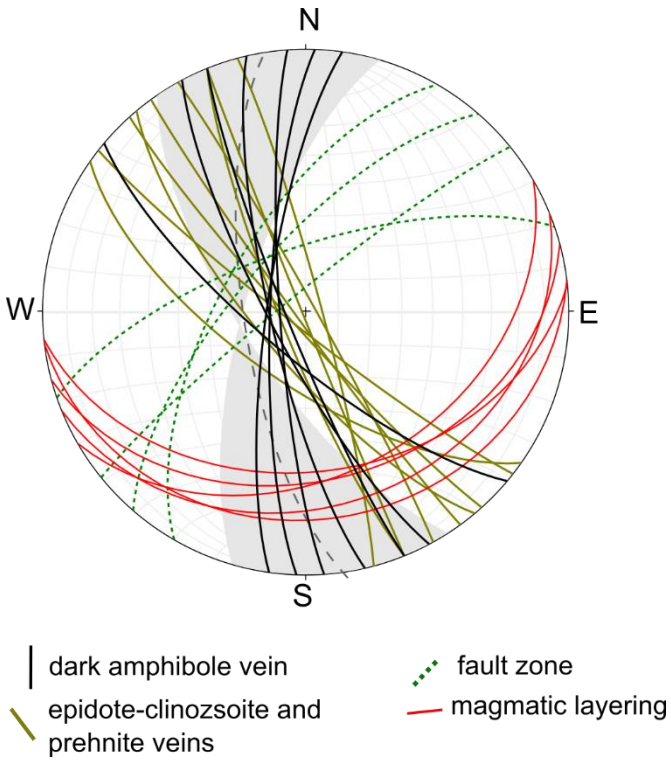

Figure 3.5: Stereographic projection of hydrothermal veins observed in the mapped outcrop.Amphibole veins (black), epidote-clinozoisite and prehnite veins (pale green), fault zones (dashed green) are shown relative to the magmatic layering measured close by (red) and the mean orientation of the sheeted dykes measured in the Ibra area (Pallister, 1981). Note the shaded grey area of the sheeted dyke represents the 1 σ (n=53) from the mean value of Pallister (1981).

3.3.3 Vein and halo analysis

Logged veins along the outcrop show thicknesses between several millimetres up to a maximum width of 4 cm. Most veins plot in the range of 0-0.5 cm and 0.5-1 cm. This includes all amphibole veins, which typically range 0.1-0.3 mm in width, and a majority of epidote-clinozoisite veins with thicknesses of 0.5-1 cm. Comparable vein apertures are reported from the lower crust in Wadi Haymiliya in the central part of the ophiolite, where epidote and zoisite veins range on average around 0.5 cm (Nehlig and Juteau, 1988a). But further to this range, there are several thicker epidote-clinozoisite veins of up to 3 cm. Overall, the highest vein thickness is shown by two prehnite veins with up to 3-4 cm.

Halo half-widths range between a few cm up to almost 2 m (Figure 3.6). This includes both, haloes around single veins of epidote-clinzoisite or prehnite, and haloes around whole vein systems. The majority of haloes plot in the range between 0-60 cm in size with only 40% greater than 60 cm

wide. The widest halo measured is 165 cm forming an area of highly altered gabbro around a network of anastomosing epidote-clinozoisite and cross-cut by prehnite veins.

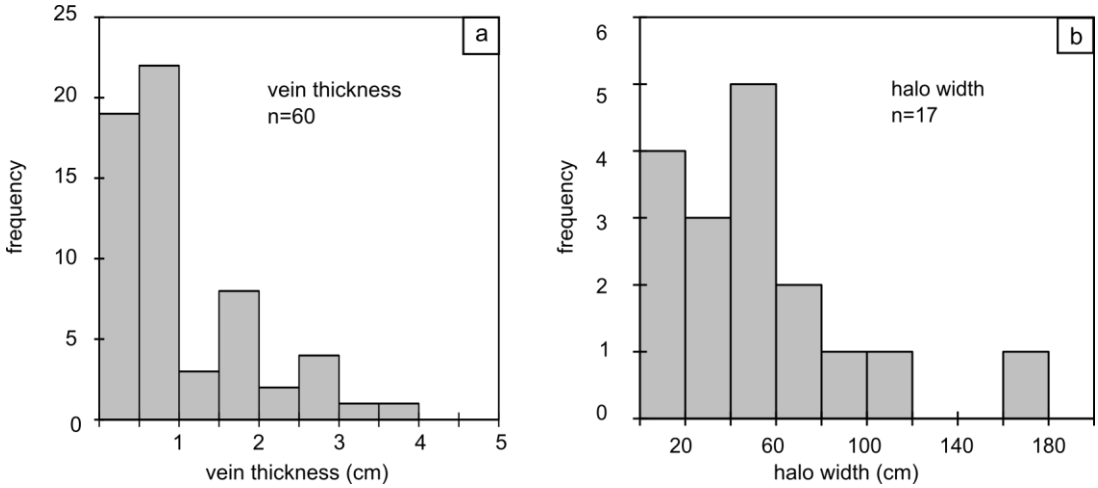

Figure 3.6: Histogram vein thickness and halo widhts (a) Vein thickness (in cm) and (b) halo width (in cm) of all mapped hydrothermal veins and vein systems. The majority of the veins range between a few millimetres up to two centimetre in size and halo width are mostly < 60 cm.

3.4 Methods

Sample preparation and analytical techniques are described in detail in Chapter 2, and are summarised here. Representative samples of fresh layered “background” gabbro (< 10 % alteration), hydrothermal veins and observed alteration types were collected along the outcrop during the first fieldwork season in January/February 2016. Samples were cut with a diamond saw, saw marks were grinded off and polished thin section were prepared. Minerals were identified using standard petrographic techniques as well as a Carl Carl Zeiss Leo1450VP electron scanning microscope (SEM), at the University of Southampton. Major element compositions of minerals were analysed by electron probe microanalysis (EPMA) at the University of Hannover operating a Cameca SC 100 and following the procedure outlined in Chapter 2. Calculated limits of detection (LOD), precision and accuracy can be found in Table 2.2.

Whole rock samples were prepared for geochemical analysis at the University of Southampton, following the protocol outlined in Chapter 2. Selected handpicked minerals of hydrothermal veins (laumontite, prehnite and chlorite) were analysed by XRD in order to confirm the composition and the purity of the picked mineral grains.

Strontium isotope composition of whole rock and handpicked mineral separates were measured by Thermal Ionization Mass-Spectroscopy (TIMS), following the procedure outlined in Chapter 2. Strontium standard NBS987 was measured as an external standard at the beginning and in the middle of each measurement cycle. External precision was monitored by calculating the two standard deviation (2 σ). Measurements of NBS987 over the period of analysis giving an average of 0.710242 ± 0.000012 (2σ). Internal precision was monitored by measuring 150 ratios per sample and reported as two standard errors (2SE).

3.5 Results

3.5.1 Petrographic description

3.5.1.1 Fresh layered background gabbro

The host rocks in the Wadi Qafifah outcrop are olivine-bearing gabbros and characterised by an olivine modal abundance of approximately 5 to max. 10 %, together with 55-60 % plagioclase and 40-45 % clinopyroxene. They show an anhedral, equigranular texture with grain sizes ranging between 0.5-2 mm, typical for lower gabbros in the Wadi Tayin area (e.g., Pallister and Hopson (1981)). In most samples the igneous layering is not visible in thin section scale. However, a few samples show domains with higher modal abundances of olivine or plagioclase alternated with domains with no olivine or lower modal abundances of plagioclase. Commonly the alteration intensity of the fresh background samples range between 10-40%, with olivine being the most altered mineral. Olivine shows the typical mesh structure of incipient serpentinisation, with serpentine and magnetite formed along cracks. In the least altered samples, cores of fresh olivine are preserved (Figure 3.7a), whereas in other samples olivine crystals are completely replaced by serpentine and/or chlorite and magnetite. Plagioclase shows variable degree of alteration. In the freshest samples plagioclase is mostly unaltered, showing only minor cracks within the grains but no replacement by secondary minerals. With increasing degree of alteration plagioclase is more abundantly fractured and partially replaced by chlorite and microcrystalline alteration phases (Figure 3.7c). Both chlorite and microcrystalline alteration phases preferentially start to grow along cracks before overgrowing the whole grain, giving it a cloudy appearance. In more altered grains, twinning is no longer visible and grain boundaries are indistinct, making it difficult to define grains properly. Clinopyroxene is commonly the least altered phase but like plagioclase it shows abundant fracturing with an increasing degree of alteration (Figure 3.7c). Inclusions of dark brown, ~100-250 µm sized hornblende and pargasitic hornblende are frequent. Also, hornblende partially overgrows clinopyroxene grains. In some samples these amphibole inclusions are rimmed by actinolite needles (Figure 3.7d). With increasing degree of alteration, clinopyroxene shows partial replacement by either greenish hornblende or is rimmed by fibrous actinolite.

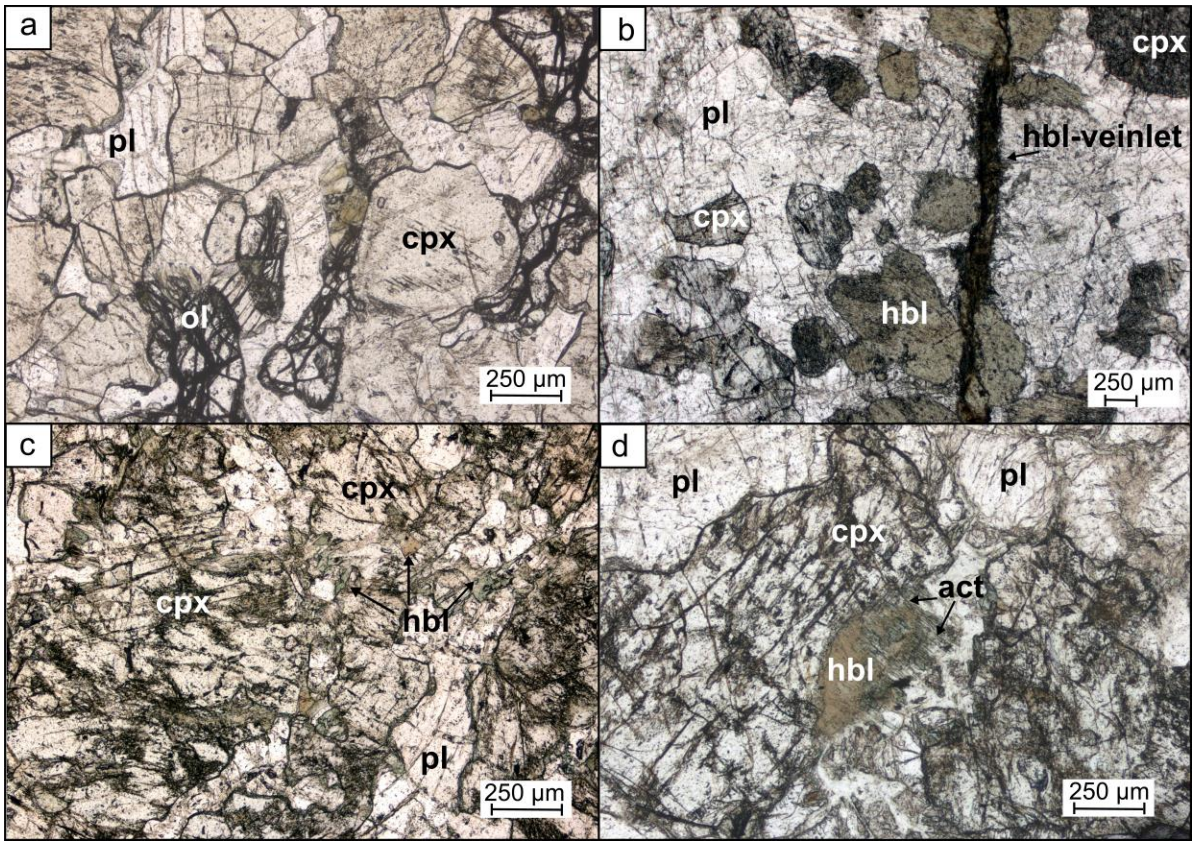

Figure 3.7: Thin section photomicrographs of fresh background samples. All photos taken under plane polarised light. (a) Fresh olivine-bearing gabbro. Clinopyroxene (cpx) and plagioclase (pl show only few fractures and are well preserved. Olivine (ol) is partially serpentinized, secondary magnetite is formed along fractures but cores are well preserved. (b) Sub-millimetre sized hornblende (hbl) veinlets are common and clinopyroxenes along the veinlet are partially or fully replaced by hornblende. Commonly, the replacement can be observed up to 2-3 mm away from the vein. (c) Photomicrograph of a more altered background gabbro. Clinopyroxene and plagioclase show abundant fractures and are partially overgrown by microcrystalline alteration phases. Clinopyroxene have a “dusty” appearance and are partially replaced by both green and brown hornblende. (d) Commonly, clinopyroxenes show inclusions of brown hornblende, indicating the beginning of a replacing reaction. In this sample, the hornblende is further rimmed by actinolite needles.this sample, the hornblende is further rimmed by actinolite needles.

3.5.1.2 Hydrothermal veins

Amphibole veinlets

Fine grained, 100-250 µm wide veinlets of fibrous, dark-brown hornblende cross-cut the magmatic assemblage and clinopyroxene are fully replaced by brownish to greenish hornblende within 1-2 mm distance to these veinlets (Figure 3.7b), forming a narrow halo, only visible under

the microscope. Plagioclase within these haloes tend to be more abundantly fractured and are partially replaced by microcrystalline alteration phases. In all samples, the vein hornblende is fibrous, in contrast to the hornblende replacing clinopyroxene.

Epidote-clinozoisite veins

Commonly, epidote and clinozoisite co-exist in one vein but veins with only one of them are observed too. Typically, these veins range between a few mm up to several cm wide (Figure 3.8a, b). Grain sizes and grain shapes are variable. Compared to clinozoisite, epidote shows more rounded, shorter grains with grain sizes typically between 250 µm up to several mm with subhedral crystal shapes. In a few samples, several generations of epidote are present (Figure 3.8c) within one vein. Commonly, the older generations shows a "dusty" appearance with epidote crystals exhibiting brownish tints. The cause of these brownish tints is not entirely clear; it is suspected that other, sub-micron sized alteration phases such as chlorite or titanite, are present as inclusions or overgrow the epidote. In contrast, clinozoisite is commonly euhedral and elongated along the c-axis and shows characteristic anomalous blue tints in cross-polarised light (Figure 3.8b, e). Commonly, epidote and clinozoisite veins show evidence that they grew from both sides of a fracture into open-space, with increasing grain sizes from the walls of the vein towards the vein centre (Figure 3.8b). Typically, open space is still visible or has been filled by later secondary mineral phases such as prehnite or calcite. This suggests that either the hydrothermal fluid composition evolved or that a second fluid moved through the fracture, precipitating minerals at a later stage under different conditions. Given that that crystal rims of epidote and clinozoisite do not show any signs of corrosion, it can be assumed that the fluid precipitating prehnite or calcite was either in equilibrium with epidote/clinozoisite or there was not enough time for any reaction to happen.

In almost all samples, epidote/clinozoisite veins are rimmed by green hornblende (250 – 1000 µm) and actinolite needles (Figure 3.8a). These amphibole selveages extends for 0.5 mm up to several mm away from the vein. Depending on the sample, it purely consists of green hornblende ± actinolite ± chlorite ± epidote and clinozoisite. In other samples, ghost crystals of clinopyroxene are present that are almost completely overgrown by hornblende. Typically, these hornblende blades are bent, showing signs of deformation (Figure 3.8d).

Prehnite ± clinozoisite ± calcite veins and vein breccias

Prehnite is the main component of this vein set and observed crystals are generally 100-250 µm but can be as big as 0.5-1 mm. Commonly, prehnite occurs as radial aggregates of several crystals with well-defined grain boundaries, indicating precipitation directly out of a hydrothermal fluid. Prehnite co-exists with both clinozoisite and calcite, although calcite is more abundant. Observations from thin section petrography show that prehnite gradually replaces clinozoisite and

remaining clinozoisite crystals typically show corroded grain boundaries (Figure 3.8e). Abundant calcite is coarse grained with grain sizes of 250 µm up to 2 mm (Figure 3.8f). Chalcopyrite and subordinate pyrite (0.5-2 mm) crystals are disseminated within two prehnite dominated veins, showing pronounced brownish to opaque weathering haloes of oxyhydroxides around them. Fine grained malachite is present too (< 5 wt. %).

Laumontite-calcite veins

Fibrous, ~ 50 µm-sized laumontite is the major component of laumontite-calcite veins. Crystals show well defined grain boundaries and the contact between the vein and the surrounding whole rock is sharp. Calcite is very fine grained (< 10 µm) and occurs either along the margins of the veins or replace parts of the veins themselves.

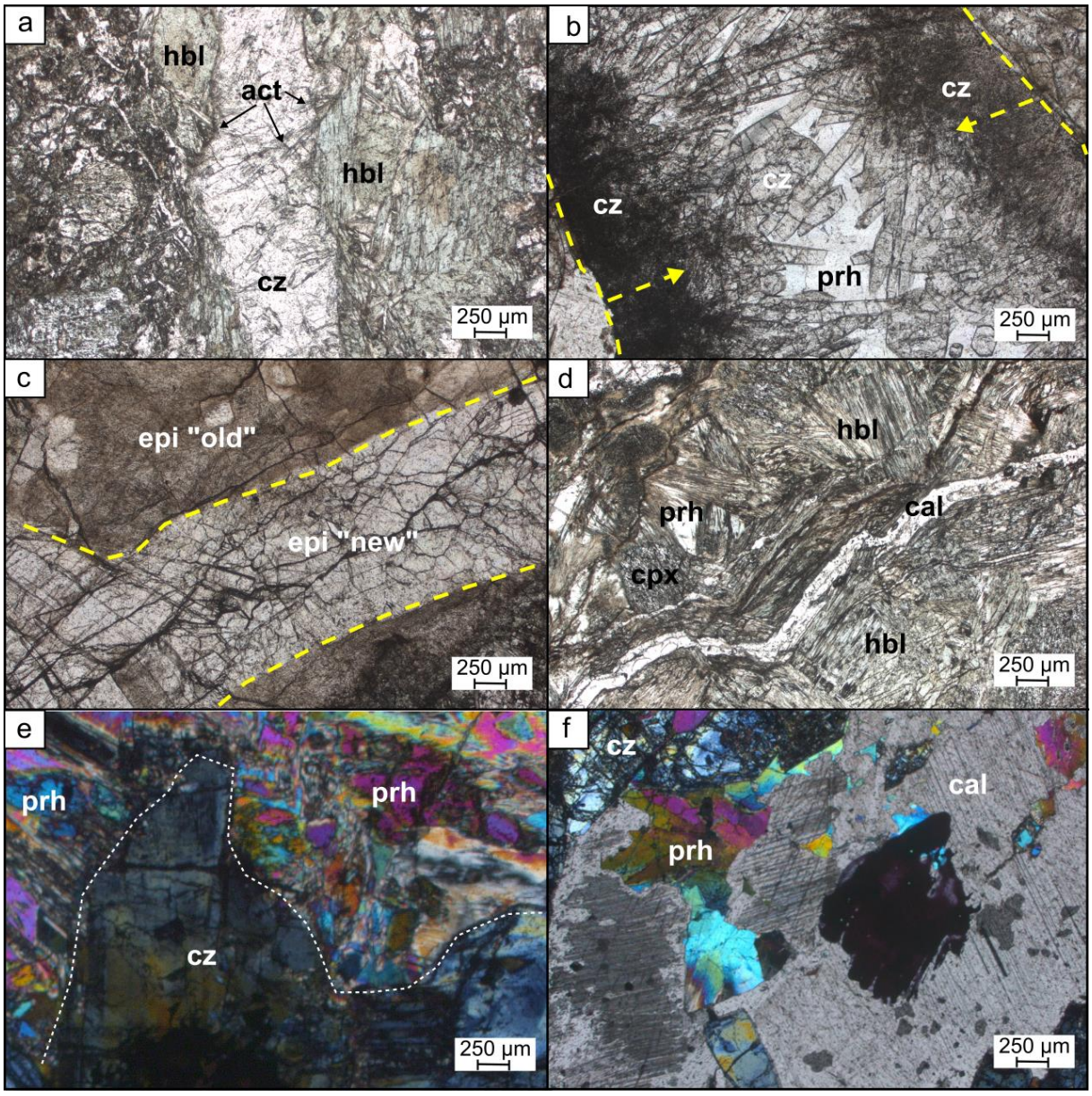

Figure 3.8: Thin section photomicrographs of hydrothermal veins and vein systems. Photos (a) - (d) taken under plane polarised lights and (e) - (f) under cross-polarised lights. (a)

Clinozoisite vein rimmed by green hornblende. Actinolite (act) needles grow from hornblende into the vein and growing over clinozoisitie (cz), indicating that they are later. (b) Clinozoisite vein with interstitial prehnite (prh). Clinozoisite is fine grained along the vein boundaries but euhedral crystals with perfect crystal habit grow into the centre of the vein. (c) Two generations of epidote in an epidote vein. Older epidote looks dustly and seems to be overgrown by a microcrystalline phase. It is cross-cut by a second epidote vein consisting of clear epidote crystals. (d) Green hornblende replacing clinopyroxene. Laumontite-calcite vein (< 1mm) cross-cutting the hornblendes. Prehnite crystals occur interstitial. (e) Prehnite replacing clinozoisite in a prehnite-clinozoisite-calcite vein. Note the corroded and diffuse grain boundaries of clinozoisite. (f) mm-sized calcite in a prehnite-clinozoisite-calcite vein with interstitial prehnite. The black dot in the middle of the picture is black ink of a marker pen.

3.5.1.3 Halo alteration around epidote-clinozoisite veins

Gabbro around epidote-clinozoisite veins and vein systems is generally altered to a high degree and original magmatic minerals and textures are only partially preserved. Alteration intensity ranges between 65-90 %. Generally, plagioclase is absent and totally replaced by either clinozoisite-epidote or chlorite ± actinolite/tremolite (Figure 3.9a, b). Only in a few haloes are fragments of heavily altered and partially replaced plagioclase present. Secondary minerals replacing plagioclase are commonly very fine grained with grain sizes < 250 µm. Outlines of former plagioclase grains are no longer visible but secondary minerals such as chlorite± actinolite/tremolite and epidote-clinozoisite grow matrix-like around clinopyroxene crystals. Clinopyroxenes are heavily fractured, and typically display a “dusty” appearance, possibly due to overgrowth by microcrystalline phases such as amphiboles and magnetite (Alt et al., 2010). Some clinopyroxenes are overgrown by large (1-2 mm), euhedral greenish-bluish hornblende blades (Figure 3.9c, d) or are clearly rimmed by hornblende or actinolite (Figure 3.9a, b). In several samples, particularly hornblendes grown close to epidote-clinozoisite veins, these large, euhedral hornblende blades are bent, showing evidence of deformation (Figure 3.9d).
In the most altered samples alteration products are generally very fine grained (< 150 µm), which makes it often very difficult to see which secondary minerals replace which primary ones. Minor prehnite and laumontite are commonly present in alteration haloes. Prehnite mainly occurs as an interstitial phase in between epidote-clinozoisite grains or hornblende-clinopyroxene grains (Figure 3.9c) whereas laumontite occurs in discontinuous veinlets, cross-cutting earlier alteration phases.

3.5.1.4 Patchy alteration

Patchy, non-vein related alteration is uncommon in the gabbros in the Wadi Qafifah outcrop. These patches commonly occur within a few centimetres of epidote-clinozoisite veins but do not rim the veins like haloes. In general, alteration observed in patches is similar to halo alteration but overall slightly less intense (~50-65 %). In contrast to halo alteration, albitised plagioclase is present, although heavily altered with abundant fractures and partially replaced by epidote-clinozoisite and chlorite.

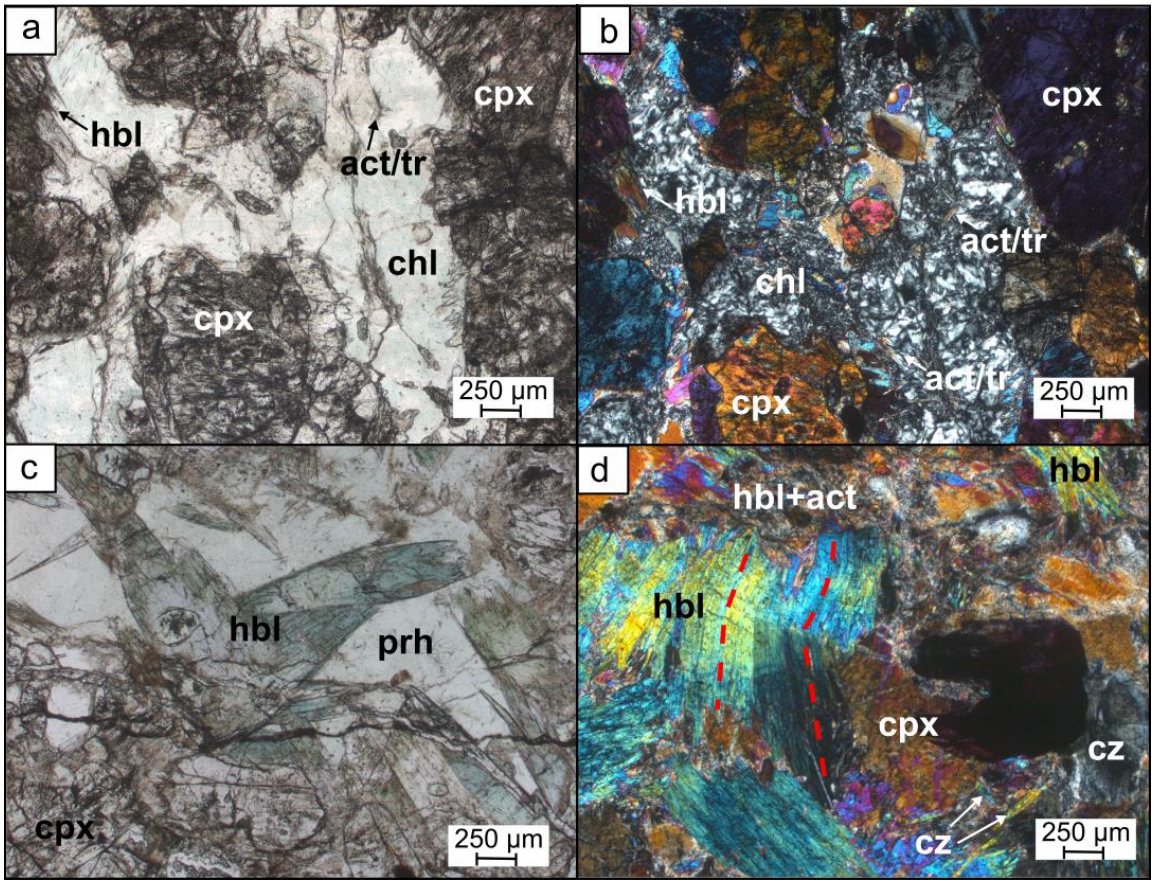

Figure 3.9: Photomicrographs of halo alteration around epidote-clinozoisite veins. (a) Plagioclase is completely replaced by chlorite ± actinolite/tremolite. Clinopyroxene show "dusty" appearance and are rimmed by hornblende and actinolite. (b) Same photomicrograph as (a) but taken under cross-polarised lights. (c) Green-bluish hornblende blades growing from clinopyroxene and interstitial prehnite. Clinopyroxene is heavily fractured, dusty and partially replaced by a fine grained mix of actinolite. Plagioclase is absent. (d) Photomicrograph of one of the most altered and almost completely recrystallised sample. Big, bent hornblende blades grow over clinopyroxene and only small parts of heavily fractured clinopyroxene are left. Fine grained hornblende, actinolite and clinozoisite grow "mat-like" and replace primary

minerals completely. Please note, the dark circle is marker pen and was used for EPMA-analysis.

3.5.2 Mineral chemistry of primary and secondary minerals (EPMA)

3.5.2.1 Olivine

Fresh olivine cores have been analysed in three samples and all of them show a narrow range of Mg# (Mg# = 100 x molar Mg/Mg+Fe) of Mg_{81-86} (Appendix A.1). These compositions are similar to what is described from olivine in the layered gabbros within Wadi Tayin and typical for lower crustal rocks with primitive compositions (Pallister and Hopson, 1981).

3.5.2.2 Clinopyroxene

Pyroxene composition has been recalculated on the basis of six oxygens and ferric iron has been estimated following the procedure of Droop (1987) (Appendix A.1). Mg# range between Mg_{82-92}, typical for primitive composition of clinopyroxenes in cumulates of the oceanic crust (Coogan et al., 2002a). No orthopyroxenes are present.

3.5.2.3 Plagioclase

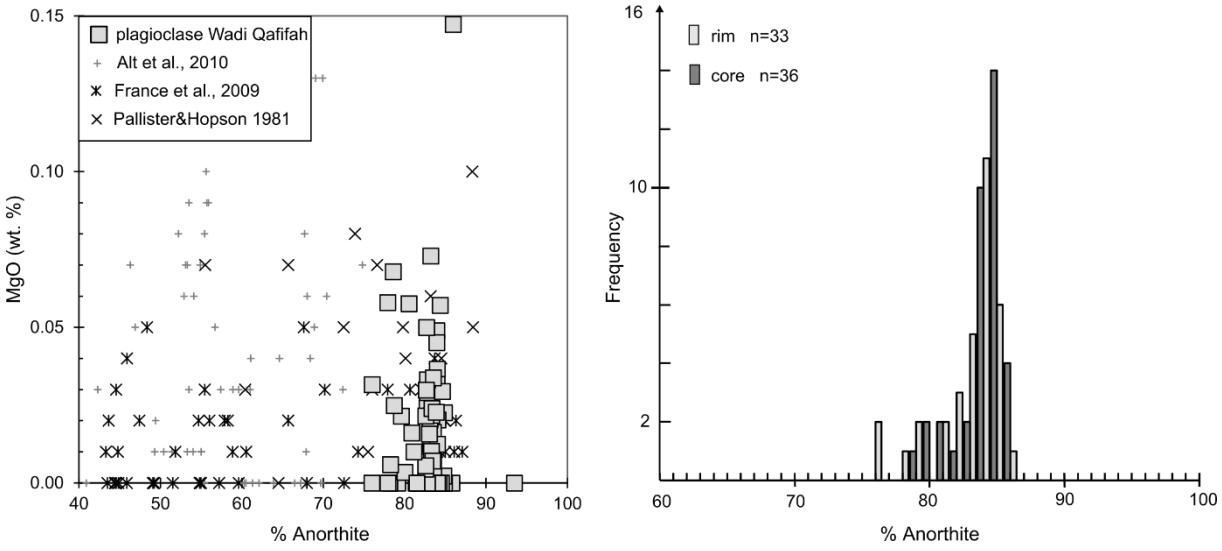

Figure 3.10: Composition of plagioclase rims and cores of six fresh layered gabbro samples. Samples show an average anorthite content of $An_{83,}$ with no trend towards more albitic composition of grain rims. Overall, plagioclase compositions are comparable to composition reported from other studies (France et al., 2009; Pallister and Hopson, 1981) of the Samail ophiolite.

Plagioclase analysed in six different layered background gabbro samples show plagioclase composition comparable to plagioclase from elsewhere in Wadi Qafifah (Pallister and Hopson,

1981) and the layered gabbros in the Wadi Tayin area (France et al., 2009; Pallister and Hopson, 1981) and in the lower crust of modern oceanic crust, measured in plagioclase from the gabbro section in ODP/IOPD Hole 1256D (Alt et al., 2010; Appendix A.1, Figure 3.10). Anorthite (An=100 x molar Ca/(Ca+Na) contents range from of An_{76-86} with an average anorthite content of An_{83}. There is no clear trend between the An-content of grain rims and cores visible, although in one sample more albitic compositions were measured in plagioclase rims. Similar observations, with no trend towards an increased An-content in crystals rims, are reported from plagioclase measured in layered gabbro in Wadi Waryia, a few kilometres to the west of Wadi Qafifah (Wolff, 2014). Albitic compositions were not present.

3.5.2.4 Amphibole

Amphibole compositions have been recalculated on the basis of 23 oxygens (Appendix A.1) and classified after Leake et al. (1997) (Figure 3.11) and ferric iron estimated after Schumacher (1997). All measured amphibole classify as Ca-amphiboles and a continuous trend from pargasitic via hornblendic to actinolitic composition is present (Figure 3.11). Such a trend is very common for Ca-amphiboles in oceanic gabbros (Bosch et al., 2004; Manning et al., 1996; Mével and Cannat, 1991; Vanko, 1986) and reflects the different formation conditions (e.g. difference in temperature) during hydrothermal fluid-rock interaction. A second, but much less pronounced and evolved trend seem to exist towards tschermakitic exchange, mainly due to a few analyses of amphibole in background gabbros plotting in the tschermakite field or just at the boundary between Mg-hornblende and tschermakite. In general, amphiboles observed in the layered background gabbro samples plot in all fields defined in the classification scheme after Leake et al. (1997) (Figure 3.11). Brown, poikilitic amphibole in clinopyroxene grains show compositions from pargasite to tschermakite and magnesiohornblende, whereas amphibole co-existing with chlorite and partially replacing plagioclase shows actinolitic- tremolitic compositions. The majority of measured amphiboles in alteration haloes around epidote-clinozoisite veins plot in the Mg-hornblende and actinolite field. Similar compositions are observed for amphiboles in selvages rimming epidote-clinozoisite veins.

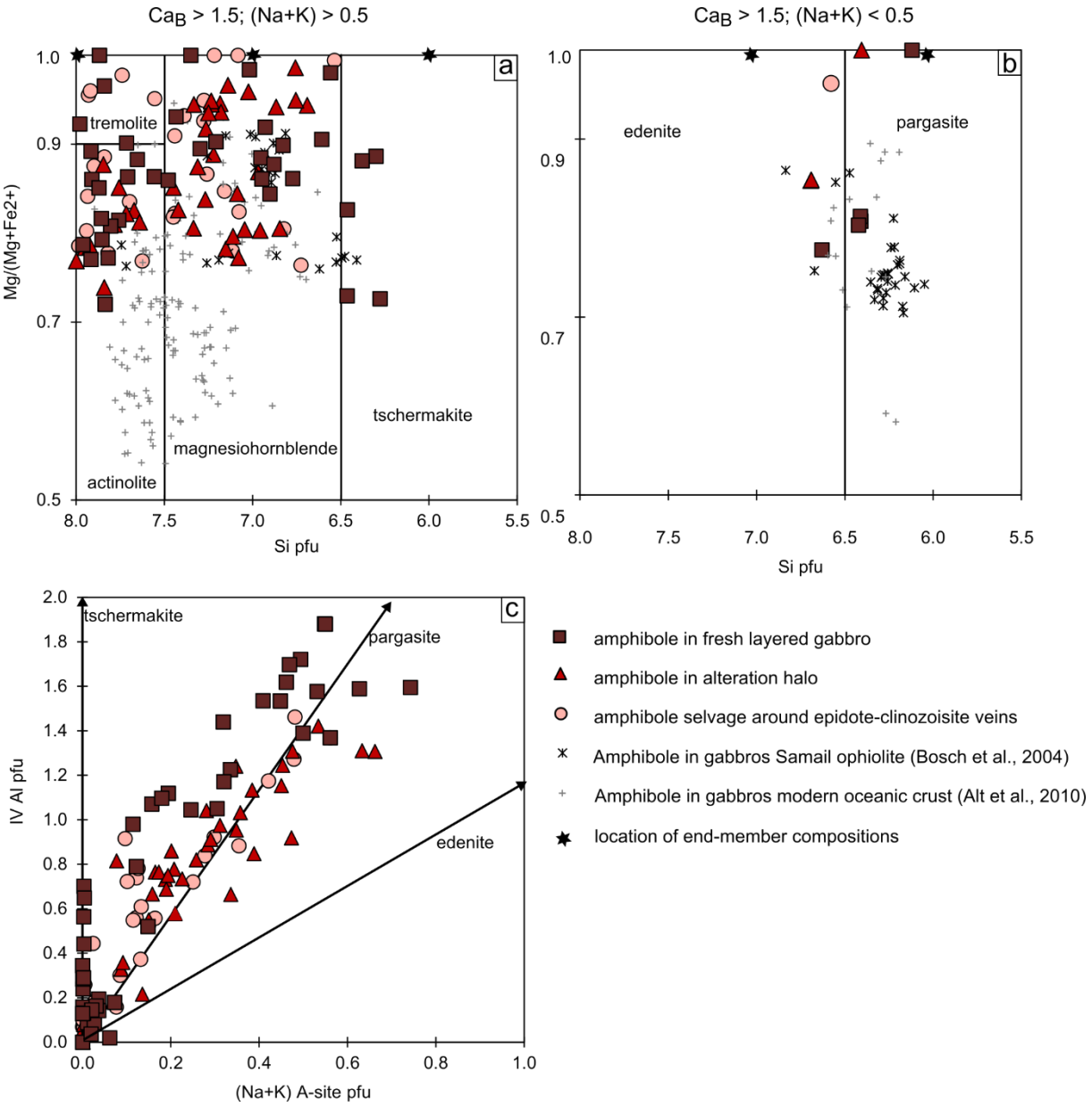

Figure 3.11: Classification of amphiboles measured in fresh layered gabbro samples, alteration haloes around epidote-clinozoisite veins and amphiboles of amphibole selvages around epidote-clinozoisite veins. Classification after Leake et al. (1997). Measured amphiboles are compared to amphiboles measured elsewhere in the layered gabbros of the ophiolite (Bosch et al., 2004) and in gabbros of modern fast-spreading oceanic crust (Alt et al., 2010). (a) Ca-amphibole with CaB>1.5; (Na+K) >0.5 and (b) with CaB >1.5; (Na+K) <0.5. (c) Continuous trend from pargasitic via hornblendic to actinolitic composition, which is very common for Ca-amphiboles in oceanic gabbros.

3.5.2.5 Chlorite

Chlorite compositions have been recalculated on the basis of 28 oxygens (Appendix A.1, Figure 3.12). Analysed chlorite includes: (i) chlorite replacing plagioclase and co-existing with actinolite/tremolite in background gabbros and altered halo; (ii) chlorite from one chlorite-patch observed as part of a clinozoisite-prehnite-calcite vein. All of the chlorite grains analysed show limited silica (5.75-6.22 Si pfu) and Fe/(Fe+Mg) =0.12-0.20 variations, compared to chlorite from elsewhere in the ophiolite and in modern oceanic crust. Their composition plots close to the ideal clinochlore composition and similar to chlorite observed in altered hanging wall and footwall samples of the chlorite-rich fault zone in Wadi Gideah (see Chapter 4 and 5).

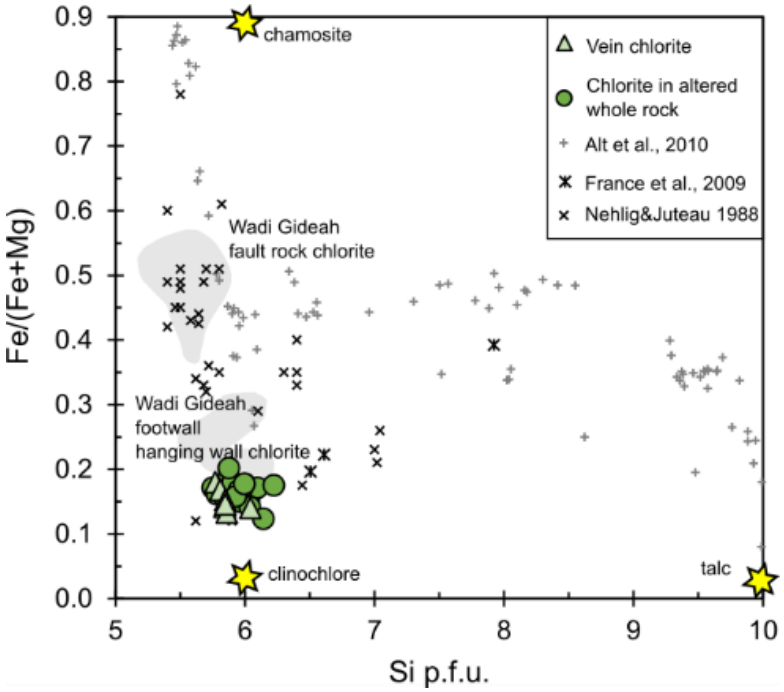

Figure 3.12: Composition of chlorite veins and chlorite patches in altered gabbro. All measured chlorites are poor in iron and plot close to ideal chlinochlore composition. Also plotted for comparison purpose, chlorite composition measured in upper and lower gabbros from Wadi Haymiliya in the central part of the ophiolite (Nehlig and Juteau, 1988), chlorite measured in isotropic high-level gabrros in Wadi Gideah (France et al., 2009) and chlorite compositions measured in gabbros of modern oceanic crust at ODP/IODP Site 1256 (Alt et al., 2010).

3.5.2.6 Epidote and clinozoisite

Epidote-clinozoisite has been calculated on the basis of 13 oxygens (Appendix A.1, Figure 3.13). Epidote and clinozoisite form a solid-solution between the iron-rich end-member and the alumina-rich end-member. X_{Fe} (X_{Fe} =100 x molar Fe/(Fe+Al)) of epidote and clinozoisite analysed in

veins as well as in alteration haloes show a range between 5-35%, with the majority of analysis between 5-20%. This is similar to what has been reported from epidote veins and epidote crystals in the alteration haloes around hydrothermal veins in gabbros from the lower crustal section of Wadi Haymiliya in the central part of the ophiolite (X_{Fe} = 0.5-20 for most analysis) (Nehlig and Juteau, 1988) and from epidote veins in Wadi Waryia (X_{Fe} =4-18) (Wolff, 2014). Epidote observed in the chlorite-rich fault zone in Wadi Gideah plots in upper range of X_{Fe} reported here (see Chapter 4 and 5).

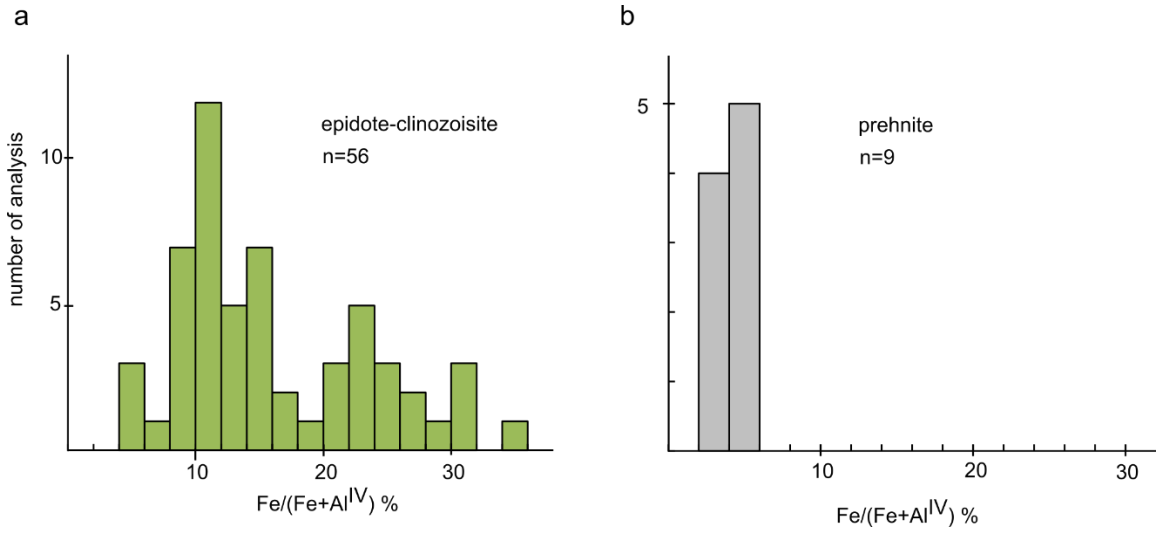

Figure 3.13: Histogram of (a) epidote and (b) prehnite compositions of hydrothermal veins. Epidote-clinozoisite show a relatively wide range, with compositions from 5-35% X_{Fe}. Prehnite compositions are uniform and relatively rich in Al.

3.5.2.7 Prehnite

Prehnite of prehnite-epidote veins have been measured and results are recalculated on the basis of 24 oxygens and 4 OH sites (Appendix A.1, Figure 3.13). In general, prehnite compositions are uniform and show low iron concentrations with X_{Fe}=100*Fe ($Fe+Al^{iV}$) between 2-4 %. With these values prehnite is comparable to prehnite analysed in veins by Nehlig and Juteau (1988) in altered gabbros of Wadi Haymiliya in the northern part of the Samail ophiolite, although the analysis of Nehlig and Juteau (1988) extend to more iron rich prehnite with X_{Fe} of up to 20% and X_{Fe} up to 48% in prehnites from the sheeted dyke complex. Moreover, interstitial prehnite measured in altered layered gabbro in Wadi Wariyah shows comparable X_{Fe} contents (Wolff, 2014).

3.5.3 Sr-isotopes

Strontium isotopes are useful tracers for hydrothermal fluid-rock interaction. During precipitation of secondary minerals no mass fractionation occurs and therefore the $^{87}Sr/^{86}Sr$ of a mineral in a hydrothermal fluid records the $^{87}Sr/^{86}Sr$ ratio of the hydrothermal fluid the mineral precipitated from. Moreover, epidote-clinozoiste show relatively high Sr concentrations of ~ 600-750 µg/g and are robust against low temperature fluid-rock Sr exchange. A hydrothermally altered whole rock therefore reflects the extent of fluid-rock interaction as its $^{87}Sr/^{86}Sr$ composition is a mix between its primary magmatic value and the hydrothermal input added by the precipitation of secondary minerals.

Strontium isotope compositions of 12 of the freshest background layered gabbros sampled along the outcrop in between veins and 14 halo and patch altered rocks were measured (Table 3.1). Halo and patch altered rock were leached with 10% acetic acid prior to analysis to remove any secondary calcium carbonate. Additionally, epidote and clinozoisite of epidote-clinozoisite veins, prehnite of a pure prehnite vein, laumontite and calcite of laumontite-calcite veins, chlorite of a chlorite vein and green hornblende of hornblende selvages around epidote-clinozoisite veins were hand-picked and measured (Table 3.1). The hand-picked laumontite was also leached with 10 % acetic acid prior to analysis to remove any secondary calcium carbonate.

Fresh layered background gabbro

Fresh background layered gabbro, sampled throughout the outcrop, show strontium isotopic compositions in the range of $^{87}Sr/^{86}Sr$=0.7032-0.7042. These Sr-ratios are elevated compared to fresh MORB from modern oceanic crust (White et al., 1987) and are slightly to considerably more elevated compared to fresh layered gabbros reported from elsewhere in the Samail ophiolite ($^{87}Sr/^{86}Sr$ ~ 0.70265 - 0.70320; Lanphere et al., 1981; McCulloch et al., 1980) (Figure 3.14, 3.15). But the majority of the samples plot in the range of $^{87}Sr/^{86}Sr$=0.7030-0.7035 (Figure 3.15), only slightly more enriched in ^{87}Sr than fresh layered gabbro (Figure 3.15) and indicating only minor Sr isotopic exchange.

Halo and patch alteration

Halo and patch altered samples show a wide range of strontium isotope composition of $^{87}Sr/^{86}Sr$=0.7039-0.7059. Half of the measured samples plot in the range of 87Sr/^{86}Sr=0.7045-0.7050, with two samples showing values lower than $^{87}Sr/^{86}Sr$=0.7045 and four samples above $^{87}Sr/^{86}Sr$=0.7050 (Figure 3.14, Figure 3.15). All four samples with values above $^{87}Sr/^{86}Sr$=0.7050 show relatively high abundances of either prehnite, chlorite or laumontite.

Table 3.1: Strontium isotope composition of Wadi Qafifah whole rock samples and mineral separates. Measured Sr-isotope compositions were corrected to an age of 95 Ma.

Rock type		Sample	de-carbonated1)	$^{87}Sr/^{86}Sr_{measured}$	± 2SE	Sr (µg/g)	Rb (µg/g)	$^{87Sr}/_{86Sr95Ma}$
fresh layered gabbro	whole rock	AD3		0.703316	11	86.8	< 0.01	0.703314
fresh layered gabbro	whole rock	AE3		0.703744	14	94.0	0.04	0.703742
fresh layered gabbro	whole rock	AE5		0.703245	13	67.7	0.03	0.703243
fresh layered gabbro	whole rock	AE8		0.704147	11	118.2	0.18	0.704141
fresh layered gabbro	whole rock	AF1		0.703429	11	111.6	0.06	0.703427
fresh layered gabbro	whole rock	AE6		0.703226	13	79.3	0.04	0.703223
fresh layered gabbro	whole rock	AD1		0.703414	10	86.3	0.06	0.703411
fresh layered gabbro	whole rock	AC9		0.703420	13	60.9	0.03	0.703418
fresh layered gabbro	whole rock	AG7bg		0.703950	12	87.9	0.01	0.703949
fresh layered gabbro	whole rock	AE9		0.703153	13	95.2	0.07	0.703151
fresh layered gabbro	whole rock	AH2b1		0.704257	13	102.1	0.27	0.704247
fresh layered gabbro	whole rock	AF2		0.704188	14	139.9	0.25	0.704181
highly altered gabbro	whole rock	AH2h2	y	0.705221	11	32.0	b.l.d	0.705221
highly altered gabbro	whole rock	AH2h4	y	0.704778	12	105.3	0.03	0.704777
highly altered gabbro	whole rock	AG7h1	y	0.704441	12	19.8	b.l.d	0.704441
highly altered gabbro	whole rock	AH2h3	y	0.705181	13	71.2	b.l.d	0.705181
highly altered gabbro	whole rock	AH2h1	y	0.704406	12	177.0	b.l.d	0.704406
highly altered gabbro	whole rock	AF9h2		0.704734	13	152.0	b.l.d	0.704734
highly altered gabbro	whole rock	AG8ah1		0.704825	10	325.1	b.l.d	0.704825
highly altered gabbro	whole rock	AG1bg1	y	0.704647	12	202.6	0.28	0.704642
highly altered gabbro	whole rock	AG4h1	y	0.704575	10	120.7	< 0.01	0.704575
highly altered gabbro	whole rock	AF5h1	y	0.705918	10	71.2	0.12	0.705912
highly altered gabbro	whole rock	AG5h1	y	0.704698	12	107.0	0.03	0.704696
highly altered gabbro	whole rock	AG6h1	y	0.705090	10	162.4	0.07	0.705088
highly altered gabbro	whole rock	AF8h1	y	0.704828	12	22.6	0.01	0.704826
highly altered gabbro	whole rock	AH4h1	y	0.703915	11	60.3	0.02	0.703914
highly altered gabbro	whole rock	AH3h1		0.704405	10	16.9	0.02	0.704405
amphibole selvage	hand-picked vein mineral	AG8bam1		0.705240	12	6.5	0.02	0.705231
amphibole selvage	hand-picked vein mineral	AG1amp2		0.704952	12	22.6	0.07	0.704941
clinozoisite	hand-picked vein mineral	AG7p1		0.704695	13	652.1	0.01	0.704695
clinozoisite	hand-picked vein mineral	AG1p1		0.704724	12	727.5	< 0.01	0.704724
clinozoisite	hand-picked vein mineral	AF9t1		0.704749	12	741.3	b.d.	0.704749
clinozoisite	hand-picked vein mineral	Ag8at1		0.704739	11	724.2	b.l.d	0.704739
epidote	hand-picked vein mineral	AF9e2		0.704833	14	709.1	b.l.d	0.704833
epidote	hand-picked vein mineral	AF9e1		0.704781	12	614.7	b.l.d	0.704781
epidote	hand-picked vein mineral	AG1e1		0.704856	12	700.9	b.l.d	0.704856
epidote	hand-picked vein mineral	AG2e1		0.704887	14	679.9	b.l.d	0.704887
prehnite	hand-picked vein mineral	AG8apr2		0.705286	13	29.8	b.l.d	0.705286
laumontite	hand-picked vein mineral	AF9lau2	y	0.706544	11	133.1	0.27	0.706536
laumontite	hand-picked vein mineral	AG6lau1	y	0.707276	13	175.4	0.33	0.707269
calcite	hand-picked vein mineral	AF9carb1		0.707913	14	71.5	b.l.d	0.707913
chlorite	hand-picked vein mineral	AG4chl1		0.706320	109	31.3	0.01	0.706319

1) decarbonated with 10% acetic acid

b.l.d below limits of detection

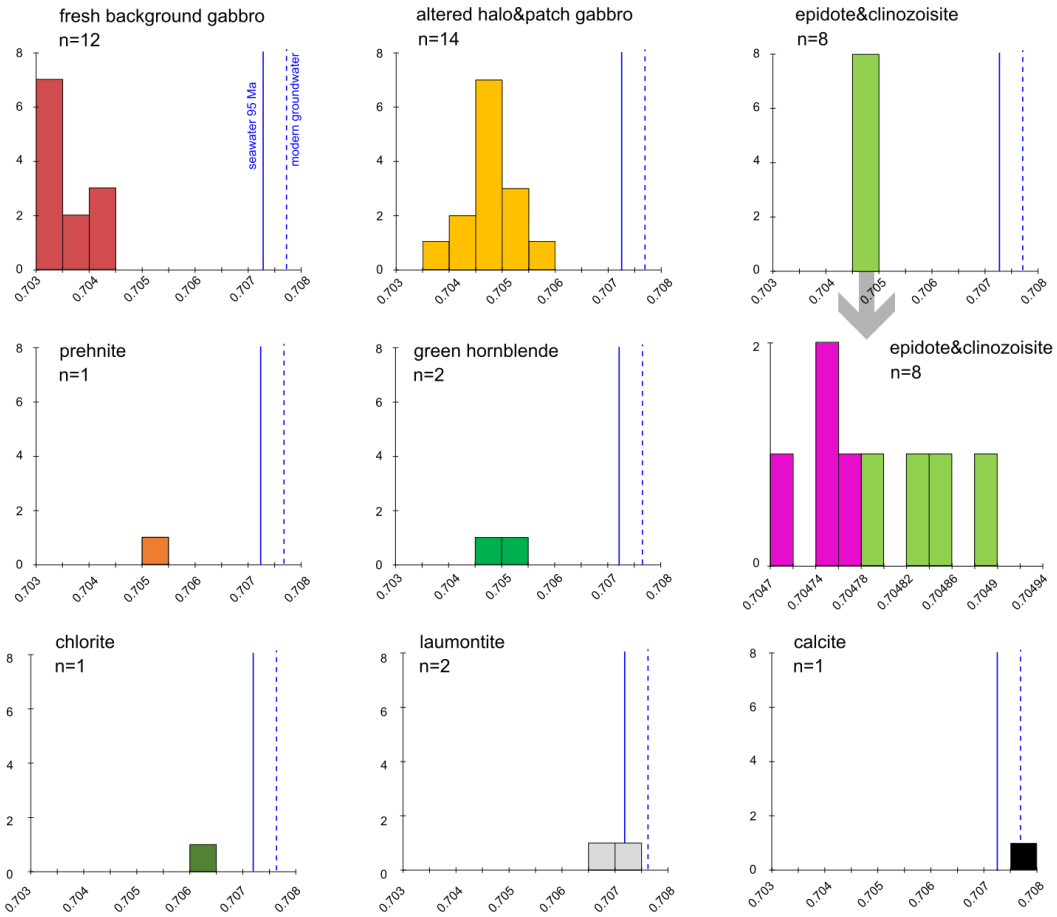

Figure 3.14: Histogram of Sr-isotopic composition of background gabbro, altered halo&patch gabbro, clinozoisite&epidotde veins, prehnite vein, green selvage hornblende, chlorite patch, laumontite veins and calcite vein.Cretaceous seawater from McArthur et al. (2001) and modern groundwater sampled in gabbro hosted wells of Wadi Qafifah from Bompard (2018).

Mineral separates

Hand-picked epidote and clinozoisite of epidote-clinozoisite veins show a narrow range of strontium isotope composition ($^{87}Sr/^{86}Sr$=0.7047-0.7049, Figure 3.14, Figure 3.15), similar to epidote compositions reported from elsewhere in the ophiolite (e.g., Bosch et al., 2004; Coogan et al., 2006). All four analysed clinozoisite samples show consistently lower values ($^{87}Sr/^{86}Sr$=0.70470-0.70475) than the four analysed epidote samples ($^{87}Sr/^{86}Sr$=0.70478-0.70489). Green hornblende of two amphibole selvages around epidote-clinozoisite veins display Sr-isotopic compositions of $^{87}Sr/^{86}Sr$=0.7049 and $^{87}Sr/^{86}Sr$=0.7052, which is in the same range to only slightly more radiogenic than epidote or clinozoisite in the vein itself. Similar Sr-isotope compositions have been reported from amphibole veins in focussed-fluid-flow zones in Wadi Namarah and Wadi Abyad as well as from green hornblende veins elsewhere in the ophiolite (Bosch et al., 2004;

Coogan et al., 2006). Sr concentrations of picked hornblende are low with Sr = 7-23 µg/g. Prehnite of a prehnite vein, cross-cutting a clinozoisite vein and a corresponding hornblende selvage, shows a Sr-isotope composition of $^{87}Sr/^{86}Sr$=0.7053, with a Sr concentration of 30 µg/g (Figure 3.15).

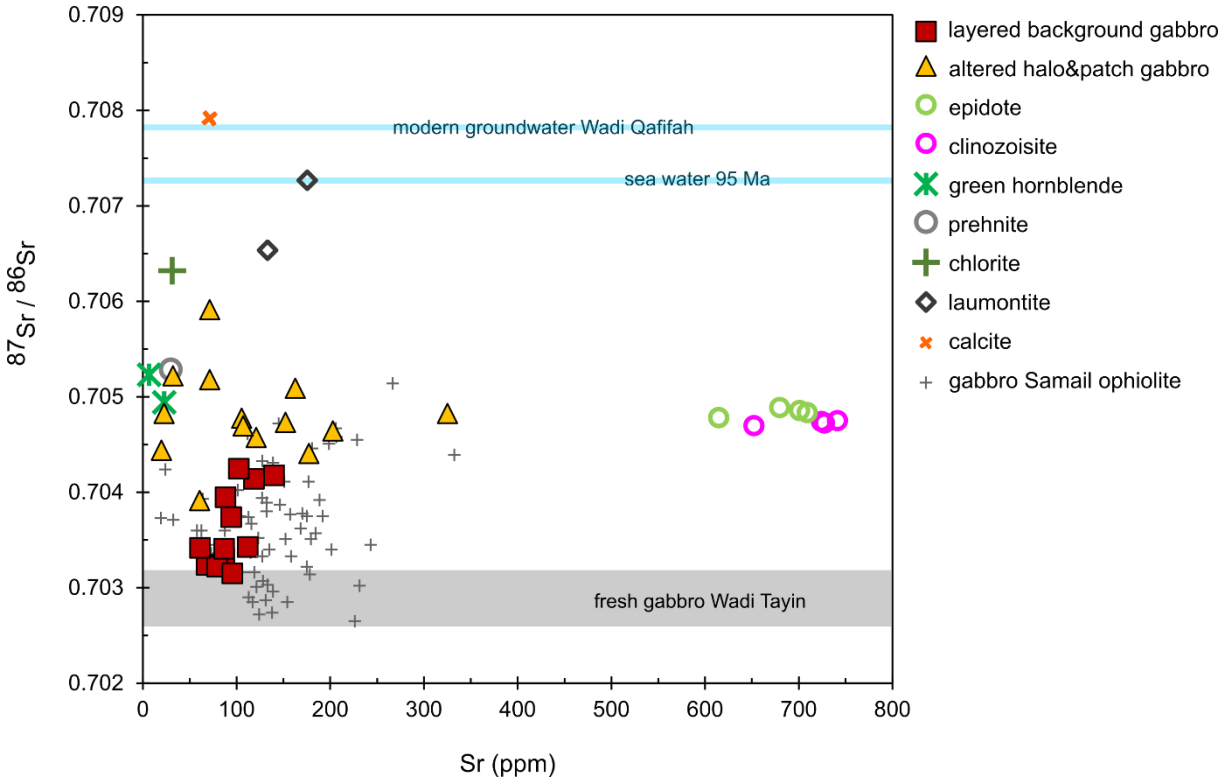

Figure 3.15: Strontium concentration (ppm) versus $^{87}Sr/^{86}Sr$ of fresh background gabbros, halo and patch altered gabbro and hand-picked mineral separates of hydrothermal veins.To compare, Sr-isotope data of whole rock from elsewhere in the ophiolite (Bosch et al., 2004; Kawahata et al., 2001; Lanphere et al., 1981) are plotted in the background. Values of layered gabbro of the Wadi Tayin area are after Lanphere et al. (1981); McCulloch et al. (1981), Cretaceous seawater from McArthur et al. (2001) and modern groundwater sampled in gabbro hosted wells of Wadi Qafifah from Bompard (2018). Error bars are smaller than the size of the symbols.

Chlorite of a chlorite patch in brecciated and highly altered gabbro along a prehnite + clinozoisite + calcite vein displays a strontium isotope ratio of $^{87}Sr/^{86}Sr$=0.7063, more radiogenic than epidote-clinozoisite, prehnite or green hornblende but with a low Sr concentration of 31 µg/g. This Sr concentration is in a similar range as prehnite and hornblende.

Hand-picked laumontite of two laumontite-calcite veins yields Sr-isotope compositions of $^{87}Sr/^{86}Sr$=0.7065 and $^{87}Sr/^{86}Sr$=0.7073, close to 95 Ma-seawater with Sr concentrations of 133 and 175 µg/g (Figure 3.15). The most radiogenic values are shown by calcite of one of the laumontite-calcite veins with $^{87}Sr/^{86}Sr$=0.7079 and a Sr concentration of 71 µg/g, plotting in the range of

Cretaceous to Miocene sediments (Weyhenmeyer, 2000) and close to the Sr-isotopic composition of modern groundwater, samples in gabbro hosted wells in Wadi Tayin (Bompard, 2018).

Strontium isotopic profiles along hand-specimen

In order to better constrain small scale strontium isotope variations in hand specimen and to determine the spatial relationship between hydrothermal veins, altered gabbro and fresh background gabbro, several samples were investigated in more detail (Figure 3.16).

In sample AF9, AG8a, AG1 and AH2 the highly altered gabbro close to the epidote-clinozoisite vein shows the same $^{87}Sr/^{86}Sr$ composition as the veins themselves. In all samples, these halo are within a distance of millimetres to a few centimetres away from the vein. For sample AH2 two analysed samples a bit further away from the vein show slightly higher $^{87}Sr/^{86}Sr$ values ($^{87}Sr/^{86}Sr$=0.70522 and 0.70518) than halo 1 ($^{87}Sr/^{86}Sr$=0.70441) and the vein itself (assuming that the clinozsoisite would show a range within $^{87}Sr/^{86}Sr$=0.7047-0.7049, as determined from similar clinozoisite-epidote veins; Figure 3.16). Within both samples interstitial prehnite and several laumontite-filled cracks can be found and are being thought to be responsible for these slightly higher Sr isotope values. Otherwise, there is a gradual decrease in $^{87}Sr/^{86}Sr$ composition away from the vein, reaching the least radiogenic, albeit strongly elevated, values ($^{87}Sr/^{86}Sr$=0.70425) furthest away from the vein where the sample looks freshest. Sample AG7 shows an altered, whitish-looking patch along a clinozoisite vein (Figure 3.16). Sr-isotope composition within this patch ($^{87}Sr/^{86}Sr$=0.7044) is slightly less radiogenic than the vein itself ($^{87}Sr/^{86}Sr$=0.7047) and less slightly radiogenic compared to halo alteration along comparable clinozoisite veins observed in other samples. This corresponds well with the overall lower degree of alteration observed in the patch (~60%) compared to typical alteration haloes (up to 90% observed alteration). Sr-isotope composition drops relatively sharply down to almost fresh background gabbro values ($^{87}Sr/^{86}Sr$=0.70395) within a few centimetres away from the patch (Figure 3.16).

Strontium concentrations in the halo rock strongly depends on the secondary mineralogy. Whereas epidote-clinozoisite bearing-altered whole rock shows higher Sr concentrations than fresh background gabbro, albite, chlorite and amphibole dominated secondary mineral assemblages show lower Sr abundances.

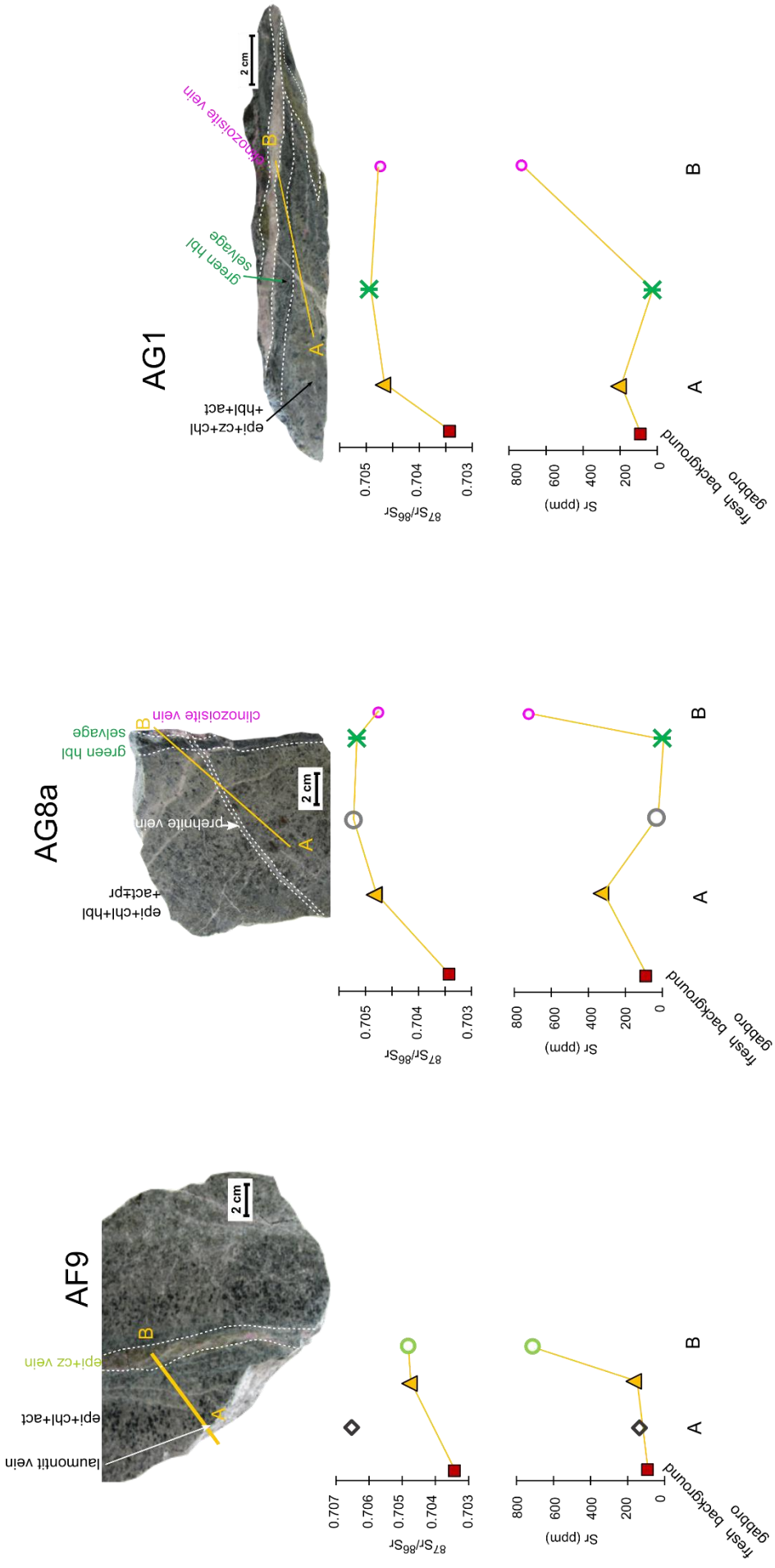
AF9
2 cm
laumontit vein
epi+chl+act
epi+cz vein
A
B
0.703
0.704
0.705
0.706
0.707
87Sr/86Sr
0
200
400
600
800
Sr (ppm)
fresh background
gabbro
A
B
AG8a
2 cm
epi+chl+hbl
+actpr
prehnite vein
A
clinozoisite vein
B
green hbl
selvage
0.703
0.704
0.705
87Sr/86Sr
0
200
400
600
800
Sr (ppm)
fresh background
gabbro
A
B
AG1
2 cm
epi+cz+chl
+hbl+act
A
green hbl
selvage
B
clinozoisite vein
0.703
0.704
0.705
87Sr/86Sr
0
200
400
600
800
Sr (ppm)
fresh background
gabbro
A
B

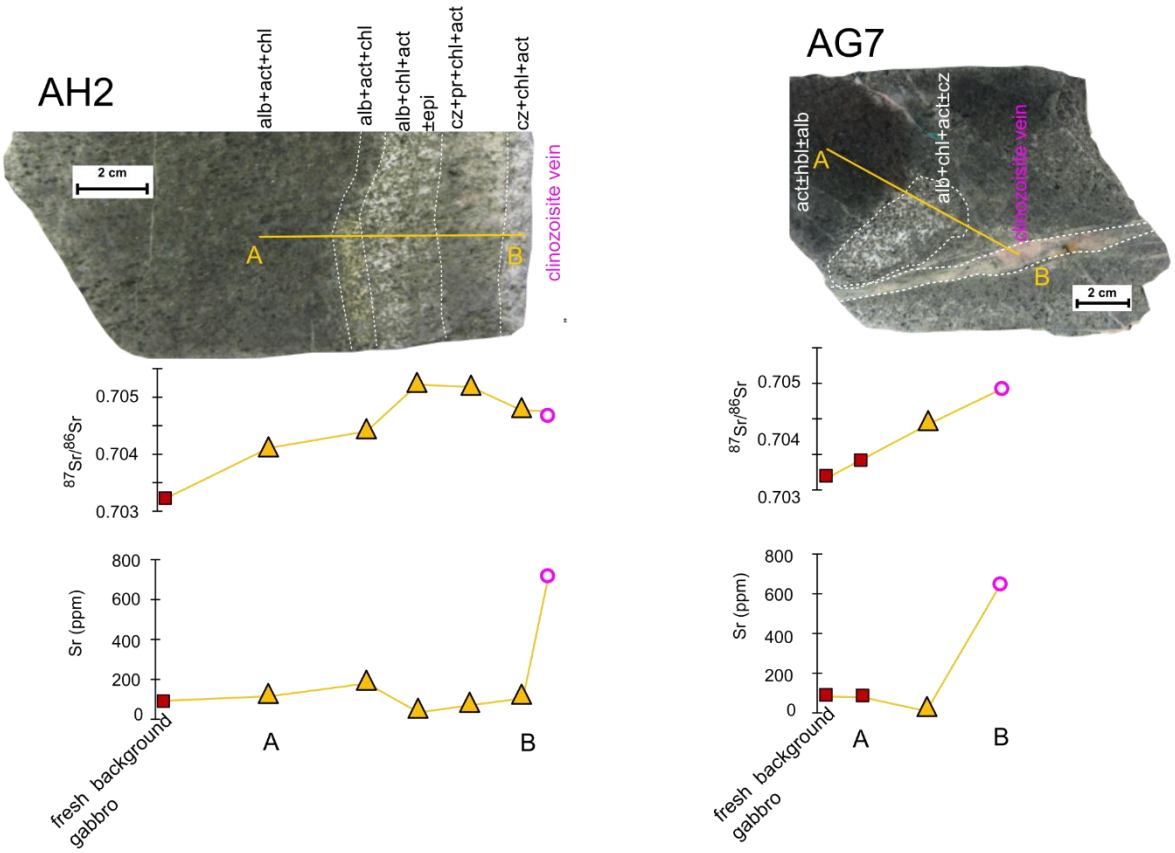

Figure 3.16: $^{87}Sr/^{86}Sr$ isotope and Sr concentration (ppm) profiles along transects in five samples. For all samples the measured median Sr-isotope composition of layered background gabbros is plotted relative to the values of observed alteration. The median Sr-isotope composition of layered background gabbro should represent the initial magmatic value. Note that slightly transparent symbol for clinozoisite vein in sample AH2 represents median $^{87}Sr/^{86}Sr$ composition of all measured epidote-clinozoisite veins ($^{87}Sr/^{86}Sr$=0.7047-0.7049) as there is no value for clinozoisite of sample AH2. It is assumed that the hypothetical value of this vein would be in the same range. Abbreviations: alb, albite; act, actinolite; chl, chlorite; epi, epidote; cz, clinozoisite; pr, prehnite; lau, laumontite; hbl, hornblende.

3.6 Discussion

3.6.1 Relative timing of hydrothermal veins and estimation of formation conditions

Hydrothermal veins provide a record of the hydrothermal fluids circulated through the oceanic crust. By studying cross-cutting relationships and multiple linings within a single vein the relative timing of hydrothermal circulation could be determined. Evidence of cross-cutting relationships of the different hydrothermal vein were observed in the field, in hand-specimen and in thin sections and the following alteration sequence is determined (Figure 3.17):

i. Widespread amphibole alteration of poikilitic pargasite and brown Mg-hornblende in clinopyroxene and formation of brown, mm-sized hornblende veins.
ii. Epidote-clinozoisite veins, parallel to sub-parallel to amphibole veins with cm-dm sized green alteration haloes.
iii. Prehnite-clinozoisite-calcite veins, subparallel to epidote-clinozoisite veins, where prehnite ± calcite partially to completely replace clinozoisite-epidote leading to prehnite (± calcite) dominated vein systems with disseminated sulphides.
iv. Laumontite-calcite veins with no preferred orientation cross-cutting all alteration stages.

Using quantitative and semi-quantitative thermometers to determine formation temperatures of hydrothermal minerals is critical to constrain formation conditions of hydrothermal veins and resulting alteration. Alternatively, formation temperatures of secondary minerals can be estimated from stability fields determined from experimental phase equilibria studies. Here, estimations based on two semi-quantitative thermometers are presented and stability fields of secondary minerals extrapolated from phase equilibria studies are discussed (Figure 3.19).

Calculated temperatures for amphibole formation using the semi-quantitative thermometer of Ernst and Liu (1998) range from 804 ± 40 °C down to 480 ± 40 °C (Appendix A.1, Figure 3.18). The applicability of this thermometer in a hydrous mafic system at low pressures has been confirmed with several studies (e.g., Koepke et al., 2011; McCaig and Harris, 2012; Wolff, 2014). Highest values (600 ± 40 - 804 ±40 °C) were calculated for poikilitic pargasites and brown Mg-hornblende – tschermakites, which partially replacing clinopyroxene of fresh background layered gabbro samples and in a Mg-hornblende veinlet in one of the fresh background gabbro samples.

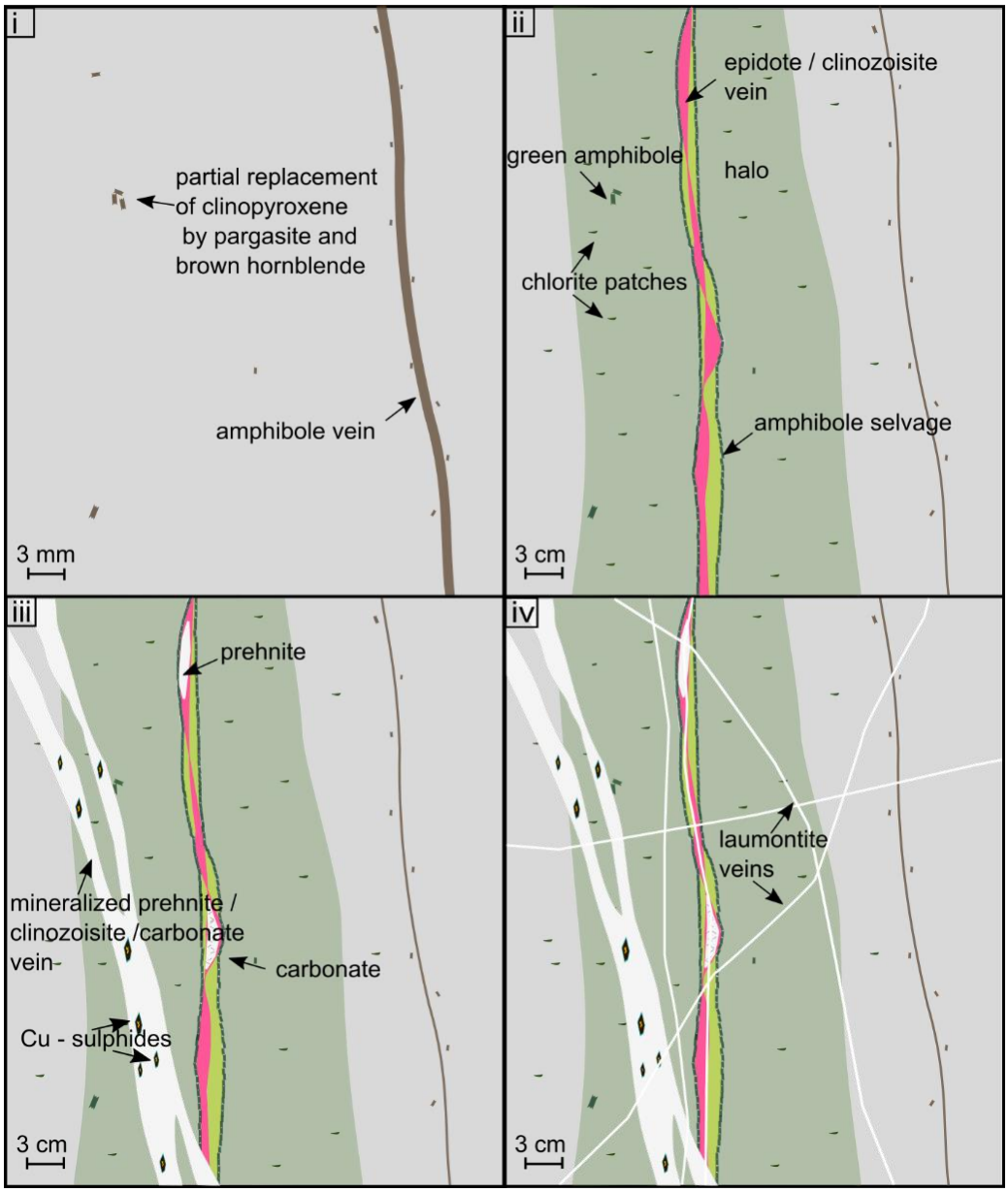

Figure 3.17: Schematic sketch showing cross-cutting relationships observed in the field, in hand-specimens and in thin sections , with stage (i) as the first alteration and (iv) the last sequence observed.

The presence of such high-temperature amphiboles clearly points toward an initial and pervasive HT alteration phase (Coogan et al., 2001; Manning et al., 2000, 1996). Even though these pargasites and hornblendes indicate a formation at high-temperature they are different from described magmatic pargasites which yield formation temperatures of > 850 °C (Wolff, 2014). Amphiboles from vein selvages around epidote-clinozoisite veins are mostly of hornblende composition and show temperatures between 500 ± 40 - 580 ± 40 °C. However, these temperatures are on the lower limit of this semi-quantitative thermometer, which is only calibrated for temperatures above 550 °C (Ernst and Liu, 1998) and therefore, values lower than 550 °C are not taken into account. Phase equilibria studies show that hornblende typically forms

at temperatures above 425 °C up to ~550 °C with pressures above 0.5 kbar and oxygen fugacity in the range of the hematite-magnetite buffer (Liou et al., 1974; Moody et al., 1983). Amphibole with actinolitic composition can be found throughout all the samples mainly co-existing with chlorite or rimming clinopyroxene or hornblende. It assumed that actinolite is formed at temperatures less than 500 °C, down to approximately 300 °C (Bird et al., 1984), indicating a formation at greenschist facies conditions.

Epidote-clinozoisite stability in low pressure and mid-ocean ridge basaltic systems is estimated to be between 350-500 °C (McCollom and Shock, 1998) and has been confirmed by phase equilibria studies of low-grade mafic rocks (Liou et al., 1985), suggesting a formation at greenschist facies conditions. Generally, Al-rich clinozoisite is assumed to form at higher temperature and less oxidizing conditions than Fe-rich epidote (Grapes and Hoskin, 2004). It is suspected that the Fe-Al ratio in epidote and clinozoisite varies as a function of $f(O_2)$ and temperature, showing higher Fe-contents at higher $f(O_2)$ and becoming more Al-rich with decreasing $f(O_2)$ and increasing temperature (Apted and Liou, 1983; Grapes and Hoskin, 2004; Liou et al., 1983). In geothermal systems epidote is observed at temperatures as low as 250 °C (Bird and Spieler, 2004), giving a lower limit of the epidote-clinozoisite stability field. In an experimental study, Liou et al. (1983) showed that prehnite can grow at the expense of epidote assemblages below 350 °C and pressures above 2 kbar. This indicates a transition from epidote to prehnite with decreasing temperatures and confirms petrographic observations, suggesting a partial replacement of clinozoisite by prehnite.

Estimated temperature for chlorite calculated with the semi-quantitative thermometer of Jowett (1991) range between 220-295 °C (Figure 3.18). This thermometer is based on the observation of a systematic decrease of Si^{iv} coupled with an increase of Al^{iv} in chlorites with increasing temperatures (Cathelineau, 1988; McDowell and Elders, 1980; Velde and Hillier , 1991). Chlorite mainly co-existing with actinolite in altered halo rocks as well as background gabbros yield temperatures between 250-300 °C. Chlorite from two chlorite patches in brecciated and highly altered rock along the margin of a prehnite vein yield a wider range of estimated formation temperatures extending towards 220 °C (Figure 3.18; Appendix A.1).

Prehnite is likely to be formed in the transition from medium to low temperature. It is stable in the range of 200-343 ± 5 °C (hematite-magnetite buffer) or up to 388 ± 5 °C (QFM buffer) with experiments showing its breaks down to clinozoisite + tremolite at higher temperatures (Frey et al., 1991; Liou et al., 1983). This is consistent with the occurrence of prehnite in active geothermal system at temperatures between 250-350 °C (Bird et al., 1984). Coarse grained, well crystallised calcite from the same vein system might be formed at comparable temperatures (Coggon, 2006;

Weinzierl et al., 2018). Coggon (2006) calculate formation temperatures for co-existing epidote and calcite of 264 ± 36 °C and 309 ± 32 °C from oxygen isotope data and indicate that calcite likely precipitated from relatively hot fluids at similar temperatures to prehnite and chlorite. Similarly, calcite from calcite veins observed in the deeper section of the Troodos ophiolite reveal temperatures of up to 218 °C, calculated from oxygen isotopes and indicate a formation from a hydrothermal fluid (Weinzierl et al., 2018). Whether the observed calcite is in equilibrium with prehnite could be tested by measuring its Sr-isotope composition. If they are in equilibrium, additional ^{18}O-isotope measurements of both the calcite and the prehnite would help to further constrain formation temperatures.

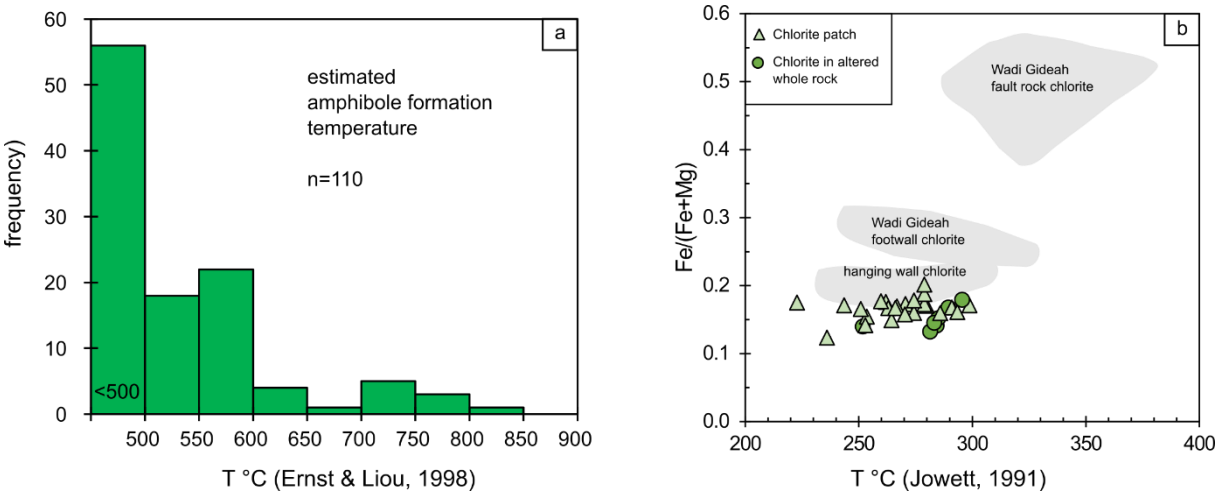

Figure 3.18: Calculated formation temperatures of amphibole (a) and chlorite (b) using semi-quantitative thermometres. (a) Histogram showing the distribution of of calculated amphibole formation temperatures after Ernst and Liu (1998). Temperatures range from up to 850 °C down to less than 500 °C. (b) Calculated formation temperature of chlorite in altered whole rock around epidote-clinozoisite veins and chlorite patches in halo rock of prehnite veins (Jowett, 1991).

Laumontite veins, cross-cutting all earlier alteration stages, are formed in the low-temperature regime, typically precipitated from highly evolved hydrothermal fluids (e.g.; Alt et al., 2010). In active geothermal systems laumontite is a common calc-silicate phase and stable at temperatures of less than 200 °C (Bird et al., 1984), further shown by laumontite stability ranging 110-190 °C observed in a geothermal system in Iceland (Schiffman and Fridleifsson, 1991). Such low-temperature stability and the occurrence of laumontite in cross-cutting hydrothermal veins indicate a late formation in an evolved hydrothermal system well off-axis (> 5 km) or possibly during obduction.

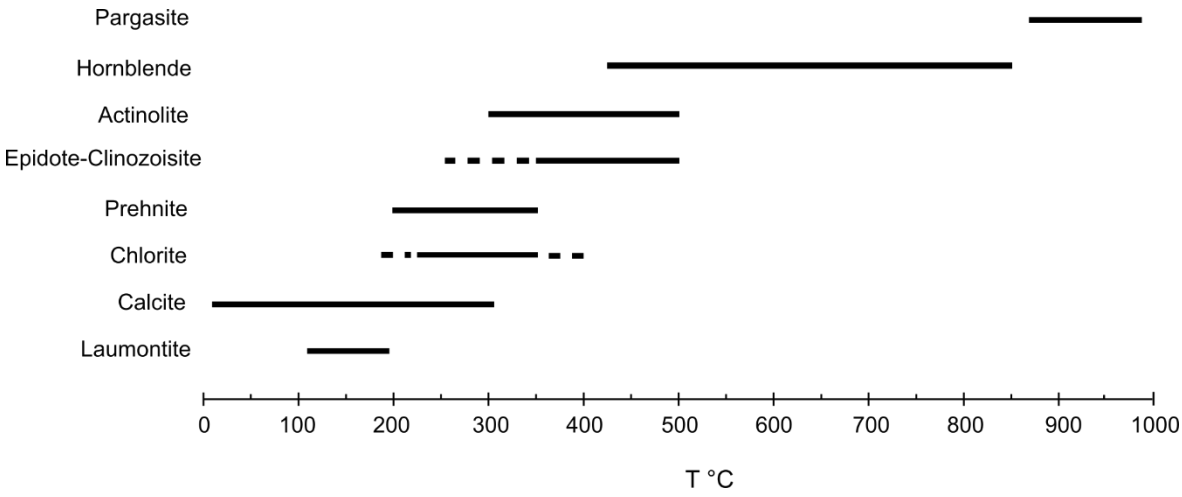

Figure 3.19: Summary figure showing the possible range of formation temperatures for secondary hydrothermal minerals. Temperature ranges and estimations from the following sources: pargasite (Bosch et al., 2004), hornblende (Bosch et al., 2004; Liou et al., 1974; Moody et al., 1983) and temperatures calculated for hornblende in this study after Ernst and Liu (1998)), actinolite (Bird et al., 1984), epidote-clinozoisite (Apted and Liou, 1983; Bird and Spieler, 2004; Grapes and Hoskin, 2004; Liou et al., 1985; McCollom and Shock, 1998), prehnite (Bird et al., 1984; Frey et al., 1991; Liou et al., 1983), chlorite estimations (Cathelineau, 1988; Cathelineau and Nieva, 1985; Jowett, 1991) in this study, calcite (Coggon, 2006; Weinzierl et al., 2018), laumontite (Alt et al., 2010; Bird et al., 1984; Schiffman and Fridleifsson, 1991).

3.6.2 Origin of the hydrothermal fluid

All analysed samples show $^{87}Sr/^{86}Sr$ compositions are elevated compared to fresh layered gabbro of the Wadi Tayin area (Lanphere et al., 1981; McCulloch et al., 1981) and primary MORB composition of $^{87}Sr/^{86}Sr \sim 0.70281$ (White et al., 1987) in particular. This strongly indicates interactions and exchange with a seawater derived hydrothermal fluid, suggesting Cretaceous seawater as a plausible source for the majority of the observed alteration. A $^{87}Sr/^{86}Sr \sim 0.70738$ for Cretaceous seawater at 95 Ma has been determined by McArthur et al. (2001). During passage through the crustal section, this seawater derived fluid became hotter and gradually changed its composition by interaction with the surrounding wall rock until reaching the composition now recorded in minerals precipitated directly out of such a fluid (Bickle and Teagle, 1992; Harris et al., 2015; Teagle et al., 2003, 1998).

3.6.3 Hydrothermal fluid compositions and evolution through time

As indicated by petrography and mineral chemistry there is a gradual evolution of alteration from temperatures ~800 °C down to < 200 °C. Hydrothermal fluid composition for the earliest stage of alteration; the formation of high-temperature amphibole veins and amphibole replacing clinopyroxene are difficult to determine. As part of this study no Sr-isotope compositions of this earliest phase of hydrothermal alteration has been analysed. However, we assume that such an alteration occurred in a rock dominated system at very low fluid-rock ratios with extensive exchange of the hydrothermal fluid with the host rock. Petrographic observations indicate only limited fluid pathways (micrometre to millimetre sized amphibole veinlets) and fluid flow is likely to have been restricted along grain boundaries. Therefore we would suspect a relatively low Sr-isotope composition, only little elevated above the fresh rock value. Such low Sr-isotope compositions of high-temperature amphiboles (mainly pargasites; $^{87}Sr/^{86}Sr$ = 0.7032-0.7035) of veins and gabbroic diklets in the layered gabbros all over the Samail ophiolite, have been reported by Bosch et al. (2004). Even though these Sr-isotope values are low, they are still elevated from fresh MORB composition and interpreted to be the result of an interaction with a high-temperature seawater derived hydrothermal fluid. Similar results have been shown by a recent study of Currin-Sala et al., (in press). Dark brown high-temperature amphiboles (pargasites and magnesiohastingsite) and green hornblende of amphibole veins and gabbroic diklets cross-cutting the magmatic layering in Wadi Wariyah in the Wadi Tayin massif show Sr-isotope composition of $^{87}Sr/^{86}Sr$ = 0.7031-0.7036. These values are only slightly elevated from fresh rock values, but some of these amphibole show high Cl concentration of up to 4 wt. % of Cl, strongly suggesting a formation with seawater-derived hydrothermal fluids which possibly reacted with a substantial amount of rock at low fluid/rock ratios in order to obtain these low values (Currin-Sala et al., in press).

Going down from the high-temperature regime to more medium-temperature dominated alteration, epidote-clinozoisite veins are the main type of veins observed in this mapped Wadi Qafifah outcrop. The formation of epidote veins in the plutonic section of ophiolites and modern ocean crust is often considered as the fossil record of upwelling “black smoker-type” hydrothermal fluids, similar to the formation of epidosites present in the sheeted dykes of ophiolites, higher up in the stratigraphy (e.g., Bickle and Teagle, 1992; Nehlig et al., 1994; Richardson et al., 1987; Schiffman et al., 1987). Hand-picked epidote and clinozoisite of sampled hydrothermal veins are euhedral with almost perfect crystal shapes in many cases. We therefore assume that these crystals were precipitated directly out of a hydrothermal fluid and reflect the strontium isotopic composition of the hydrothermal fluid that precipitated these phases. All picked and analysed samples plot in a relatively narrow range of $^{87}Sr/^{86}Sr$=0.7047-0.7049, similar

to what is reported from other studies in the Samail ophiolite (Bosch et al., 2004; Coogan et al., 2006; Wolff, 2014). Interestingly, picked clinozoisite of monomineralic clinozoisite veins as well as clinozoisite from veins co-existing with epidote show slightly lower Sr-isotope compositions ($^{87}Sr/^{86}Sr$=0.70470-0.70475) than co-existing epidote and epidote from monomineralic veins ($^{87}Sr/^{86}Sr$=0.70478-0.70489), although differences are small. There are two hypotheses to explain these differences: (i) this is either coincidental resulting from a relatively small dataset (8 samples) and would disappear if a larger dataset was analysed; or (ii) it reflects a real difference and points towards a minor evolution of the hydrothermal fluid. If there is a fluid evolution it would suggest that clinozoisite was formed earlier than epidote, indicating a higher degree of fluid-rock interaction and therefore a lower, less radiogenic Sr-isotope composition for clinozoisite. But petrographic indications supporting this hypotheses were not found. Epidote would be formed from a somewhat more evolved fluid, re-using existing and still connected pathways along cracks and fractures partially filled by clinozoisite, resulting in slightly less fluid-rock exchange with the whole rock and therefore slightly higher $^{87}Sr/^{86}Sr$ composition. From detailed thin section studies of samples from the plutonic section of Wadi Haymiliyah, Oman, Nehlig and Juteau (1988) suggest that the formation of zoisite (in this study named clinozoisite) ± epidote veins pre-dates the formation of pure epidote veins. This might support a formation of clinozoisite before epidote, although there are no clear petrographic indications and cross-cutting relationships from samples of the studied Wadi Qafifah outcrop.

Hand-picked green hornblende crystal of hornblende selvages around epidote-clinozoisite veins have Sr-isotope compositions in the same range as epidote-clinozoisite ($^{87}Sr/^{86}Sr$=0.7049) and slightly more radiogenic ($^{87}Sr/^{86}Sr$=0.7052). This either suggests a growth of the hornblende in presence of the same fluid epidote and clinozoisite precipitate from, or previously crystallised hornblende re-equilibrated their Sr-isotope composition during the formation of the epidote-clinozoisite veins. Coogan et al. (2006) discusses the possibility of strontium exchange via diffusion after the formation of amphiboles using diffusion data of Brabander and Giletti (1995) and concludes that it is highly unlikely that the initial Sr-isotope composition of amphibole can be reset at temperatures below 700 °C, as diffusion distances are sufficiently short (1-5 µm). We therefore assume that the hornblende rimming epidote-clinozoisite veins grew during the formation of the vein or completely recrystallised in presence of the hydrothermal fluid precipitating epidote-clinozoisite and therefore inherited the same Sr-isotopic composition.

With decreasing temperature prehnite veins subparallel to epidote-clinozoisite veins are formed as well as prehnite partially replacing clinozoisite and filling open space in both epidote and clinozoisite veins. Furthermore, monomineralic prehnite veins cross-cut all earlier alteration stages and prehnite from such a cross-cutting veinlet shows Sr-isotope composition

($^{87}Sr/^{86}Sr$=0.7053) slightly more radiogenic than epidote-clinozoisite vein minerals, indicating only a minor evolution of the hydrothermal fluid.

Laumontite mineral separates of late laumontite-calcite veins ($^{87}Sr/^{86}Sr$=0.7065 – 0.7073) show even more radiogenic compositions. This has previously been reported from modern oceanic crust (Alt, 1998, 1995; Alt et al., 2010) where the formation of zeolites is thought to be related to off-axis circulation at low temperature. Similar results are reported from the Troodos ophiolite (Alt and Teagle, 2000; Gillis et al., 1992) where laumontite yields Sr-isotope compositions close to Cretaceous sweater, implying precipitation from seawater-dominated fluids (Gillis et al., 1992) with little interaction of the fluid with the crustal rocks.

The highest, most radiogenic value is shown by calcite ($^{87}Sr/^{86}Sr$=0.7079) of laumontite-calcite veins. This composition is close to present day groundwater observed in gabbro hosted wells in Wadi Tayin and within the range of Miocene sediments that once covered the ophiolite (Coleman, 1981), implying that calcite formed late in the history of the ophiolite. Similarly high results are reported from late laumontite-calcite veins observed in Wadi Gideah (Chapter 2, 3). Such a high composition suggest a precipitation from fluids that had undergone little interaction with the oceanic crust. A precipitation of calcite in these veins during or after obduction of the ophiolite is likely and a formation continuing to present day cannot be excluded.

3.6.4 Hydrothermal fluid-rock exchange and scale of hydrothermal alteration

Sr-isotope compositions are useful tracers for fluid-rock reactions. The strontium isotopic composition of altered whole rock is a function of the abundance of primary minerals still present in the sample showing initial MORB composition and secondary minerals that have partly to completely equilibrated with the $^{87}Sr/^{86}Sr$ signature of the fluid they precipitated from. Therefore, whole rock samples showing a high degree of alteration (i.e., highest modal proportions of Sr-bearing secondary hydrothermal minerals) should yield $^{87}Sr/^{86}Sr$ compositions closest to hydrothermal fluid composition. This can be observed from whole rock halo samples around epidote-clinozoisite veins. The majority of these samples are almost entirely recrystallised such that primary igneous minerals and textures are no longer present (up to 90% alteration). Consequently, corresponding whole rock Sr-isotope compositions broadly plot in the range of the hydrothermal veins ($^{87}Sr/^{86}Sr$=0.70464-0.70482). Other halo samples as well as sampled background gabbro show compositions clearly elevated from the median composition of fresh background gabbro ($^{87}Sr/^{86}Sr$=0.70342) but not as elevated as the composition of the hydrothermal fluid itself ($^{87}Sr/^{86}Sr$=0.7039-0.7045), indicating only partial exchange of the rock with the hydrothermal fluid. In fact, all sampled background gabbro in between veins and vein

systems show at least slightly elevated Sr-isotope compositions ($^{87}Sr/^{86}Sr$=0.70324-0.70374) relative to fresh gabbro in Wadi Tayin ($^{87}Sr/^{86}Sr$~ 0.7029 - 0.70320; Lanphere et al., 1981; McCulloch et al., 1980), correlating with an observed alteration intensity of 10-30 %. This suggests a partial exchange with a hydrothermal fluid for all samples, although very minor for some of them (e.g. sample AD3, AE5, AE6, AE9). This can further be evidenced in Figure 3.20 where strontium isotope compositions of whole rock halo and background samples plus all mineral separates are plotted along the outcrop. Here, it is clear that the most elevated compositions plot within the three areas of high vein densities but that Sr-isotope compositions drop to close to fresh gabbro values in areas with few epidote-clinozoisite veins, indicating a channelling of the hydrothermal fluid flow. Such channels or areas with a high vein density respectively, are of the scale of 3-7 m.

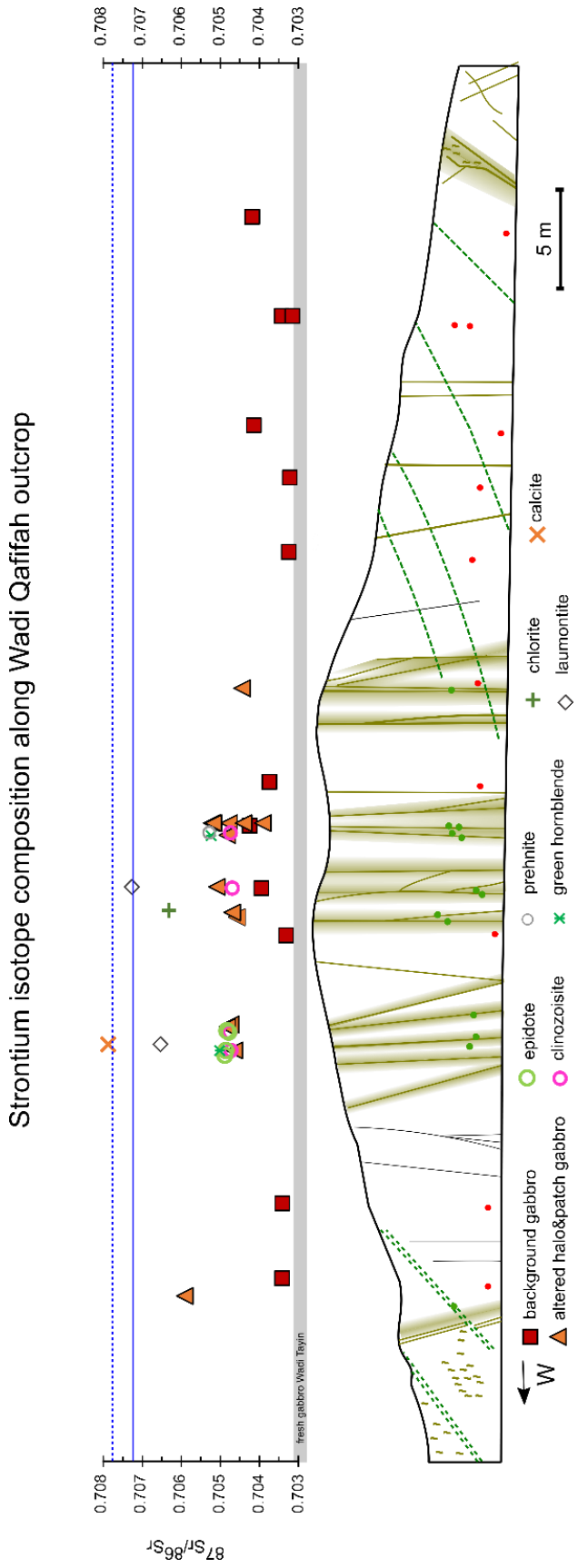

Figure 3.20: Sr-isotope compositions of mineral separates and whole rock samples plotted along the outcrop. Blue line indicates composition of Cretaceous seawater McArthur et al. (2001) and dashed blue line indicates modern groundwater sampled in gabbro hosted wells of Wadi Qafifah (Bompard, 2018).

Zooming into areas of high densities an overall positive correlation between vein aperture and corresponding halo width can be observed (Figure 3.21). The thicker the vein (or the cumulative vein aperture) the wider the halo, suggesting that in a thicker vein more fluid could be channelled, therefore more fluid could infiltrate into the wall rock leading to wider alteration haloes. For the majority of haloes mapped along the outcrop several veins contribute to one halo. To account for this, the sum of all corresponding vein apertures are compared to the observed halo width. Single veins and vein systems of 1-3 veins show cumulative vein apertures of 1-4 cm and corresponding halo widths of 10-50 cm. More complex vein systems with cumulative vein apertures of up to ~ 10 cm show haloes extending for greater than 1.5 m (Figure 3.21c).

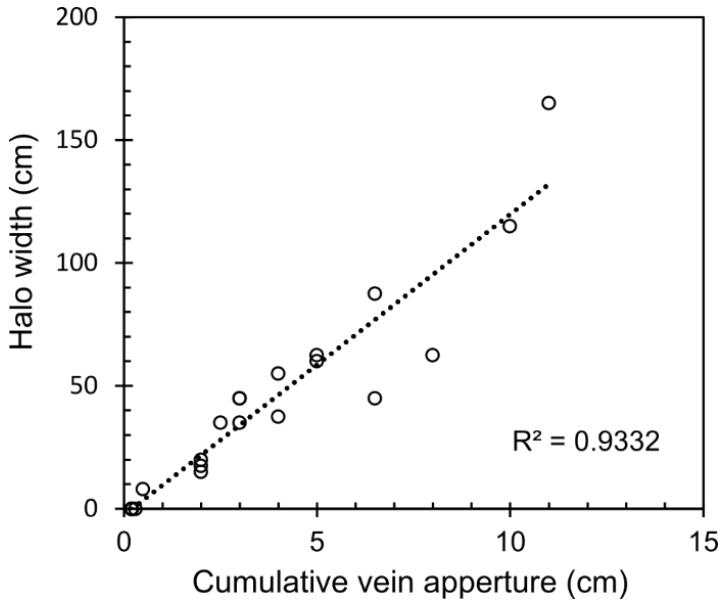

Figure 3.21: Correlation between cumulative vein aperture (in cm) and halo width (in cm) observed around veins and vein system. For some veins the vein aperture could directly be related to the surrounding halo widths but for many haloes a direct link between halo width and vein aperture was difficult. Therefore, vein apertures in the vicinity of a halo were summed up to a cumulative vein aperture which was then compared to the halo width. This comparison leads to the conclusion that the thicker the vein is, the more fluid could be channelled and the further the alteration front propagated away from the vein.

3.7 Conclusions

Detailed mapping and sampling combined with petrographic observations, mineral chemistry and strontium isotope compositions of hydrothermal veins, altered and fresh background whole rock reveal a complex alteration history of the gabbro in the lower crust of the Wadi Tayin massif and the following conclusions can be drawn:

Cross-cutting relationships of hydrothermal veins indicate a clear and continuous alteration sequence from temperatures ~800 °C down to temperature ~100-200 °C, although the alteration of the outcrop is dominated by greenschist-facies assemblages. The highest temperature alteration is manifested in poikilitic amphibole observed in clinopyroxene and brown hornblende veinlets cross-cutting the initial magmatic layering. Ti in amphibole thermometry reveal temperatures for amphibole formation from 800 °C down to < 500°C, into greenschist-facies conditions and therefore into the stability field of clinozoisite and epidote (~300-500 °C). Epidote-clinozoisite veins are sub-parallel to early amphibole veins but are cross-cut by sub-parallel prehnite-clinozoisite-calcite veins, with estimated prehnite formation temperatures of 200-350 °C. Laumontite of cross-cutting laumontite-calcite veins is assumed to be formed at temperatures roughly between 100-200 °C and mark the last stage of the hydrothermal activity preserved in the rocks in Wadi Qaiffah.

Epidote-clinozoisite veins are considered as the fossil record of upwelling “black smoker-type” hydrothermal fluids with $^{87}Sr/^{86}Sr$=0.70470-0.7049, similar to epidote of hydrothermal veins elsewhere in the ophiolite. Field observations, thin section petrography and Sr-isotope composition suggest that the hydrothermal system evolved towards lower temperature, precipitating prehnite in open-space, sub-parallel veins with slightly more elevated Sr-compositions of $^{87}Sr/^{86}Sr$=0.7053. Observed disseminated chalcopyrite and pyrite within prehnite vein systems further support the assumption of hot, up-welling and metal-bearing black smoker hydrothermal fluids.

Along the outcrop three main areas of high vein densities are observed, each ranging between 3-7 m in size. Sr-isotope compositions show highly elevated compositions within these areas but composition drop back to almost “fresh” values outside where hydrothermal veins are less frequent and more restricted. Zooming into such areas of high vein densities, single veins and complex vein systems of epidote-clinozoisite and prehnite-calcite-clinozoisite with extensive alteration haloes are present. Whole rock in haloes are partially to almost completely altered, dominated by a secondary mineral assemblage of epidote-clinozoisite + chlorite + actinolite + hornblende ± albite ± prehnite. Strontium isotope compositions of altered halo samples range up to the composition of the hydrothermal fluid, shown by epidote-clinozoisite mineral separates,

indicating a full exchange with a hydrothermal fluid. Alteration along single veins and small vein systems may extend for up to several decimetres away of the vein(s). Alteration around more extensive vein systems are observed to extend up to more than one metre and positively correlates with observed cumulate vein aperture.

Laumontite of late, cross-cutting veinlets show Sr-isotope compositions of $^{87}Sr/^{86}Sr$=0.7065 – 0.7073, strongly suggesting a formation from less evolved hydrothermal fluids at relatively low temperatures, possibly as the hydrothermal system cooled.

Calcite within a laumontite vein yields the most radiogenic Sr-isotopic value of $^{87}Sr/^{86}Sr$=0.7079 in the same range as Miocene sediments that once covered the ophiolite and in the range of modern groundwater of this area, favouring a precipitation of calcite late in the history of this ophiolite.

Chapter 4 Fossil hydrothermal discharge zones in the lower oceanic crust, Samail ophiolite Oman

4.1 Introduction

Hydrothermal circulation in the oceanic crust is not pervasive at all scales, and fluids can be focussed along channels, due to heterogeneous permeability. In particular, the focussed discharge of hydrothermal fluids along highly permeable zone, such as faults are crucial for many models of hydrothermal systems at fast spreading mid-ocean ridges (e.g., Cann et al., 1985; Lowell et al., 1993; Strens and Cann, 1982). Focussed upflow zones of discharging hydrothermal fluids at temperatures around ~400 °C have been observed and described in the upper crust from both ophiolites (e.g., Harper et al., 1988; Nehlig et al., 1994; Richardson et al., 1987; Schiffman et al., 1987) and also in modern ocean crust (e.g., Barker et al., 2010; Hayman and Karson, 2009, 2007; Haymon et al., 1989; Humphris et al., 1998; Saccocia and Gillis, 1995). In ophiolites, discharge zones of hydrothermal fluids are characterised by the presence of epidosites, which are equigranular epidote + quartz + titanite rocks, mainly formed in the deeper portions of the sheeted dykes (Harper et al., 1988; Nehlig et al., 1994; Richardson et al., 1987; Schiffman et al., 1987; Schiffman and Smith, 1988). Fluid-inclusion data and evidence for the general loss of metals as well as sulphur from the host rock indicate alteration temperatures of 350-440 °C (Alt, 1994; Richardson et al., 1987; Schiffman and Smith, 1988) at very high fluid-rock ratios (Bickle and Teagle, 1992; Harper et al., 1988; Richardson et al., 1987; Seyfried et al., 1988) for the formation of epidosites along these upflow zones. Relative to fresh MORB, epidosites show an increased $^{87}Sr/^{86}Sr$ ratio and are depleted in ^{18}O (Bickle and Teagle, 1992; Harper et al., 1988; Richardson et al., 1987; Schiffman and Smith, 1988). Although epidosites are widespread in the upper crust of ophiolites, they have not been described from modern fast-spreading ocean crust.

To date, there are few studies describing zones of channelled discharging hydrothermal fluid in modern ocean crust. Samples studied from several areas including Hess Deep (Hayman and Karson, 2007; Saccocia and Gillis, 1995), Pito Deep (Barker et al., 2010; Hayman and Karson, 2009) and the MARK-area (Delaney et al., 1987; Saccocia and Gillis, 1995) indicate that mineral assemblages of variable amounts of quartz + chlorite + sulphides (mainly chalcopyrite and pyrite) + minor epidote are characteristic for upflow zones of hydrothermal fluids. Fluid-inclusion studies of quartz from Hess Deep and the MARK area (Saccocia and Gillis, 1995) as well as titanium in quartz geothermometry from Pito deep samples (Barker et al., 2010) indicate formation temperatures of roughly 300-450 °C. Such temperatures are similar to high-temperature

hydrothermal fluids that discharge on the seafloor of fast-spreading centres (Von Damm et al., 2003). Simple mass balance calculation from Pito Deep samples show large fluid/rock ratios of ~50-100 (Barker et al., 2010), further indicate that fluid-flow was focussed and channelled. Observed samples from discharge zones where hydrothermal fluids were focussed, commonly show indications of brittle deformations such as brecciation (Barker et al., 2010; Delaney et al., 1987; Saccocia and Gillis, 1995). Two studies of fault scarps from Hess Deep and Pito Deep describe abundant cataclastic and damaged zones and further indicate that brittle deformation likely accompanied fluid-flow of discharging fluids (Hayman and Karson, 2009, 2007).

Even though discharge zones of hydrothermal fluids have been described from the upper crust of both, ophiolites and modern ocean crust, little is known about how fluid-flow occurs in the lower oceanic crust and whether focussed fluid-flow plays a crucial role in mining heat of the cooling crust. Evidence of focussed fluid-flow has been documented in areas of significantly higher permeability in the lower crust of the Samail ophiolite in Oman (Coogan et al., 2006). Field, petrological and geochemical investigations show that fluid-flow started at temperatures of > 800 °C and continued down to < 300 °C within these regions of focussed fluid flow, leading to a reset of the Sr-isotopic composition of the crust within these zones and enhanced cooling rates in the surrounding crust.

In this chapter, several outcrops comprising zones of focussed fluid-flow and faulting are characterised in terms of structure, mineralogical and Sr-isotope composition. All outcrops are located along Wadi Gideah in the lower crust of the Samail ophiolite in Oman. Secondary mineral assemblages within these fluid-flow and fault zones together with Sr-isotope signature similar to black-smoker signatures observed elsewhere in the ophiolite provide compelling arguments for channelled recharge and discharging of hydrothermal fluids throughout the lower oceanic crust.

4.2 Geological background: Wadi Gideah

Wadi Gideah is a roughly north to south orientated valley in the Wadi Tayin massif of the Samail ophiolite and is situated approximately 15 km north of the town of Ibra as part of the northern limb of the Ibra syncline (Pallister, 1981). In this part of the Wadi Tayin massif initial descriptions of the ophiolite and classical structural, petrographic and isotopic geochemical observations on the accretion of the crustal section of the ophiolite were made (Gregory and Taylor, 1981; Lanphere et al., 1981; Pallister, 1981; Pallister and Hopson, 1981; Pallister and Knight, 1981). The valley has an overall length of ~ 12 km and cuts through a coherent section of lower oceanic crust exposing rocks form the Moho transition zone, to the layered gabbros and up to high-level gabbros. Sheeted dykes are partially eroded and only exposed in small hills at the valley entrance

and further out on the Ibra Plain. Lavas are mostly eroded and only few outcrops are reported from this area of the core of the Ibra syncline (Figure 4.1).

The Moho transition zone (MTZ) is on average ~300 m thick (Müller, 2016) and marks the gradual transition from tectonised, residual mantle harzburgites into the layered gabbros. The layered gabbro section consists of cumulate olivine gabbro and olivine-bearing gabbro displaying a typical layering in the scale of centimetres to decimetres or even metres defined by variations in modal abundances of clinopyroxene, plagioclase and olivine. Observed magmatic layering in Wadi Gideah is characteristic for lower crustal gabbros in the Samail ophiolite and has previously been described in detail (e.g. Browning, 1984, 1982; Pallister and Hopson, 1981). A layering-parallel foliation of mineral grains is present. The layering is typically parallel to the Moho and dips on average 28 ° south (Pallister and Hopson, 1981). Large displacement faults are rare and constrained to the Moho transition zone (Pallister and Hopson, 1981; Peters et al., 2008).

Up-section, the layered gabbro grade into the foliated gabbros. Modal layering within the foliated gabbros is minor or mostly absent. Observed foliated gabbros in Wadi Gideah are typical for foliated gabbros in the whole ophiolite, characterised by a strong preferred orientation of the primary minerals. This foliation is typically sub-orthogonal to the Moho (France et al., 2009) and generally foliated gabbro in the Wadi Gideah area are characterised by smaller grain sizes when compared to layered gabbros (Müller, 2016). In the field the difference between the layered and foliated gabbro are not always obvious and often difficult to see as the transition is gradual over hundreds of metres. Especially across the transition zone of the layered to the foliated gabbros, gabbros show a discontinuous layered appearance (MacLeod and Yaouancq, 2000), which is no longer parallel to the Moho but is commonly much steeper.

High-level or varitextured gabbros are the topmost layer of the gabbroic sequence and are characterised by extreme heterogeneity in both grain sizes and modal abundances of different minerals at small scales (MacLeod and Yaouancq, 2000). Fine grained micro-gabbros alternate with pegmatitic gabbro which shows grain sizes up to several millimetres. Magmatic amphiboles are a typical constituent of such pegmatitic patches within the high-level gabbros.

Up-section the high-level gabbros grade into the dyke rooting zone where the intrusion of dykes are more frequent. This can be observed in several outcrops at the Gideah valley entrance and has previously been described either from the Gideah area or from other localities in the ophiolite (e.g. Lippard et al., 1986; MacLeod and Yaouancq, 2000; Müller et al., 2017). More evolved, SiO_2-rich plutonic rocks (diorites, quartz diorites, trondhjemites and tonalities) are common late-stage intrusions at the high-level-dyke transition zone. They typically post-date the high-level gabbros but pre-date the intrusions of the dykes (e.g. Müller et al., 2017).

The sheeted dykes are rarely preserved outside of the main Wadi in small hills in the alluvium plains towards Ibra. The sheeted dyke section is made of steeply dipping, fine grained, doleritic

dykes, up to one metre-thick and chilled margins versus adjacent dykes. Dykes outside Wadi Gideah are representative for the general orientation of the sheeted dykes in this area (France et al., 2009; Pallister, 1981). A mean strike of 347° ± 21° (1σ) has been determined for the sheeted dykes in the northern limb of the Ibra syncline, indicating the orientation of the paleo-ridge axis relative to the other members of the ophiolite (Pallister, 1981).

Alteration in Wadi Gideah is widespread and has been mentioned previously (Mueller et al., 2017; Müller, 2016). Müller (2016) described the occurrence of multiple, up to 100 m wide hydrothermal fault zones, similar to focussed fluid flow zones (FFFZ) described by Coogan et al. (2006), which cross-cut the magmatic layering generally orthogonal and display alteration from the amphibolite to greenschist facies.

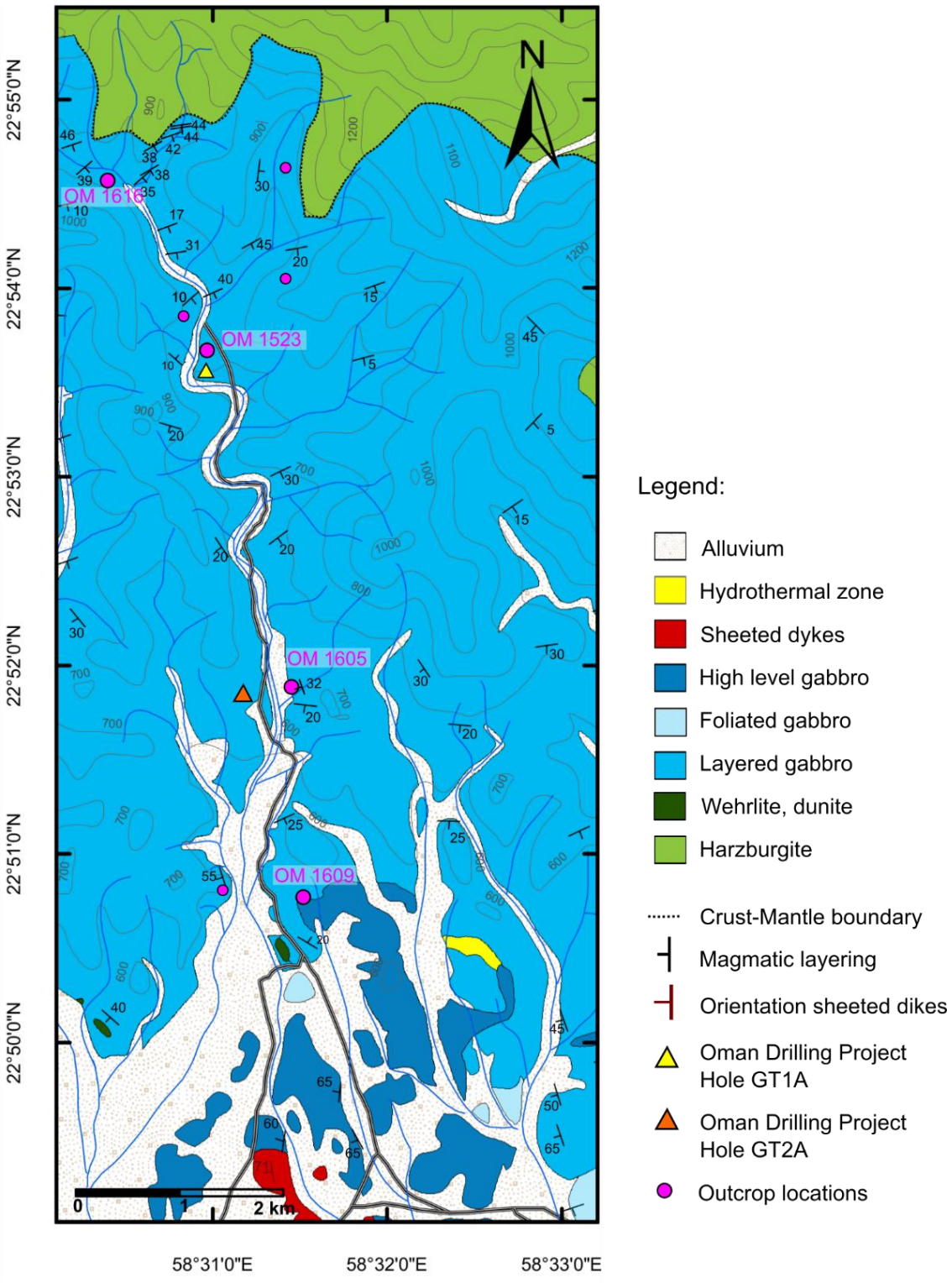

Figure 4.1: Geological map of Wadi Gideah showing location of major fluid-flow zones and fault zones. Map after Peters et al. (2008). Orientation of magmatic layering in northern part of the valley by courtesy of S. Müller.

4.3 Methods

During fieldwork in February-March 2016 four outcrops revealing major fluid-flow zones and vein systems along Wadi Gideah were chosen and investigated in detail. Overall, 67 samples, including whole rock and mineral separates, were collected and analysed from these four main outcrops and several additional smaller outcrops along Wadi Gideah. Height above Moho for outcrops and individual samples was calculated following the method outlined in Müller (2016) and using UTM coordinates (in metres) obtained with a standard GPS. With this method the height above Moho (h) is determined by equation (1)

$$Height\ above\ Moho\ (h) = (y_{sample} - y_{Moho}) * sin(\alpha) \quad (1)$$

where y_{sample} represent the y-coordinate of the measured UTM coordinate of a sample and y_{Moho} is defined as the mean value of the y-coordinate of the last lower crustal sample (2534884) and the first mantle sample (2534953) described in Müller (2016) results in a values of 2534919. Angle α (28°) is defined as the average dip of 23 measurements of the magmatic layering measured along the Wadi Gideah (Pallister and Hopson, 1981). This method is suitable as Wadi Gideah valley trends north-south and the paleo-Moho is suspected to have an orientation roughly the same as that of the magmatic layering, dipping approximately 28° to the south. As the outcrops and other sampled localities are located along the main valley and close to the valley ground, lateral and altitude differences were not considered. Thicknesses of individual lithologies are taken after Müller (2016).

Sample preparation and analytical techniques are described in detail in Chapter 2, and are summarised here. For thin section and geochemical analysis a selection of samples were cut with a diamond saw, saw marks were grinded off and polished thin section were prepared. After detailed petrographic descriptions samples for electron probe micro-analysis (EPMA) were selected and major element composition of minerals were analysed at the University of Hannover. The analytical protocol can be found in Chapter 2.5. Calculated precision and accuracy are listed in Table 2.2.

A selection of whole rock and mineral separate samples were prepared for trace elemental and Sr-isotope analysis following the procedure outlined in Chapter 2.6 and 2.8. All samples were leached with 10 % acetic acid prior to digestion in order to remove any secondary calcite. Hand-picked laumontite and prehnite separates were leached with 10 % acetic acid for the same reason.

Trace elemental composition of whole rock and mineral separate samples was measured by ICP-MS (Chapter 2.10). Precision and accuracy are reported in Table 2.4 and 2.5. Strontium isotope

composition of both whole rock and handpicked mineral separates were measured by thermal ionization mass-spectroscopy (TIMS), following the procedure outlined in Chapter 2.13. Srontium standard NBS987 was measured as an external standard at the beginning and in the middle of each measurement cycle. External precision was monitored by calculating the two standard deviation of NBS987. Over the period of four months, NBS987 yielded an average of 0.710238 ± 0.000017 (2σ). Internal precision was monitored by measuring 150 ratios per sample and reported as two standard errors (2SE).

In addition to the collected samples during field work in 2016, strontium isotopes of a subset of sheeted dyke and a few lava samples from across the Ibra area has been analysed. These samples were collected during a field campaign in 2001 by Peter Kelemen. The analytical procedure followed the same guidelines as for the gabbro samples outlined Chapter 2.13. Strontium standard NBS987 was measured as an external standard at the beginning and in the middle of each measurement cycle. External precision was monitored by calculating the two standard deviation of six measurements of NBS987 over the period of analysis (2 months) giving an average of 0.710248 ± 0.000016 (2σ). Internal precision was monitored by measuring 150 ratios per sample and reported as two standard errors (2SE).

For height above Moho calculations of the sheeted dyke and lava samples, the Ibra syncline structure was taken into account, assuming that the fold axis represent the top of the lavas. The distance (along a straight and orthogonal line) of each sample localities to the fold axis was measured in ArcGIS and sample location was calculated relative to the whole distance beginning of the sheeted dykes to the fold axis. All obtained results were normalised to a total thickness of the sheeted dykes plus lavas of 2100 m (1500 m of sheeted dykes and 600 m of lavas) (Müller, 2016) and height above Moho was calculated relative to the rest of the crust.

Definition of terms:

Major zones of alteration were studied and sampled throughout Wadi Gideah. They are divided into two distinctive groups following the definition outlined here:

Fluid-flow zone (ffz): A fluid-flow zone consists of rock completely recrystallised in greenschist facies with primary mineralogy and initial magmatic texture no longer visible. Compared to a vein, a fluid-flow zone has less defined boundaries and is generally wider. In size, they range between several centimetres (cm) up to several decimetres (dm) and show pronounced alteration haloes of up to several metres around them. Fluid-flow zones do not display clear signs of deformation.

Fault zone (fz): A fault zone, or a fault is defined as “a plane of fracture which exhibits obvious signs of differential movements of the rock mass on either side of the plane. Faults are therefore planes of shear failure, i.e., they are planes along which there has been movement parallel to the plane”, after Price (2016) andPeacock et al. (2016). More recent definitions show that fault zones are “zones, having a volume that includes interacting and linked segments, breccias and fault rocks (Childs et al., 2009; Davatzes and Aydin, 2003)” in Peacock et al. (2016). Following this definition, the term fault zone is used for zones similar to fluid-flow zones but with a clear indication of any movement shown by the occurrence of breccias, fault gauge or shear-sense indications.

4.4 Outcrop description along Wadi Gideah

Overall, four outcrops (OM1616, OM1523, OM1605, OM1609; Figure 4.1) revealing major fluid-flow zones, fault zones and vein systems recrystallised mainly at greenschist facies were sampled and studied in more detail. In the following section, these outcrops are characterised and mineral assemblages of fluid-flow zones and veins are described. Veins are reported in order of observed cross-cutting relationships, starting with the oldest veins and mineral assemblages within fluid-flow zones and veins are reported in the order of abundance, starting with the most abundant mineral. All orientation of magmatic layering and hydrothermal veins are reported in terms of dip direction and dip.

4.4.1 Outcrop OM1616

Outcrop OM1616, at approximately 260 metres above the Moho is the deepest crustal outcrop along the lower crustal profile in Wadi Gideah (Figure 4.1). It is located slightly elevated above the wadi bed along a river bend in the upper part of the main valley. The outcrop is orientated E-W and is about 25 m long and about 15 m high (Figure 4.2a). On both sides of the outcrop there is abundant fresh layered gabbro. The magmatic layering (134/35°) is in the size of dm and visible in several places along the outcrop. Overall, the outcrop consist of relatively fresh layered gabbro with in total three gullies cross-cutting the layered gabbros in a steep angle. Within these gullies there are three major fluid-flow zones (282/73°) on a decimetre scale, where rocks are completely recrystallised to greenschist facies assemblages comprising various amounts of epidote + prehnite + chlorite and disseminated, weathered sulphides (Figure 4.2b, c, d). In addition, one of these zones contains an approximately 6 cm wide quartz-vein with disseminated sulphides (Figure 4.2b). Gabbro around this fluid-flow zones is heavily altered within 0.5-1 m. Gabbro outside of these zones is generally fresh. Additional to the fully altered and recrystallised fluid-flow zones, there are dark brown to blackish

mm-sized amphibole veins, cross-cutting the magmatic layering in a steep angle (285/75°). Further there are prehnite and epidote-clinozoisite bearing cm-sized veins (211/76°) and randomly orientated fractures filled with laumontite and calcite.

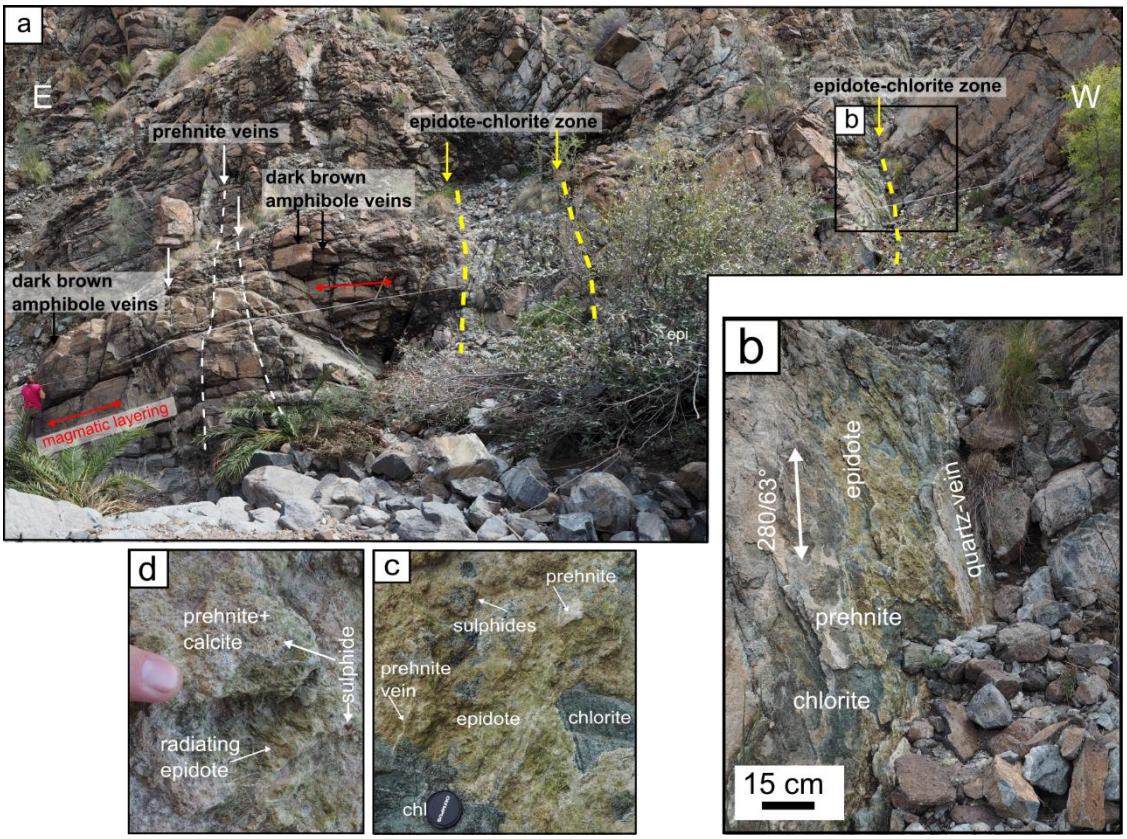

Figure 4.2: (a) Overview of outcrop OM1616. The outcrop is approximately 40 m long and consists of layered gabbros with cross-cutting zones of highly altered gabbro and completely recrystallised zones, found in gullies. Fresh layered gabbro is cross-cut by dark brown to blackish amphibole veins and white prehnite veins. (a) Overview of one of the completely recrystallised zone containing areas of pure epidote, chlorite or prehnite but in most parts all three minerals are mixed. On the right hand side there is one single quartz vein showing abundant open-space and disseminated sulphides. (c) Zoom in into the epidote-chlorite-prehnite part of the zone. Millimetre-sized sulphides are abundant. (d) Epidote shows perfect crystal habits, typically with a radiating orientation. Minor amounts of calcite on the surface is present too.

Fluid-flow zones are completely recrystallised with no traces of the primary mineralogy or texture left. In all three observed zones the dominant mineral is epidote, with single crystals showing perfect crystal habits and grain sizes of up to several millimetre (Figure 4.3). Several samples show macroscopic and microscopic cross-cutting evidences that prehnite grew in a later stage, after the

crystallisation of epidote (Figure 4.3a). Thin section petrography reveal abundant open space within areas dominated by epidote. Some of this open-space has been re-filled by either prehnite or calcite (Figure 4.3b), similar to observations from epidote-clinozoisite veins from Wadi Qafifah (see Chapter 3). Other areas are clearly dominated by prehnite, occurring as mm-sized veins cross-cutting epidote and as patches within epidote-rich areas (Figure 4.2d). The textural relationship between epidote and chlorite is not entirely clear. Field observation show that there is a several cm-wide rim of pure chlorite between the epidote-dominated part of the fluid-flow zone and the highly altered wall-rock but within the epidote dominated part of the zone, patches of almost pure chlorite can be found.

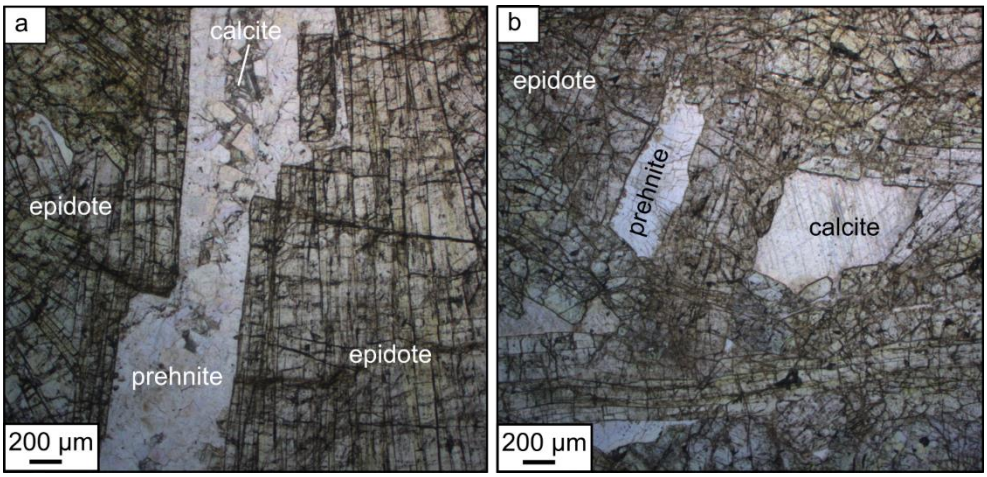

Figure 4.3: Microphotograph of epidote-rich fluid-flow sample AN3. (a) Epidote of fluid-flow zone showing perfect crystal habits and grain sizes up to more than 1 millimetre. Epidote is fractured and fracture was infilled by fine-grained (< 250 µm), blocky prehnite in a second stage. (b) Open-space in-between epidote crystals, now filled with either prehnite or coarse grained calcite.

Summary of observed secondary mineral assemblages:

Fluid-flow zones

- Epidote + prehnite + chlorite ± quartz ± sulphides

Veins

- Amphibole veins
- Prehnite ± epidote ± clinozoisite veins
- Laumontite ± calcite veins

4.4.2 Outcrop OM1523

Outcrop OM1523 is situated approximately 1 km above the Moho transition zone and crops out in a gully above the Wadi bed (Figure 4.1, 4.4). It consists of a 1 m wide normal fault (251/55°) made of chlorite-rich fault gouge, surrounding heavily altered gabbro (Figure 4.4). Hanging- and footwall are heavily veined by epidote, prehnite, laumontite and carbonate veins for about 2.5-3 m and 0.5 m respectively. Alteration in the hanging wall extends for approximately 30 m and is manifested in a general bleaching of the rock. The magmatic layering of the gabbro is not visible within these 30 m but can be measured about 50 metres further away. Its orientation is on average 154/38°.

Thin section petrography reveal that the fault rock comprises chlorite + epidote ± sulphides ± Fe-oxyhydroxides ± titanite, with chlorite being the major constituent. Chlorite replaces primary igneous minerals completely. Outlines of relict igneous mineral grains such as plagioclase and clinopyroxene remain visible (Figure 4.5a). Chlorite co-exists with fine grained, granular epidote and fine grained titanite. There are areas dominated by epidote, with euhedral crystals and abundant open-space (Figure 4.5b). Sulphides (chalcopyrite and pyrite) are disseminated, although there are areas clearly dominated by sulphides and their weathering products such as secondary iron-oxyhydroxides and malachite. In most samples sulphides are fully weathered. Late calcite partially fills open space.
A detailed macroscopic and microscopic description of the clast and wall rock samples can be found in Chapter 5.

Summary of observed secondary mineral assemblages:

Fault rock

- Chlorite + epidote ± sulphides (mainly weathered to Fe-oxyhdroxides and malachite) ± titanite

Veins observed in the wall rock of the fault zone

- Sub-millimetre sized brown hornblende veinlets
- Epidote veins
- Prehnite veins
- Prehnite-laumontite veins
- Laumontite-calcite veins

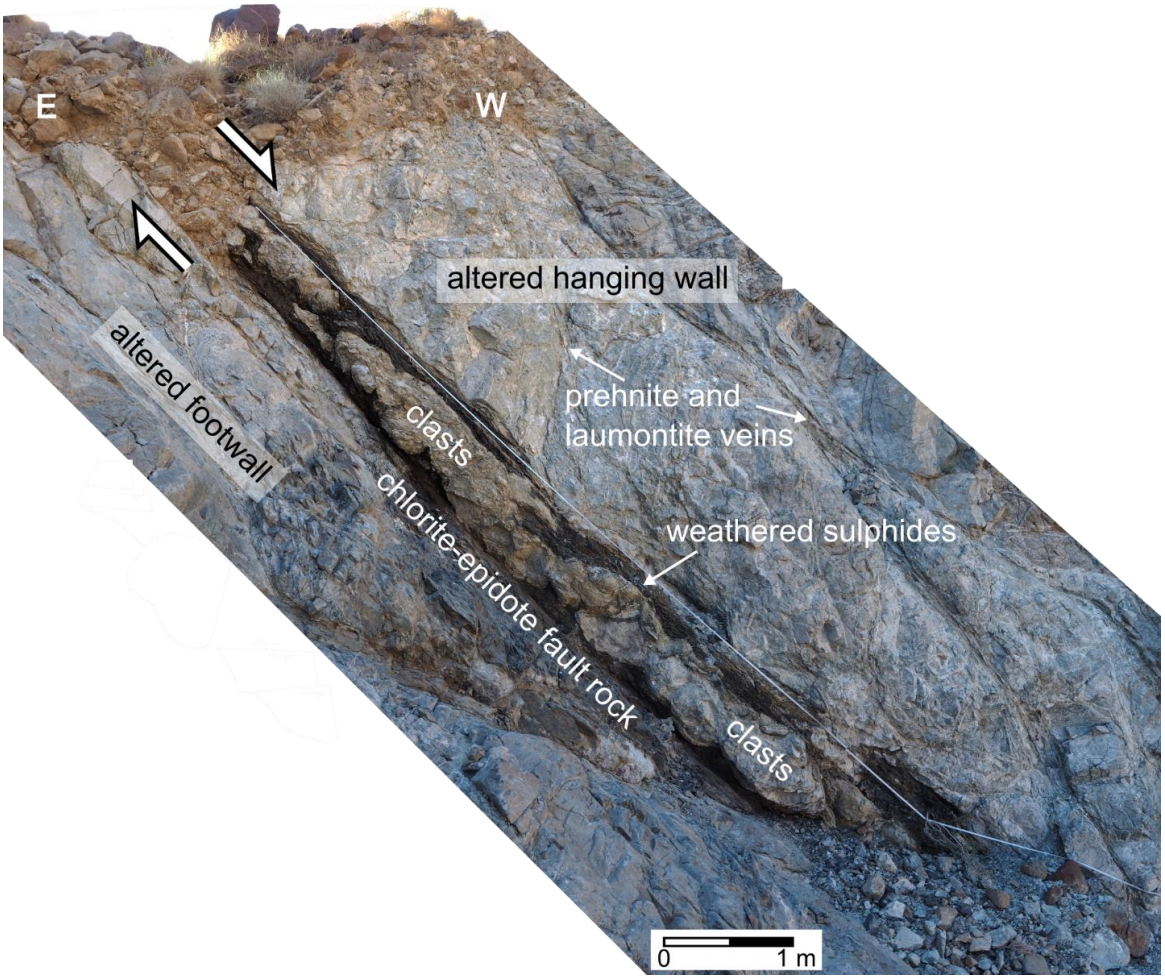

Figure 4.4: Overview of the chlorite-rich fault zone at outcrop OM1523. The photograph shows the chlorite-epidote fault rock surrounded by a heavily veined and altered hanging wall and footwall. The fault zone, including chlorite-rich fault rock and altered gabbroic clasts, is approximately 0.8 m wide and laterally crops out over a length of 8 m.

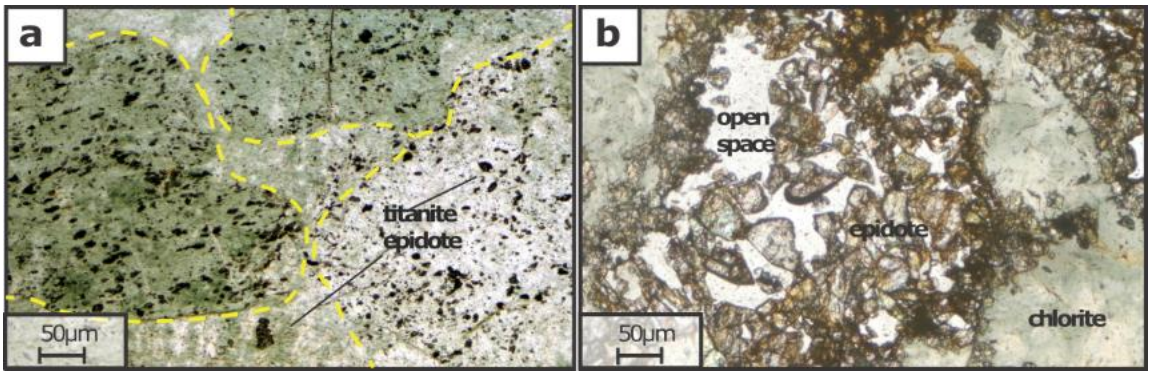

Figure 4.5: Photomicrograph of chlorite-rich fault rock. (a) Chlorite replacing the initial magmatic texture of the gabbro but outlines of former mineral grains are still visible. Chlorite is

associated with fine grained granular titanite and epidote. (b) Euhedral epidote crystal growing into open space.

4.4.3 Outcrop OM1605

Outcrop OM1605 is located approximately 2.6 km above the Moho transition zone, oriented N-S and crops out along the wadi bed between two smaller side-valleys (Figure 4.1, 4.6a). The outcrop location is close to the transition of the layered to the foliated gabbro. The outcrop is characterised by multiple main fluid-flow zones and one fault zone cross-cutting fresh layered gabbro (Figure 4.6a). These fluid-flow zones are several decimetres wide and show pronounced alteration haloes of up to several metres around them. In between these zones of high alteration intensity, there are areas of relatively fresh gabbro (Figure 4.6a). This gabbro is veined with millimetre sized dark brown to blackish amphibole veins without any macroscopically visible alteration halo. Several amphibole veins are re-filled with epidote and/or clinozoisite. The magmatic layering is not visible in the fresh parts of the outcrop however, it has been observed and measured in two smaller, separate blocks about 20 and 30 m to the south of the outcrop.

The chlorite-epidote fault zone is about 0.4 m wide and is made of chlorite fault gouge comprising abundant discontinuous areas of epidote (Figure 4.6b, Figure 4.7a). Prehnite is observed in the epidote-rich part of the zone only, mainly in cross-cutting veins and as void-filling textures. Thin section petrography reveals that chlorite-rich fault rock is texturally and in terms of mineralogy similar to the observed chlorite-rich fault rock of OM1523. Chlorite replaces primary minerals (Figure 4.7a, b), but unlike in chlorite-rich fault rock of OM1523, there are areas which are only partially overgrown by chlorite and igneous mineral phases as well as hornblende are still partially preserved (Figure 4.7c, brown hornblende patches and hornblende blades). The occurrence of hornblende suggests an earlier and presumably higher temperature phase of alteration, replacing clinopyroxene by hornblende. In addition to hornblende, there is also actinolite present in the fault rock (Figure 4.7b). Actinolite needles show a kinking, indicating a growth either previous to deformation or during deformation. In parts where chlorite is the major component, outlines of original mineral phases remain visible. Fine grained titanite and epidote co-exist with chlorite (Figure 4.7b). There are abundant fractures, cross-cutting the sample. No mineralisation in form of sulphides was observed.

Epidote dominated fluid-flow zones are similar to epidote-rich fluid-flow zones from outcrop OM1616, described previously. Epidote is relatively coarse grained with crystals up to several millimetres in size and prehnite in veins and open-space is abundant. Small and weathered sulphide grains occur sporadically within epidote-rich fluid-flow zones but they are less frequent compared to

outcrop OM1616, OM1523 or outcrop OM1609. Most of the epidote fluid-flow zones are rimmed by a cm-sized rim of chlorite on one or both sides. Gabbro is extensively altered around these zones, showing a partial to complete replacement of plagioclase and clinopyroxene by epidote, chlorite, actinolite and hornblende. Altered gabbro less than 0.5 m away of these zones, typically show a "spotty" appearance due to abundant chlorite patches.

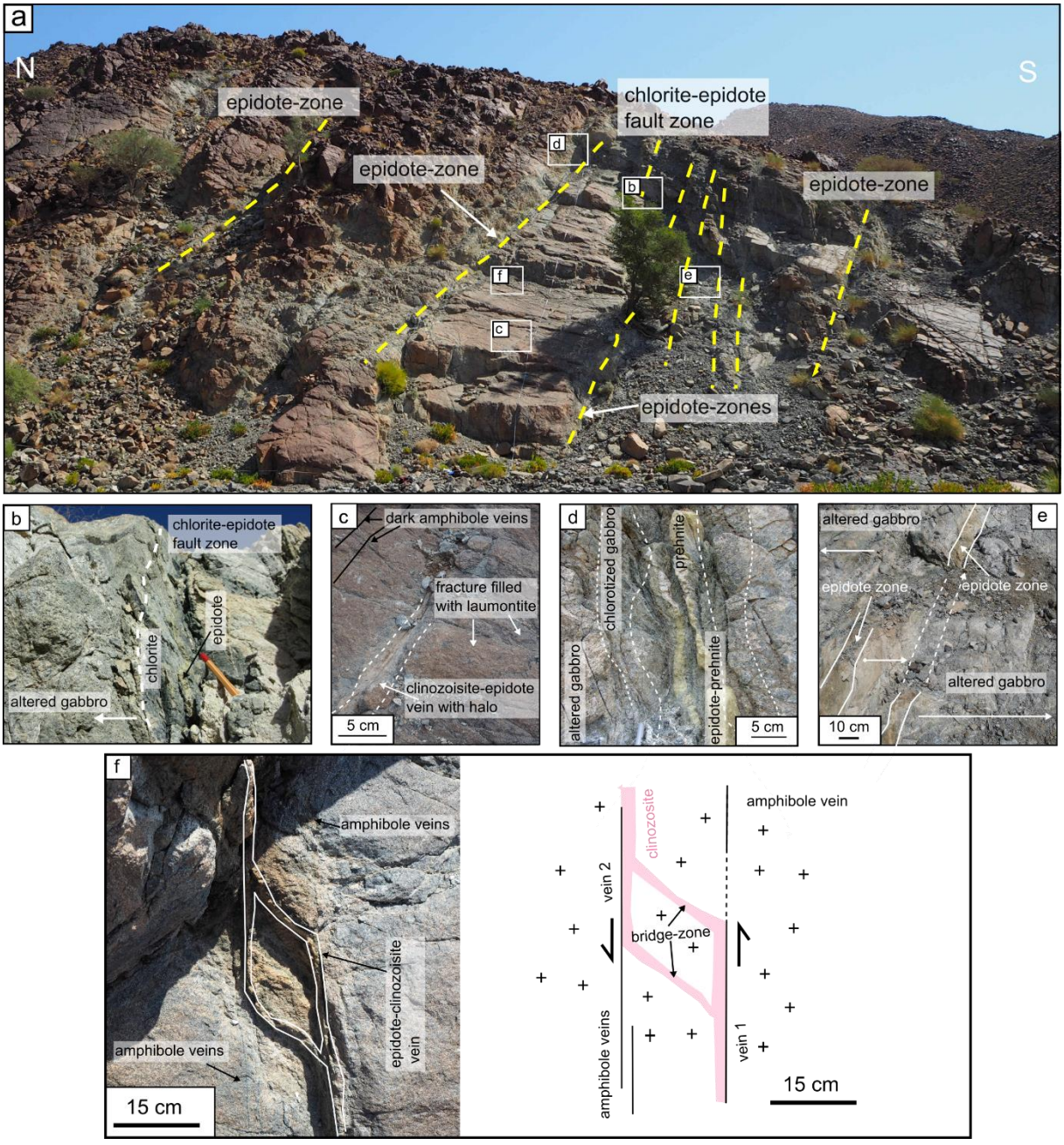

Figure 4.6: Overview photo and zoon-in into outcrop OM1605. (a) Overview of outcrop OM1605 showing several fluid-flow zones and one fault zone. (b) Zoom-in into the chlorite-epidote zone with heavily altered gabbro surrounding the zone. (c) Dark amphibole veins and a clinozoisite-epidote vein cross-cutting a block of relatively fresh gabbro in

between two large fluid-flow zones. (d) Zoom-in into an epidote + chlorite + prehnite fluid-flow zone with a pronounced alteration halo on both sides. (e) Two smaller epidote-rich fluid-flow zones next to each other with intensively altered gabbro surrounding them. (f) Photo and sketch of an observed linkage structure of two parallel and coeval clinozoisite veins, formed along amphibole veins. Such linkage structures typically form when fracture tips approaching each other during shearing, characteristic for extensional setting (Peacock et al., 2016; Pollard and Aydin, 1988).

The mostly fresh part of the outcrop comprises mm-sized dark brown to greenish amphibole veins of predominantly hornblende composition (Figure 4.8). In several samples there are patches of large, dark-brown pargasite crystals (> 1 mm in size). In places, pargasite is replaced by brownish to greenish hornblende, similar to what is described from layered gabbro in Wadi Wariyah (Wolff, 2014).

Several of the observed hornblende veins show a secondary filling of epidote or clinozoisite or a mix of both in the centre of the vein. This indicates a re-opening of the veins and a re-sealing by a second hydrothermal fluid.

Summary of observed secondary mineral assemblages:

Fault zone

- Chlorite + epidote ± prehnite ± titanite
- Fluid-flow zones
- Epidote + chlorite + prehnite ± sulphides

Veins

- Hornblende veins
- Hornblende-clinozoisite-epidote veins
- Clinozoisite-epidote veins
- Laumontite veins

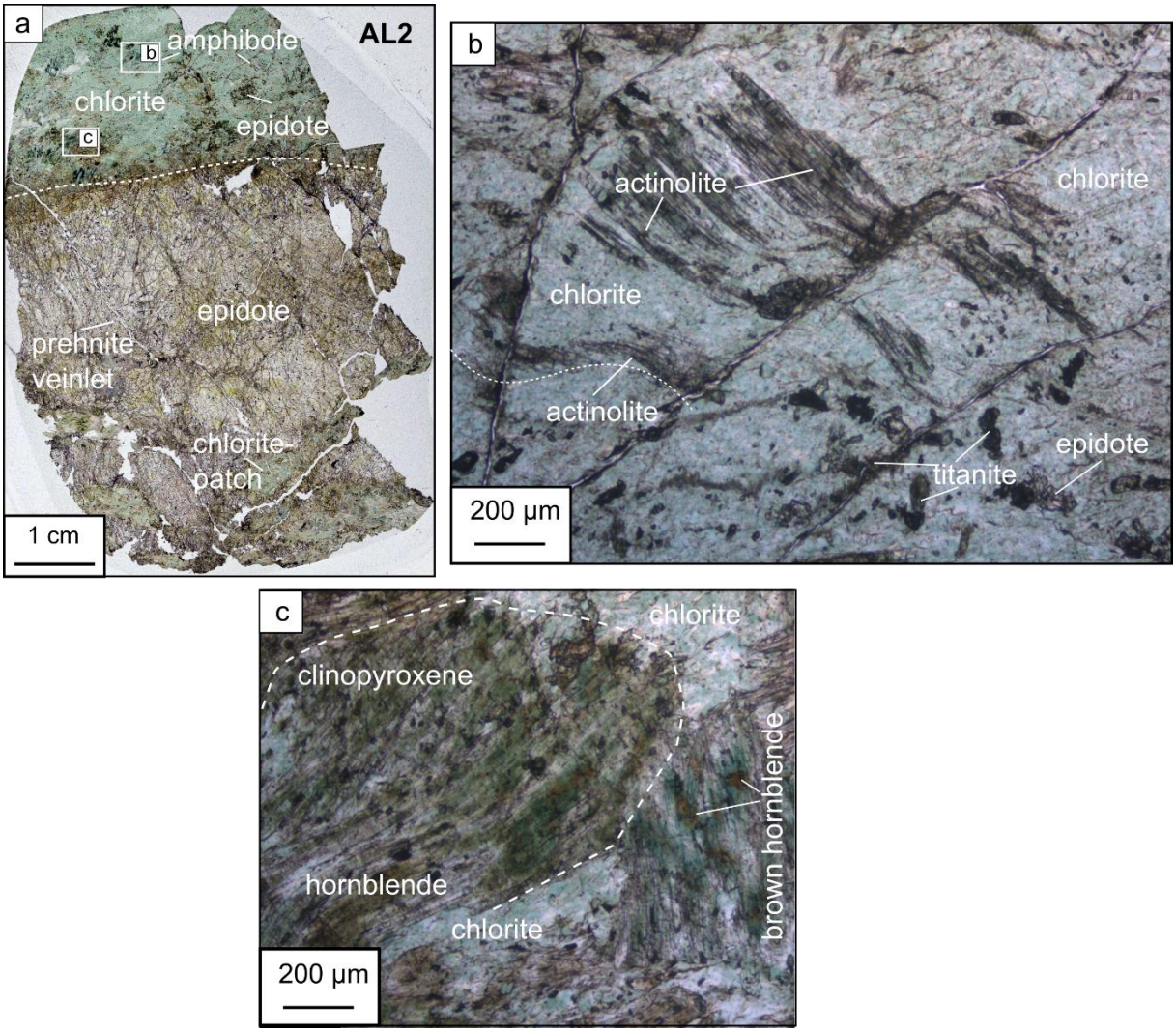

Figure 4.7: Thin section photo and microphotograph of the chlorite-rich fluid-flow zone in outcrop OM1605. (a) Thin section overview showing a chlorite-rich and an epidote-rich part. Note that along the boundary toward the chlorite-rich part epidote is finer grained and becomes gradually less frequent over a distance of approximately 0.5 cm. (b) Zoom-in into a part where primary minerals are almost completely replaced by chlorite. Actinolite is still preserved and shows slight kinking. Chlorite is associated with fine grained titanite and epidote. (c) Zoom-in into an area where primary minerals are still partially preserved (e.g. clinopyroxene). Relict hornblende is partially overgrown by chlorite too and indicates a previous, and likely higher-temperature alteration phase.

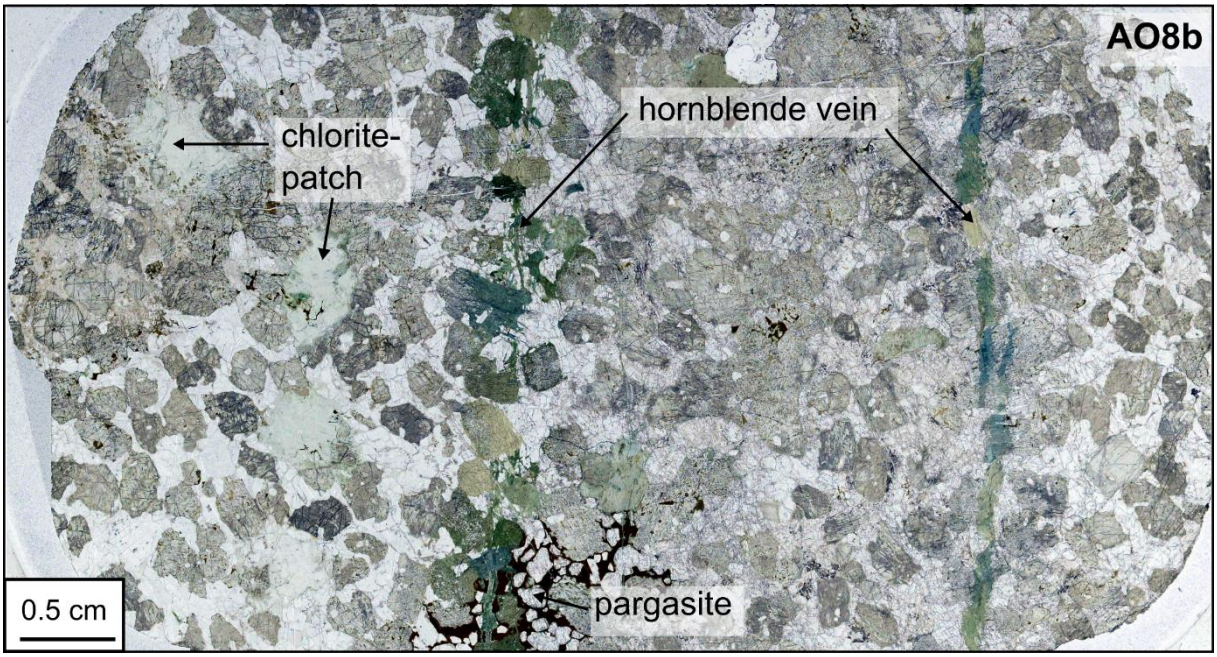

Figure 4.8: Overview of a thin section of sample AO8b, sampled within the relatively fresh part of outcropOM1605. This photomicrograph shows hornblende veins. Both veins are made of sub-millimetre sized veinlets of green hornblende with clinopyroxene being completely replaced by hornblende within a distance of 3-5 mm. One of these hornblende veins cross-cuts a patch of brown magmatic pargasite.

4.4.4 Outcrop OM1609

Outcrop OM1609 is located in a small side valley along the main road, about 1 km south of the village of Wadi Gideah (Figure 4.1). It lies approximately 3590 m above the Moho transition zone and therefore part of the upper foliated gabbros (Müller, 2016). This small side valley is approximately 25-30 m wide and is roughly trending NNW-SSE. Over a distance of about 100 m several fluid-flow and one major fault zone were observed on the valley floor. In size, they range between a few decimetre up to more than a metre wide. In terms of mineralogy they are somehow different compared to previously described alteration zones. Overall, they are rich in quartz and large accumulations of Fe-oxyhydroxides (in the size of dm), and malachite suggesting that sulphides were abundant. Several fluid-flow zones exhibit still fresh sulphides (mainly chalcopyrite). Gabbro around these zones is altered, although many parts are covered by gravel and an estimation of the area altered is difficult to obtain. In addition to the large fluid-flow and fault zones there are abundant mm to cm-sized veins of epidote or epidote + quartz. Vein density and the overall degree of alteration generally decrease uphill, suggesting that the valley formed along the most altered part of the area. All observed fluid-flow and fault zone show a mean orientation of 044/75°. A magmatic

layering is absent. In the following paragraph one example of a fluid-flow zone and the fault zone are described in more detail.

The fluid-flow zone is approximately 45 cm wide zone, comprising fine grained epidote-quartz rock which gradually becomes coarser grained toward the centre of the zone. The centre of the zone is made of centimetre-sized quartz, rimmed by radiating millimetre-sized epidote (Figure 4.9). Epidote crystals show perfect acicular crystal habits. Several crystals indicate two stages of growth, with an outer part in yellow-greenish colours (Figure 4.9), indicating a more Fe-rich composition. The perfect and radiating habit of the epidote crystals demonstrate a growth in open-space, with quartz likely being precipitated in a second stage. Quartz crystals comprise fluid-inclusions. Small grains of Fe-oxyhydroxides (< 200 µm) grow preferentially along quartz grain boundaries. In addition to the quartz-epidote part of the zone, there are several cm-sized areas made entirely of Fe-oxyhydroxides.

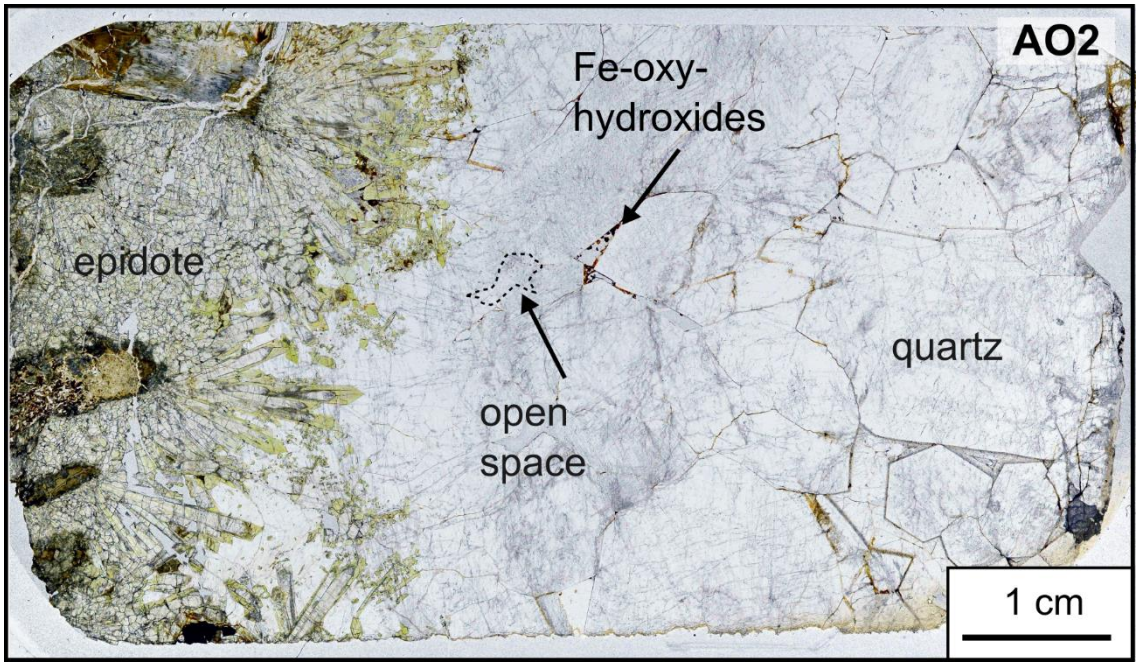

Figure 4.9: Thin section of sample AO2 taken from the core of an epidote-quartz fluid-flow zone. The core of this zone is coarse grained with radiating, mm-sized epidote crystals with perfect crystal habits implying a growth into open-space. Quartz crystals reach up to more than 1 cm in size and comprise fluid inclusions.

The fault zone is approximately 1.8 m wide and comprises a brecciated epidote-quartz rich zone in the middle, surrounded by two chlorite-rich fault rock parts. The epidote-quartz rich part of the fault zone is relatively fine grained (< 1mm, determined from macroscopic observations only), partially heavily brecciated (Figure 4.7c) and shows abundant open-space in the size of several mm. Brecciated parts comprise variably-sized quartz clasts (mm to cm-sized) which are embedded in a

fine grained (< 250 µ) matrix made of chlorite + epidote + Fe-oxyhydroxides. Fe-oxyhydroxides are abundant along fractured grain boundaries of quartz. As part of this inner, quartz-epidote zone, mm-sized fresh chalcopyrite, embedded in Fe-oxyhydroxides and malachite were observed in the field. The outer part of the fault is made of chlorite-rich fault gouge, similar to fault rock from outcrop OM1523 and OM1605 (Figure 4.7a). Chlorite is the major constituent and replaces primary minerals. It co-exists with epidote + quartz + titanite and abundant Fe-oxyhydroxides. Chlorite grows in radiating, < 200 µm sized flakes (Figure 4.7b). Epidote is mostly granular and fine grained (<50 µm), forming rounded areas which are preferentially filled by quartz (Figure 4.7b). Partially preserved primary clinopyroxene (200-750 µm) is common. In a few cases clinopyroxene was initially replaced by hornblende, similar to sample AL2 of outcrop OM1605.

Fresh sulphides are absent in the chlorite-rich fault rock, although Fe-oxyhydroxides are present as either fine grained (<50 µm) flakes mixed with epidote and chlorite, as vein filling or as mm-sized patches overgrowing the chlorite-dominated matrix. In some areas the chlorite is clearly grown together with Fe-oxyhydroxides giving the matrix a brownish shading. Two cm-sized clasts of a fine grained mixture of epidote + chlorite + Fe-oxyhydroxides are embedded within the matrix. One of these clasts is fractured and shows signs of brecciation (Figure 4.10b).

Summary of observed mineral assemblages:

Fluid-flow zones

- Epidote + quartz + sulphides (mostly weathered to Fe-oxhydroxides)
- Epidote + quartz + chlorite + sulphides (mostly weathered to Fe-oxhydroxides)

Fault zone

- Chlorite + epidote + sulphides (mostly weathered to Fe-oxhydroxides) + quartz

Veins

- Amphibole veins
- Epidote veins
- Laumontite-calcite veins

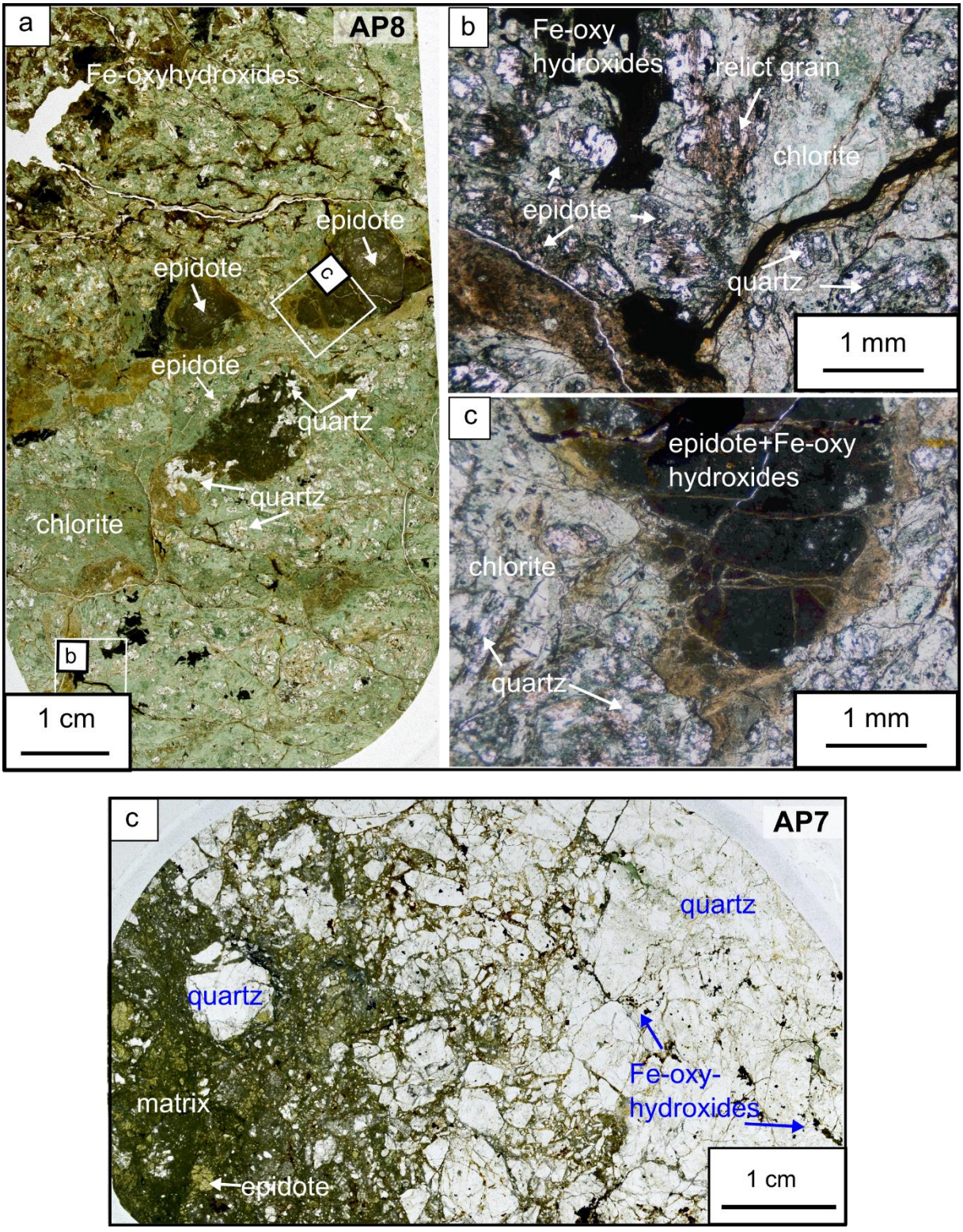

Figure 4.10: Photomicrograph of chlorite-rich fault rock from outcrop OM1609. (a) Overview of a thin section from the chlorite-rich part of the fault zone in outcrop OM1609. Chlorite is replacing primary igneous minerals and co-exists with epidote, quartz and titanite. (b) Zoom-in: outlines of relict mineral phases are partially visible. Fe-oxyhydroxides occur as patches and within veins. (c) Zoom-in, showing a clasts made of a fine grained (< 100

µm) mix of epidote + chlorite + Fe-oxyhydroxides which is embedded in the chlorite-rich matrix. The clast shows signs of brecciation. (c) Breccia from the inner part of the fault zone. Quartz clasts are embedded in a fine grained matrix of epidote + chlorite + Fe-oxyhydroxides.

4.5 Results

4.5.1 Field results

4.5.1.1 Widths of fault zones, fluid-flow zones and corresponding haloes

The width of all three fault zones as well as several fluid-flow zones and corresponding haloes have been logged during fieldwork and are plotted in Figure 4.11. Logged fault zones show widths of 0.4-1.8 m. The width of a fault zones comprises the chlorite-rich fault rock and brecciated clasts or epidote-rich parts in the centre of each zone. Corresponding haloes show widths of about 12-30 m. A positive correlation between fault zone width and halo width can be observed.

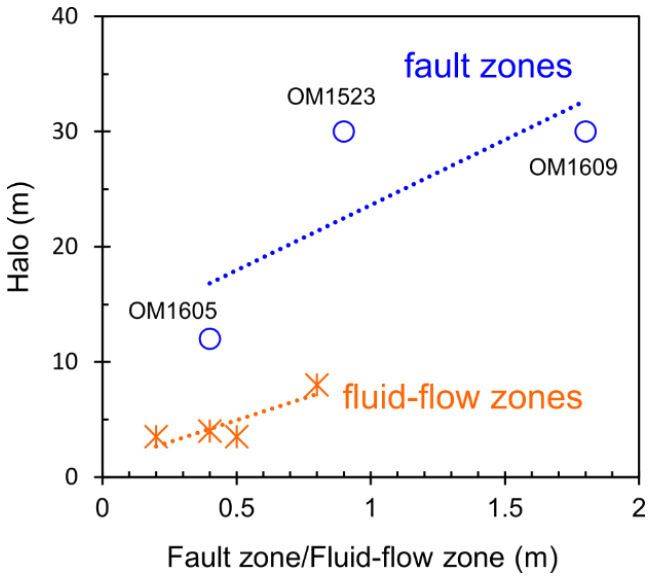

Figure 4.11: Fault zone/Fluid-flow zone width versus corresponding halo width. For both zones, a positive correlation between zone width and halo width can be observed. However, fluid-flow zone are generally less wide than fault zones and show smaller alteration haloes around them.

Fluid-flow zones are generally smaller than chlorite-rich fault zones, showing widths of 0.2-0.8 m. Similar to fault zones, a positive correlation between fluid-flow zone width and corresponding halo width can be observed. Haloes range in the size of 0.4-8 m. However, the estimation of the halo

width is not always straightforward and has proven difficult. For several fluid-flow zones, there are epidote-clinozoisit veins in the halo of the zone and therefore it is not entirely clear whether the alteration in the halo only corresponds to the fluid-flow zone or if it is partly related to additional veining. Therefore, the alteration haloes of fluid-flow zones may be slightly overestimated and the values presented here are maximum estimates.

4.5.1.2 Orientations of veins, fluid-flow zones and fault zones

The orientation of veins (amphibole, epidote-clinozoisite, prehnite and laumontite veins), fluid-flow zones and fault zones was measured in all four described outcrops (Figure 4.12). In all four outcrops, hydrothermal veins, fluid-flow zones and fault zones show moderate to steep inclinations (dip between 55-89°) and are orthogonal to sub-orthogonal to the magmatic layering measured at the corresponding outcrop. In outcrop OM1616, this is true for most veins, although prehnite veins show a trend towards more oblique orientation with respect to the magmatic layering. Outcrop OM1609 lies within the upper foliated gabbros and no magmatic layering could be observed directly at the outcrop location. However, all veins, fluid-flow and fault zones are orthogonal to the magmatic layering observed approximately 500 m to the north (Peters et al., 2008).

Measurements of orientations from all localities show that epidote-clinozoisite veins are parallel to sub-parallel to dark amphibole veins which are thought to have formed in an earlier stage. Fluid-flow zones as well as fault zones generally show an orientation parallel to amphibole and epidote-clinozoisite veins.

In most cases, fluid-flow and fault zones show orientations parallel to sub-parallel to the general orientation of the sheeted dykes measured in the northern limb of the Ibra syncline (Pallister, 1981). Especially in outcrop OM1616 and OM1523 is this trend very clear (Figure 4.12). The chlorite-rich fault zone observed in OM1523 is parallel to dyke orientations and amphibole veins and epidote-prehnite fluid flow zones of OM1616 are parallel to sub-parallel to the general dyke orientation. As previously mentioned, prehnite veins in OM1616 show a slightly larger spread in orientation and they range from parallel to more sub-parallel to the sheeted dykes. Epidote veins observed in OM1609 range from parallel to sub-parallel to the dyke orientation, whereas epidote-quartz fluid-flow zones and the chlorite-rich fault zone are more sub-parallel orientated. Dark amphibole veins further show a more sub-parallel orientation (Figure 4.12).

In outcrop OM1605 the magmatic layering as well as all observed veins, fluid-flow and fault zones show a different orientation compared to orientations observed in all other outcrops. The magmatic layering trends more NW-SE compared magmatic layering in other areas (more NE-SW) and consequently all veins and fluid-flow/fault zones are orientation differently too, as they remain

orthogonal to sub-orthogonal to the magmatic layering. There are two different plausible explanations for this observation: (i) because outcrop OM1605 is located at the boundary between the layered and the foliated gabbros, the change in orientation of the magmatic layering may be related to this transition.

It has previously been reported that the magmatic layering across the transition of the layered to the foliated gabbros changes its orientation towards more foliation parallel orientations and therefore orthogonal, to instead of parallel, to the Moho (MacLeod and Yaouancq, 2000). However, on the geological map of Peters et al. (2008) an orientation of the magmatic layering more like the orientation described previously is indicated from a locality less than 100 m to the south of the outcrop, even further into the foliated gabbros. This locality is like the outcrop on the eastern side of the main Gideah valley but across a small side stream (Figure 4.1). This would indicate that the magmatic layering changes orientation drastically within a distance of a few hundred meters only. (ii) Another explanation could be that a block of layered gabbro within this valley is rotated relative to its initial positions. Such rotations may happen during the obduction and have been reported from other massifs of the ophiolite (see discussion in Nehlig and Juteau, 1988a). In fact, the magmatic layering on the west-side of the main valley shows orientations different from the east-side (starting from about 2 km south of outcrop OM1523; Figure 4.1), indicating structural differences. If the orientation of the magmatic layering would be rotated back to a position more parallel to the inferred paleo-Moho, hydrothermal veins, fluid-flow and fault zones would show very similar orientation as observed from the other outcrops. Such a rotation is regarded as more likely than a change in orientation due to transition of layered gabbro into foliated gabbro and back again.

The orientation of laumontite veins were measured throughout the whole valley and a lower hemisphere projection of the poles to the planes show that their orientation is random. No preferred orientation could be detected (Figure 4.12).

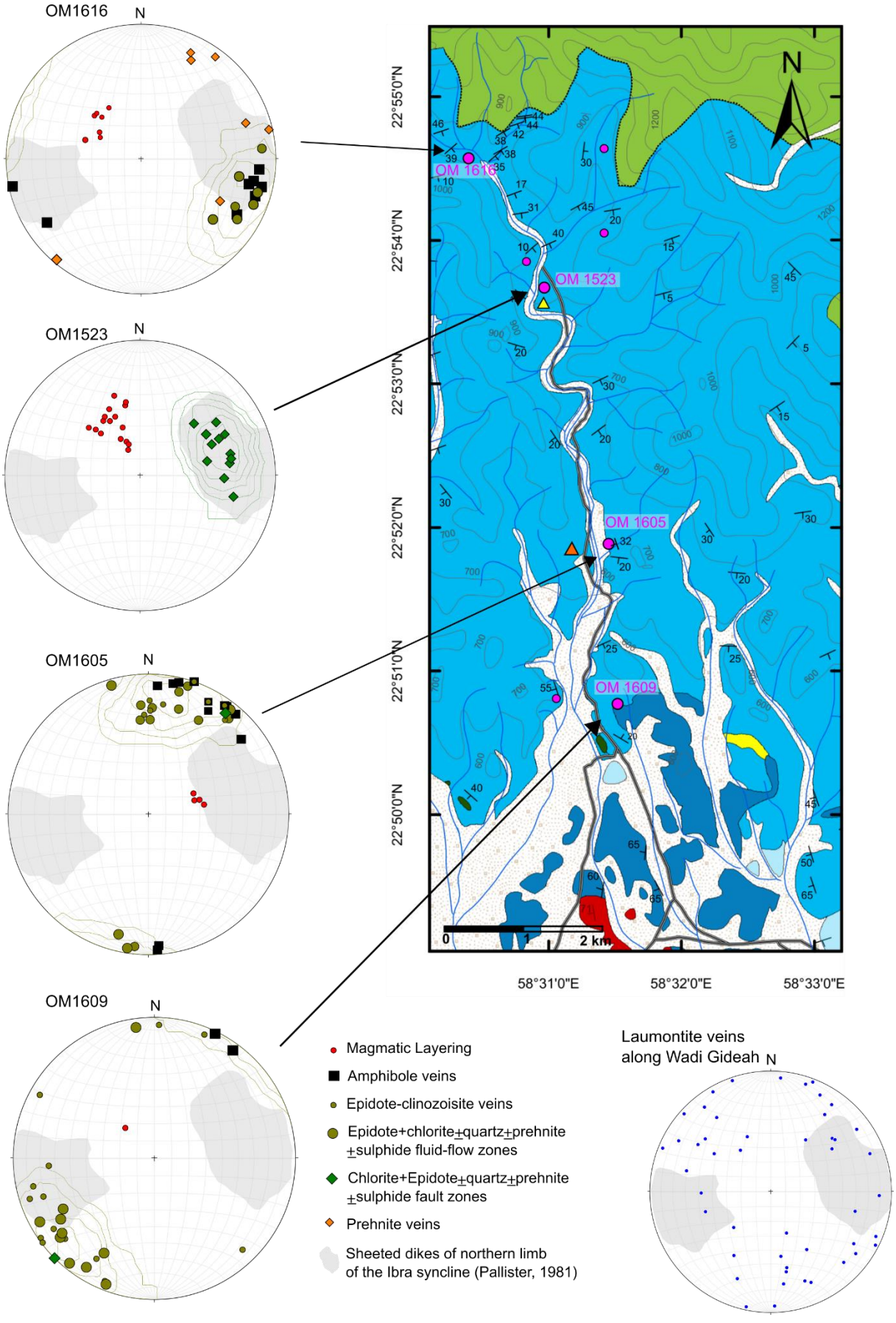
OM1616
N
OM1523
N
OM1605
N
OM1609
N
22°55'0"N
22°54'0"N
22°53'0"N
22°52'0"N
22°51'0"N
22°50'0"N
58°31'0"E
58°32'0"E
58°33'0"E
OM 1616
OM 1523
OM 1605
OM 1609
0
1
2 km
Magmatic Layering
Amphibole veins
Epidote-clinozoisite veins
Epidote+chlorite±quartz±prehnite ±sulphide fluid-flow zones
Chlorite+Epidote±quartz±prehnite ±sulphide fault zones
Prehnite veins
Sheeted dikes of northern limb of the Ibra syncline (Pallister, 1981)
Laumontite veins along Wadi Gideah
N

Figure 4.12: Lower hemisphere equal area projections of poles to planes of all hydrothermal vein systems, fluid-flow zones and fault zones relative to the magmatic layering throughout Wadi Gideah.Kamb-contours of epidote + chlorite ± quartz ± sulphides ± prehnite fluid-flow zones for outcrops OM1616, OM1605 and OM1609. Kamb-contours of chlorite-epidote fault zone for outcrop OM1523. The shaded grey areas correspond to dyke orientation measured in the northern limb of the Ibra syncline (Pallister, 1981). Measured laumontite veins show random orientation throughout the Wadi Gideah. Geological map adapted after Peters et al. (2008). For more detailed information see 2.2.2 Geological Background.

4.5.2 Mineral chemistry

4.5.2.1 Plagioclase

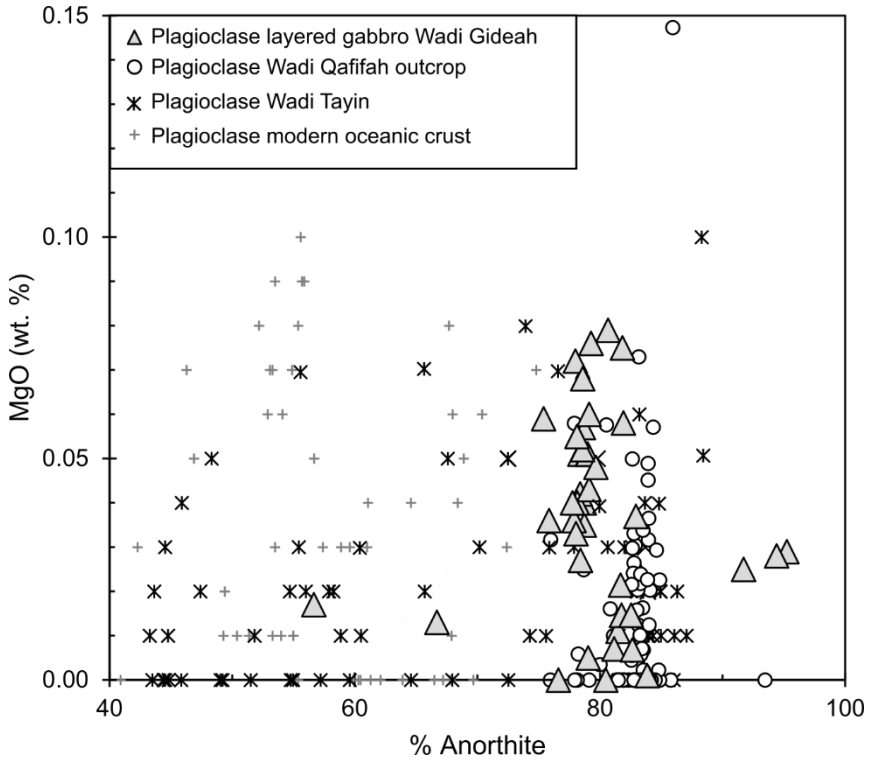

Figure 4.13: Plagioclase composition of fresh to altered gabbro of samples outside fluid-flow zones. For comparison, gabbro from Wadi Tayin massif (France et al., 2009; Pallister and Hopson, 1981) and the mapped outcrop in Wadi Qafifah (Chapter 2) are plotted. Further plagioclase composition of gabbros from modern oceanic crust measured from ODP/IODP hole 1256 (Alt et al., 2010).

Plagioclase of both fresh layered gabbro samples and altered gabbro from outcrop OM1523 (hanging- and footwall of the fault zone), OM1605 and OM1606 is compositionally similar to plagioclase from the layered gabbro section elsewhere in the Wadi Tayin area (Pallister and Hopson, 1981) with a few analysis towards more albitic composition (sample AK5 of OM1606; Figure 3.13; Appendix B.1). Anorthite (An=Ca/(Ca+Na*100) contents range from of An_{56-95} with an average anorthite content of An_{78}.

4.5.2.2 Amphibole

Amphiboles of gabbro outside fluid-flow zones, of altered gabbro within metres of fluid-flow zones and amphiboles found in fluid-flow zone samples were analysed by electron microprobe, and results are recalculated to 23 oxygens (Appendix B.1) and classified after Leake et al. (1997) (Figure 4.14). Ferric iron is estimated after Schumacher, (1997) in Leake et al. (1997). All measured amphibole classify as Ca-amphibole and plot in the fields of pargasite-magnesio-hastingsite and edenite for Ca_B > 1.5 and $(Na+K)_A$ > 0.5 and in the fields of actinolite-tremolite, magnesiohornblende and tschermakite for compositions with for Ca_B > 1.5 and $(Na+K)_A$ < 0.5. There are few analysis showing higher iron concentrations and consequently plot in the field of ferrroactinolite and ferrohornblende (Figure 4.14b). Such a continuous chemistry is common for amphiboles observed in oceanic gabbros and similar composition have been reported previously, from both modern oceanic crust and ophiolites (Alt et al., 2010; Bosch et al., 2004; Manning et al., 1996; Mével and Cannat, 1991; Vanko, 1986).

Amphibole veins of relatively fresh gabbro sampled outside the alteration influence of fluid-flow zone mainly plot in the composition field of hornblende, with a few analysis towards more actinolite or tschermakite compositions. Amphibole co-existing with chlorite in small alteration patches of pervasive background alteration show predominantly composition in the field of actinolite and tremolite. Large and anhedral, in plane-polarised light dark brown, amphiboles observed in several samples from various outcrops show pargasitic compositions, which are characterised by high titanium concentrations (typically 3-4 wt.%, compared to a TiO_2 concentration of actinolite < 1 wt.%). These pargasites occur in patches with sizes of several millimetres and are distributed all over the samples (Figure 4.14).

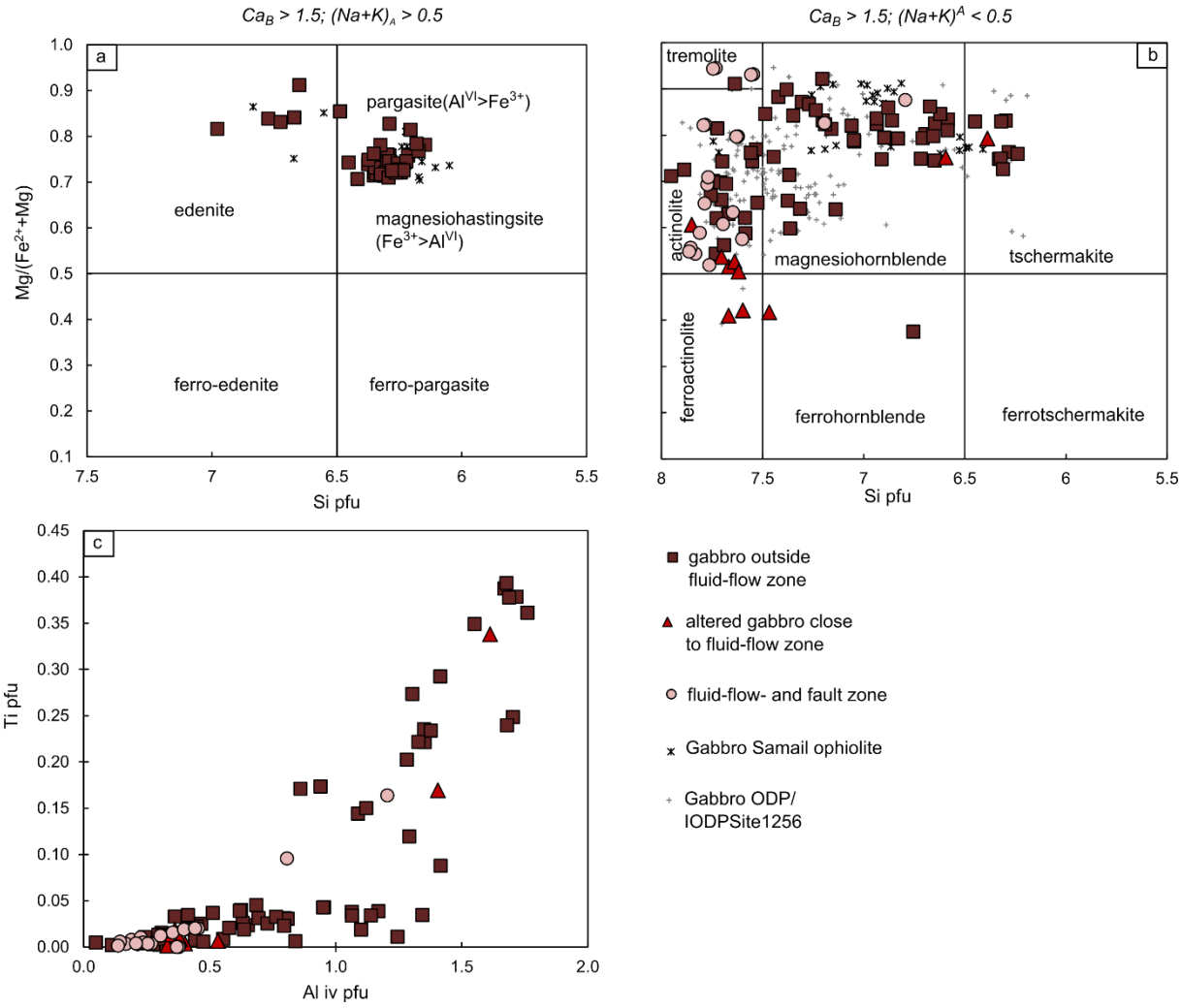

Figure 4.14: Composition of amphibole measured in fresh gabbro, altered gabbro within metres of fluid-flow zones and amphibole in fluid-flow zones compared to amphiboles from layered gabbros elsewhere in the ophiolite (Bosch et al., 2004) and in the plutonic section of modern oceanic crust at ODP/IODP Site 1256 (Alt et al., 2010). Amphibole analysis are classified after Leake et al. (1997). Several amphibole crystals in fluid-flow- and fault zones as well as in altered gabbro close to those zones show relatively high Ti-content, similar to amphiboles (hornblende-tschermakite-magnesiohastingsite-pargasite) replacing clinopyroxene in fresh gabbro (see 3.6.1 “Relative timing of hydrothermal veins and estimation of formation conditions”). This suggests an earlier alteration phase at higher (> 500 °C) temperatures.

Amphibole compositions observed in one altered sample, collected about a metre away of an epidote + quartz + chlorite + sulphide fluid-flow zone in outcrop OM1609, range from actinolite to hornblende with three analyses being more iron-rich and are classified as ferro-hornblende and ferro-actinolite.

Two chlorite-epidote fluid-flow samples collected in outcrop OM1605 display amphibole grains within the chlorite-rich fault rock (Figure 4.14). This amphibole predominantly plots in the field of actinolite compositions with one analysis yielding a tremolite composition and two analyses a relatively Ti-rich hornblende composition (Figure 4.14b).

4.5.2.3 Chlorite

Chlorite of all three fault zones as well as chlorite of background alteration observed in variably altered samples collected outside of fluid-flow zones were analysed and recalculated on the basis of 28 oxygens (Appendix B.1, Figure 4.15). Generally, chlorite of the fault zone is richer in iron than chlorite observed in patches of background alteration, although the composition of sample AL2 from outcrop OM1605 (Figure 4.15) mostly overlaps with the composition measured in background alteration. Chlorite of both fault rocks from OM1523 and OM1609 show overall the most iron-rich compositions with the majority yielding compositions between Fe/(Fe+Mg) 0.4-0.58. Composition of chlorite from fluid-flow zone in OM1609 shows a larger variation in iron-content and extends to less iron-rich compositions, similar to those observed from fluid-flow zone in OM1605. In terms of silica content, chlorite of the background alteration shows larger compositional variations and is overall silica richer (Si pfu 5.8-6.2 for majority of the samples) compared to chlorite of fluid-flow zones and chlorite in the fault rock (Si pfu 5.4-5.8 for the majority of the samples).

Overall, chlorite of fault zones are similar in composition to chlorite reported of brecciated and altered gabbro from Wadi Haymiliya (Nehlig and Juteau, 1988b), whereas chlorite of the background alteration is similar to chlorite reported from chlorite veinlets and chlorite patches observed in layered gabbro from Wadi Haymiliya (Nehlig and Juteau, 1988b).

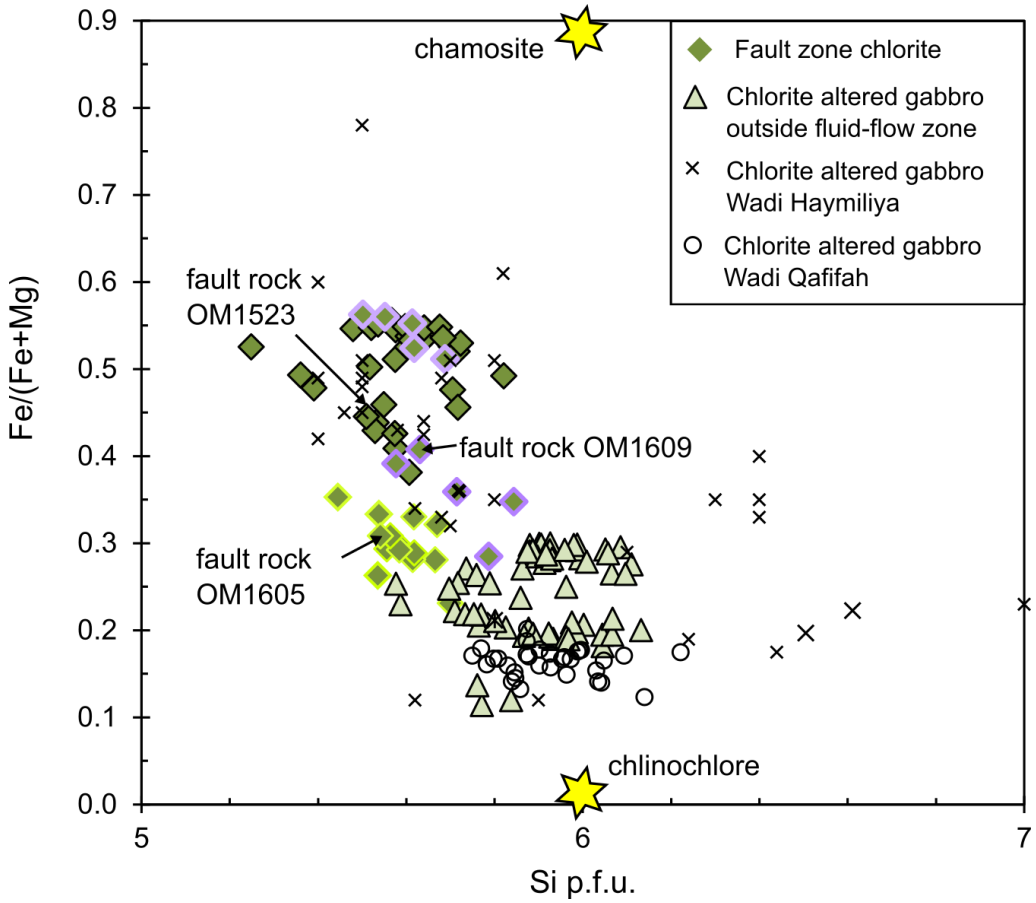

Figure 4.15: Chlorite composition of chlorite from fault zones in outcrop OM1609, OM1605 and OM1523 compared to chlorite of background alteration observed in variably altered gabbro of samples collected outside of fault-flow zones. In addition there are chlorite composition of chlorite measured in variably altered gabbro in Wadi Haymiliya (Nehlig and Juteau, 1988b) and chlorite measured in altered gabbro in Wadi Qafifah (this study, Chapter 3.5.2.5). Fault zone chlorite has a distinctive composition, with more Fe and less Si per formula unit than chlorite in background altered gabbro.

4.5.2.4 Epidote

Epidote from one epidote vein (sample AK5) in altered gabbro outside a fluid-flow zone (at outcrop OM1606) and epidote of several fluid-flow samples where epidote co-exists with either chlorite and prehnite (outcrop OM1616, OM1605) or quartz ± sulphides (OM1609) have been analysed and recalculated on the basis of 13 oxygens (Appendix B.1, Figure 4.16). Clinozoisite is rare in Wadi Gideah and was only observed in two sample from outcrop OM1605 but was not analysed by electron microprobe. Epidote of fluid-flow zones show compositions with X_{Fe} (X_{Fe} =Fe/(Fe+Al) ranging between 10-35 % with a clear majority between 20-25% $X_{Fe.}$ Compared to epidote and clinozoisite of veins cross-cutting layered gabbro in Wadi Haymiliya (Nehlig and Juteau, 1988b) and epidote-

clinozoisite compositions measured in Wadi Qafifah (Chapter 2, section 5.2.6), epidote of fluid-flow zones are overall more Fe-rich, although some X_{Fe} up to 35% were measured in Wadi Qafifah. Similar values are reported from epidote co-existing with quartz and pyrite in the sheeted dyke of Wadi Haymiliya (Nehlig and Juteau, 1988b) and from epidote in the sheeted dyke complex and the upper gabbros at ODP/IODP Site 1256 (Alt et al., 2010) as well as the sheeted dyke complex at IODP Site 504B (X_{Fe} 25-30 %; Laverne et al., 1995). Epidote of an epidote-prehnite vein in altered gabbro from outcrop OM1606 shows similar composition but with a slight trend towards lower abundance of iron, more similar to what has been reported for the gabbroic section (Alt et al., 2010; Nehlig and Juteau, 1988b).

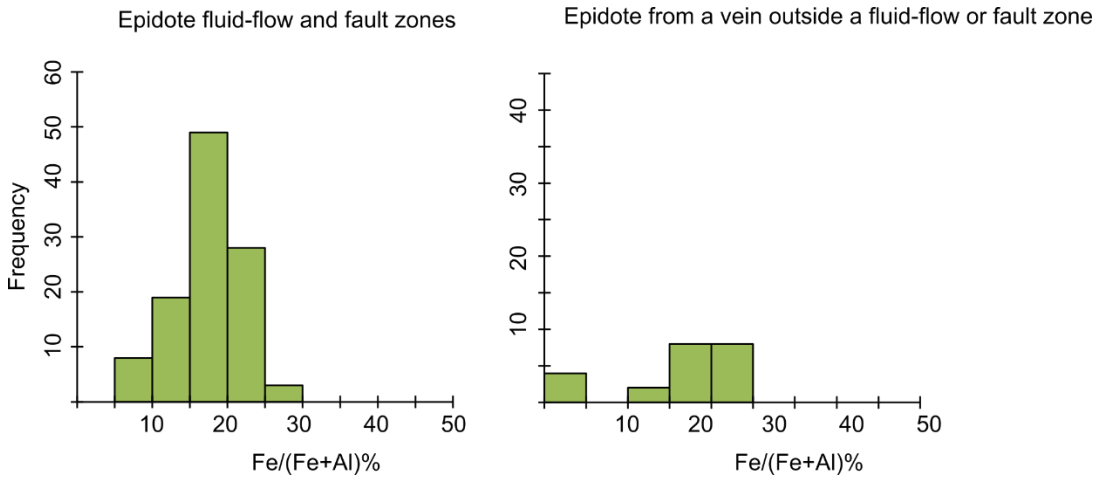

Figure 4.16: Epidote composition of epidote from fluid-flow and fault zones (samples from outcrop OM1616, OM1605 and OM1609) and epidote measured in a vein outside a fluid-flow zone (sample AK5 outside a fluid-flow zone). Epidote measured outside the fluid-flow zone shows composition expanding towards lower abundance of iron and corresponds to what has been observed and reported for the lower crustal section (Alt et al., 2010; Nehlig and Juteau, 1988b).

4.5.2.5 Prehnite

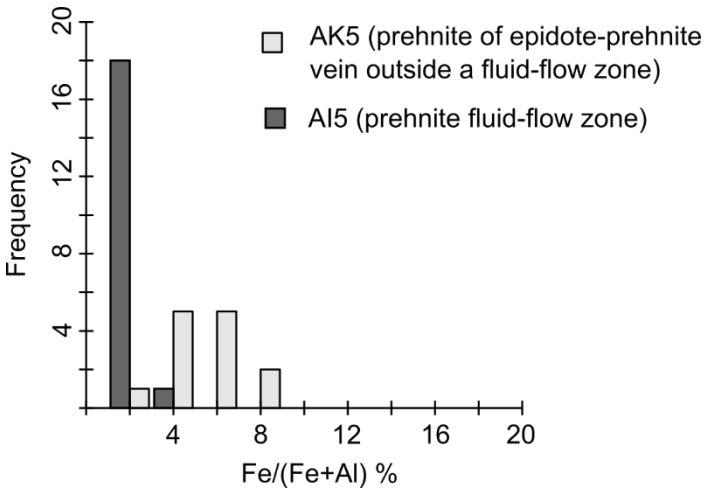

Figure 4.17: Comparision of prehnite composition measured from prehnite sampled in a fluid-flow zone and prehnite outside a fluid-flow zone. Prehnite crystals sampled inside a fluid-flow zone show a trend towards lower abundance of Fe and a higher abundance of Al compared to prehnite sampled in a vein outside a fluid-flow zone.

Prehnite crystals of sample AI6 of the fluid-flow zone in outcrop OM1616 and prehnite of an epidote-prehnite vein in sample AK5 outside a fluid-flow zone were analysed by electron microprobe and are recalculated on the basis of 24 oxygens and 4 OH sites (Appendix B.1, Figure 4.17). The two samples are distinctive in terms of iron concentrations. Whereas prehnite of fluid-flow zone sample AI5 shows iron-poor compositions with X_{Fe}=Fe/(Fe+Al^{iV}) of up to 4% in total, prehnite of an epidote-prehnite vein of sample AK5 shows X_{Fe} compositions of up to 9% and is therefore richer in iron. Compared to prehnite measured elsewhere in the lower crust of the ophiolite these compositions are relatively low in iron (Nehlig and Juteau, 1988).

4.6 Sr-isotope compositions

Strontium isotope compositions of overall 65 sample collected from all four described outcrops and a few locations between those outcrops were analysed (Table 4.1). This includes: whole rock samples of fluid-flow/fault zones, whole rock of variably altered gabbro within a short distance (maximum 2-3) metres of one or several fluid-flow/fault zones and whole rock sampled in fresh gabbro, well away of fluid-flow/fault zones. Mineral separates of fluid-flow/fault zones and veins from fresh to variably altered gabbo outside of fluid-flow zones were analysed in addition to whole rock samples. Furthermore, strontium isotope compositions of 29 samples of dyke sampled in the Ibra syncline

were analysed and all data are displayed and compared to available literature data across the whole crust (Figure 4.18).

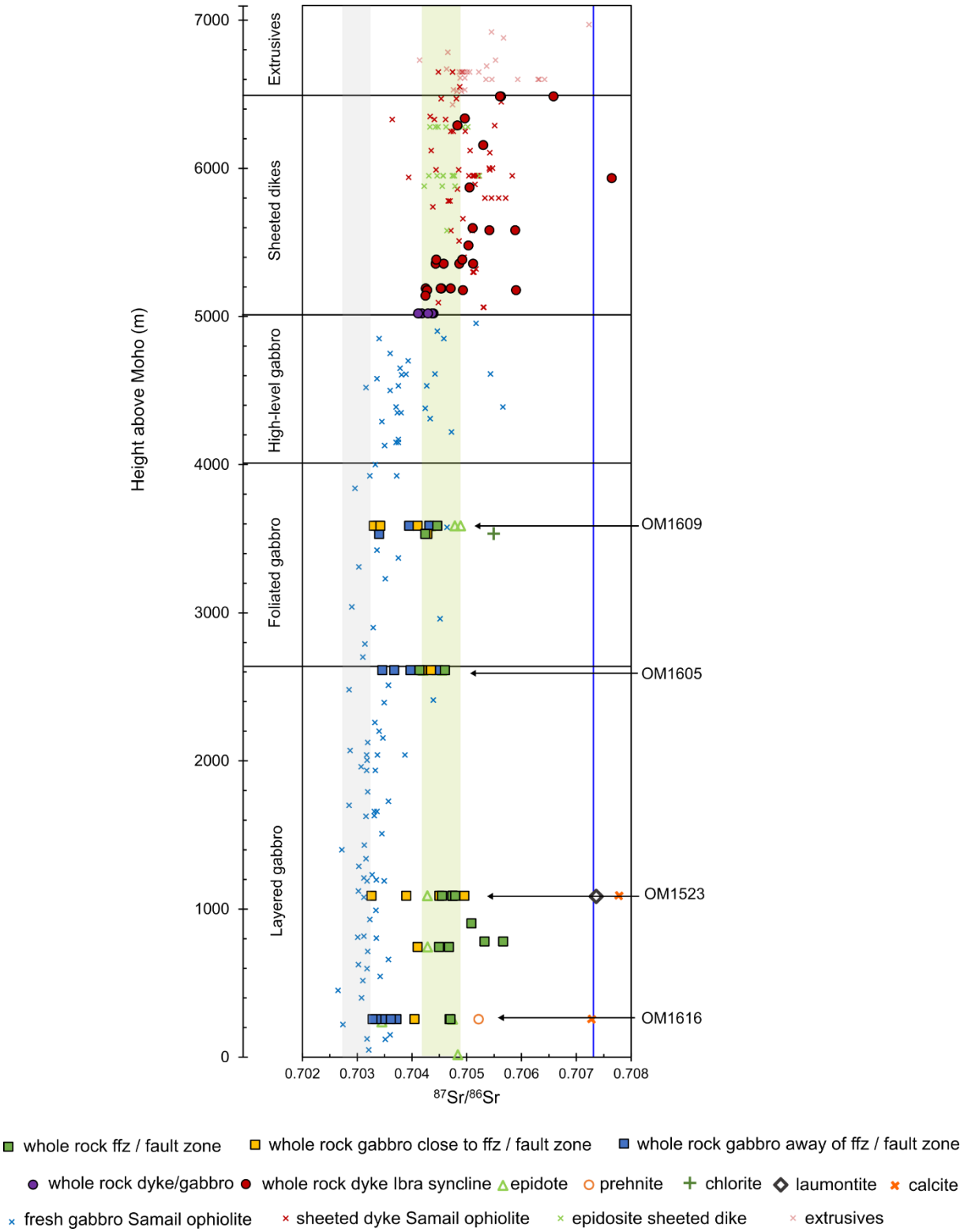

Figure 4.18: (a) Sr-isotope profile of whole rock and mineral separate samples through Wadi Gideah. Fresh gabbro composition of the whole ophiolite (Kawahata et al., 2001; Lanphere et al., 1981; Müller, 2016), sheeted dyke samples (Davis, 2004; Kawahata et al., 2001;

Lanphere et al., 1981; Müller, 2016), epidotised sheeted dyke samples (Davis, 2004) and lava samples (Davis, 2004; Kawahata et al., 2001; Müller, 2016) are plotted for comparison in the background. The shaded grey area represent fresh layered gabbro composition sampled in Wadi Tayin (Lanphere et al., 1981; McCulloch et al., 1981) and the shaded light green area represents the range of epidote composition measured from both, epidote from fluid-flow zones and epidote from single veins.

Upper crust: Lavas and sheeted dyke complex

Sr-isotope composition of variably altered sheeted dyke and two lava samples collected in the core of the Ibra syncline show Sr-isotope compositions highly elevated from magmatic $^{87}Sr/^{86}Sr$ values (White et al., 1987) or fresh values observed in the Samail ophiolite $^{87}Sr/^{86}Sr$ = 0.70265 - 0.70320; Lanphere et al., 1981; McCulloch et al., 1980). Sr-isotopic composition range between $^{87}Sr/^{86}Sr$=0.7042 - 0.7076 (Figure 4.18, Figure 4.19 and Table 4.2) and are therefore comparable to whole rock sheeted dyke compositions measured elswhere in the ophiolite (Davis, 2004; Kawahata et al., 2001; Lanphere et al., 1981; Müller, 2016). Approximately half of the samples plot within the Sr-isotope composition of epidosites, sampled in the northern part of the Samail ophiolite (Davis, 2004) and the rest of the samples yield more radiogenic compositions.

Sheeted dyke-gabbro transition zone

Overall 5 samples were collected at the dyke-gabbro transition about 10 km to the east of the Wadi Gideah valley entrance. These samples comprise a selection of fresh to variably altered dykes and gabbros as well as one more evolved, SiO_2-rich sample. One additional fresh dyke sample was collected on top of a hill right at the gabbro-dyke transition outside Wadi Gideah (Figure 4.1). Sr-isotope composition of all six samples range between $^{87}Sr/^{86}Sr$=0.7041-0.7044, regardless of their degree of alteration. With such Sr-isotopic composition they plot in the lower range of Sr-composition observed in the sheeted dykes (Davis, 2004; Kawahata et al., 2001; Lanphere et al., 1981; Müller, 2016) and in the upper range of Sr-isotope compositons observed for high-level gabbros in Wadi Gideah (Müller, 2016; Figure 4.18).

Table 4.1: Sr-isotope compositions of whole rock and mineral separates of samples from fluid-flow and fault zone outcrops as well as samples collected in between. All $^{87}Sr/^{86}Sr$ are corrected for 95 Ma.

Sample	Outcrop	UTM N	UTM E	Relation to ffz or fz	Rock type	Degree of alteration[2)]	Secondary mineralogy[3)]	Height above Moho	$^{87}Sr/^{86}Sr$ measured	2SE	Sr (ppm)	Rb (ppm)	$^{87}Sr/^{86}Sr_{95\ Ma}$
AM5bg1dec	OM1612	665765	2529160	outside ffz/fz	dyke whole rock	moderate	epi+qz	5020	0.704128	0.0000010	179.5	0.06	0.704127
AM4dec	OM1612	665765	2529160	outside ffz/fz	tronhjemite whole rock	moderate	epi+qz+sulph±Fe-oxy	5020	0.704197	0.0000010	90.9	0.43	0.704179
AM7dec	OM1612	665765	2529160	outside ffz/fz	dyke whole rock	slight	±alb±chl±act	5020	0.704434	0.0000010	175.3	1.86	0.704393
AM5dec	OM1612	665765	2529160	outside ffz/fz	dyke whole rock	high	qz+epi+chl	5020	0.704367	0.0000010	580.0	0.02	0.704367
AM3dec	OM1612	665765	2529160	outside ffz/fz	gabbro whole rock	moderate	alb+chl+act	5020	0.704326	0.0000012	181.6	1.67	0.704291
AM2dec	OM1611	656319	2524704	outside ffz/fz	dyke whole rock	slight	±chl±act	5020	0.704112	0.0000012	190.5	0.12	0.704110
AO8abg1dec	OM1605	656260	2529355	outside ffz/fz	gabbro whole rock	slight	chl+alb±hbl±act	2612	0.703457	0.0000010	147.1	0.04	0.703456
AJ8bg1dec	OM1605	656260	2529355	outside ffz/fz	gabbro whole rock	slight	alb±chl±hbl±act	2612	0.703674	0.0000010	131.5	0.16	0.703669
AP5bg1dec	OM1609	656496	2527278	outside ffz/fz	gabbro whole rock	slight	±chl±pre±lau	3587	0.703370	0.0000011	171.6	0.49	0.703359
AP6bg1dec	OM1609	656496	2527278	outside ffz/fz	gabbro whole rock	slight	±chl±alb±act±hbl	3587	0.703395	0.0000010	176.1	0.15	0.703392
AN5dec	OM1616	654383	2534374	outside ffz/fz	gabbro whole rock	moderate	alb+chl+act+hbl	256	0.703476	0.0000012	220.5	0.01	0.703476
AN4dec	OM1616	654383	2534374	outside ffz/fz	gabbro whole rock	slight	±chl±alb±act	256	0.703350	0.0000010	131.2	0.02	0.703349
AN2bg1dec	OM1616	654383	2534374	outside ffz/fz	gabbro whole rock	slight	±chl±alb±act±hbl	256	0.703279	0.0000010	133.1	0.02	0.703279
AN8dec	OM1616	654383	2534374	outside ffz/fz	gabbro whole rock	moderate	alb+hbl+thom	256	0.703716	0.0000011	258.0	0.03	0.703715
AK5bg1dec	OM1606	655849	2527393	outside ffz/fz	gabbro whole rock	moderate	chl+alb±hbl±act	3533	0.703398	0.0000011	169.3	0.34	0.703390
AO5bg1dec	OM1605	656260	2529355	outside ffz/fz	gabbro whole rock	moderate	±alb±chl±act	2612	0.704158	0.0000011	150.9	0.19	0.704153
AJ8h1dec	OM1605	656260	2529355	outside ffz/fz	gabbro whole rock	moderate	cz+chl+act+hbl+alb	2612	0.704442	0.0000011	131.1	0.19	0.704438
AP5h1dec	OM1609	656496	2527278	outside ffz/fz	gabbro whole rock	moderate	alb+epi+chl+hbl	3587	0.704315	0.0000012	285.4	0.63	0.704306
AN2h1dec	OM1616	654383	2534374	outside ffz/fz	gabbro whole rock	slight	±alb±act±hbl	256	0.703610	0.0000010	288.3	0.02	0.703610
AJ3bg1dec	OM1605	656260	2529355	outside ffz/fz	gabbro whole rock	slight	alb+chl+hbl	2612	0.703971	0.0000010	163.4	0.35	0.703962

AO3bg1dec	OM1609	656496	2527278	outside ffz/fz	gabbro whole rock	moderate	hbl+chl	3587	0.703948	0.0000009	134.3	0.13	0.703944
AI5bg1dec	OM1602	656222	2533335	close to ffz/fz	gabbro whole rock	moderate	alb+chl+hbl+act	743	0.704104	0.0000011	185.4	0.09	0.704102
AQ1bg1dec	OM1609	656496	2527278	close to ffz/fz	gabbro whole rock	slight	±act±hb±chl	3587	0.703306	0.0000011	125.7	0.16	0.703301
AH9dec	OM1523	655498	2532598	close to ffz/fz	gabbro whole rock	high	alb+hbl+act+chl+pre+lau	1089	0.703896	0.0000012	145.6	0.11	0.703893
OM15_3Adec	OM1523	655498	2532598	close to ffz/fz	gabbro whole rock	high	pre+chl+lau+tre+hbl	1089	0.704749	0.0000011	437.9	0.26	0.704747
OM15_3Fdec	OM1523	655498	2532598	close to ffz/fz	gabbro whole rock	slight	chl+tre+Mg-hbl	1089	0.703267	0.0000011	56.57	0.08	0.703262
AJ5Bdec	OM1605	656260	2529355	close to ffz/fz	gabbro whole rock	high	epi+chl+hbl+act	2612	0.704178	0.0000012	303.2	0.10	0.704177
AO6h1dec	OM1605	656260	2529355	close to ffz/fz	gabbro whole rock	high	cz+chl+act+hbl±alb	2612	0.704346	0.0000011	284.1	0.17	0.704344
AP1bg1dec	OM1609	656496	2527278	close to ffz/fz	gabbro whole rock	moderate	alb+hbl+chl	3587	0.703434	0.0000009	189.1	0.64	0.703421
AK5h1dec	OM1606	655849	2527393	close to ffz/fz	gabbro whole rock	moderate	alb+hbl+epi+chl±preh	3533	0.704282	0.0000010	241.0	0.19	0.704279
AP3dec	OM1609	656496	2527278	close to ffz/fz	gabbro whole rock	moderate	hbl+act+chl±epi	3587	0.704109	0.0000012	212.4	0.39	0.704102
AN3h1dec	OM1616	654383	2534374	close to ffz/fz	gabbro whole rock	high	chl+act+hbl	256	0.704685	0.0000010	71.22	0.01	0.704685
AH6dec	OM1523	655498	2532598	close to ffz/fz	gabbro whole rock	high	alb+hbl+act+lau+cal±epi±tit	1089	0.704503	0.0000013	216.1	0.09	0.704501
AH7dec	OM1523	655498	2532598	close to ffz/fz	gabbro whole rock	high	chl+alb+hbl+act+epi+cal	1089	0.704962	0.0000013	97.29	0.11	0.704958
AJ2h1dec	OM1604	656225	2534413	close to ffz/fz	gabbro whole rock	moderate	alb+chl+act+hbl	237	0.704045	0.0000011	210.4	0.04	0.704044
AK2dec	OM1605	656260	2529355	ffz/fz	fault rock	complete	chl+epi+act+hbl	2612	0.704601	0.0000011	357.8	0.02	0.704601
AP7dec	OM1609	656496	2527278	ffz/fz	fault rock	complete	epi+qz+sulph+Fe-oxy	3587	0.704461	0.0000009	326.1	0.01	0.704461
AL2dec	OM1605	656260	2529355	ffz/fz	fault rock	complete	chl+epi	2612	0.704137	0.0000010	126.0	0.02	0.704136
AI6dec	OM1602	656222	2533335	ffz/fz	fault rock	complete	epi±preh±sulph+Fe-oxy	743	0.704675	0.0000010	57.9	0.01	0.704675
AI3dec	OM1602	656222	2533335	ffz/fz	fault rock	complete	epi+chl+act±qz±pre	743	0.704492	0.0000011	677.1	0.01	0.704492
AN3dec	OM1616	654383	2534374	ffz/fz	fault rock	complete	epi+pre+sulph+Fe-oxy	256	0.704702	0.0000010	509.1	<0.01	0.704702
AK4dec	OM1606	655849	2527393	ffz/fz	fault rock	complete	epi+chl+preh+sulph+Fe-oxy	3533	0.704243	0.0000012	165.1	0.03	0.704242
AD5dec	OM1523	655498	2532598	ffz/fz	fault rock	complete	chl+epi+tit+Fe-oxy	1089	0.704546	0.0000013	78.0	<0.01	0.704546
AD7dec	OM1523	655498	2532598	ffz/fz	fault rock	complete	chl+epi+tit+sulph+Fe-oxy	1089	0.704735	0.0000013	51.8	0.01	0.704734

OM15_3Cdec	OM1523	655498	2532598	ffz/fz	fault rock	complete	chl+sulph+Fe-oxy	1089	0.704738	0.0000010	34.2	0.04	0.704734
OM15_3Edec	OM1523	655498	2532598	ffz/fz	fault rock	complete	chl+epi	1089	0.704795	0.0000009	13.2	0.03	0.704785
AE1dec	close to OM1523	655097	2533254	ffz/fz	fault rock	complete	pre+chl	781	0.705664	0.0000010	11.8	<0.01	0.705664
AE2dec	close to OM1523	655097	2533254	ffz/fz	fault rock	complete	pre+chl+lau	781	0.705325	0.0000011	10.9	0.01	0.705323
AD8dec	close to OM1523	655349	2532993	ffz/fz	fault rock	complete	preh+chl+hbl+act+lau	904	0.705084	0.0000010	63.2	0.04	0.705082
AO2epi1	OM1609	656496	2527278	ffz/fz	minerals separate	-	epidote	3587	0.704782	0.0000010	649.6	b.d.	0.704782
AO3epi1	OM1609	656496	2527278	ffz/fz	minerals separate	-	epidote	3587	0.704887	0.0000010	627.4	b.d.	0.704887
AP7epi1	OM1609	656496	2527278	ffz/fz	minerals separate	-	epidote	3587	0.704340	0.0000010	652.2	<0.01	0.704340
AI3epi1	OM1602	656222	2533335	ffz/fz	minerals separate	-	epidote	743	0.704282	0.0000012	441.0	b.d.	0.704282
AL1epi1	OM1605	656260	2529355	ffz/fz	minerals separate	-	epidote	2612	0.704547	0.0000010	748.7	b.d.	0.704547
AN3epi1	OM1616	654383	2534374	ffz/fz	minerals separate	-	epidote	256	0.704735	0.0000010	529.6	b.d.	0.704735
AN6epi1	OM1616	654383	2534374	ffz/fz	minerals separate	-	epidote	256	0.704739	0.0000011	375.9	b.d.	0.704739
AN6pr2dec	OM1616	654383	2534374	ffz/fz	minerals separate	-	prehnite	256	0.705215	0.0000010	8.2	<0.01	0.705217
AK4chl1	OM1606	655849	2527393	ffz/fz	minerals separate	-	chlorite	3533	0.705494	0.0000009	48.1	0.05	0.705492
AI3epi1	OM1523	655498	2532598	outside ffz/fz	minerals separate	-	epidote	1089	0.704280	0.0000011	428.6	0.08	0.704279
AJ2epi1	OM1604	656225	2534413	outside ffz/fz	minerals separate	-	epidote	237	0.703450	0.0000010	697.5	b.d.	0.703450
AM9cz1	at Moho			outside ffz/fz	minerals separate	-	clinozoisite	16	0.704837	0.0000009	515.8	< 0.01	0.704837
AJ9cz1	OM1605	656260	2529355	outside ffz/fz	minerals separate	-	clinozoisite	2612	0.704202	0.0000010	640.5	b.d.	0.704202
AH6lau1	OM1523	655498	2532598	outside ffz/fz	minerals separate	-	laumontitie	1089	0.707371	0.0000014	199.9	0.62	0.707359
AH5carb1	OM1523	655498	2532598	outside ffz/fz	minerals separate	-	calcite	1089	0.707771	0.0000012	106.0	0.31	0.707760
AH9carb1	OM1523	655498	2532598	outside ffz/fz	minerals separate	-	calcite	1089	0.708235	0.0000011	118.5	0.27	0.708226

Ffz => fluid-flow zone

fz => fault zone

Lower crust and fluid-flow zone outcrops

All four outcrops exposing fluid-flow zones or a fault zone are characterised by slightly to considerably elevated Sr-isotope composition compared to fresh MORB from modern oceanic crust (White et al., 1987) and fresh layered gabbro reported from Wadi Gideah (Müller, 2016) and elsewhere in the Samail ophiolite ($^{87}Sr/^{86}Sr$ 0.70265 - 0.70320; Kawahata et al., 2001; Lanphere et al., 1981; McCulloch et al., 1980).

All fluid-flow and fault zone whole rock samples yield compositions of $^{87}Sr/^{86}Sr$=0.7041-0.7057. The majority of these samples plot in the range of epidote mineral separates sampled along the lower crust (Figure 4.19). There are three exceptions: Samples of three individual small fault zones, sampled on the hill opposite fault zone outcrop OM1523 yield slightly more radiogenic values of $^{87}Sr/^{86}Sr$=0.7051-0.7056. The secondary mineral assemblage of all three samples comprises albite + prehnite + laumontite + chlorite, with no epidote present. With prehnite, chlorite and laumontite yielding isotopic compositions >$^{87}Sr/^{86}Sr$=0.7050, whole rocks samples consequently show more radiogenic values too.

Variably altered gabbro samples collected within a distance of a few metres away of one or several fluid-flow zones show composition with a larger spread ($^{87}Sr/^{86}Sr$=0.7033 - 0.7050) but the majority of them is elevated above fresh values. Fresh to slightly altered whole rock gabbro sampled well away of fluid-flow and fault zones display Sr-isotope compositions in the range of $^{87}Sr/^{86}Sr$=0.7032 - 0.7044, overall less radiogenic than altered samples in the vicinity of a fluid-flow zone. Notably, gabbro sampled in outcrop OM1616 and outcrop OM1605 show compositions relatively close to fresh gabbro sampled along the valley (Müller, 2016) and elsewhere in the ophiolite (Kawahata et al., 2001; Lanphere et al., 1981; McCulloch et al., 1980).

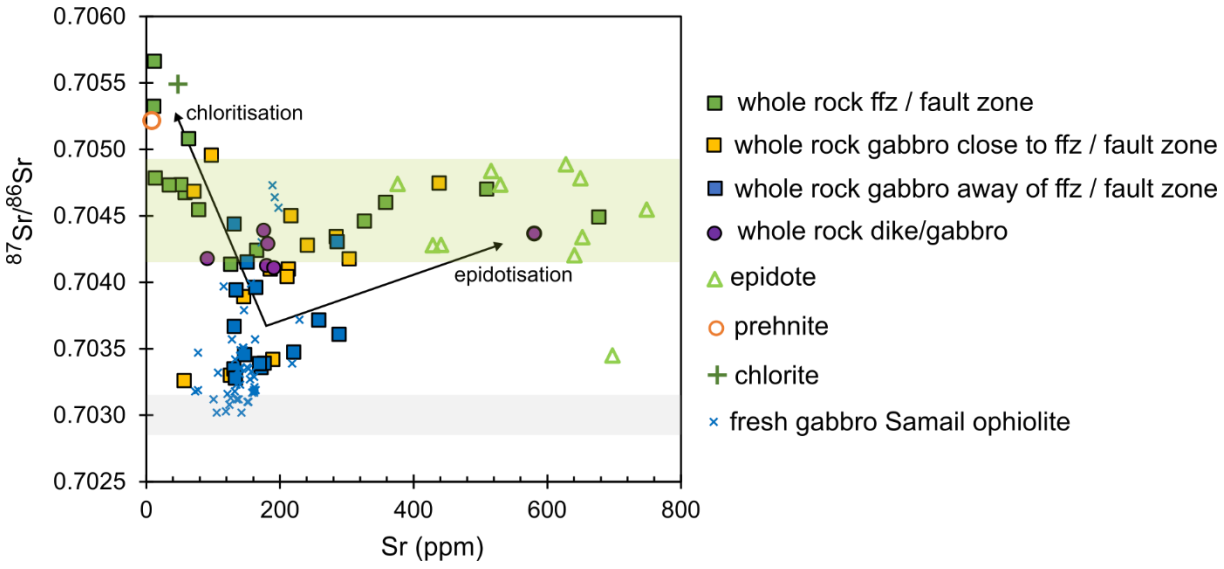

Figure 4.19: Strontium concentration (ppm) versus strontium isotope composition of whole rock and mineral separates. For comparison, strontium data of fresh layered gabbro

samples along Wadi Gideah are plotted in the background (Müller, 2016). The shaded grey area represent freshest layered gabbro composition sampled in Wadi Tayin (Lanphere et al., 1981; McCulloch et al., 1981) and the shaded light green area represents the range of epidote composition measured from both, epidote from fluid-flow zones and epidote from single veins. Error bars are smaller than the data points.

Mineral separates along the lower crust

Hand-picked epidote from fluid-flow zones show a relatively narrow range of strontium isotope composition ($^{87}Sr/^{86}Sr$=0.7043-0.7049, Figure 4.18, 4.19), similar to epidote-clinozoisite compositions measured in Wadi Qafifah (see Chapter 2) and epidote compositions reported from elsewhere in the ophiolite (e.g., Bosch et al., 2004; Coogan et al., 2006). Epidote and clinozoisite picked from veins outside of fluid-flow zones show comparable composition of $^{87}Sr/^{86}Sr$=0.7035-0.7048 (Figure 4.18, 4.19), although one vein shows considerably lower values of $^{87}Sr/^{86}Sr$=0.7035. This picked epidote originates from a single epidote-clinozoisite vein within fresh layered gabbro, sampled at the Moho transition zone. The vein is approximately 1.5 cm wide and shows a narrow alteration halo of only a few millimetres in size. No relationship between sample depth and Sr-isotope composition of epidote can be observed but with the exception of the sample yielding the lowest Sr-isotopic composition all samples plot within the range of epidosites in the sheeted dyke complex (Davis, 2004).

Prehnite from an epidote + prehnite + chlorite fluid-flow zone shows slightly more radiogenic Sr-isotope composition than epidote, similar to prehnite sampled in Wadi Qafifah (see Chapter 3). Chlorite of a chlorite vein in fresh gabbro sampled in outcrop OM1606 yields a Sr-isotope composition of $^{87}Sr/^{86}Sr$=0.7055. This is slightly more radiogenic than epidote and prehnite mineral separates but considerably less radiogenic than picked chlorite of a chlorite patch in Wadi Qafifah (Figure 4.18, 4.19). Separated laumontite of a prehnite-laumontite hanging wall vein of fault zone OM1523 displays a composition of $^{87}Sr/^{86}Sr$=0.7074. Sr-isotope composition of picked calcite from two laumontite-calcite veins and a leachate of an epidote-prehnite fluid-flow zone of outcrop OM1616 show Sr-isotope compositions of $^{87}Sr/^{86}Sr$=0.7073-0.7082 (Figure 4.18, 4.19). These Sr-isotope values of calcite plot in the range of Cretaceous to Miocene sediments (Weyhenmeyer, 2000) and close to the Sr-isotopic composition of modern groundwater, samples in gabbro hosted wells in Wadi Tayin (Bompard, 2018).

Table 4.2: Sr-isotope compositions of dyke samples from the Ibra area. Measured composition are corrected to 95 Ma.

Sample	Type	UTM N	UTM E	Distance above Moho	Sample type	$^{87}Sr/^{86}Sr$ measured	2 SE	Rb (ppm)	Sr (ppm)	$^{87}Sr/^{86}Sr$ 95 Ma
OM-01-9	dyke	649196	2515356	5189	chilled margin	0.704720	0.0000014	1.25	351.5	0.704707
OM-01-10	dyke	649196	2515356	5189	-	0.704270	0.0000012	1.88	338.7	0.704248
OM-01-11dec	dyke	649196	2515356	5178	medium grained,	0.705913	0.0000010	0.25	72.4	0.705900
OM-01-12	dyke	649159	2515385	5178	chilled margin	0.704290	0.0000013	1.24	329.2	0.704275
OM-01-13A	dyke	649144	2515386	5189	chilled margin	0.704555	0.0000013	1.27	312.2	0.704540
OM-01-13B	dyke	649144	2515386	5189	chilled margin	0.704546	0.0000013	1.51	270.7	0.704524
OM-01-14	dyke	649144	2515386	5178	medium-grained	0.704934	0.0000013	0.15	163.1	0.704930
OM-01-15	dyke	649004	2515511	5141	chilled margin	0.704286	0.0000014	1.96	190.9	0.704246
OM-01-16	dyke	649004	2515511	5357	margin of older	0.704453	0.0000013	1.24	200.2	0.704429
OM-01-17	dyke	649004	2515511	5357	chilled margin	0.704599	0.0000013	1.03	193.2	0.704579
OM-01-18	dyke	649004	2515511	5357	massive dyke	0.705144	0.0000013	0.85	108.5	0.705113
OM-01-20	dyke	649004	2515511	5357	chilled margin	0.704883	0.0000013	0.74	137.2	0.704862
OM-03-21	dyke	648978	2515585	5384	chilled margin	0.704949	0.0000014	0.83	104.9	0.704919
OM-01-22	dyke	648978	2515585	5384	medium-grained,	0.704469	0.0000014	1.53	222.1	0.704442
OM-01-23dec	dyke	646697	2517840	5480	-	0.705042	0.0000010	0.12	44.4	0.705031
OM-01-26	dyke	646702	2518229	5582	-	0.705438	0.0000013	0.73	107.6	0.705411
OM-01-28	dyke	646702	2518229	5582	irregular dyke	0.705894	0.0000011	0.40	155.8	0.705884
OM-01-29	dyke	646749	2518271	5597	medium-grained	0.705120	0.0000012	0.35	106.1	0.705108
OM-01-30	dyke	653678	2521694	5871	chilled margin	0.705069	0.0000013	1.05	213.8	0.705050
OM-01-33	dyke	653500	2521311	6338	-	0.704987	0.0000013	0.99	172.3	0.704964
OM-01-34	dyke	653511	2521349	6291	massive dyke	0.704847	0.0000012	0.63	148.6	0.704830
OM-01-35	dyke	653835	2521407	6157	medium-grained	0.705311	0.0000012	0.16	47.8	0.705298
OM-01-36dec	dyke	660201	2521737	6700	medium-grained,	0.706610	0.0000010	2.19	290.8	0.706581
OM-01-37dec	dyke	660216	2521732	6700	medium-grained	0.705710	0.0000010	3.16	139.5	0.705622
OM-01-38	dyke	660216	2521732	6700	fine-grained dyke	0.705633	0.0000013	0.89	130.2	0.705607
OM-01-39dec	basalt	662410	2522076	6709	pillow basalt,	0.705801	0.0000009	6.51	266.2	0.705706
OM-01-40	basalt	662467	2522511	7097	pillow lava	0.705379	0.0000015	2.38	205.3	0.705334
OM-01-41dec	dyke	661330	2523263	6167	medium-grained	0.706098	0.0000011	3.82	233.4	0.706034
OM-01-42dec	dyke	661180	2523511	5935	fine-grained dyke	0.707666	0.0000014	2.39	467.9	0.707647

4.7 Discussion

All studied fluid-flow and fault zones observed in the four outcrops along the lower crust in Wadi Gideah show characteristics of channelled discharge of hydrothermal fluids, known and previously described from shallow hydrothermal systems in the upper oceanic crust at fast spreading ridges situated in ophiolites and modern ocean crust (e.g., Barker et al., 2010; Nehlig et al., 1994; Richardson et al., 1987; Saccocia and Gillis, 1995). In the following paragraph, structural, mineralogical, and Sr-isotopic indications are discussed in more detail.

4.7.1 Structural indications

Measurements of the orientation of the main vein systems including amphibole and epidote-clinozoisite veins as well as the orientation of fluid-flow and fault zones show that the majority of them are sub-parallel to parallel to the orientation of the sheeted dykes, observed in the Ibra syncline (Pallister, 1981). This strongly indicates that the veins, fluid-flow and fault zones formed in the same regional stress field as the sheeted dykes, during initial spreading of the ridge. The mean attitude of the sheeted dykes is assumed to represent the orientation of the fossil spreading centre (Cann, 1974). Thus, hydrothermal veins and fault zones are mostly parallel to the inferred axial plane of the paleo-spreading centre. Transverse, cross-cutting veins are rare. This indicates that permeability throughout the lower crust was anisotropic. Such an anisotropy has previously been suggested from vein orientations measured in the sheeted dykes and the lower crust in Wadi Haymiliyah of the ophiolite, where hydrothermal veins are strictly oriented parallel to the axial plane of the paleo-spreading centre and hydrothermal circulation is suspected to have occurred in vertical planes along-strike down to the base of the crust (Nehlig and Juteau, 1988a).

4.7.2 Indications from secondary mineralogy and mineral chemistry observed in fluid-flow and fault zones

Presented hydrothermal fluid-flow and fault zones show a secondary mineral assemblage dominated by either epidote or chlorite, together with variable amounts of quartz, sulphides (mainly weathered to oxy-hydroxides and malachite), prehnite and titanite. Such mineral assemblages are similar to assemblages of hydrothermal upflow zones in the upper oceanic crust, reported from ophiolites (Haymon et al., 1989; Nehlig et al., 1994; Schiffman et al., 1987) and modern oceanic crust (Barker et al., 2010; Hayman and Karson, 2009, 2007; Saccocia and Gillis, 1995). Especially the occurrence of observed Cu-sulphides and their weathering products suggest a formation of these zones with metal-saturated fluids, which previously reacted with a substantial amount of rock. Presumably, the alteration occurred at relatively high temperatures

(~350 °C), where metal solubility in hydrothermal fluids is significantly increased (Seewald and Seyfried, 1990).

Alteration in both fluid-flow and fault zones is predominantly complete and most zones are fully recrystallised to secondary mineral assemblages either dominated by epidote ± quartz ± prehnite ± sulphides or zones where chlorite almost fully replaces primary minerals and is associated with variable amounts of epidote, titanite and sulphides. Such high degrees of alteration have been documented from other focussed upflow zones at high fluid-rock ratios and therefore it is suspected, that observed alteration within the presented fluid-flow and fault zones occurred at high fluid-rock ratios (Barker et al., 2010; Teagle and Alt, 2004)

Epidote measured in both fluid-flow zones and fault zones are overall Fe-richer compared to composition reported of epidote and zoisite veins from the lower crust in the ophiolite (Nehlig and Juteau, 1988b). Furthermore, they are more comparable to reported compositions from epidote co-existing with quartz and sulphides in the sheeted dyke complex of Wadi Haymiliya (Nehlig and Juteau, 1988b), and epidote from veins in the sheeted dykes of modern ocean crust (ODP Hole 1256D; Alt et al., 2010) , 504B; Laverne et al., 1995) as well as epidote reported from fossil upflow zones in the Hess Deep area (Gillis et al., 2001; Saccocia and Gillis, 1995). In contrast to Al-rich compositions, Fe-rich compositions indicate more oxidising conditions, often observed in a rather fluid-dominated than rock dominated system (Apted and Liou, 1983; Grapes and Hoskin, 2004; Liou et al., 1983).

Chlorite is the major constituent of chlorite-rich fault rocks but is also one of the main minerals present in both, epidote-rich fluid-flow zones and epidote-quartz fluid-flow zones and breccias. Three samples from the three different chlorite-rich fault rock have been studied and described in more detail. In all three fault zones chlorite grows as a replacement after primary mineral phases and co-exists with minerals precipitated directly from the fluid (e.g., epidote, sulphides). Microprobe analysis of chlorite from fault rocks in outcrop OM1523 and OM1609 reveal an overall Fe-richer composition compared to chlorite measured from pervasive background alteration observed in altered gabbro outside of fluid-flow and fault zones. Chlorite from fault zone in outcrop OM1605 shows a composition more similar to background alteration chlorite with only a slight trend toward more Fe-rich compositions. Fe-rich chlorite compositions have been described previously from hydrothermal discharge zones in the upper oceanic crust (e.g., Saccocia and Gillis, 1995) and were thought to be a key element in identifying zones of discharging hydrothermal fluids (e.g., Richards et al., 1989). However, a variety of processes contribute to chlorite composition and it was shown that Mg-rich chlorite may be stabilised if other Fe-rich phases (e.g., epidote, sulphides) precipitate, causing a decrease in the Fe/Mg ratio of the fluid

(Saccocia and Seyfried, 1994). Therefore, a more Mg-rich chlorite composition for fault rock of outcrop OM1605 may not be an indication of a different fluid composition but might indicate a co-precipitation of epidote, which is abundant in the zone.

Several studies report a decrease in Si^{iv} coupled with an increase of Al^{iv} in chlorites with increasing temperatures (Cathelineau, 1988; Cathelineau and Nieva, 1985; McDowell and Elders, 1980; Velde and Hillier S, 1991). This correlation was used to develop an empirical geothermometer of general applicability in diagenetic, hydrothermal and metamorphic settings (Cathelineau, 1988). It is based on the incorporation of Al^{iv} as exchange for Si^{iv}. This thermometer has been used previously to calculate formation temperature of chlorite in hydrothermal systems (e.g., Gillis et al., 2001; Laverne et al., 1995) and the cumulative error of this thermometer has been estimated to be ~ 50 °C (Laverne et al., 1995). However, several studies indicate the Al^{iv}-temperature correlation is likely to be influenced by the Fe/(Fe+Mg) ratio of the chlorite (Jowett, 1991; Kranidiotis and MacLean, 1987) and the thermometer of Cathelineau (1988) was extended by a correction factor to account for this influence (Jowett, 1991). Formation temperature of chlorite in all three fault rocks were calculated using the thermometer of Jowett (1991). The majority of chlorites from all three fault rocks show a consistent formation temperature of 300-350 °C, compared to a calculated temperature of chlorites observed in background alteration of relatively fresh layered gabbro.

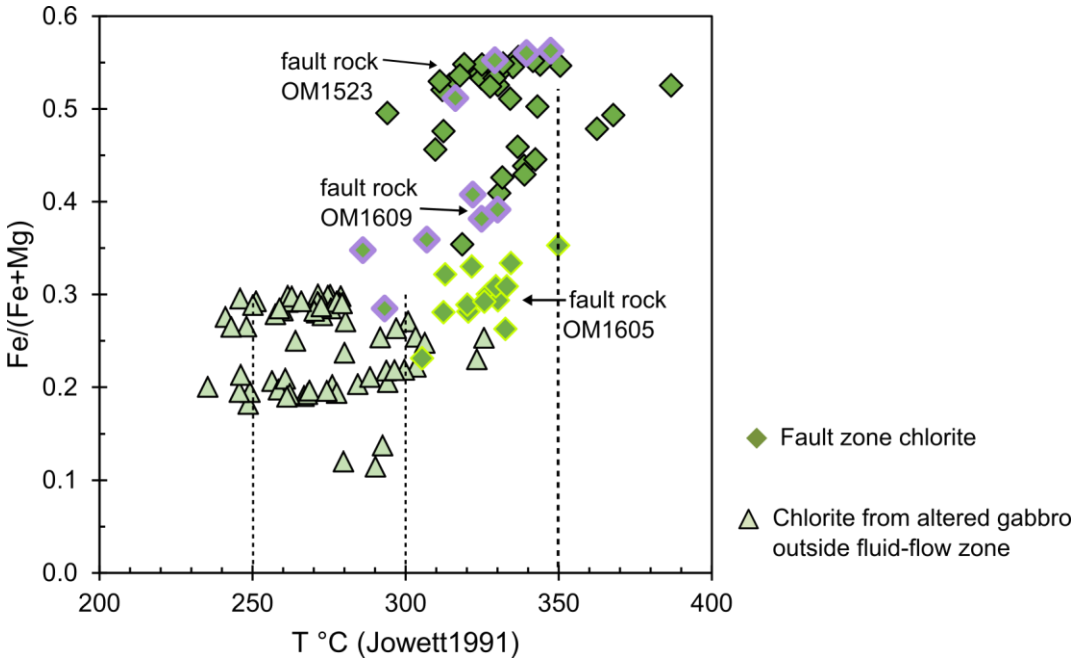

Figure 4.20: Estimated temperature for chlorite formation of fluid-flow and fault zone chlorite and chlorite of pervasive background alteration after the thermometer of Jowett (1991).

This indicates a formation of the fault rock, at temperatures roughly between 300-350 °C. The consistency in formation temperature between the three different fault zones, indicate that

similar formation conditions for all three fault zones are likely. However, the degree to which chlorite replaces primary mineral phases is variable in the three fault zones. Whereas in both fault rocks (OM1523 and OM1609) hardly any traces of primary magmatic minerals remain, chlorite in the fault zone in OM1605 only partially replaces the primary minerals. Clinopyroxene grains are preserved to some extent and hornblende as well as actinolite could be detected. The existence of hornblende and actinolite are interpreted to represent an earlier stage of hydrothermal alteration, pre-dating the formation of the fault rock. Partially preserved hornblende within the fault rock yield relatively high concentrations of Ti (Figure 4.14c, Appendix B.1) and using the semi-quantitative thermometer of Ernst and Liu (1998) show temperatures of 657±40 °C and 767±40 °C for both measured hornblende crystals of sample AL2 from fault rock chlorite of outcrop OM1605 (Appendix B.1). This clearly indicates an earlier alteration event at higher temperature.

Formation temperature for epidote + prehnite + chlorite ± sulphides fluid-flow zones and epidote + quartz + sulphide fluid-flow zones were not determined, although they can be roughly estimated from the stability field of epidote as well as from previous studies (Nehlig and Juteau, 1988a). The epidote stability in low pressure and mid-ocean ridge basaltic systems is estimated to be between 350-500 °C (McCollom and Shock, 1998) and has been confirmed by phase equilibria studies of low-grade mafic rocks (Liou et al., 1985). Fluid-inclusion studies on epidote-quartz veins from high-level gabbros sampled in Wadi Haymiliya indicate formation temperatures of 400-530 °C (Nehlig and Juteau, 1988a). This suggests that especially epidote-quartz fluid-flow zones might form at temperatures slightly higher than the chlorite-rich fault zones. To further constrain this, reliable temperature information from either quartz or epidote micro-thermometry on fluid-inclusions would need to be obtained.

4.7.3 Indications from Sr-isotope compositions

In the following paragraph Sr-isotope composition measured in the sheeted dyke and throughout the lower crust are being discussed and possible recharge and discharge mechanisms are evaluated.

4.7.3.1 Sr-isotope composition of the sheeted dyke complex

Whole rock Sr-isotope compositions of sheeted dykes from the Ibra area indicate $^{87}Sr/^{86}Sr$ ratios clearly shifted from fresh MORB compositions with a majority of them plotting in the same range as Sr-isotope compositions measured from epidosites (Davis, 2004) (Figure 4.18). Epidosites, equigranular and completely recrystallised epidote + quartz + titanite rocks, known from the sheeted dyke complex in ophiolites are thought to represent zones of discharging, hydrothermal

fluids (Harper et al., 1988; Nehlig et al., 1994; Richardson et al., 1987; Schiffman et al., 1987).This strongly indicates that fluid recharge was pervasive, and a near fluid-rock equilibrium was attained throughout the dykes, similar to what is reported from the Troodos ophiolite (Bickle and Teagle, 1992).

4.7.3.2 Sr-isotope composition of the lower crust including fluid-flow and fault zones

Strontium isotope composition of both, epidote mineral separates from fluid-flow samples as well as whole rock samples of fluid-flow and fault zones show a more radiogenic but restricted range of $^{87}Sr/^{86}Sr$=0.7043-0.7049, compared to fresh layered gabbro observed elsewhere in the ophiolite (e.g., Kawahata et al., 2001; Lanphere et al., 1981; McCulloch et al., 1980). This range is remarkably similar to epidosites sampled in the dyke complex (Davis, 2004) and the general composition of sheeted dykes from both the Ibra syncline area (Müller, 2016 and this study) and sheeted dykes observed all over the ophiolite (Davis, 2004; Kawahata et al., 2001; Lanphere et al., 1981). Taking this into account, measured Sr-isotope compositions of fluid-flow zones and fault zones clearly indicate an interaction with a seawater derived fluid and because of the similarity to Sr-isotope compositions of epidosites in the upper crust a formation of these zones as the result of an intense interaction with a discharging hydrothermal fluid is suggested.
There is no systematic decrease in the $^{87}Sr/^{86}Sr$ with depth of either epidote-mineral separates from fluid-flow zones and veins outside, nor whole rock from fluid-flow zones and fault zones. Therefore, it is likely that the fluid passing down from the sheeted dykes had the same composition as the fluid reaching the base of the crust. A similar observations has been made from Wadi Namarah, to the East of Wadi Gideah (Coogan et al., 2006). This ultimately leads to the question how this metasomatic front can be transported down to the base of the crust without changing its composition significantly and consequently, how recharge works.

4.7.3.3 Fluid-recharge in the lower crust

Unlike observed in the dyke complex of the Samail ophiolite as well as the dyke complex in Cyprus, where recharge is pervasive and a near fluid-rock equilibrium was attained throughout the dykes (Bickle and Teagle, 1992), recharge in the lower crust is likely to be dominantly channelled. There are two arguments for this: (i) First of all, if fluid recharge would happen pervasively, mainly along grain boundaries and small fractures, fluid-flow would occur at very low fluid-rock ratios and hence, the Sr-isotope signature of the hydrothermal fluid would be in equilibrium with the rock. This would lead to an isotopic signature of the hydrothermal fluid at the base of the crust of magmatic values, roughly around $^{87}Sr/^{86}Sr$ ~0.7028 – 0.7030 (White et al., 1987). Therefore, secondary minerals precipitated from upwelling hydrothermal fluid, such as epidote, should yield values of roughly $^{87}Sr/^{86}Sr$ ~0.7028 – 0.7030 (White et al., 1987). But in

contrary to that, values of $^{87}Sr/^{86}Sr$ ~0.7043 – 0.7049, similar to values observed in the sheeted dykes, are observed down to the base of the crust. (ii) If fluid recharge would happen pervasively at relatively high fluid-rock ratios, fresh layered gabbro outside of fault- and fluid-flow zones would yield Sr-isotopic compositions similar to that of the hydrothermal fluid, clearly elevated from fresh magmatic values. And even though there are elevated Sr-isotope compositions observed throughout the lower crust in the Oman ophiolite (Kawahata et al., 2001b; Müller, 2016), indicating a partial exchange of the rock with a hydrothermal fluid, they are not as high as the composition of the hydrothermal fluid itself.

Therefore, it is likely that a significant portion of the fluid recharge in the lower crust occurs along channels, in order to bring down fluid to the base of the crust without much fluid-rock interaction and to explain Sr-isotope compositions similar to compositions observed in the sheeted dykes. Fault zones and other zones of high permeability can serve as such channels. A likely possibility is that recharge and discharge happens along the same fluid-pathways. Evidence for this has been shown by a study of focussed fluid flow zones by Coogan et al. (2006) where temperatures of > 800 °C and down to < 300 °C have been observed within one zone and therefore a continuous alteration from high- to low temperature is inferred.

4.7.3.4 Re-use of existing fluid pathways?

Also the observation of high-temperature hornblende within one of the chlorite-rich fault rocks indicate that the pathway of the fault zone was used previously and at higher temperature. However, estimating to which degree and at which conditions (other than a temperature estimation) this pathway was used previously, and whether it served as a channel for recharging fluid, is currently not possible.

Nonetheless, the fact that hydrothermal circulation operates via existing pathways has been proposed previously (Coogan et al., 2006; Nehlig and Juteau, 1988b; Stakes and Vanko, 1986; Wolff, 2014). Furthermore, observations made in several outcrops (e.g., Figure 4.6f) indicate that early amphibole veins were re-filled in a second stage with either epidote or clinozoisite or both.

4.7.4 Frequency of observed fluid-flow and fault zones

Field observations along Wadi Gideah reveal that the described fluid-flow and fault zone occur approximately every 1 km (Figure 4.1). From the Moho transition zone up to the transition of the foliated to the high-level gabbros four outcrops with major fluid-flow or fault zones were observed and presented in this thesis. In between these major outcrops there are numerous smaller outcrops, mainly characterised by a high-vein density but large fluid-flow zones or fault zones are absent. A similar spacing of zones with focussed fluid flow has been proposed by

Coogan et al. (2006), in Wadi Namarah, to the east of Wadi Gideah and Wadi Abyad in the Rustaq massif, north of Wadi Tayin. They used with a combination of field observations and the distribution of photo-lineaments on aerial photos which are interpreted as traces of faults. However, it is almost impossible to quantify the spacing and the distribution of fault- and fluid-flow zones accurately, despite great exposure of rocks in the area. It is likely that fault- and fluid-flow zones are more susceptible to erosion and therefore not exposed. A further limiting factor is that the studied section here does not give any constraints on the lateral frequency of the fluid-flow and fault zones. Wadi Gideah valley cuts across the section from the Moho transition zone up to the sheeted dykes but lateral information are missing. To further constrain this lateral spacing, more detail field investigations to the east and west of Wadi Gideah are required.

4.8 Conclusions

Within this chapter hydrothermal fluid-flow and fault zones throughout the lower oceanic crust are characterised and discussed. The following conclusions can be drawn:

Fluid-flow zones as well as fault zones predominantly show orientations parallel to earlier amphibole veins and orientation parallel to sub-parallel to the orientation of the sheeted dykes in the Ibra area. This indicates a formation of hydrothermal veins, fluid-flow and fault zones within the same stress-field as the sheeted dykes and a formation during the initial spreading of the ocean crust is considered as likely.

Fluid-flow and fault zones are fully recrystallised under greenschist-facies conditions. Fluid-flow zones display a secondary mineral assemblage of epidote + chlorite ± quartz ± prehnite ± sulphides. Quartz-rich assemblages were mainly observed in the upper part of the lower crust. Fault zones are characterised by a mineral assemblage of chlorite + epidote ± sulphides. Epidote measured from fluid-flow and fault zones show relatively Fe-rich compositions. Such Fe-rich compositions are reported from the sheeted dykes of ophiolites and modern ocean crust, whereas epidote compositions reported from the lower crust in the Samail ophiolite are generally more Al-rich.

Microprobe analysis of chlorite of all three fault zones throughout Wadi Gideah reveal comparable compositions between chlorite of the different fault zones but distinct compositions when compared to chlorite observed in more pervasive background alteration. Fault-rock chlorite is slightly to considerably more Fe-rich than chlorite observed in more pervasive background alteration. The semi-quantitative thermometer of Jowett (1991) was used to calculate formation temperatures of chlorite. A temperature range of 300-350 °C was estimated for chlorite formation in all three fault zones.

Sr-isotope compositions of whole rock and mineral separates from fluid-flow zones and fault zones show Sr-isotope compositions of $^{87}Sr/^{86}Sr$=0.7043-0.7049. These compositions are more radiogenic than fresh layered gabbro from the Samail ophiolite and remarkably similar to Sr-isotope compositions measured from epidosites in the sheeted dyke complex and composition of the sheeted dykes in general. This indicates alteration with a hydrothermal fluid similar in composition to a fluid altering the compositions of the sheeted dykes. No systematic decrease in the $^{87}Sr/^{86}Sr$ composition with depth of either epidote mineral separates from the fluid-flow zones and veins outside, nor from whole rock from fluid-flow and fault zones could be observed. In order to transport this metasomatic front down to the base of the crust, a channelled recharge is regarded as likely.

Recharge and discharge of hydrothermal fluids within the lower oceanic crust may occur along the same pathways. Indications supporting this assumption were found within one chlorite-rich fault rock sample. Hornblende, partially overgrown by chlorite, found within one chlorite-rich fault rock displays formation temperatures of 650-760 °C and indicates that a previous, higher temperature alteration occurred along this fluid-pathway.

Chapter 5 Hydrothermal fault zones in the lower oceanic crust: An example from Wadi Gideah, Samail ophiolite, Oman

Abstract

Hydrothermal circulation is a key process for chemical and isotopic exchange between the solid Earth and oceans, and for the extraction of heat from newly accreted crust at mid-ocean ridges. However, due to a dearth of samples from intact oceanic crust, or continuous sample suites from ophiolites, there remain major shortcomings in our understanding of hydrothermal circulation in the oceanic crust, especially in the lower plutonic crust. In particular, it remains unknown whether fluid recharge and discharge occurs pervasively or if it is mainly channelled within discrete zones such as faults.

Here, we describe a hydrothermally-altered fault zone that crops out in the Wadi Gideah in the layered gabbro section of the Samail ophiolite of Oman. A one metre wide normal fault comprising deformed chlorite ± epidote fault rock with disseminated chalcopyrite and pyrite, offsets gently dipping layered olivine gabbros. The chlorite-rich fault rocks surround strongly altered clasts of layered gabbro, 50 to 80 cm in size. Layered gabbros in the hanging wall and the footwall are partially altered and pervasively veined by epidote, prehnite, laumontite and calcite. In the wall rocks, igneous plagioclase ($An_{82\pm2\%}$) is partially altered towards more albitic compositions ($An_{75\text{-}81}$), and chlorite + tremolite partially replaces plagioclase and clinopyroxene. Clinopyroxene is moderately overgrown by Mg-hornblende.

Whole rock mass change calculations show that the chlorite-rich fault rocks are enriched in Fe, Mn, H_2O+CO_2, Co, Cu, Zn, Ba, and U, but have lost significant amounts of Si, Ca, Na, Cr, Ni, Rb, Sr, Cs, light rare earth elements (LREE), Eu, and Pb. Gabbro clasts within the fault zone as well as altered rock from the immediate hanging wall show enrichments in Na, volatiles, Sr, Ba and U and depletions of Si, Ti, Al, Fe, Mn, Mg, Ca, Cu, Zn, Rb, Cs, LREE, and Pb. Chlorite thermometry suggests a formation temperature of 300-350 °C for the fault rock and based on the Si loss and solubility of silica in hydrothermal fluids the intensity of alteration requires a fluid to rock ratio of up to 900:1. Strontium isotope whole rock data of the chlorite-rich fault rock yield $^{87}Sr/^{86}Sr$ ratios of 0.7043-0.7048, which is considerably more radiogenic than fresh layered gabbro from this locality ($^{87}Sr/^{86}Sr$ = 0.7030 – 0.7033), and similar to black smoker hydrothermal signatures based on epidote, measured from epidote veins in the footwall and elsewhere in the ophiolite

($^{87}Sr/^{86}Sr$ = 0.7043-0.7051). Altered gabbro clasts within the fault zone show similar values with $^{87}Sr/^{86}Sr$ ratios of ~ 0.7045 – 0.7050. In contrast, the hanging and footwall gabbros display values only slightly more radiogenic than fresh layered gabbro. The elevated strontium isotope composition of the fault rock and clasts together with the observed secondary mineral assemblages and calculated mass changes strongly supports the intense interaction with seawater-derived up-welling hydrothermal fluids, active during oceanic spreading. Assuming that such a fault zone is globally representative of faulting in the lower crust, an extrapolation of our results from mass change calculations to elemental fluxes, shows a significant contribution to the global hydrothermal budgets of Si, Ti, Fe, Mn, Mg, Ca, H_2O, Cu, Zn, Sr and Cs.

5.1 Introduction

Hydrothermal circulation throughout the oceanic crust is a fundamental process resulting in the exchange of chemical elements between the oceans and the solid Earth (Palmer and Edmond, 1989) as well as for extraction of heat from newly formed crust at mid-ocean ridges (Morton and Sleep, 1985; Sleep, 1991). Hydrothermal fluid flow permeating the upper part of the oceanic crust is widely accepted for playing a vital role in cooling young crust at mid-ocean ridges. However, to date there remain major shortcomings in our understanding of the geometry and intensity of the deep circulation of seawater-derived hydrothermal fluids extending into the lower plutonic rocks of the ocean crust. In particular, the effectiveness of hydrothermal circulation in removing latent heat from the crystallizing magmas is not clear. There remain two, now long-standing, end-member conceptual models of how oceanic crust is accreted: The gabbro glacier model (e.g., Henstock et al., 1993; Morgan and Chen, 1993; Quick and Denlinger, 1993) and the sheeted sills model (e.g., Kelemen et al., 1997; MacLeod and Yaouancq, 2000), although hybrid models are also proposed (e.g., Boudier et al., 1996). The gabbro glacier model proposes the cooling of magma exclusively in a shallow melt lens and the formation of the lower crust by subsidence and downward flow of a crystal mush. In contrast, the sheeted sills model requires that substantial hydrothermal heat extraction occurs deep within the plutonic crust to remove latent heat and allow in-situ crystallization. Thermal models (Chen, 2001; Maclennan et al., 2004; Theissen-Krah et al., 2016) suggest a mix between both end-member models is most likely but the proportion of crust crystallizing in-situ remains unclear. Cooling rate estimates derived from studies of Ca diffusion in olivine in the lower crust of the Samail ophiolite yield contrasting results as to whether the crust was cooled purely conductively or via hydrothermal circulation. Although data presented by Coogan et al. (2002) favours near conductive cooling, VanTongeren et al. (2008) suggest that hydrothermal circulation is likely to have extended to the base of the crust. Near conductive cooling in the upper plutonic section of the East Pacific Rise was also inferred from

rate estimates based upon Mg in plagioclase (Faak et al., 2015) and from a combined Mg in plagioclase and Ca in olivine cooling rate study of gabbros from Hess Deep (Faak and Gillis, 2016). However, Mg and REE bulk diffusion between co-existing plagioclase and pyroxene in gabbros from the East Pacific Rise and Hess Deep (Sun and Lissenberg 2018) and coupled thermal modelling (Hasenclever et al., 2014) strongly support deep hydrothermal circulation. Due to insufficient observations of intact lower ocean crust it is poorly refined whether the circulation and cooling occurs via pervasive fluid flow along grain boundaries and vein networks or is focussed along major structures such as faults. Millimetre-scale amphibole vein networks are common in the lower gabbros of the ocean crust, and formed at near magmatic temperatures (Bosch et al., 2004; Coogan et al., 2007; Manning et al., 2000, 1996; Nicolas et al., 2003) but it is not clear if these features provide sufficient permeability to allow vigorous enough hydrothermal circulation to extract significant heat (Coogan et al., 2007; Manning et al., 2000, 1996). An alternative mechanism is to remove heat from the lower crust via more discrete, widely spaced regions of focussed fluid flow and discontinuous zones that preserve hydrothermal assemblages of high-temperature (~880 °C) to lower greenschist facies (< 300 °C) alteration, observed every ~1 km throughout the crust in the Samail ophiolite in Oman. Enhanced cooling rates are indicated in the surrounding crust of such focussed fluid flow zones (Coogan et al. 2006).

Here we present detailed field, petrographic and geochemical observations of a hydrothermal fault zone located within the lower layered gabbro section of the Samail ophiolite in Oman, approximately 6 km below the paleo-seafloor and 1 km above the Moho transition zone (MTZ). We document the characteristics of a hydrothermal system deep in the crust which is so far only known from shallow hydrothermal environments and show that this fault provided a pathway for focussed hydrothermal discharge, giving evidence that hydrothermal activity was effective in mining heat from the plutonic section. Our primary aim of this study is to discuss the nature of the hydrothermal environment and to quantify elemental changes occurring within the fault zone itself and the alteration halo during intense hydrothermal alteration. Finally, we provide first estimates on the contribution of such a fault zone to the global chemical cycle.

5.2 Geological Overview

5.2.1 The Samail ophiolite

The Samail ophiolite is widely regarded as the best analogue of fast-spreading oceanic crust preserved on land (e.g., Nicolas et al., 2000), and stretches approximately 550 km in length and 50 km in width along the coast of the Sultanate of Oman and the United Arab Emirates (UAE). The ophiolite is divided into several massifs (Figure 5.1) and shows the complete “Penrose” sequence

of rock types expected to be formed at a fast spreading mid-ocean ridge, from extrusive lavas, sheeted dykes, gabbros, layered gabbros and cumulate ultramafic rocks through the crust-mantle transition zone into the mantle sequence comprising harzburgite and locally dunite.

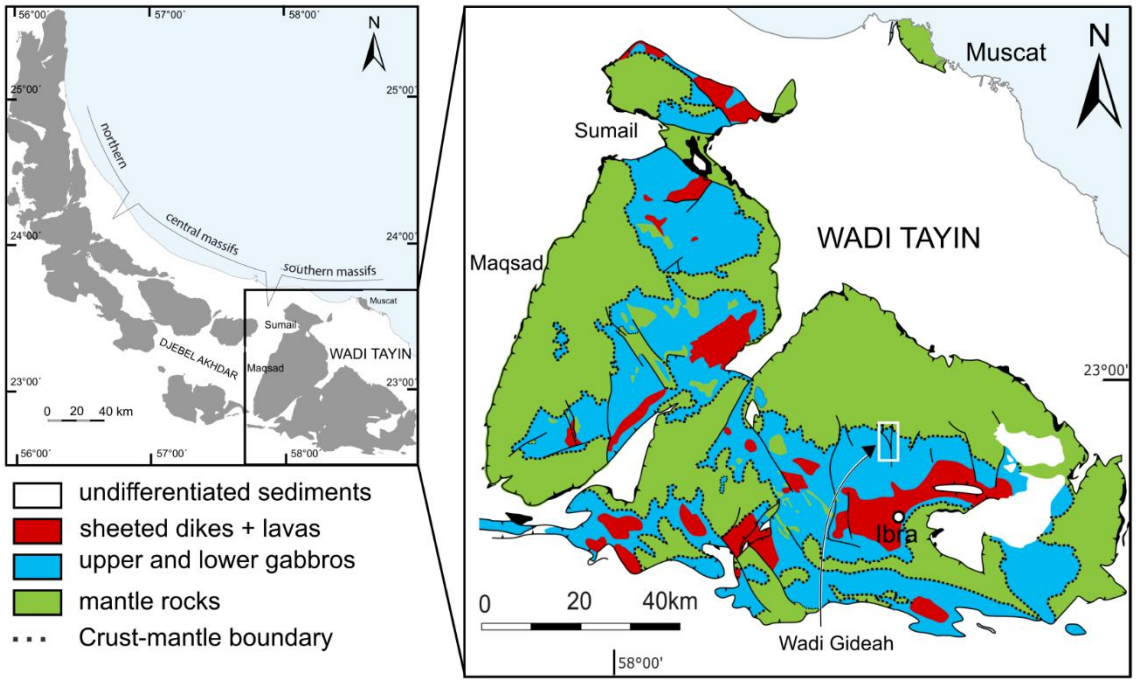

Figure 5.1: (a) Overview of the Samail ophiolite and (b) Wadi Tayin massif. Wadi Gideah is located approximately 20 km north of the town of Ibra. Map modified after Nicolas et al. (2000).

The ophiolite was formed in a spreading centre in the Neotethyan ocean during the Late Cretaceous (Searle and Cox, 1999). Late stage intrusive plagiogranitic bodies within the gabbro section yield ages of 97 to 93 Ma (Rioux et al., 2013) and mark the formation age of the crustal rocks within the ophiolite. There remains ongoing debate as to whether the Samail ophiolite formed at a mid-ocean ridge (MOR) in a major ocean basin or some form of supra-subduction zone setting (SSZ; e.g., Alabaster et al., 1982; Boudier and Nicolas, 2007; Warren et al., 2007, 2005). Most evidence points to the partial influence of a subduction zone (e.g., Godard et al., 2003; Goodenough et al., 2014; Koepke et al., 2009; MacLeod et al., 2013). Although not completely absent, there is general consensus that the subduction zone influence is less pronounced in the southern part of the Samail ophiolite. Second stage magmatic intrusions are limited to minor intrusions in the mantle and V2 lavas are mostly absent (e.g., Godard et al., 2003; MacLeod et al., 2013). Consequently, the lower crustal rocks exposed in the Wadi Tayin block of the ophiolite are an ideal location to investigate processes that occur during the accretion of the lower crust at fast spreading mid-ocean ridges.

5.2.2 The fault zone outcrop in Wadi Gideah

The studied fault zone is located in Wadi Gideah (22.894 °N, 58.516 °E), about 15 km north of Ibra, in the crustal section of the Wadi Tayin massif. Wadi Gideah is situated to the west of Wadi Qafifah and Waid Khadir and to the east of Wadi Saq, Wadis where classic structural, petrographic and isotope geochemical observations on accretion of the crustal section of the ophiolite were made (Hopson et al., 1981; Pallister, 1981; Pallister and Knight, 1981), including oxygen- and strontium isotope studies (Gregory and Taylor, 1981; Lanphere et al., 1981). The north to south oriented Gideah valley cuts through a coherent series of lower oceanic crust and upper mantle rocks, exposing lithologies from the Moho transition zone up to the sheeted dyke complex (Pallister and Hopson, 1981). Layered gabbros are the primary rock type and are exposed for ~6.5 km along the length of the valley. The magmatic layering of the gabbros dips ~28 ° to the south indicating a true thickness of ~3 km for the layered gabbro series. These rocks are overlain by foliated gabbros and isotropic high-level gabbros. Sheeted dykes are mostly eroded and are only exposed in small hills at the valley entrance and further out towards the Ibra syncline (Figure 5.2). The Wadi Gideah area has been extensively sampled, and major rock types are well characterised in terms of their petrographic and geochemical properties (France et al., 2009; Haase et al., 2016; Müller, 2016; Müller et al., 2017), including sulphur isotopes (Oeser et al., 2012).

Throughout the valley, from the layered gabbros up to the sheeted dykes, there are sub-vertical chlorite-rich zones, decimetres to metres-thick. They consist of dark green, weakly foliated, chlorite-rich rocks with the surrounding wall rock gabbros heavily altered for metres or up to tens of metres (Fig.4.2a). Field observations indicate that they occur every 1-2 km, either as isolated features or as part of a more extensively altered zone, similar to what has been described as a focussed fluid flow zone by Coogan et al. (2006). The zone investigated here consists of a chlorite-rich rock surrounded by heavily altered wall rock gabbro but in contrast to other observed zones it clearly crops out as a fault, making it unique. It is located within the layered gabbro section, approximately 1 km above the Moho transition zone (Figure 5.2). A second fault zone is located about 40 metres to the east (Figure 5.3a). Approximately 500 m towards south-east along strike of this fault zone outcrop, on the southern flank of a small ridge, partially to completely altered, gabbros crop out along the edge of the wadi terrace giving evidence for the continuity of this feature (Figure 5.2b).

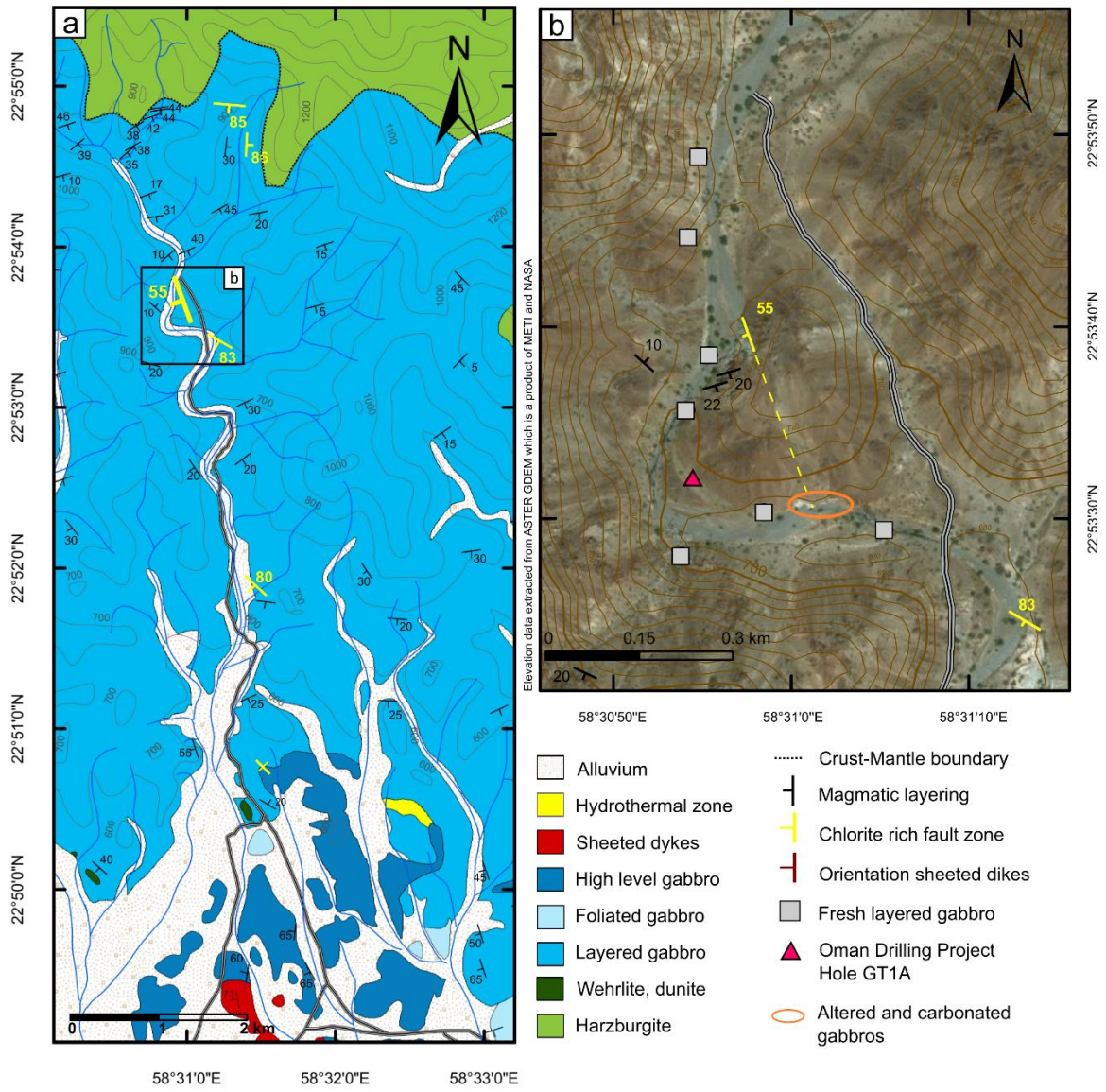

Figure 5.2: (a) Geological map of Wadi Gideah modified after Peters et al. (2008). Wadi Gideah cuts through a coherent series of oceanic crustal rock from the Moho transition zone up to the layered gabbros, foliated gabbros, high-level gabbros, and the sheeted dykes. The magmatic layering dips on average 28° S in the upper part of the valley. Approximately orthogonal to the layering, steeply oriented chlorite-rich zones were mapped with a spacing of 1-2 km throughout the whole valley. The chlorite-rich fault zone investigated here is located about 1 km above the Moho. (b) Overview of the area around the chlorite-rich fault zone (displayed in yellow). Locations of layered gabbro samples are shown in light grey squares and the location of the ICDP Oman Drilling Project Hole GT-1A is displayed with a red triangle.

The fault zone is a normal fault, approximately one metre wide (including fault rock and altered gabbroic clasts, Figure 5.3b) and is lateraly continuous on the surface over a length of eight metres. Its orientation of 251/55° (dip direction/dip) is sub-orthogonal to the magmatic layering (154/38°) nearby and sub-parallel to the mean strike of the sheeted dykes in this area (261/71°; Pallister, 1981), although dykes generally dip more steeply (on average 71°). The fault rock consists of a foliated Cu-sulphide-bearing dark greenish to blackish chlorite-rich rock that anastomoses around angular to lensoidal clasts (up to 50-80 cm) of altered gabbro. The hanging wall and footwall gabbros are altered and heavily veined by epidote, prehnite, laumontite and carbonate veins for 2.5 - 3 metres. The layered gabbro in the hanging wall is partially altered for about 30 m, manifested in a general bleaching of the rocks (Figure 5.3b). The size of this halo was estimated in the field and has been confirmed on aerial photographs. A less intense halo extends only about 1 m into the footwall. Representative samples of the fault-rocks, clasts and surrounding altered wall rocks were collected during fieldwork in 2015 and 2016. These samples are compared with relatively fresh layered gabbro samples, collected within < 500 m distance of the outcrop (Figure 5.2b; Mueller et al., 2017).

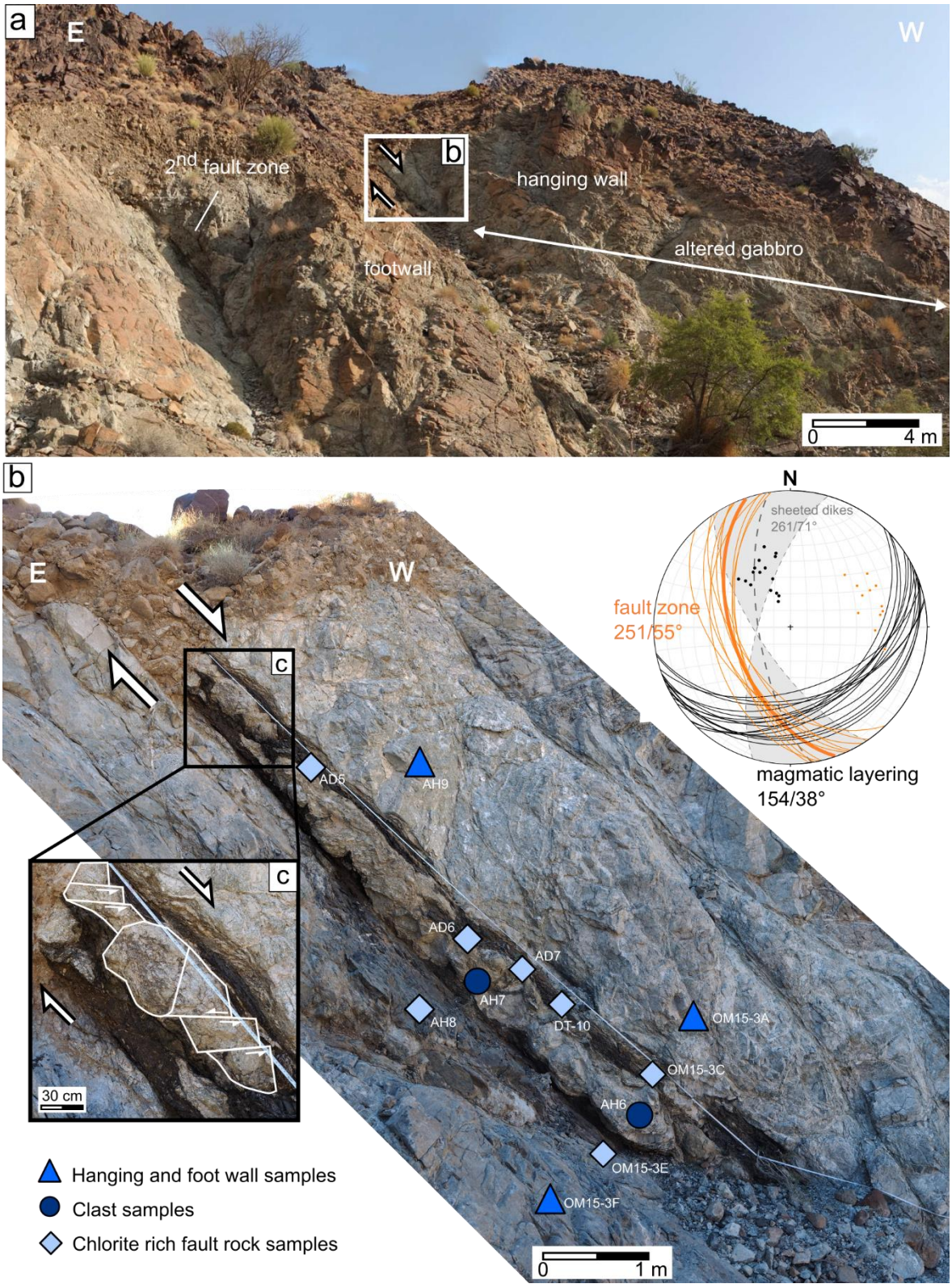

Figure 5.3: Overview and zoon-in of the fault zone outcrop (a) Overview photo of the fault zone area. Note a second chlorite-rich fault zone is located to the East. Especially in the hanging wall, the gabbros are intensely altered. Not that not the entire alteration halo is visible on this photograph. (b) A detailed overview of the fault zone. Sample locations are marked; chlorite-rich fault zone (light blue diamonds), clasts (dark blue circles), hanging wall and footwall (royal blue triangles). The stereographic projection

shows the orientation of the fault zone relative to the orientation of the magmatic layering around the fault zone and the upper part of the valley as well as the orientation of sheeted dykes (Pallister, 1981). (c) Expanded view of part of the fault zone in which a shear sense could be inferred based on domino-type fracturing of the clasts, indicating a normal fault by top to the left.

5.3 Analytical techniques

Sample preparation and analytical techniques are described in detail in Chapter 2, and are summarised here.

Polished thin sections were prepared from all samples. Minerals were identified using optical microscopy as well as a Carl Zeiss Leo1450VP Scanning Electron Microscope (SEM), at the University of Southampton, equipped with an Oxford Instruments EDS detector coupled to the Aztec Energy software system. Major element compositions of most minerals were analysed by electron probe microanalysis (EPMA) at the University of Kiel using a JEOL JXA 8900 R EMP. Compositions of chlorite, epidote and sulphides in the chlorite-rich fault rock were measured at the Leibniz University in Hannover in Germany using a Cameca SX100 EMPA. Analytical conditions are described in Chapter 2.5 and precision and accuracy are reported in Table 2.2.

Whole rock samples were prepared for geochemical analysis at the University of Southampton following the procedures outlined in Chapter 2 section 2.6 and 2.8. Major and trace element (V, Cr, Co, Ni, Cu, Zn, Rb, Sr, Y, Zr, Nb, Cs, Ba, La and Ce) concentrations were analysed by X-ray fluorescence (XRF) using a Spectro XEPOS_HE Energy Dispersive Polarised X-ray Fluorescence (EDPXRF) Analyser at the University of St. Andrews. The detailed measurement protocol as well as precision and accuracy are outlined in section 2.9. Four samples were analysed at the University of Hamburg, using a PanAnalytical MagixPro X-ray fluorescence spectrometer and following the procedure of Vogel and Kuipers (1987).
Trace element concentrations were measured by Inductively Coupled Plasma Mass-Spectrometry (ICP-MS) at the University of Southampton using a Thermo X-series II ICP-MS. Precision and accuracy were better than ± 5% RSD and ± 4% RMSD respectively for the majority of the elements (Table 2.4 and 2.5).

Major and trace elements of four fault zone samples and the eight background gabbros (Appendix C.2) were analysed at Kiel University. All samples were prepared following the protocol outlined in section 2.12. Major elements were analysed using a Spectro CIROS SOP ICP-OES. Because SiO_2 cannot be analysed after digestion procedures including hydrofluoric acid it was calculated to 100% oxides with due regard to loss on ignition. Analytical precision was found to be better than

0.5-1 % (Table 2.6). Minor and trace element mass fractions were determined using an AGILENT 7500cs with (Be, In, Re) internal standardisation. The analytical precision is typically better than 0.5-2 %RSD (1SD) for all elements analysed (Table 2.6).
Most trace elements were analysed by LA-ICP-MS on nano-particulate pressed powder pellets (NPP). Analysis were performed using a 193 nm ArF excimer laser ablation system (GeoLasPro, Coherent) coupled to an Agilent 7500s ICP-MS, detailed in section 2.12 of Chapter 2 and in Garbe-Schönberg and Müller (2014). Analytical precision was better than 1-5 %RSD (1SD) for all elements analysed at concentrations > 10x LOD (Table 2.6).

Strontium isotope composition were measured by Thermal Ionization Mass-Spectroscopy (TIMS), following the procedure outlined in Chapter 2. All samples were leached with 10% analytical grade acetic acid prior to digestion to remove secondary calcium carbonate. Strontium was separated from dissolved samples using Strontium spec^{TM} columns (for details see Harris et al., 2015) and analysed using a ThermoFisher Scientific TritonPlus TIMS. Strontium standard NBS987 was measured as an external standard. Throughout the analytical period the mean value of NBS987 (n=25) was $^{87}Sr/^{86}Sr$ =0.710241 ± 0.000018 (2SD). Internal precision was monitored by measuring 150 ratios per sample and the error of each measurement is reported as the two standard error (2SE).

5.4 Petrography

5.4.1 Fresh layered gabbro

Eight samples of fresh layered gabbro within 500 m of the fault zone outcrop were taken to provide background reference samples. These samples are a subset of a larger suite of rocks focussing on a reference section through the lower oceanic crust of fast-spreading ridges in the Wadi Gideah (Mueller et al., 2017). These olivine-bearing to olivine gabbros are fine to medium grained and consist of 50% plagioclase, 40% clinopyroxene and 10% olivine. Orthopyroxene is absent. The original magmatic assemblage is mostly preserved although in some rocks hornblende and actinolite partially overgrow clinopyroxene. Primary oxides are rare. Igneous plagioclase is partially altered to more albitic compositions. Where clinopyroxenes are in contact with plagioclase, chlorite is developed along some grain boundaries and fractures, commonly with secondary oxides (Figure 5.4a, b). Olivine is heavily fractured, serpentinised and partially forms iddingsite, but cores are mostly unaltered. Total alteration is typically less than 5 to 10 vol. %.

5.4.2 Footwall and hanging wall

The footwall sample (OM15-3F) is relatively fresh compared to the other fault zone-related samples, showing alteration of 30 - 40%. The style of alteration is similar to that in the background gabbros. The formation of chlorite after plagioclase and clinopyroxene as well as actinolite + tremolite after clinopyroxene mostly occurs along grain boundaries. Fresh olivine is rare. Cores of clinopyroxenes are preserved although they are heavily traversed by a dense networks of fractures which is accompanied by secondary oxides and sub-microscopic alteration phases growing into fresh crystals. Plagioclase shows yellowish to light-brownish shading. A fracture related overprint is also present in plagioclase but this is not as strong as for clinopyroxene (Figure 5.4c, d).

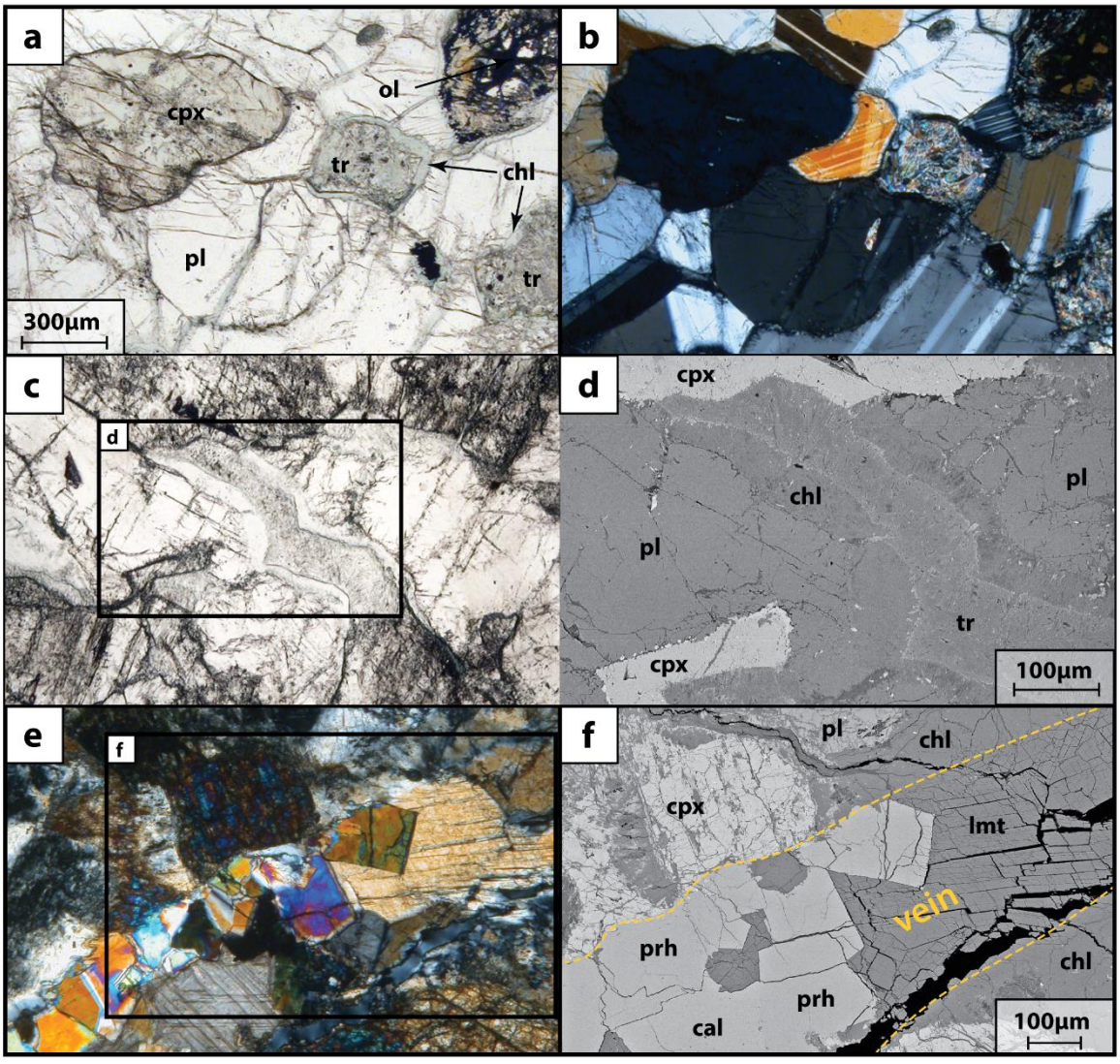

Figure 5.4: Thin section photomicrographs of typical alteration pattern. (a) Background gabbro in plane-polarised light. Clinopyroxene is partially replaced by tremolite. Intact crystals

show the formation of secondary oxides and partial overgrow of microcrystalline alteration phases. Plagioclase is well preserved, the formation of chlorite is focussed to grain boundaries. Olivine is heavily fractured and serpentinized, partially decomposed into iddingsite and opaque oxides, cores are mostly preserved. (b) Same area in cross-polarised light, revealing the mostly anhedral granular structure of tremolite and polysynthetic twinning of plagioclase. Note the microcrystalline chlorite at grain boundaries of plagioclase. (c & d) Plane polarised micrograph and BSE image of typical alteration within the footwall following the same systematics as for the background gabbros but forming veinlets by dissolving the magmatic phases. Pervasive disaggregation of clinopyroxene is more advanced. (e) Prehnite-laumontite vein through heavily altered gabbro of the hanging wall, in cross-polarised light. The magmatic assemblage is almost entirely replaced by pervasive fracturing-initiated alteration. The rock is intensely crosscut by a dense network of veins. Secondary phases, e.g., prehnite are well crystallised and intergrown with laumontite. (f) BSE image, details of a late vein, euhedral prehnite associated with laumontite and calcite. pl – plagioclase, cpx – clinopyroxene, ol – olivine, tr – tremolite, chl – chlorite, prh – prehnite, lmt – laumontite, cal – calcite.

The alteration intensity for the two hanging wall samples (AH9, OM15-3A; Figure 5.4e, f) ranges between 50 – 80 % with the initial magmatic texture and mineralogy being only partially preserved. Clinopyroxenes have a “rusty” appearance with corroded grain boundaries and abundant fractures and are commonly replaced by sub-micron to micron scale brown to green hornblende blades and tremolite/actinolite needles. More altered clinopyroxenes show coronas of chlorite ± tremolite when in contact with plagioclase. Plagioclases are more altered than clinopyroxenes, showing abundant fractures and partial replacement by fine-grained chlorite. Fresh olivine is absent. There are abundant veins in the hanging wall samples ranging from < 10 µm to 1 mm width. Prehnite and prehnite-laumontite veins cross-cut earlier alteration phases and are being cross-cut by later laumontite-calcite veins (Figure 5.4e, f).

5.4.3 Clasts

The two clast samples (AH6, AH7) from the central part of the fault rock display variable degrees of alteration. Sample AH6 has a very similar alteration assemblage and intensity to the hanging wall samples but includes two (<1 mm) veinlets of brown hornblende, possibly formed during higher temperature (> 500 °C) hydrothermal alteration (Manning et al., 2000). Laumontite veins (<1 mm) cross-cut earlier alteration and are themselves cross-cut by later calcite veins. Late stage calcite also fills small open spaces (< 30 µm) between mineral grains, and appears to be the last

alteration phase. In contrast, sample AH7 is almost completely altered with abundant calcite (40 %). Epidote partially replaces plagioclase and clinopyroxene. Clinopyroxene is mostly overgrown by green hornblende, actinolite/tremolite and chlorite. As a whole, the sample is brecciated and cemented by calcite, with prominent calcite veins (~ 1mm) cross-cutting earlier alteration phases and veins.

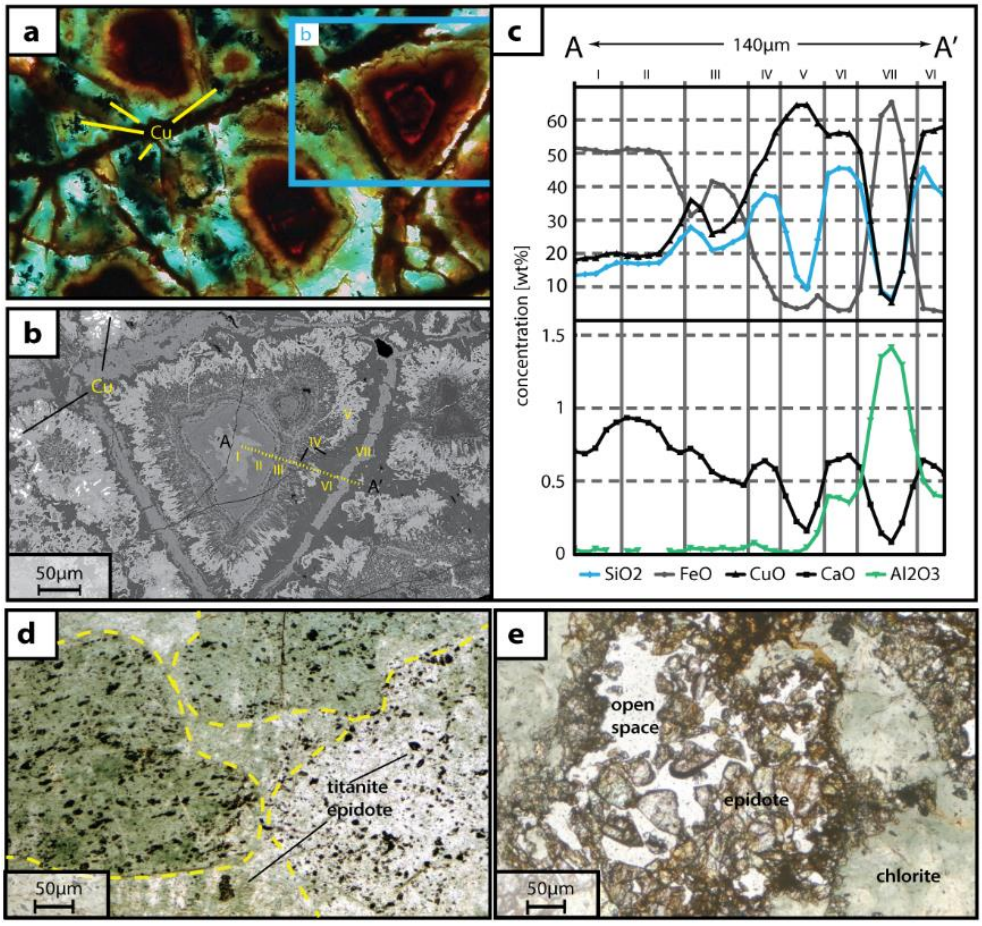

Figure 5.5: Thin section photomicrographs of fault rock samples. (a) Chlorite-rich fault rock in plane polarised light showing concentrically zoned alteration pattern of semi-opaque to opaque phases. Note the solid Cu grains. (b) BSE micrograph of concentrically layered alteration revealing the complexity of zoning. (c) Major element composition along a profile from A to A'. Concentrically zoned phases show variable contents of CuO, FeO and SiO_2. Zones are numbered according to (b) No primary phases are preserved. (d) Chlorite replacing magmatic minerals completely but outlines of former mineral grains are still visible (yellow dotted lines). Chlorite is associated with fine-grained granular (< 20 µm) titanite and epidote. (e) Euhedral epidote crystals precipitated directly out of a hydrothermal fluid into open space. Associated chlorite is clean and does not co-exist with granular titanite and epidote, suggesting

precipitation from hydrothermal fluid rather than replacement of primary minerals as shown in (d).

5.4.4 Chlorite-rich fault rock

Seven samples (AD5, AD6, AD7, DT-10, AH8, OM15-3C and OM15-3E) of the chlorite-fault rock have been analysed by thin section petrography. For all these samples the alteration intensity is close to 100%. The major constituents are chlorite (60 – 80 %), epidote (5 – 15 %), titanite (< 5 %), chalcopyrite and pyrite (< 5 %) and native copper (< 1 %). Moreover, most samples contain weathering products of sulphides such as iron-oxyhydroxides (5 – 10%), malachite (5%) as well as calcite (5 - 10 %). In mineralised samples, layered fine-grained, concentric zonations (Figure 5.5a, b) with variable contents of SiO_2, CuO and FeO (Figure 5.5c) are common. Sample DT-10 is dominated by weathering products and consists mainly of iron-hydroxides (65 %) and malachite (25 %) with chlorite (10 %) as a subordinate phase. Thin section petrography reveals the complete replacement of the original igneous minerals but a relict igneous texture is still visible (Figure 5.5d). Radiating chlorite crystals (~ 250 µm) replace primary plagioclase and clinopyroxene and relict outlines of primary mineral grains remain visible in cross-polarised light. This indicates that the chloritised fault rocks are strongly altered gabbros rather than sheared hydrothermal veins. Commonly, chlorite coexists with fine-grained, granular titanite (<20 µm) and epidote crystals (~ 50 - 100 µm) (Figure 5.5e). Most samples show patches (1 – 5 mm) dominated by epidote, with euhedral crystals (100 – 250 µm) grown into open-space (Figure 5.5e) that is partially filled by chlorite or secondary calcite. Typically, open-space filling chlorites are inclusion-free, and not associated with titanite, suggesting that it may be precipitated directly from a hydrothermal fluid instead of replacing primary minerals. Although chalcopyrite and pyrite grains are now only very small (5 - 20 µm) and rare in most samples, the abundant areas (> 5 mm) with iron-hydroxides and malachite suggest they were previously abundant. Similar to the hanging wall, footwall and clast samples, calcite is the latest stage alteration mineral, mainly filling open spaces and thin veins that cross cut earlier alteration phases.

5.5 Mineral chemistry

5.5.1 Plagioclase

Plagioclase from the hanging wall and footwall samples is compositionally similar to plagioclase from the layered gabbro section elsewhere in the Wadi Tayin area (Pallister and Hopson, 1981). Most footwall plagioclase display anorthite compositions (An_{75-81}), slightly lower than the median composition of plagioclase in fresh layered gabbros ($An_{82\pm2\%}$) in Wadi Gideah (Figure 5.6a;

Appendix C.3), but strongly albitised plagioclase are not present (<An_{60}). In contrast, plagioclase in the hanging wall rocks has very high anorthite contents (>An_{90}).

5.5.2 Amphibole

All measured amphiboles classify as Ca-amphiboles following the classification scheme of Leake et al. (1997) (Figure 5.6b; Appendix C.3) and compositions range from tremolite to actinolite, magnesiohornblende and tschermakite, with most analyses plotting in the tremolite-actinolite field. All analysed amphiboles show compositions similar to amphiboles observed elsewhere in the ophiolite's gabbro section (Bosch et al., 2004) as well as in the plutonic section of modern oceanic crust (Alt et al., 2010). Amphiboles co-existing with chlorite in hanging and footwall samples have tremolite compositions with high Si and low Fe^{2+} abundances (Mg# >0.95). In contrast, amphiboles replacing clinopyroxenes in hanging wall sample OM15-3A mainly plot in the magnesiohornblende field with a few tschermakite compositions. All measured amphiboles display low Cl concentrations of < 0.05 wt. %.

5.5.3 Epidote

Epidote from the fault rock display a range of compositions with XFe (XFe =Fe/(Fe+Al)) ranging between 0.2-0.34 (Appendix C.3). This is somewhat higher than previously reported from epidote veins and epidote crystals in the alteration haloes around hydrothermal veins in gabbros from the lower crustal section of Wadi Haymiliya in the central part of the ophiolite (XFe = 0 - 0.2 for most analysis; Nehlig and Juteau, 1988). Similar X_{Fe} compositions of epidote with XFe=0.17-0.36 have been measured from the sheeted dykes and upper gabbros in ODP/IODP Hole 1256D (Alt et al., 2010).

5.5.4 Chlorite

Chlorite is the most abundant mineral in the fault rocks and also a major secondary phase in hanging wall and footwall samples. Chlorite replaces plagioclase and co-exists with tremolite along grain boundaries between plagioclase and pyroxene crystals. This is similar to how it is commonly observed in many ocean crustal rocks (e.g. Alt et al., 2010) as well as reported from experiments of gabbroic rocks with seawater at temperatures between 300-475 °C (Beermann et al., 2017). Both in hanging wall and footwall samples, chlorite replacing plagioclase and chlorite co-existing with tremolite display a narrow range in silica (5.3-6.1 Si pfu), in contrast to chlorite from elsewhere in the ophiolite (France et al., 2009; Nehlig and Juteau, 1988b) and in modern oceanic crust (e.g. Alt et al. (2010); Figure 5.6c). Chlorites from the fault rocks yield a similar

narrow range of silica but have considerably higher Fe/(Fe+Mg) ratios of 0.38 to 0.56 than hanging wall and footwall samples, with some samples being iron-rich, Fe/(Fe+Mg) > 0.55 (Figure 5.6c; Appendix C.3). Furthermore, chlorite from the hanging wall and footwall gabbros also have distinctive compositions, with footwall chlorites Fe/(Fe+Mg) ratio at 0.23 to 0.3 being more iron-rich than hanging wall chlorites with Fe/(Fe+Mg) ratio from 0.18 to 0.22.

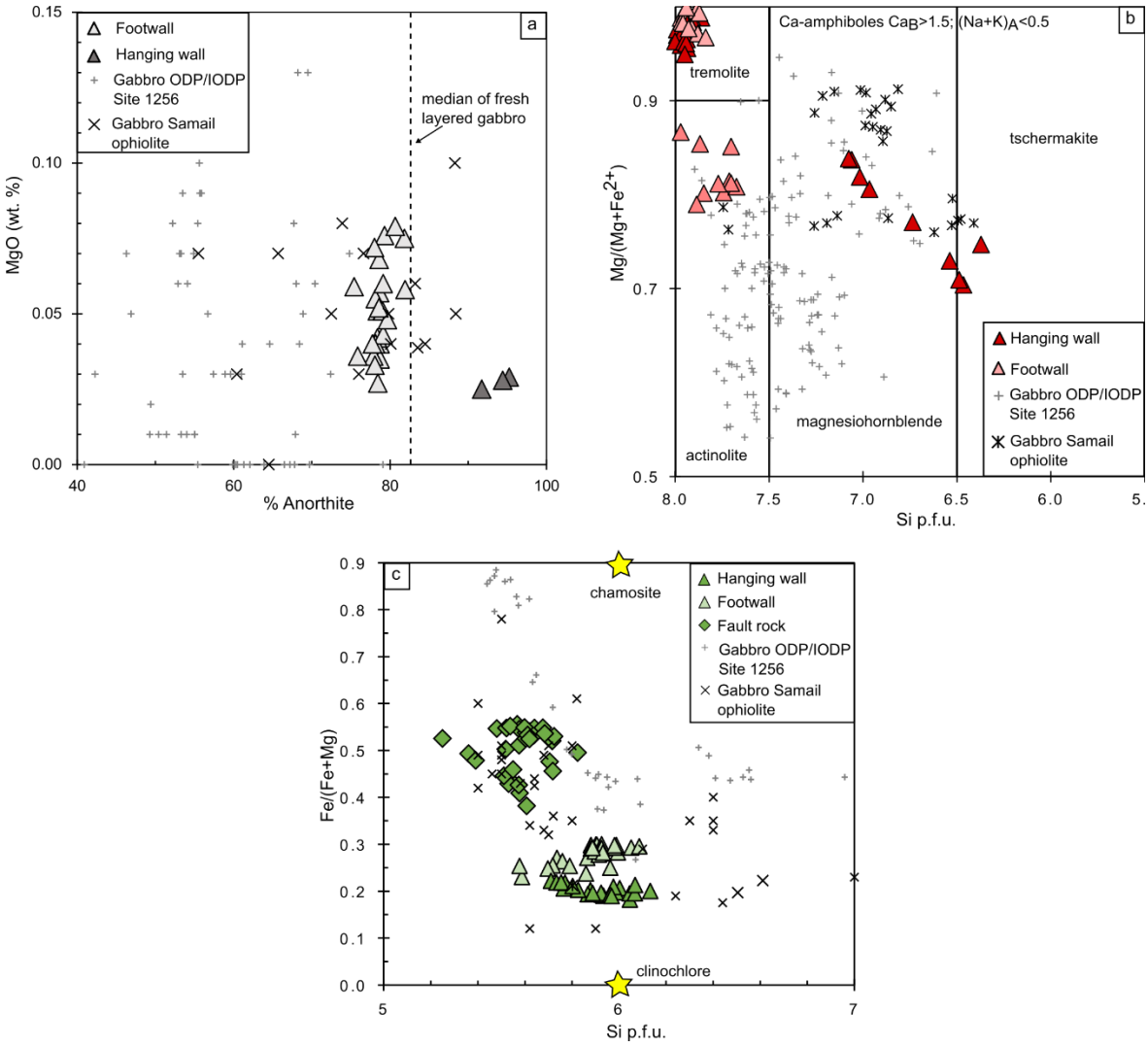

Figure 5.6: Mineral compositions of plagioclase, amphibole and chlorite measured in fault zone, clast as well as hanging wall and footwall samples (a) % Anorthite measured in feldspars from hanging wall and footwall samples vs MgO (wt. %) content, compared to plagioclase compositions of gabbros from modern ocean crust (Alt et al., 2010) and of layered gabbros elsewhere in the Wadi Tayin massife (Pallister and Hopson, 1981). The dashed line represents the median value of % anorthite ($An_{82\pm2\%}$) measured in fresh layered gabbros of samples close to the fault zone outcrop (J. Koepke, unpublished data). High An-content of $An_{91\text{-}95}$ measured in fresh plagioclase suggest very primitive compositions. (b) Compositions of amphiboles measured in

hanging wall and footwall samples compared to amphibole composition measured in layered gabbros elsewhere in the ophiolite (Bosch et al., 2004) and in the plutonic section of modern oceanic crust at ODP/IODP Site 1256 (Alt et al., 2010). Note the high amount of tremolite pointing towards a formation regime of high Mg concentration. (c) Compositions of chlorite replacing plagioclase and chlorite-tremolite patches in between plagioclase and pyroxene grains (Fig.4.4b) measured in hanging wall and footwall samples in contrast to chlorite compositions of the fault rock. Also plotted for comparison purposes are chlorite composition measured in upper and lower gabbros from Wadi Haymiliya in the central part of the ophiolite (Nehlig and Juteau, 1988b), chlorite measured in isotropic high-level gabbros in Wadi Gideah (France et al., 2009) and chlorite compositions measured in gabbros of modern oceanic crust at ODP/IODP Site 1256 (Alt et al., 2010). Note that error bars are smaller than data symbols.

5.5.5 Prehnite and laumontite

Prehnite crystals from prehnite-laumontite veins have been analysed with the electron microprobe in the hanging wall sample OM15-3A (Appendix C.3). Prehnite compositions are uniform with a calculated formula of $Ca_{1.98\text{-}2}Na_{0\text{-}0.02}(Al_{0.96\text{-}0.98}Fe_{0.01\text{-}0.02}^{3+})Al_{0.94\text{-}0.97}Si_{3.03\text{-}3.06}O_{10}(OH)_2$. Prehnite shows low iron concentrations with X_{Fe}=100*Fe (Fe+Al^{iV}) of 0.33-1.55. These results are comparable to the lowermost values reported by Nehlig and Juteau (1988) from late prehnite veins in the layered gabbro section of Wadi Haymiliya.

Laumontite in the prehnite-laumontite veins in hanging wall sample OM15-3A is homogeneous with low iron and sodium concentrations (Appendix C.3). The calculated formula is $Ca_{3.38\text{-}3.91}Na_{0\text{-}0.15}K_{0.01\text{-}0.39}(Al_{7.51\text{-}7.81}Fe_{0\text{-}0.13}Si_{16.19\text{-}16.44})*18H_2O$.

5.6 Bulk rock major- and trace element compositions

5.6.1 Fresh layered gabbro

Eight samples of fresh layered gabbro that crop out within 500 m of the fault zone have compositions typical of mafic cumulates from Wadi Tayin area (Peucker-Ehrenbrink et al., 2012), the Samail ophiolite in general (Browning, 1984; Pallister and Hopson, 1981; Pallister and Knight, 1981), and modern fast-spreading ocean ridges (Gillis et al., 2014). These rocks have magnesium numbers that cluster in a narrow range of Mg# = 88 - 90 and the incompatible minor and trace element concentrations (e.g., K_2O, TiO_2, Zr, Y, Nb) are low to very low, demonstrating the gabbros primitive compositions (Figure 5.7; Table, 5.1; Appendix C.2). Loss on ignition (LOI) averages ~2

wt. %, indicating the presence of some minor alteration products. Chondrite-normalised rare earth element patterns show a depletion of the light rare earth element (LREE) and slightly decreasing abundance of the heavy rare earth elements (HREE). There is a strong positive Eu anomaly, reflecting the high modal abundance of plagioclase in the samples (Figure 5.8).

5.6.2 Hanging wall and footwall samples

Relative to the unaltered layered gabbro, rocks from the hanging wall and the footwall have comparable major element compositions, with only subtle variations (Figure 5.7). One hanging wall sample yields slightly lower values of CaO but still plots in the range of overall layered gabbro samples of the Wadi Tayin area (Peucker-Ehrenbrink et al., 2012). All three samples plot in the lower range of SiO_2 concentration. The hanging wall and footwall samples have higher concentrations of volatiles with loss on ignition (LOI) of 7.4 wt. % on average, indicating that they are more strongly altered than the fresh layered gabbro samples. Trace element concentrations are not significantly different compared to fresh layered gabbro concentrations (Figure 5.7, Table 5.1), but tend to have slightly increased Sr concentrations and generally lower concentrations of Cu. Chondrite-normalised rare earth element pattern are identical to fresh layered gabbro (Figure 5.8)

Table 5.1: Mineral paragenesis, whole rock major- and trace element data and Sr-isotope data of all samples.

Typ			fresh background gabbro[1)]	hanging wall	hanging wall	foot wall	clast	clast	fault rock	fault rock	fault rock	fault rock	fault rock	fault rock	fault rock
Sample			md ± MAD (n=8)[2)]	AH9	OM15-3A*	OM15-3F *	AH6	AH7	AD5	AD6	AD7	DT-10	OM15-3C*	OM15_3E*	AH8
Mineral assemblage	Primary minerals		plagiocalse, clinopyroxene, olivine ± oxides	clinopyroxene and plagioclase partially preserved	clinopyroxene and plagioclase partially preserved	clinopyroxene and plagioclase partially well preserved	clinopyroxene and plagioclase partially preserved	clinopyroxene + plagioclase only rarely preserved	no primary minerals preserved	no primary minerals preserved	no primary minerals preserved	no primary minerals preserved	no primary minerals preserved	no primary minerals preserved	some clinopyroxene relics preserved
	Secondary minerals		± chlorite, ± Mg-hornblende, ± tremolite	albite, Mg-hornblende, actinolite, chlorite, prehnite, laumontite	prehnite, chlorite, laumontite, tremolite, Mg-hornblende, pumpellyite	chlorite, tremolite, Mg-hornblende, oxides	albite, Mg-hornblende, actinolite, chlorite, laumontite carbonate, ± epidote, ± titanite	chlorite, albite, Mg-hornblende, actinolite, epidote	chlorite, epidote, titanite	chlorite, epidote, titanite	chlorite, epidote, titanite, chalcopyrite	chlorite	chlorite	chlorite, epidote	chlorite, epidote, titanite
	Weathering minerals		-	minor amount of Fe-hydroxides, calcite	calcite, Fe-hydroxides	-	-	calcite	Fe-hydroxides, calcite	Fe-hydroxides, malachite, calcite	Fe-hydroxides, malachite, calcite	Fe-hydroxides, malachite, calcite	Fe-hydroxides, malachite, native Cu, calcite	calcite, malachite	Fe-hydr-oxides, malachite, calcite
	Vein	hornblende					x								
		tremolite				x									
		chlorite				x									
		prehnite		x	x										
		zeolite		x	x		x	x						x	
		calcite		x	x		x	x	x	x	x	x	x	x	x
SiO_2	wt. %	XRF	46.72 ± 0.6	45.18	43.43	46.54	46.77	49.56	26.49	25.95	30.10	23.17	27.24	22.68	26.85
Al_2O_3	wt. %	XRF	17.99 ± 0.7	17.81	16.04	13.55	19.08	15.82	19.64	19.41	20.93	14.49	19.15	14.68	18.92
Fe_2O_3	wt. %	XRF	5.28 ± 0.4	5.68	3.15	5.77	3.28	6.56	27.97	29.99	22.42	32.12	27.62	16.69	22.72
MnO	wt. %	XRF	0.09 ± 0.01	0.10	0.06	0.11	0.05	0.07	0.27	0.25	0.22	0.18	0.26	0.24	0.24
MgO	wt. %	XRF	10.58 ± 1.2	11.19	8.08	11.80	8.50	10.84	13.81	13.33	11.81	8.38	13.01	12.73	18.09
CaO	wt. %	XRF	16.44 ± 0.4	12.60	16.06	15.27	15.53	6.50	2.71	0.88	4.71	0.42	1.58	13.71	0.16
Na_2O	wt. %	XRF	0.99 ± 0.1	1.48	1.04	0.82	1.41	1.62	0.09	0.11	0.09	0.61	< 0.2	0.49	0.11
K_2O	wt. %	XRF	<0.02	< 0.01	0.04	0.01	< 0.01	< 0.01	< 0.01	< 0.01	< 0.01	0.02	< 0.02	< 0.02	< 0.01
TiO_2	wt. %	XRF	0.22 ± 0.02	0.16	0.19	0.24	0.22	0.41	0.28	0.46	0.26	0.13	0.27	0.64	0.31
P_2O_5	wt. %	XRF	<0.08	0.01	< 0.08	< 0.08	0.01	0.02	0.02	0.03	0.01	0.06	0.01	0.07	0.01
SO_3	wt. %	XRF	-	< 0.01	0.00	0.01	< 0.01	0.02	0.01	< 0.01	< 0.01	0.01	0.01	0.02	< 0.01
LOI[3)]	wt. %	XRF	1.95 ± 0.2	5.60	10.97	5.57	5.00	14.56	8.56	8.81	8.92	11.17	10.88	17.16	13.59
Total	wt. %	XRF	100.00	99.81	99.06	99.69	99.83	99.57	99.83	99.21	99.48	90.78	100.04	99.11	99.84
Mg#			88-90	88.63	91.04	89.01	91.13	86.76	66.18	63.77	67.61	50.84	65.12	75.14	75.93
Li	µg/g	ICP-MS / LA-ICP MS	0.82 ± 0.2	0.73	0.41	0.33	0.24	1.14	0.84	0.61	1.02	0.82	2.16	1.44	0.90
Sc	µg/g	ICP-MS / LA-ICP MS	41.77 ± 6.4	33.27	33.50	46.71	39.71	51.71	53.71	51.10	44.63	27.68	50.14	51.10	44.75
V	µg/g	ICP-MS / LA-ICP MS	119.74 ± 20.9	84.30	117.57	149.20	107.30	113.50	167.60	219.70	124.50	1547.00	222.27	238.49	131.20

Cr	µg/g	XRF / LA ICP-MS	685.34 ± 109.3	548.15	366.56	651.22	437.65	798.10	581.40	642.50	531.10	409.00	743.76	806.35	1140.67
Co	µg/g	XRF / LA ICP-MS	40.32 ± 4.6	45.60	21.26	41.06	9.90	54.50	131.80	344.00	112.30	161.00	175.34	105.06	121.50
Ni	µg/g	XRF / LA ICP-MS	172.15 ± 30.1	194.35	118.62	172.70	113.15	146.15	168.90	182.20	147.40	200.30	240.99	247.78	240.00
Cu	µg/g	ICP-MS / LA-ICP MS	119.71 ± 30.4	92.76	6.37	196.40	44.03	1339.00	76.68	4557.00	3406.00	75790.00	6514.16	34.64	8.84
Zn	µg/g	ICP-MS / LA-ICP MS	21.68 ± 1	23.30	6.79	18.18	10.50	88.10	147.30	161.50	168.60	1141.00	366.11	170.81	119.00
Rb	µg/g	ICP-MS / LA-ICP MS	0.08 ± 0.01	0.06	0.15	0.09	0.05	0.07	0.01	0.01	0.02	0.02	0.15	0.12	0.01
Sr	µg/g	ICP-MS / LA-ICP MS	139.16 ± 2.8	179.50	221.08	89.66	292.90	105.70	81.69	21.43	53.71	15.73	50.37	54.64	22.81
Y	µg/g	XRF / LA ICP-MS	4.32 ± 0.5	6.60	4.22	5.76	7.80	10.10	7.52	13.20	5.86	3.00	6.44	12.03	8.10
Zr	µg/g	XRF / LA ICP-MS	3.21 ± 0.3	7.60	2.92	3.67	8.30	13.60	5.10	16.50	5.96	4.80	4.81	-	11.10
Cs	µg/g	ICP-MS / LA-ICP MS	<0.01	0.00	0.00	0.00	0.00	0.00	0.00	<0.0003	0.00	0.00	0.01	0.00	<0.0003
Ba	µg/g	ICP-MS / LA-ICP MS	2.21 ± 0.2	5.54	3.09	7.43	9.26	3.61	<0.45	<0.45	3.70	0.62	13.96	9.03	<0.45
La	µg/g	ICP-MS / LA-ICP MS	0.21 ± 0.02	0.13	-	0.23	0.10	0.21	0.91	0.23	0.27	0.14	0.24	0.63	0.13
Ce	µg/g	ICP-MS / LA-ICP MS	0.63 ± 0.1	0.51	-	-	0.45	0.80	2.81	1.01	0.82	0.52	0.71	2.68	0.51
Pr	µg/g	ICP-MS / LA-ICP MS	0.14 ± 0.02	0.11	0.11	0.16	0.11	0.19	0.53	0.21	0.17	0.09	0.13	0.53	0.14
Nd	µg/g	ICP-MS / LA-ICP MS	0.93 ± 0.1	0.73	0.78	1.01	0.78	1.33	2.89	1.40	1.08	0.59	0.87	3.14	1.02
Sm	µg/g	ICP-MS / LA-ICP MS	0.44 ± 0.1	0.32	0.38	0.52	0.40	0.62	0.88	0.80	0.50	0.33	0.50	1.28	0.52
Eu	µg/g	ICP-MS / LA-ICP MS	0.29 ± 0.01	0.22	0.21	0.28	0.20	0.35	0.35	0.24	0.19	0.06	0.17	0.51	0.19
Gd	µg/g	ICP-MS / LA-ICP MS	0.68 ± 0.1	0.53	0.57	0.81	0.65	0.99	1.16	1.40	0.82	0.54	0.83	1.68	0.84
Tb	µg/g	ICP-MS / LA-ICP MS	0.12 ± 0.02	0.10	-	-	0.12	0.19	0.20	0.28	0.16	0.11	0.18	0.33	0.16
Dy	µg/g	ICP-MS / LA-ICP MS	0.83 ± 0.1	0.65	0.74	1.06	0.84	1.27	1.32	1.82	1.03	0.75	1.20	2.08	1.05
Ho	µg/g	ICP-MS / LA-ICP MS	0.18 ± 0.02	0.14	0.16	0.23	0.18	0.27	0.28	0.39	0.22	0.16	0.27	0.44	0.22
Er	µg/g	ICP-MS / LA-ICP MS	0.47 ± 0.1	0.38	0.43	0.61	0.50	0.77	0.77	1.07	0.60	0.46	0.74	1.26	0.60
Tm	µg/g	ICP-MS / LA-ICP MS	0.07 ± 0.01	0.05	0.06	0.08	0.07	0.11	0.11	0.16	0.09	0.07	0.10	0.18	0.09
Yb	µg/g	ICP-MS / LA-ICP MS	0.41 ± 0.1	0.34	0.39	0.53	0.45	0.69	0.70	0.89	0.54	0.45	0.63	1.24	0.51
Lu	µg/g	ICP-MS / LA-ICP MS	0.06 ± 0.01	0.05	0.06	0.08	0.06	0.10	0.10	0.14	0.08	0.06	0.09	0.18	0.07
Hf	µg/g	ICP-MS / LA-ICP MS	0.15 ± 0.02	0.29	0.13	0.18	0.29	0.28	0.22	0.41	0.23	0.21	0.21	-	0.37
Pb	µg/g	ICP-MS / LA-ICP MS	10.83 ± 10.6	<0.08	0.03	0.13	<0.08	<0.08	<0.08	0.47	0.12	3.25	0.66	0.22	<0.08
Th	µg/g	ICP-MS / LA-ICP MS	<0.005	0.01	0.00	0.00	0.01	0.01	0.01	0.02	0.01	0.02	0.01	0.08	0.01
U	µg/g	ICP-MS / LA-ICP MS	<0.005	0.02	0.01	0.01	0.01	0.06	0.02	0.58	0.05	10.24	0.17	0.04	0.01
$^{87}Sr/^{86}Sr$ measured				0.703903	0.704756	0.703274	0.704510	0.704969	0.704553	-	0.704742	0.705480	0.704745	0.704802	-
$^{87}Sr/^{86}Sr$ 95 Ma				0.703900	0.704754	0.703269	0.704508	0.704965	0.704553	-	0.704741	0.705444	0.704741	0.704792	-
± 2 SE (error)				14	13	14	16	16	16	-	16	14	12	11	-

Picked minerals	**foot wall epidote (vein)**	**hanging wall laumontite (vein)**	**hanging wall calcite (vein)**	**fault rock calcite (vein)**
$^{87}Sr/^{86}Sr$ measured	0.704280	0.707378	0.708242	0.707778
$^{87}Sr/^{86}Sr$ 95 Ma	0.704279	0.707366	0.708233	0.707767
± 2 SE	14	17	14	14

[1)] Major elements measured with ICP-OES, trace elements measured with liq. ICP-MS and LA-ICP-MS

[2)] Medium ± median absolute deviation, see Table Appendix C.2

[3)] LOI determined by loss-on ignition experiments at 1000 °C

[4)] Trace elements measured with LA-ICP-MS on pressed powder tablets

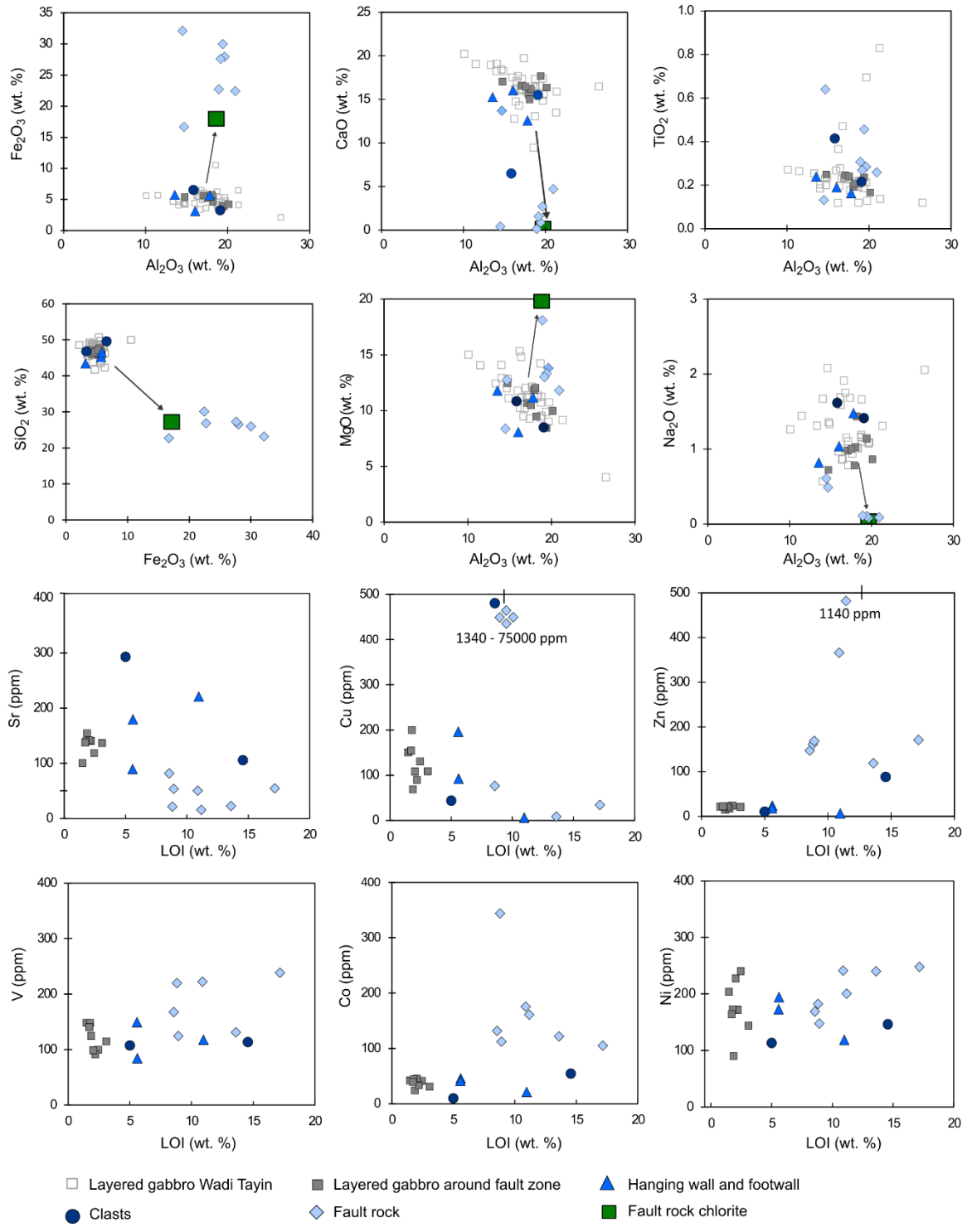

Figure 5.7: Major- and trace element covariation diagrams for selected elements.Fault rock is shown in light blue diamonds, clast samples in dark blue circles, and hanging wall and footwall samples in royal blue triangles. Background layered gabbros are shown as grey squares and are from eight samples within a distance of 500 m to the fault zone outcrop. Open squares are olivine gabbro from elsewhere in Wadi Tayin (Peucker-Ehrenbrink et al., 2012). Green square represents the composition of chlorite

measured in the fault rock and arrows indicate alteration vectors. Note that error bars are smaller than data symbols.

5.6.3 Clast samples

The two clast samples are slightly more variable in terms of major- and trace element composition when compared to hanging wall and footwall samples. The highly altered sample AH7 has clearly lower CaO and higher TiO_2 concentrations, similar to the chlorite fault rocks (Figure 5.7; Table 5.1). Both clast samples show slightly higher concentrations for Na_2O, possibly reflecting the presence of more albitic plagioclase as well as elevated volatile contents with LOI of 5 wt. % and 14.5 wt. %. Concentrations of V, Co, Zn and Ni are comparable to those of fresh olivine gabbro, whereas sample AH7 has a higher concentration for Cu. Rare earth element patterns are very similar to fresh layered gabbro although with a less pronounced Eu anomaly for the more altered sample AH7 (Figure 5.8).

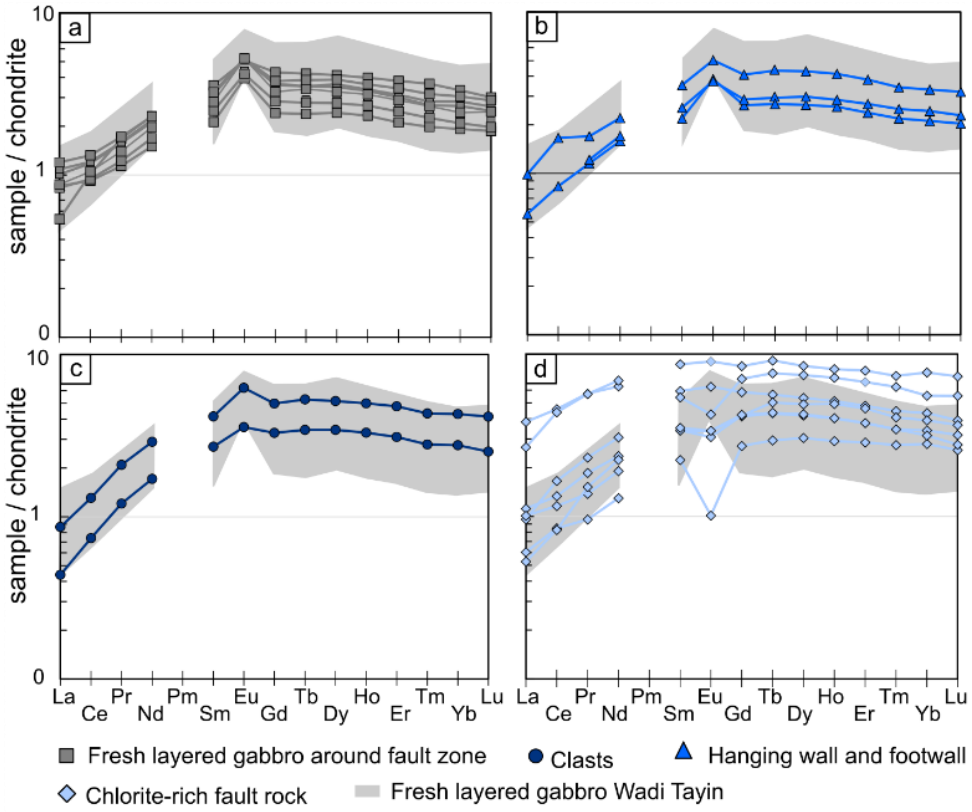

Figure 5.8: Chondrite-normalised (McDonough and Sun, 1995) REE plot for (a) background layered gabbros, (b) hanging wall and footwall, (c) clasts, and (d) chlorite-rich fault rock. The shaded grey area represents chondrite-normalised REE of olivine gabbro observed elsewhere in the Wadi Tayin (Peucker-Ehrenbrink et al., 2012).

5.6.4 Chlorite-rich fault rocks

Major and trace element compositions of the chlorite-rich fault rock reflect the secondary mineral assemblage (Table 5.1; Figure 5.8). All fault zone samples show high LOI values of 8-17 wt. %, resulting from the high abundance of hydrous minerals such as chlorite and epidote and weathering products (e.g., malachite and iron oxyhydroxides). The chlorite-fault rock samples show different and more variable major elemental compositions compared to fresh layered gabbro (Fig.5.7; Table 5.1). Total Fe_2O_3 is up to six times higher than in fresh samples, whereas CaO, SiO_2 and Na_2O concentrations are considerably lower. TiO_2 and MgO concentrations are slightly higher whereas Al_2O_3 appears unchanged. In terms of minor and trace elements, the concentrations of Cu, Co, Zn and V are strongly increased compared to fresh gabbros for some of the samples. Cu concentrations are very high for some of the samples, reflecting the presence of chalcopyrite and its weathering products such as malachite. Strontium concentrations are generally lower than in fresh samples, in parallel with lower CaO values. Rare earth elements concentrations and patterns show some differences compared to fresh layered gabbro samples (Figure 5.8): All samples display no or negative Eu anomalies, compared to a positive anomaly in unaltered layered gabbro. This possibly reflects the disappearance of plagioclase, which is no longer present in fault rock samples (see 5.4.4, petrographic description of the chlorite-rich fault rock). Furthermore, two samples yield significantly higher REE concentrations (up to 8x chondrite).

5.7 Strontium isotope compositions

Strontium isotope bulk compositions of six fault rock samples, two clast samples, three hanging and footwall samples were determined and are compared to eight fresh layered gabbro samples collected within 500 m of the fault zone outcrop. Additionally, epidote from an epidote vein in the footwall, laumontite from a laumontite-calcite vein in the hanging wall, and calcite from a calcite vein in the fault rock and from a calcite-laumontite vein in the hanging wall were mechanically separated by hand picking and analysed (Figure 5.9; Table 5.1). Fresh layered gabbros display a relatively narrow range of Sr concentrations (100 – 150 µg/g) and isotope compositions ($^{87}Sr/^{86}Sr$ = 0.70299 – 0.70332). These Sr-ratios are slightly elevated compared to fresh MORB ($^{87}Sr/^{86}Sr$ = 0.70281) from modern oceanic crust (White et al., 1987) and some show slightly more radiogenic values compared to fresh layered gabbro elsewhere in the Samail ophiolite ($^{87}Sr/^{86}Sr$ ~ 0.70265-0.70320, McCulloch et al., 1980, Lanphere et al., 1981). The footwall sample plots with $^{87}Sr/^{86}Sr$ = 0.70327 close to fresh layered gabbro, indicating only very minor Sr isotopic exchange. In contrast, the hanging wall samples have more radiogenic values of $^{87}Sr/^{86}Sr$ = 0.70390-0.70475 compared to fresh layered gabbro ($^{87}Sr/^{86}Sr$ = 0.70299-0.70332), with sample OM15-3A also

showing higher Sr concentration (221 µg/g) than fresh layered gabbro due to high abundance of hydrothermal laumontite and prehnite. The clast samples as well as the chlorite-rich fault rocks show a narrow range of strontium isotope composition ($^{87}Sr/^{86}Sr$ = 0.70451 – 0.70450), clearly shifted towards more radiogenic compositions, combined with low Sr concentrations compared to fresh layered gabbro (Sr=50-100 µg/g). These Sr-isotope ratios are similar to the range of hydrothermal epidote and amphiboles, and highly altered gabbros from the Wadi Tayin area (e.g., Bosch et al., 2004; Coogan et al., 2006). Moreover, epidote from a monomineralic epidote vein of the footwall shows very similar Sr-isotope composition ($^{87}Sr/^{86}Sr$ = 0.70428). These epidote grains have euhedral crystal habits and appear to have precipitated directly out of a hydrothermal fluid and therefore should directly reflect the Sr-isotopic composition of the fluid.

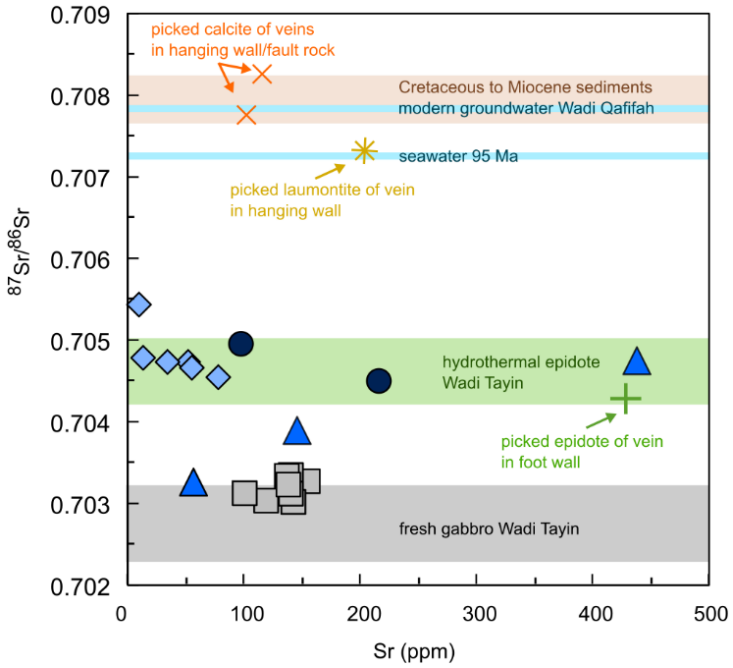

Figure 5.9: Strontium isotope composition of whole rock and mineral separate samples. $^{87}Sr/^{86}Sr$ is plotted vs Sr content (ppm) of fresh layered gabbro within 500 m distance of the fault zone outcrop (grey squares), hanging wall and footwall samples (blue triangles), clast samples (dark blue dots), chlorite-rich fault rock (light blue diamonds), picked epidote from a epidote vein in the footwall (green cross), picked laumontite of a laumontite-calcite vein in the hanging wall (yellow star) and two picked calcite samples of a calcite vein within the fault rock and a calcite-laumontite vein in the hanging wall (orange crosses). Values of fresh layered gabbro of Wadi Tayin after Lanphere et al., (1981); McCulloch et al., (1981), Cretaceous seawater from McArthur et al., (2001), modern groundwater sampled in gabbro hosted wells of Wadi Qafifah (Bompard, 2018) and values of Cretaceous to Miocene sediments from Weyhenmeyer (2000). Error bars are smaller than the symbols.

The separated laumontite of sub-millimetre thick veinlets, cross-cutting all other alteration stages yields Sr-isotope ratios ($^{87}Sr/^{86}Sr$ = 0.70737) close to 95 Ma-seawater (Figure 5.9). Hand-picked calcite of laumontite-calcite veinlets display the most radiogenic values of $^{87}Sr/^{86}Sr$ = 0.70777 – 0.70823 and plot in the range of Cretaceous to Miocene sediments (Weyhenmeyer, 2000) and close to the strontium isotope composition of modern groundwater ($^{87}Sr/^{86}Sr$ = 0.7078) from gabbro hosted wells in Wadi Tayin (Bompard, 2018).

5.8 Discussion

5.8.1 Secondary mineralogy and hydrothermal fluid characteristics

Chlorite is a major constituent in both the fault rock as well as in hanging wall and footwall gabbros and its composition can be used as a geothermometer to estimate alteration temperatures. Several studies report a systematic decrease of Si^{iV} coupled with an increase of Al^{iV} in chlorites with increasing temperature (Cathelineau, 1988; Cathelineau and Nieva, 1985; McDowell and Elders, 1980; Velde, 1991). This correlation was used by Cathelineau (1988) to develop an empirical geothermometer of general applicability in diagenetic, hydrothermal and metamorphic settings based on the incorporation of Al^{iV}. Several studies show that the Al^{IV}-temperature correlation is likely to be influenced by the Fe/(Fe+Mg) ratio of the chlorite (Jowett, 1991; Kranidiotis and MacLean, 1987) and the empirical geothermometer of Cathelineau (1988) was extended by a correction factor (Jowett, 1991). Using this adapted thermometer of Jowett (1991) we calculated temperatures of chlorite formation in the fault rock as well as chlorite in hanging wall and footwall (Figure C.1 in Appendix C; Appendix C.3). The majority of fault rock chlorites were formed at temperatures between 300-350 °C (median temperature 330 °C), whereas hanging wall and footwall chlorite show a slightly larger spread of temperatures but most plot in the range of ~ 250-300 °C with a median temperature of 275 °C for footwall and 268 °C hanging wall chlorite (Figure C.1 in Appendix C). Statistical analysis on the temperature range of all three lithology's show that the temperature difference between fault rock and both wall rocks are significant (see box plot in Figure C.1 in Appendix C). However, petrographic observations indicate that chlorites of the fault and chlorites within the walls have formed under different conditions (e.g. different fluid/rock ratio, pH and time). Therefore, an additionally influence of the host rock composition on the chlorite formation temperature as stated by Xie et al. (1997) cannot be entirely ruled out (e.g. Fe_2O_3 content is very different between hanging- and footwall: ~5 wt% and fault rock: ~25 wt%). The difference in chlorite formation temperatures between the fault rock (~ 300-350 °C) and the hanging- and footwall (~ 250-300 °C) suggest an open system of multi-stage alteration and a fluid evolution towards a highly charged composition.

The formation of chlorite in the hanging- and footwall during initial fluid migration along the fault at slightly lower temperatures (~ 250-300 °C), subsequent evolution and channeling of the hydrothermal fluids, accompanied by a temperature rise to 300-350 °C, re-equilibration the chlorite along the fault but not the chlorite in the wall rocks, is a likely scenario.

The fault rock and clast samples have similar Sr-isotope compositions (Figure 5.9) as the epidote vein in the footwall as well as epidote veins observed elsewhere in the ophiolite (e.g., Bosch et al., 2004; Coogan et al., 2006). The epidotes have relatively high Sr concentrations (400 to 750 µg/g) and are robust against low-temperature fluid-rock Sr exchange. Hence analyses of epidote precipitated in veins are commonly used to estimate the Sr-isotopic compositions of the hydrothermal fluids (e.g., Bickle and Teagle, 1992; Harris et al., 2015; Teagle et al., 2003). Epidosites, equigranular epidote-quartz-titanite rocks, are present in the sheeted dyke complexes of many ophiolites, and thought to record zones of concentrated “black smoker-type” hydrothermal upwelling fluid flow (e.g., Richardson et al., 1987; Schiffman et al., 1987) and have similar Sr-isotopic compositions to epidote veins. The Oman epidote $^{87}Sr/^{86}Sr$ ratios are clearly elevated relative to fresh layered gabbro indicating the extensive exchange of the rock with a seawater-derived hydrothermal fluid. We propose that this fluid had a $^{87}Sr/^{86}Sr$ in the range of 0.7043-0.7048, and that the passage of a black smoker-like fluid with this Sr-isotopic composition resulted in the alteration of the fault rocks, clasts and surrounding wall rocks.
The degree of alteration, the strontium isotopic composition of the fault rock and particularly the observed secondary mineral assemblage with abundant Cu-sulphides suggest a formation of the fault rock during fluid-rock interactions with up-welling, discharging hydrothermal fluids at chlorite formation temperatures of about 300-350 °C. Minor but pervasive replacement of clinopyroxene by Mg-hornblende in the altered clast and hanging wall samples indicates an earlier phase of higher temperature hydrothermal alteration which is now mostly overprinted by the described, lower-temperature alteration phases.

5.8.2 Mass changes during hydrothermal fluid-rock interaction

5.8.2.1 Calculating mass changes

Comparison of altered bulk rock composition with relatively fresh rocks allow us to estimate the effects of hydrothermal alteration more quantitatively. These calculations indicate which elements are either immobile, mobilized or precipitated, and ultimately lost or gained during fluid-rock interactions. To calculate net mass changes, it is essential that altered rocks are compared with appropriate precursor compositions. Widely available analyses for fresh Oman gabbros makes this simpler than in more complex or metamorphosed terranes. A widely applied

method to monitor changes during hydrothermal alteration uses the behaviour of immobile elements that are passively concentrated or diluted by whole rock mass loss or mass gain, respectively (Grant, 1986; Gresens, 1967; MacLean, 1990; MacLean and Barrett, 1993). Therefore, concentration ratios of these immobile elements in the rock before and after alteration can be used to calculate changes of other, mobile elements. Grant (1986) re-defined the original equation of Gresens (1967), relating the concentration of an element *i* in the altered rock to the concentration of the same element in the precursor rock through a mass change term ($\frac{M^0}{M^A}$). The change of concentration of element *i* during alteration is the difference between the concentration of element *i* before (c_i^0) and after (c_i^A) alteration. The equation is formulated as:

$$c_i^A = \frac{M^0}{M^A}\,(c_i^0 + \Delta c_i) \qquad (1)$$

where c_i^A = concentration of component *i* in the altered rock, c_i^0 = concentration of element *i* in the precursor rock, M^0 = mass of the precursor rock, M^A = mass of the altered rock and Δc_i = change in concentration of element *i*. This equation describes a straight line with a slope defined by the mass change term ($\frac{M^0}{M^A}$) and the y-axis intercept ($\frac{M^0}{M^A} * \Delta c_i$).

To calculate elemental gains and losses for each altered sample, precursor compositions need to be defined. In the case of the chlorite-rich fault rock within the layered gabbros presented here, a single precursor system is assumed, as the layered gabbros are chemically reasonably homogenous (Fig 4.7, 4.8). For this study, the median concentrations of eight samples of the fresh layered gabbro within 500 m of the fault zone outcrop was taken as a precursor composition (Table C.1 in Appendix C). To select which elements can be considered as immobile and are, therefore, appropriate for calculating the mass change term, each of the seven samples from the chlorite-fault zone was examined individually, by comparing the concentration of element *i* in the altered rock (c_i^A) to the median value of the precursor rock (c_i^0). For all the fault-rock samples the c_i^A / c_i^0 for HREE cluster together (Figure 5.10). Hence, we have selected the HREE (Dy and heavier) to calculate the mass change term ($\frac{M^0}{M^A}$).

5.8.2.2 Chemical changes during hydrothermal alteration

Results of mass change calculations are summarised in Table 5.2 and median mass changes are plotted in Figure 5.10. Chlorite-rich fault rock samples show on average a significant mass loss of 67% and clast samples a loss of 34%. In contrast, there is no significant mass change (- 1%) for hanging and footwall samples. Major element changes are variable, both within and between the three rock types, mainly reflecting differences in the secondary mineral assemblages formed and the extent of fluid-rock exchange.

SiO_2 is slightly to highly reduced in all samples with increasing alteration (Figure 5.10). Chlorite fault rock samples have lost >60 % of their silica compared to fresh layered gabbro. This is a substantial part of the total mass loss calculated for chlorite-rich rocks. There is no altered gabbro sample showing any silica enrichment. This agrees well with the absence of secondary quartz and suggests that silica has been transported away from these rocks by the passage of hydrothermal fluids. The general silica loss due to hydrothermal alteration of oceanic crust has been described previously (e.g., Coggon et al., 2016). The behaviour of silica in hydrothermal fluids is relatively well understood (Von Damm et al. (1991), and the silica-loss (63%) from the chlorite-rich fault zones can be used to calculate how much fluid has flowed through this fault zone. The solubility of SiO_2 in hydrothermal fluids principally depends on temperature, pressure and salinity. Using the quartz solubility in seawater of 15.7 and 31.2 mmol/kg, at 300 and 400°C, respectively (Von Damm et al., 1991), results in fluid/rock ratios between 450:1 to 900:1. This estimation is possibly an upper limit as some mid-ocean ridge hydrothermal fluids have salinities greater than seawater, and quartz solubility increases with increasing salinity (Xie and Walther, 1993), but it assumes that the mobilisation of silica is 100% efficient. Regardless, the chlorite-rich fault rocks forms at extreme fluid/rock ratios (Teagle and Alt, 2004).

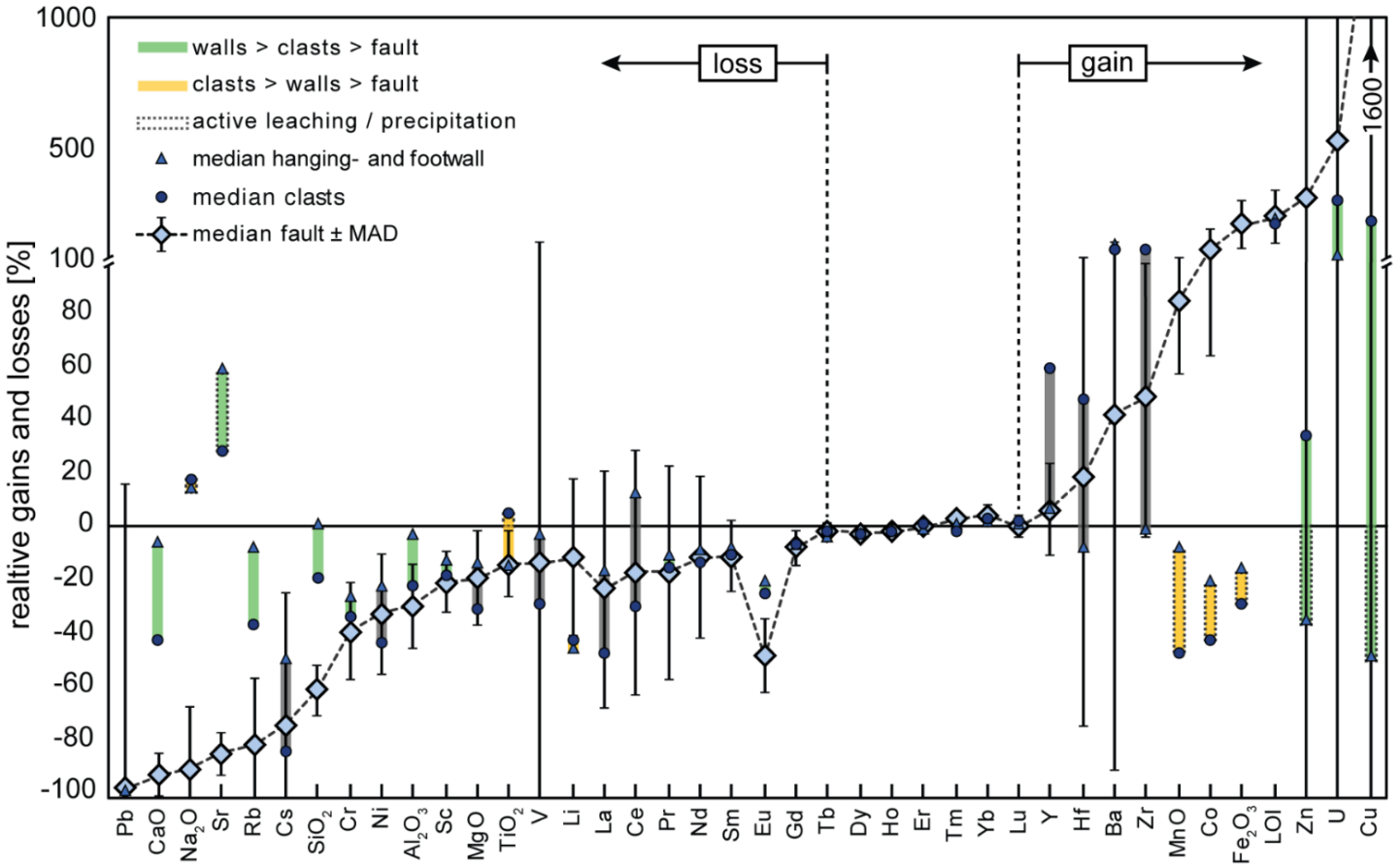

Figure 5.10: Calculated major-and trace element gains and losses for all three rock types shown relative to the median value of fresh background layered gabbro (n=8) shown in the horizontal line (y=0).Elements are ranged by highest loss (left-hand side) to highest gain (right-hand side) plotted for the median fault rock. Note change in scale for gains greater than 100%. Error bars represent the median absolute deviation (MAD) of the median fault rock values.

Titanium and aluminium are traditionally assumed to be immobile during hydrothermal alteration (e.g., MacLean and Barrett, 1993), but these elements display slight mobility in all three of the altered rock types. Titanium shows changes in the range of slightly more than ± 10% which is consistent with the formation of secondary titanite in the chlorite fault rock. Despite the localised formation of secondary titanite, the fault rocks have lost titanium compared to fresh layered gabbro (median= -14%). Alumina is slightly to moderately depleted. This loss of alumina may relate to the strong losses of calcium for all three rock types and a gain of sodium for hanging and footwall samples as well as clasts, due to the partial albitisation of plagioclase (Figure 5.6, 5.11). The chlorite-rich fault rocks have lost >90 % of calcium compared to fresh layered gabbro reflecting the complete breakdown of plagioclase, with only minor epidote present. Iron and manganese are moderately to highly depleted in hanging and footwall rocks and clasts respectively, whereas the chlorite-rich fault rocks are highly enriched in both elements (Figure 5.10). The high iron concentrations mainly reflect hydrothermal sulphide mineralisation and their subsequent iron oxyhydroxide weathering products, respectively.

The most significant feature of all three rock types is the large increase of volatiles, inferred in an increase of loss on ignition (LOI) when compared to fresh layered gabbro. This increase mainly is thought to reflect hydration during fluid-rock interaction with only minor carbonation. The hanging and footwall samples as well as clast sample AH6 have only minor calcium carbonates present in small veins. Consequently, most of the increase in LOI is due to the formation of hydrous hydrothermal minerals such as chlorite, amphibole, prehnite and laumontite. Hanging wall sample OM15-3A shows a considerable gain of volatiles, reflecting high modal abundances of laumontite and prehnite. For clast sample AH7 and all the fault rock samples the increase of LOI is mainly due to high abundances chlorite (± minor epidote).

Even though Y, Zr and Hf are generally considered to be immobile elements during hydrothermal processes (MacLean and Barrett, 1993; MacLean and Kranidiotis, 1987), they show considerable mass gains in all three rock types. However, fresh layered gabbros and altered samples have low concentrations of Zr (~ 3-15 µg/g) and Y (~ 4-13 µg/g), and consequently, minor variations in concentration can result in considerable relative mass gains or losses. However, mobility of high-field strength elements (HFSE) in hydrothermal systems and hydrothermal zircons have been reported from MOR settings (e.g., Augustin et al., 2008).

Table 5.2: Major- and trace element summary of mass changes calculated in wt. %/ µg/g and percent relative to fresh layered gabbro.

	Layered gabbro	hanging wall				foot wall				clast					
	median (n=8)	AH9		OM15-3A		OM15-3F		*Med (n=3)*	*MAD (n=3)*	AH6		AH7		*Med (n=2)*	*MAD (n=2)*
		wt. % µg/g	%	wt. % µg/g	%	wt. % µg/g	%	%		wt. % µg/g	%	wt. % µg/g	%	%	
SiO_2	**46.62**	9.05	19.4	0.68	1.5	-10.51	-22.5	***1.5***	***14.0***	-1.76	-3.8	-16.04	-34.3	***-19.0***	***15.3***
Al_2O_3	**17.89**	3.99	22.2	-0.48	-2.7	-7.45	-41.4	***-2.7***	***21.2***	0.35	1.9	-8.20	-45.6	***-21.8***	***23.8***
Fe_2O_3	**5.05**	1.73	32.8	-1.84	-34.9	-0.79	-15.0	***-15.0***	***22.6***	-2.13	-40.4	-1.23	-23.2	***-31.8***	***8.6***
MnO	**0.09**	0.03	32.4	-0.03	-29.0	-0.01	-7.2	***-7.2***	***20.5***	-0.04	-46.1	-0.05	-49.8	***-48.0***	***1.9***
MgO	**10.68**	3.23	30.5	-1.76	-16.6	-1.40	-13.2	***-13.2***	***15.7***	-2.41	-22.8	-3.87	-36.6	***-29.7***	***6.9***
CaO	**16.38**	-0.89	-5.4	1.09	6.6	-4.56	-27.7	***-5.4***	***11.4***	-1.52	-9.2	-12.42	-75.5	***-42.4***	***33.2***
Na_2O	**0.99**	0.84	84.4	0.14	14.5	-0.35	-35.7	***14.5***	***40.0***	0.37	37.0	0.01	0.9	***19.0***	***18.0***
TiO_2	**0.22**	-0.03	-14.4	-0.03	-12.1	-0.05	-20.9	***-14.4***	***2.9***	-0.03	-12.2	0.02	8.7	***-1.8***	***10.5***
LOI	**2.07**	4.97	255.3	10.03	515.5	2.39	122.8	***255.3***	***130.9***	2.86	147.1	7.07	363.3	***255.2***	***108.1***
Li	**0.81**	0.07	8.9	-0.37	-45.2	-0.56	-68.6	***-45.2***	***25.8***	-0.59	-71.7	-0.12	-14.4	***-43.0***	***28.6***
Sc	**42.51**	-0.70	-1.7	-5.20	-12.5	-5.42	-13.0	***-12.5***	***3.8***	-3.59	-8.6	-9.76	-23.4	***-16.0***	***7.4***
V	**120.73**	-15.67	-13.1	8.60	7.2	-3.63	-3.0	***-3.0***	***6.8***	-16.56	-13.8	-49.47	-41.3	***-27.6***	***13.7***
Cr	**- 327.44**	-8.65	-1.3	-285.21	-41.6	-178.56	-26.1	***-26.1***	***13.5***	-264.51	-38.6	-191.24	-27.9	***-33.3***	***5.3***
Co	**37.52**	15.97	39.6	-17.11	-42.4	-8.36	-20.7	***-20.7***	***27.4***	-30.80	-76.4	-6.58	-16.3	***-46.4***	***30.0***
Ni	**176.69**	67.77	39.4	-42.67	-24.8	-37.76	-21.9	***-21.9***	***21.4***	-63.36	-36.8	-81.67	-47.4	***-42.1***	***5.3***
Cu	**126.58**	-5.19	-4.3	-112.75	-94.2	-58.23	-48.6	***-48.6***	***29.9***	-77.37	-64.6	709.26	592.5	***263.9***	***328.6***
Zn	**20.76**	4.05	18.7	-14.26	-65.8	-7.53	-34.7	***-34.7***	***28.2***	-12.59	-58.1	25.37	117.0	***29.5***	***87.6***
Rb	**0.07**	-0.01	-7.3	0.08	100.3	-0.01	-9.4	***-7.3***	***36.6***	-0.03	-35.0	-0.04	-49.6	***-42.3***	***7.3***
Sr	**134.01**	82.43	59.2	102.17	73.4	-69.39	-49.9	***59.2***	***41.1***	142.48	102.4	-73.72	-53.0	***24.7***	***77.7***
Y	**4.28**	3.82	88.5	0.28	6.5	0.16	3.6	***6.5***	***28.3***	3.18	73.5	1.93	44.6	***59.1***	***14.4***
Zr	**3.41**	6.17	192.0	-0.03	-1.0	-0.36	-11.2	***-1.0***	***67.7***	4.77	148.4	5.21	162.0	***155.2***	***6.8***
Cs[1)]	**0.01**	< -0.01	-49.7	< -0.01	-19.5	< -0.01	-59.9	***-49.7***	***13.5***	< -0.01	-80.4	< -0.01	-87.4	***-83.9***	***3.5***
Ba	**2.34**	4.63	209.3	1.16	52.3	3.57	161.4	***161.4***	***52.3***	6.69	302.7	0.02	1.0	***151.8***	***150.9***
La	**0.22**	-0.04	-20.8	-	-	-0.03	-12.2	***-16.5***	***8.4***	-0.11	-51.8	-0.08	-38.8	***-45.3***	***6.5***
Ce	**0.66**	0.00	-0.5	-	-	-	-	***-0.5***	***0.3***	-0.20	-31.1	-0.14	-21.7	***-26.4***	***4.7***
Pr	**0.13**	-0.01	-4.1	-0.01	-10.7	-0.02	-11.1	***-10.7***	***2.3***	-0.03	-21.9	-0.02	-12.8	***-17.3***	***4.5***
Nd	**0.90**	-0.04	-4.2	-0.08	-8.9	-0.15	-16.0	***-8.9***	***3.9***	-0.18	-19.4	-0.11	-12.2	***-15.8***	***3.6***
Sm	**0.43**	-0.04	-9.0	-0.03	-6.2	-0.03	-7.7	***-7.7***	***0.9***	-0.06	-12.5	-0.06	-13.4	***-13.0***	***0.4***
Eu	**0.27**	-0.02	-7.4	-0.06	-20.5	-0.07	-23.7	***-20.5***	***5.4***	-0.09	-32.9	-0.07	-24.5	***-28.7***	***4.2***
Gd	**0.66**	-0.03	-4.6	-0.06	-8.5	-0.05	-6.8	***-6.8***	***1.3***	-0.05	-7.6	-0.07	-9.7	***-8.6***	***1.0***
Tb	**0.12**	-0.01	-4.2	-	-	-	-	***-4.2***	***2.8***	-0.01	-4.6	-0.01	-5.4	***-5.0***	***0.4***
Dy	**0.81**	-0.02	-2.9	-0.03	-3.3	-0.01	-1.0	***-2.9***	***0.8***	-0.02	-2.2	-0.04	-5.2	***-3.7***	***1.5***
Ho	**0.17**	< -0.01	-1.2	-0.01	-3.4	< -0.01	-0.3	***-1.2***	***1.0***	< -0.01	-1.7	-0.01	-4.0	***-2.9***	***1.2***
Er	**0.47**	< -0.01	-0.7	< -0.01	-0.6	< 0.01	0.4	***-0.6***	***0.4***	0.01	1.2	< 0.01	0.5	***0.9***	***0.3***
Tm	**0.07**	< 0.01	0.9	< 0.01	2.1	< -0.01	-0.9	***0.9***	***1.0***	< 0.01	0.4	< 0.01	0.3	***0.3***	***0.1***
Yb	**0.42**	0.01	2.3	0.02	4.3	< 0.01	0.9	***2.3***	***1.1***	0.02	4.3	0.02	4.6	***4.4***	***0.1***
Lu	**0.06**	< 0.01	1.5	< 0.01	1.0	< 0.01	0.9	***1.0***	***0.2***	< -0.01	-1.9	< 0.01	3.9	***1.0***	***2.9***
Hf	**0.15**	0.21	135.7	-0.01	-7.3	-0.02	-10.7	***-7.3***	***48.8***	0.13	83.0	0.02	11.8	***47.4***	***35.6***
Pb	**14.82**	-	-	-10.79	-99.7	-10.72	-99.1	***-99.4***	***50.0***	-	-	-	-		***-***
U	**0.01**	0.02	354.8	0.01	124.6	< -0.01	-10.3	***124.6***	***121.7***	0.01	119.3	0.03	551.7	***335.5***	***216.2***
mass change term		0.8		0.9		1.3		**1.0**		1.0		1.6		**1.3**	
total mass change (%)								**-1.1**						**-33.7**	

Table 5.2 continued

	chlorite fault rock															
	AD5		**AD6**		**AD7**		**DT-10**		**OM15-3C**		**OM15_3E**		**AH8**		***Med (n=7)***	***MAD (n=7)***
	wt. % µg/g	***%***	**wt. % µg/g**	***%***	**wt. % µg/g**	***%***	**wt. % µg/g**	***%***	**wt. % µg/g**	***%***	**wt. % µg/g**	***%***	**wt. % µg/g**	***%***	***%***	
SiO_2	-30.42	-65.1	-35.14	-75.2	-23.12	-49.5	-23.29	-49.8	-28.72	-61.5	-38.24	-81.8	-25.04	-53.6	***-61.5***	**9.9**
Al_2O_3	-5.91	-32.8	-9.33	-51.9	-1.58	-8.8	-3.34	-18.6	-5.34	-29.7	-12.50	-69.5	-2.71	-15.1	***-29.7***	**16.0**
Fe_2O_3	11.93	225.8	8.10	153.4	12.30	232.8	27.19	514.7	12.97	245.5	0.96	18.2	13.07	247.3	***232.8***	**87.2**
MnO	0.07	79.5	0.02	22.3	0.08	91.0	0.09	97.0	0.08	84.8	< -0.01	-2.7	0.10	107.9	***84.8***	**28.1**
MgO	-2.08	-19.6	-4.63	-43.8	-1.32	-12.5	-2.10	-19.9	-1.98	-18.7	-5.82	-55.0	4.03	38.1	***-19.6***	**17.9**
CaO	-14.78	-89.9	-16.05	-97.6	-12.75	-77.5	-16.02	-97.4	-15.40	-93.6	-11.32	-68.8	-16.32	-99.2	***-93.6***	**8.3**
Na_2O	-0.94	-94.7	-0.94	-95.3	-0.92	-92.9	-0.37	-37.8	-	-	-0.81	-81.5	-0.90	-90.9	***-90.9***	**23.4**
TiO_2	-0.06	-25.9	-0.03	-13.7	-0.03	-14.1	-0.10	-43.6	-0.06	-24.7	<0.01	1.4	0.01	5.0	***-14.1***	**12.4**
LOI	3.32	170.9	1.99	102.1	5.05	259.6	9.35	480.6	5.25	269.7	4.47	229.9	9.03	464.2	***259.6***	**101.7**
Li	-0.31	-37.3	-0.55	-67.0	-0.02	-3.0	0.01	0.7	0.60	73.5	-0.28	-34.5	-0.10	-11.6	***-11.6***	**30.0**
Sc	-8.71	-20.8	-18.96	-45.4	-6.77	-16.2	-13.78	-33.0	-8.63	-20.7	-22.66	-54.2	-5.63	-13.5	***-20.8***	**11.8**
V	-16.57	-13.8	-21.68	-18.1	-22.09	-18.5	1444.52	1206.4	27.15	22.7	-30.53	-25.5	-13.77	-11.5	***-13.8***	**182.8**
Cr	-327.44	-47.8	-398.57	-58.2	-268.80	-39.2	-271.78	-39.7	-193.82	-28.3	-383.73	-56.0	236.00	34.4	***-39.7***	**18.4**
Co	40.81	101.2	113.22	280.8	47.76	118.4	122.48	303.8	75.55	187.4	-1.02	-2.5	57.82	143.4	***143.4***	**79.3**
Ni	-68.18	-39.6	-90.83	-52.8	-56.55	-32.8	30.38	17.6	-12.90	-7.5	-79.48	-46.2	21.70	12.6	***-32.8***	**23.0**
Cu	-72.50	-60.6	1914.22	1599.1	2551.61	2131.6	76515.73	63919.6	4185.20	3496.2	-106.75	-89.2	-112.57	-94.0	***1599.1***	**9970.2**
Zn	62.54	288.5	35.19	162.3	90.87	419.2	980.89	4525.4	220.27	1016.2	42.21	194.7	71.70	330.8	***330.8***	**759.3**
Rb	-0.07	-90.8	-0.08	-97.2	-0.07	-82.3	-0.06	-81.0	0.02	22.1	-0.03	-41.6	-0.08	-93.9	***-82.3***	**25.9**
Sr	-88.87	-63.9	-129.59	-93.1	-97.03	-69.7	-123.25	-88.6	-105.87	-76.1	-118.72	-85.3	-120.73	-86.8	***-85.3***	**8.4**
Y	0.31	7.1	1.57	36.3	0.27	6.2	-1.29	-29.8	-0.06	-1.5	0.17	4.0	2.22	51.3	***6.2***	**17.4**
Zr	-0.07	-2.3	4.15	129.2	1.46	45.5	1.64	51.0	-0.04	-1.2	-	-	5.75	179.0	***48.3***	**52.2**
Cs[1)]	0.00	-87.5	-	-	<-0.01	-68.0	<-0.01	-79.4	<-0.01	-1.1	<-0.01	-74.3	-	-	***-74.3***	**49.3**
Ba	-	-	-	-	0.69	31.3	-1.58	-71.6	7.02	317.2	1.16	52.7	-	-	***42.0***	**134.0**
La	0.35	168.6	-0.11	-50.9	<0.01	0.2	-0.06	-30.3	-0.05	-23.6	0.03	13.8	-0.11	-51.3	***-23.6***	**45.0**
Ce	1.10	173.2	-0.18	-28.5	0.01	1.4	-0.11	-17.0	-0.16	-25.8	0.37	58.5	-0.22	-35.3	***-17.0***	**46.1**
Pr	0.19	136.8	-0.04	-30.7	<0.01	-2.1	-0.05	-34.7	-0.05	-38.8	0.06	42.8	-0.02	-17.4	***-17.4***	**40.2**
Nd	0.84	90.2	-0.31	-33.1	-0.09	-9.8	-0.33	-35.8	-0.36	-38.5	0.24	25.6	-0.11	-11.7	***-11.7***	**30.5**
Sm	0.10	22.7	-0.08	-18.8	-0.05	-11.2	-0.11	-24.3	-0.11	-24.7	0.04	8.8	-0.02	-4.6	***-11.2***	**13.5**
Eu	-0.07	-24.3	-0.18	-63.0	-0.14	-48.5	-0.23	-80.0	-0.17	-60.2	-0.10	-34.3	-0.13	-46.7	***-48.5***	**14.0**
Gd	0.03	4.9	-0.06	-8.2	-0.03	-5.1	-0.13	-19.8	-0.13	-19.2	-0.05	-7.8	<-0.01	< -0.01	***-7.8***	**6.7**
Tb	<0.01	<0.01	<-0.01	-1.8	<0.01	-2.7	-0.02	-14.2	<-0.01	-4.0	<-0.01	-1.4	<0.01	1.5	***-1.8***	**3.0**
Dy	-0.02	-2.1	-0.02	-1.9	-0.02	-2.7	-0.07	-8.9	-0.03	-4.1	-0.05	-6.4	0.02	2.1	***-2.7***	**2.5**
Ho	<-0.01	-2.1	<-0.01	-1.2	< 0.01	-2.5	-0.02	-8.7	<0.01	1.1	-0.01	-6.3	<0.01	0.9	***-2.1***	**2.6**
Er	<-0.01	<-0.01	0.01	1.5	<-0.01	-0.4	-0.01	-2.2	0.02	3.5	<-0.01	<-0.01	0.01	3.0	***<-0.01***	**1.5**
Tm	<0.01	2.5	<0.01	4.7	<0.01	0.9	<0.01	4.1	<0.01	0.6	<0.01	2.5	<0.01	3.9	***2.5***	**1.2**
Yb	0.02	4.6	-0.01	-3.0	0.02	4.0	0.04	10.9	0.01	1.4	0.05	13.0	<-0.01	-0.2	***4.0***	**4.3**
Lu	<-0.01	-2.8	<-0.01	-0.2	<0.01	0.6	<0.01	4.8	<-0.01	-2.3	0.01	10.3	-0.01	-9.7	***-0.2***	**4.4**
Hf	-0.02	-10.9	0.03	18.4	0.03	17.1	0.06	39.7	-0.01	-8.4	0.79	513.8	0.15	96.9	***18.4***	**93.2**
Pb	-	-	-10.62	-98.1	-10.73	-99.1	-7.54	-69.6	-10.39	-96.0	-10.75	-99.2	-	-	***-98.1***	**114.5**
U	<0.01	72.8	0.06	1058.9	0.03	533.0	10.35	181558.3	0.10	1819.6	0.01	167.5	<0.01	70.1	***533.0***	**26303.8**
mass change term	1.6		2.3		1.3		1.0		1.5		2.7		1.2		**1.7**	
total mass change (%)															**-67.0**	

[1)]Cs is median value of Cs from layered gabbros in Wadi Tayin published in Peucker-Ehrenbrink et al. (2012)

In general, the alkali elements are very sensitive tracers of hydrothermal activity. Lithium is depleted in all three rock types, up to 50% in hanging wall and footwall and clasts but slightly less so in the chlorite-rich fault rocks (Figure 5.10). Lithium is known to be highly mobile during hydrothermal processes in oceanic crust: low-temperature processes lead to an increase in Li concentration in host rocks but, Li is significantly mobilised by hydrothermal processes at greenschist to sub-amphibolite facies conditions (Chan et al., 2002). Interestingly, Li is less depleted in the chlorite-rich fault rock compared to the other two rock types, despite the higher alteration degree. This may be explained by the substitution of Li for Mg, due to their similar ionic radii (~ 0.76 Å), and the high abundance of Mg-chlorite in these rocks. Both, Rb and Cs are depleted in all three rock types (Figure 5.10), suggesting they were leached and lost to the hydrothermal fluid. From black smoker systems it is well known that Rb and Cs are leached almost completely during intensive fluid-rock interaction at temperatures ~350 °C leading to Rb and Cs concentrations of black smoker fluids nearly as high as measured in basalts (Palmer and Edmond, 1989; Von Damm, 1995). Sr and Ba have an affinity for Ca, and Sr is predominantly incorporated in secondary minerals such as secondary plagioclase, prehnite and laumontite in hanging wall and footwall and is therefore gained. Even though Sr substitutes for Ca of epidote in the fault rock, it cannot counterbalance the loss of Sr due to the decay of plagioclase and therefore Sr is highly depleted in the fault rock. Ba is enriched in both the wall samples and the clasts and slightly enriched in the fault rock, although the range in the fault rock is large.

Sc, V, Cr, Ni and Pb are all depleted in hanging and footwall, clasts and the fault rock, whereas Co, Cu and Zn are depleted in hanging and footwall but present in high concentrations in the chlorite-rich fault rocks, reflecting sulphide mineralisation and their weathering products (Figure 5.10). Although clast sample AH6 shows similar behaviour to the hanging and footwall samples, the more altered sample AH7 has elevated Cu and Zn concentrations, reflecting the presence of sulphides. Mass change calculations indicate that Co, Zn, and Cu are leached out of the precursor rock during intensive hydrothermal fluid-rock interaction and precipitated locally in the fault rock. Presumably, this alteration occurred at relatively high temperatures (~350 °C), where the solubility of metals in hydrothermal fluids is significantly increased (Seewald and Seyfried, 1990). Such a metal depletion during hydrothermal alteration has been observed in other oceanic and ophiolitic crustal sections, from both the lower and the upper crust (Alt et al., 2010; Coggon et al., 2016; Coogan et al., 2006; Heft et al., 2008; Humphris et al., 1998; Nehlig et al., 1994).

For all three alteration types the behaviour of the LREE (La-Sm) is decoupled from the HREE (Gd-Lu). The HREE have been assumed to be immobile and were used to normalise mass changes. In contrast, the LREE are depleted in most samples when compared to fresh layered gabbro, with La being most depleted. A pronounced negative Eu anomaly is common to all altered rock types

(Figure 5.10) and is presumably related to both, albitisation of plagioclase (Klinkhammer et al., 1994) and fluid chemistry coupled with specific pressure and T conditions (Beermann et al., 2017). This is most extreme in the chlorite-rich fault rocks, where plagioclase is completely dissolved and replaced, leading to a release of Eu into the hydrothermal fluid. In contrast, there are three samples (AD5, AD7 and OM15-3E) that display gains of LREE and less pronounced negative Eu anomalies (Figure C.2 in Appendix C). This reflects the presence of void-filling epidote in these samples that appear to have precipitated directly from the hydrothermal fluid rather than as a replacement of primary igneous minerals. Hydrothermal epidote tends to show flat to slightly LREE-enriched patterns, with a pronounced positive Eu anomaly (Gillis et al., 1992).

U is generally highly enriched in all three rock types (Figure 5.10) whereas it shows low abundances in fresh layered gabbro. Previous studies from the upper oceanic crust have shown that U is enriched during low-temperature (<100 °C) hydrothermal process (Bloch, 1980; Hart and Staudigel, 1982), although Bach et al. (2003) suggest that U uptake continues under lower greenschist facies conditions. Ba is enriched in all three rock types, indicating an uptake during hydrothermal alteration.

5.8.3 The effect of weathering

Some of the samples are not only affected by hydrothermal alteration but also show signs of weathering (e.g. formation of oxyhydroxides, carbonates). In particular some of the fault rock samples (DT-10 and OM15-3C) show high contents of CO_2 and H_2O-bearing weathering minerals such as malachite and Fe-hydroxide. Such weathering minerals also contribute to the high observed gain of volatiles. Moreover, Fe-oxyhydroxides are proposed to host or adsorb U (Bach et al., 2003; Staudigel et al., 1996; Teagle et al., 1996), indicating that U uptake might extend to the surface weathering processes.

Additionally, calcite from laumontite-calcite veins shows the most radiogenic compositions, close to present day groundwater observed in gabbro hosted wells in Wadi Tayin and within the range of Miocene sediments that once covered the ophiolite. This indicates that calcite is likely to have formed later in the history of the ophiolite and is not necessarily related to the ocean ridge hydrothermal circulation and alteration previously described.

5.8.4 Importance of lower crustal fault zone for global elemental fluxes

To assess the hydrothermal contribution of fault zones similar to the feature described above to global geochemical cycles, we have converted our estimated hydrothermal mass changes to net elemental fluxes into or from the lower crust. Given our field observations and aerial photograph

observations on the occurrence of these altered zones (Coogan et al., 2006), we assume that similar faults are spaced every 1000m perpendicular to the ridge axis and continue along strike for 500 m, such that there is one fault zone per square kilometre of seafloor. The modelled fault zones comprise 0.6 m of fault rock and 0.4 m of clasts, flanked by a of 30 m wide alteration halo (total width, including hanging wall and footwall as observed in the field and on aerial photographs) and cut through 4000 m of gabbro (Figure 5.11). The net mass flux (F_i) of component *i* through 1 square kilometre of seafloor due to lower crustal faulting is therefore given by:

$$F_i = \sum_{z}^{FZ} V_z \rho_z \Delta m_{i-z}$$

Where $\Delta m_{i\text{-}z}$ is the average change in mass of component *i* per kilogram of rock in each sub-zone (z) of the fault zone (FZ), V_z is the volume of each sub-zone (fault rock = 1.2 x 10^6 m^3, clasts = 0.8 x 10^6 m^3, halo = 100 x 10^6 m^3) and ρ_z is the density of each sub-zone (assumed to be 3100, 2700 and 2800 kg/m^3, for the fault rock, clasts and halo respectively). Sources of uncertainty in the calculated values of F_i will include (i) geochemical analytical uncertainty; (ii) uncertainty in calculated hydrothermal mass changes, for example reflecting the choice of precursor composition, the assumptions regarding element immobility, and the compositional variability within each altered sub-zone of the fault; and (iii) uncertainty in fault geometry and spacing, and hence the modelled volumes of fault sub-zones (V_z). A full propagation of these errors is beyond the scope of this chapter. Here the net elemental mass fluxes (F_i) due to lower crustal faulting are therefore determined from the median calculated chemical changes for each sub-zone of the fault (see Section 8.2.2), with the uncertainty propagated from the median absolute deviation of the calculated chemical changes for each rock type, as compositional variability of the altered rocks is expected to be the dominant source of uncertainty. The impact of uncertainty in fault geometry/spacing is discussed below.

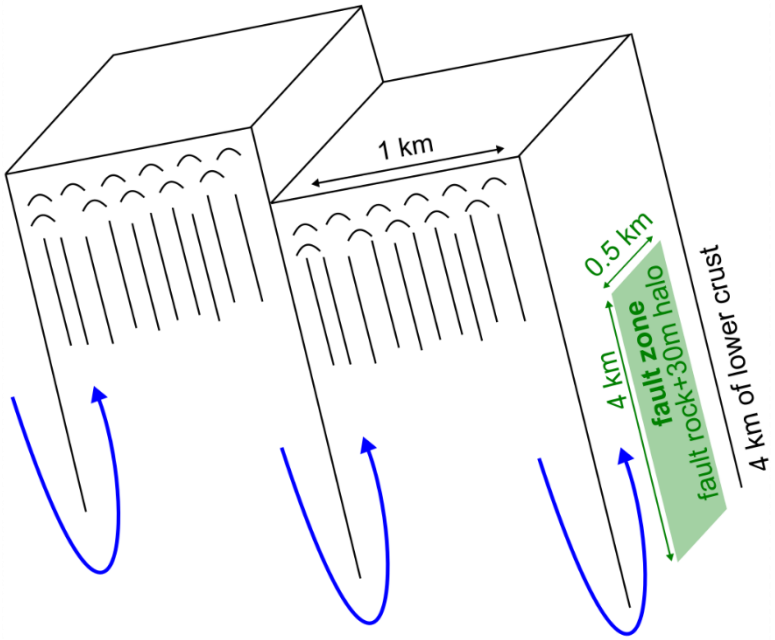

Figure 5.11: Schematic sketch showing the model set up for the elemental flux calculation. It consists of one fault zone (0.6 m of fault rock + 0.4 m of clasts with a total alteration halo of 30 m) in one block of lower crust (1 km x 1 km x 4 km). The ridge-parallel fault zone continues for 500 m and faults are spaced every 1 km perpendicular to the ridge axis.

To assess the importance of such fault zones to global hydrothermal budgets, we compare our calculated hydrothermal fluxes due to lower crustal faulting with published estimates of the hydrothermal fluxes associated with the pervasive 'background' alteration of ocean crust determined from analyses of: (i) a full section of 10 Ma ocean crust sub-aerially exposed in the sub-Antarctic Maquarie Island ophiolite; and (ii) samples of ocean crust recovered from several sites by scientific ocean drilling, that were combined to yield a composite full-crustal section (Staudigel, 2014; Table 5.3). The 2.7 km thick Macquarie crustal section includes lavas, a mineralised lava-dyke transition zone, sheeted dykes, and 1 km of lower crustal gabbros produced at a slow spreading rate (10 mm/y half rate). The hydrothermal fluxes of the composite section were predominantly determined from analyses of 120 Ma slow-spread lavas and 9 Ma ultra-slow spread gabbros. Note that there are significant discrepancies between the results of these two studies, which likely reflect both global variations in the nature and extent of hydrothermal alteration and the differing methods used to calculate the hydrothermal fluxes (see discussion in Coggon et al., 2016). Here we consider lower crustal hydrothermal faulting to make a significant contribution to global hydrothermal budgets for a given element if the magnitude of our calculated flux is >10% of the hydrothermal flux in, to or from either the Macquarie crust or the

composite crustal section (Table 5.3). Our results indicate that given our assumed fault spacing and geometry, lower crustal faults contribute significantly to the global hydrothermal budgets of Si, Ti, Al, Fe, Mn, Mg, Ca, H_2O, Cu, Zn, Sr and Cs (Figure 5.12).

Table 5.3: Comparison of estimated hydrothermal net fluxes in (+) and out (-) of the lower oceanic crust due to faulting in comparison with extrapolated global hydrothermal from Macquarie island ophiolite (Coggon et al., 2016) and a composite section (Staudigel, 2014). Significant fluxes (magnitude at least 10% of background hydrothermal flux) are highlighted in light green and fluxes of 1-10% of total Macquarie Island fluxes are highlighted in light yellow.

	Total flux Fault zone		**Macquarie Island ophiolite[a)]**	**Composite section ODP[b)]**
	median	range	range	
Major elements				
	10^{12}mol/year	10^{12}mol/year	10^{12}mol/year	10^{12}mol/year
Si	0.054	-0.857 to 0.960	-1.17 to 0.33	2.78
Ti	-0.039	-0.039 to -0.038	-0.25 to -0.08	< 0.01
Al	-0.161	-0.789 to 0.467	-1.94 to 0.10	1.89
Fe	-0.113	-0.238 to 0.0132	-0.28 to 0.66	-
Mn	-0.001	-0.003 to 0.001	-0.01 to 0.01	-
Mg	-0.503	-0.850 to -0.157	2.26 to 4.35	-2.75
Ca	-0.287	-0.569 to -0.005	-5.48 to -4.16	1.68
Na	0.060	-0.047 to 0.168	1.79 to 2.81	1.49
H2O	3.940	2.755 to 5.130	17.6 to 19.8	17.6
Trace elements				
	10^{8} mol/year	10^{8} mol/year	10^{8} mol/year	10^{8} mol/year
Cu	-6.690	-41.896 to 28.569	-78 to -51	-
Zn	-1.400	-2.311 to -0.484	-12 to -1.0	-
Rb	-0.001	-0.004 to 0.002	- 1.2 to 2.2	0.77
Sr	12.961	7.477 to 18.446	- 7.1 to 22	11.00
Cs	< -0.001	< -0.001 to - <0.001	- 0.005 to 0.04	0.01
Ba	0.368	0.297 to 0.439	3.8 to 22	-
U	< 0.001	-0.001 to 0.002	-0.03 to -0.01	0.11

[a)]Coggon et al. (2016)

[b)]Staudigel (2014)

Assuming that hydration is the main cause of volatile enrichment within the sampled fault zones, our results indicate that the previously undocumented additional water-uptake during lower crustal faulting is equivalent to 20% of the total water uptake during background alteration of ocean crust (Coggon et al., 2016; Staudigel, 2014).

For elements such as Ca, Al, Fe, Na, Zn and Sr, where the change is in the same sense, our results

clearly indicate a significant previously unquantified flux. For other elements such as Si or Cu, where the change is not the same sense and elements previously were assumed to leave the crust, it may be that they are partially remobilised into the fault zones.

Here we have shown that if the lower crustal faulting observed within the Semail ophiolite is globally representative of faulting within lower ocean crust, then such fault zones contribute significantly to the global hydrothermal budgets for many elements.

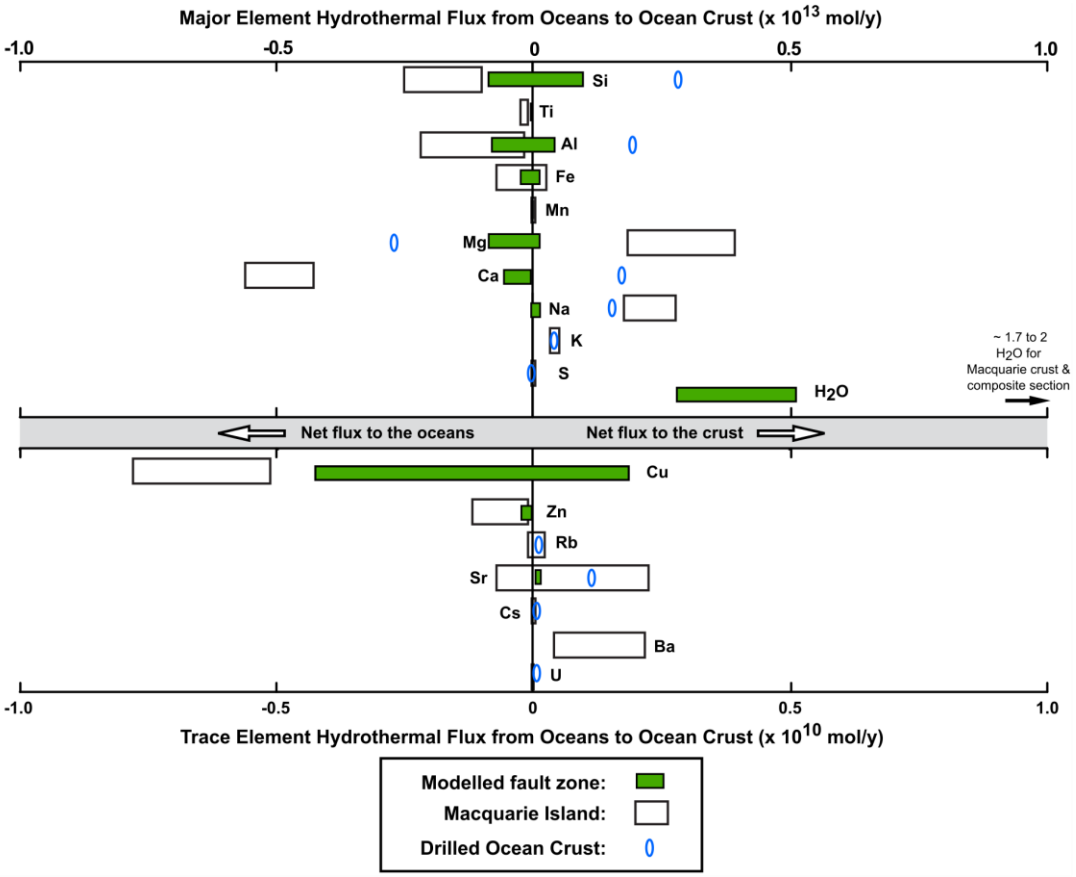

Figure 5.12: Hydrothermal fluxes (mol/y) extrapolated from estimated mass changes occurring during hydrothermal alteration in a lower crustal fault (green bars). In comparison hydrothermal fluxes calculated from pervasive hydrothermal background alteration for the Macquarie Island ophiolite (white bars; Coggon et al., 2016) and a composite crustal section recovered by scientific ocean drilling (blue ovals; Staudigel, 2014). Diagram modified after Coggon et al. (2016). Fluxes for Ti, Mn, Cs, Ba and U are too small to be shown in this diagram.

5.8.5 Limitations and uncertainties on the calculation of global elemental fluxes

One of the main uncertainties when calculating elemental fluxes and extrapolating them to the global chemical budget, is the assumption regarding the fault geometry. For the discussed chlorite-rich fault zone, the dominant mass fraction is the halo and therefore the width of the halo is the greatest source of uncertainty. If the halo width of total 30 m estimated from field observations was an overestimate, the consequential elemental fluxes in and out of the fault zone will be overestimated too.

Table 5.4: Comparison of estimated hydrothermal net fluxes in (+) and out (-) of the lower oceanic crust due to faulting with an estimated halo of 15 m. Elemental fluxes are compared to the initial calculation assuming a halo width of 30m and the extrapolated global hydrothermal from Macquarie island ophiolite (Coggon et al., 2016) and a composite section (Staudigel, 2014). Fluxes of at ≥ 10% of the background hydrothermal flux of Macquarie Island are highlighted in light green and fluxes of 1-10 % of Macquarie Island ophiolite are highlighted in light yellow.

	Total flux Fault zone (15 m halo)		**Total flux Fault zone (30 m halo)**		**Macquarie Island ophiolite[a)]**	**Composite section ODP[b)]**
	median	range	median	range	range	
Major elements						
	10^{12}mol/year	10^{12}mol/year	10^{12}mol/year	10^{12}mol/year	10^{12}mol/year	10^{12}mol/year
Si	-0.057	-0.513 to 0.399	0.054	-0.857 to 0.960	-1.17 to 0.33	2.78
Ti	-0.002	-0.003 to -0.002	-0.039	-0.039 to -0.038	-0.25 to -0.08	0
Al	-0.068	-0.382 to 0.247	-0.161	-0.789 to 0.467	-1.94 to 0.10	1.89
Fe	-0.015	-0.079 to 0.048	-0.113	-0.238 to 0.0132	-0.28 to 0.66	-
Mn	< -0.001	-0.001 to 0.001	-0.001	-0.003 to 0.001	-0.01 to 0.01	-
Mg	-0.164	-0.337 to 0.010	-0.503	-0.850 to -0.157	2.26 to 4.35	-2.75
Ca	-0.131	-0.273 to 0.010	-0.287	-0.569 to -0.005	-5.48 to -4.16	1.68
Na	0.015	-0.039 to 0.068	0.060	-0.047 to 0.168	1.79 to 2.81	1.49
H_2O	1.240	0.646 to 1.834	3.940	2.755 to 5.130	17.6 to 19.8	17.6
Trace elements						
	10^{8} mol/year	10^{8} mol/year	10^{8} mol/year	10^{8} mol/year	10^{8} mol/year	10^{8} mol/year
Cu	2.291	-32.727 to 37.303	-6.690	-41.896 to 28.569	-78 to -51	-
Zn	-0.269	-0.881 to 0.342	-1.400	-2.311 to -0.484	-12 to -1.0	-
Rb	< -0.001	-0.002 to 0.0001	-0.001	-0.004 to 0.002	- 1.2 to 2.2	0.77
Sr	3.742	0.997 to 6.486	12.961	7.477 to 18.446	- 7.1 to 22	11.00
Cs	< -0.001	< -0.001 to - <0.001	< -0.001	< -0.001 to - <0.001	- 0.005 to 0.04	0.01
Ba	0.113	0.078 to 0.149	0.368	0.297 to 0.439	3.8 to 22	-
U	< 0.001	-0.001 to 0.001	< 0.001	-0.001 to 0.002	-0.03 to -0.01	0.11

[a)] Coggon et al., 2016
[b)] After Staudigel (2014)

Therefore, it needs to be tested whether chemical fluxes remain a significant contribution to the global chemical budget if the halo fraction is smaller. Hence, fluid fluxes were calculated assuming a considerably smaller halo of 15 m instead of the 30 m. Such a halo width is comparable to halo widths observed from other fault zones in Wadi Gideah (see Figure 4.11 in Chapter 4).

For some elements such as Si, Sr and Cs the calculation with a halo width of 15 m still results in a significant contribution (≥ 10% of Macquarie Island ophiolite) to the global chemical budget. For most other elements (Al, Fe, Mg, Ca, H_2O, Cu and Zn) the calculation shows net fluxes of 1-10 % of the total Maquarie Island ophiolite contribution (Table 5.4). This is still a considerable amount when comparing to the global flux resulting from background hydrothermal alteration. This calculation also shows that with a halo size of 15 m instead of 30 m, the halo fraction is less dominant compared to the fault rock and clast fraction. This becomes clear when comparing elements such as Si or Cu (see Table 5.4). Although Si was overall gained with a large halo, a Si loss results from a calculation with a halo only half the width. Similarly, Cu is lost when the halo fraction is large but Cu is gained when the halo is narrower and the fault rock and clast fractions become relatively more important.

In addition, to the fault geometry the frequency of fault (e.g., faults/km) also remains uncertain. Several studies from the East Pacific Rise on fast-spreading oceanic crust indicate that faults occur every few hundred metres (e.g., Bicknell et al., 1987; Bohnenstiehl and Carbotte, 2001; Edwards et al., 1991). Therefore, if we have underestimated the spacing of lower crustal fault zones (e.g. fault spacing of only a few hundred metres instead of 1 kilometre), then their contribution to global hydrothermal fluxes might be even more significant.

5.9 Conclusions

Secondary mineral assemblages, major- and trace element mass change calculations and strontium isotope compositions suggest that this chlorite-rich fault zone represents a fossilized discharge zone of hot, upwelling hydrothermal fluids with Sr-isotopic compositions in the range $^{87}Sr/^{86}Sr$ = 0.7043-0.7048, similar to epidote present in hydrothermal veins in the Samail ophiolite. Chlorite thermometry indicates formation temperatures of 300-350 °C for the fault rock and calculations based on silica solubility in hydrothermal fluids give an estimate of high fluid/rock ratios up to 450:1-900:1. Due to intensive fluid-rock interaction elements were mobilized and locally redistributed. Ca, Na, Si, Al, Mg, Mn, Fe, Ti as well as Pb, Rb, Cs, Cr, N, Sc, V, Cu, LREE, Co, Zn and Li were leached and either transported away by the passage of hydrothermal fluids or were partially incorporated into secondary phases such as chalcopyrite and pyrite (Fe, Cu, Zn, Co) or epidote (LREE) in the fault rock itself or into secondary phases such as plagioclase, prehnite and

laumontite (Na, Sr) in the wall rocks. H_2O and other elements such as Ba and U were transported with the hydrothermal fluid and scavenged within the system. Exchange of the hydrothermal fluid with the rock is limited to between 1 and 30 metres from the fault zone, as evidenced by the alteration around the fault zone observed in the field. Our results suggest that hydrothermal fluids reach deep into the lower plutonic oceanic crust and, hence, provide an efficient cooling system being the prerequisite for in situ crystallization and accretion as proposed in the sheeted sills model.

From calculated mass changes we estimated global hydrothermal fluxes for one lower crustal fault zone per one cube of lower oceanic crust (1 km x 1 km x 4 km), assuming a crustal production rate of 5 km^2/y. Our results indicate that given the assumed fault spacing and geometry, lower crustal faults contribute significantly to the global hydrothermal budgets of Si, Ti, Al, Fe, Mn, Mg, Ca, H_2O, Cu, Zn, Sr and Cs.

Chapter 6 Conclusions and outlook

6.1 Conclusions

The aim of this thesis was to explore and further constrain hydrothermal alteration in the lower oceanic crust, outcropping in the Samail ophiolite of the Sultanate of Oman. To do so, an outcrop located in the lower layered gabbro section was mapped and sampled in detail and cross-cutting hydrothermal veins and alteration was characterised from outcrop- to microscopic-scale. In addition, zones of intense hydrothermal alteration, from the Moho transition zone up to the sheeted dyke complex, were described and characterised in terms of secondary mineral assemblages and Sr-isotope composition. As part of the last chapter, mass-change calculations were carried out for one fault zone located in the lower crust in order to quantify elemental changes related to hydrothermal fluid-rock exchange. Calculated mass-changes were extrapolated to global hydrothermal fluxes and the impact of a lower crustal fault zone to the global hydrothermal budget was assessed. In the following chapter the key results of this study are summarised and ideas for further work are presented.

Cross-cutting relationships of high-to low temperature hydrothermal alteration in the lower oceanic crust, evidence from detailed mapping of an outcrop located in the lower layered gabbro section of the Samail ophiolite

Cross-cutting relationships of hydrothermal veins indicate a clear and continuous alteration sequence from ~800 °C down to temperatures < 100-200 °C. The highest temperatures are recorded in poikilitc brown hornblende partially replacing clinopyroxene and in hornblende veinlets cross-cutting the gabbroic texture. Amphibole alteration grades into greenschist facies with the occurrence of green hornblende and actinolite. Greenschist facies alteration is dominated by centimetre-sized epidote-clinozoisite veins displaying extensive alteration haloes. The transition to lower temperature alteration is marked by the occurrence of prehnite and calcite filling open space and prehnite veinlets cross-cutting earlier alteration. The youngest alteration phase is marked by laumontite veinlets.

Epidote-clinozoisite yields strontium isotope compositions of $^{87}Sr/^{86}Sr$=0.7047-0.7049, within uncertainty of epidote compositions measured from other localities in the ophiolite, and are distinctively elevated from fresh MORB values and fresh gabbro in the ophiolite. These Sr-isotope compositions indicate formation from a seawater-derived hydrothermal fluid. Sr-isotope composition of prehnite is slightly more radiogenic than epidote-clinozoisite compositions and

evolution of the hydrothermal fluid towards a less rock-dominated composition is proposed. Laumontite in late, cross-cutting veinlets yields Sr-isotope compositions of $^{87}Sr/^{86}Sr$=0.7065 – 0.7073, supporting formation from a more radiogenic hydrothermal fluid at relatively low temperatures, possibly as the hydrothermal system cooled. It is likely that these veinlets formed during obduction.

Epidote-clinozoisite veins show pronounced alteration haloes with whole rock gabbro being partially to almost completely altered and dominated by a secondary mineral assemblage of epidote-clinozoisite + chlorite + actinolite + hornblende ± albite ± prehnite. For the most altered halo gabbro, $^{87}Sr/^{86}Sr$ ratios are identical to hydrothermal fluid compositions, indicating a full exchange with the hydrothermal fluid. A positive correlation between vein aperture and observed alteration is observed.

Evidence for localised discharge zones of hydrothermal fluids in the lower ocean crust

Decimetres-to metres-wide zones of intense hydrothermal alteration were studied from a range of levels of the lower oceanic crust exposed in Wadi Gideah. These zones were completely re-equilibrated under greenschist-facies conditions and are characterised by mineral assemblages typically observed in hydrothermal upflow zones in the upper oceanic crust. The studied zones were classified as (i) fluid-flow zones displaying a mainly static replacement and growth of secondary minerals and (ii) fault zones, where clear indicators of movements such as the occurrence of fault gouge or brecciation, could be detected. Fluid-flow zones are characterised by a secondary mineral assemblage of epidote + chlorite ± quartz ± prehnite ± sulphides. Sulphides are pervasively weathered. Quartz-rich assemblages were observed in the upper part of the lower crust. Fault zones display a secondary mineral assemblage of chlorite + epidote ± quartz ± sulphides. Chlorite replaces primary mineral assemblages and yields relatively Fe-rich compositions, distinct from chlorite observed in background altered gabbros from outside fault zones. Calculated formation temperatures for chlorite from all three observed fault zones throughout the lower crust range between 300-350 °C. The widespread occurrence of sulphides within both fluid-flow and fault zones further indicates alteration with discharging, metal-saturated hydrothermal fluids at relatively high temperatures (~350 °C), at which metal solubility is significantly increased.

Whole rock and mineral separates from fluid-flow zones and fault zones yield Sr-isotope compositions of $^{87}Sr/^{86}Sr$=0.7043-0.7049. These compositions are more radiogenic than fresh layered gabbro from the Samail ophiolite and are remarkably similar to Sr-isotope compositions measured from epidosites in the sheeted dyke complex and to whole rock composition of the sheeted dykes in general. No systematic decrease with depth of the $^{87}Sr/^{86}Sr$ ratio of either

epidote mineral separates from the fluid-flow zones and veins outside, nor from fluid-flow and fault zone whole rock, could be observed. Therefore, alteration within these zones occurred in the presence of a fluid similar in composition to discharging hydrothermal fluids that produced the alteration observed in the sheeted dykes. In order to move the observed metasomatic front down to the base of the crust, a channelled recharge is regarded as likely. The observation of high-temperature amphiboles within a fault zone, now partially overgrown by chlorite, indicates an earlier and higher-temperature alteration within this fault. It further indicates that fluid-pathways may be used multiple times, with fluid recharge and discharge channelled along the same zones of high-permeability.

Fluid-flow and fault zones show orientations parallel to earlier and higher-temperature amphibole veins as well as parallel to other epidote-clinozoisite veins. In the wider structural context, fluid-flow and fault zones are predominantly parallel to sub-parallel to the mean orientation of the sheeted dykes in the Ibra area. This indicates formation of hydrothermal veins, fluid-flow and fault zones within the same stress-field as the sheeted dykes, hence formation during the initial spreading of the ocean crust is considered to be likely.

Elemental mass-changes during lower crustal faulting - indications from a deep hydrothermal fault zone

Detailed petrographic and geochemical descriptions of one chlorite-rich fault zone in the lower crust exposed in Wadi Gideah was carried out and mass-changes related to intensive hydrothermal fluid-rock exchange were calculated for the fault rock, clasts and wall rocks. Field observations indicate that the exchange of hydrothermal fluid with the rock is limited to between 1 and 30 metres from the fault zone, as evidenced by the alteration around the fault zone.

Mass-change calculations show that the chlorite-rich fault rock as well as the clast samples embedded in the fault rock underwent a significant mass-loss of ~ 67 % for the fault rock and ~ 34% for the clasts. Calculations for the wall rocks show that no significant mass-change (1%) occured within the hanging- and footwall of the fault zone. Due to intensive exchange of the rock with a hydrothermal fluid at temperatures of approximately 300-350 °C, indicated by chlorite thermometry, most elements were mobilised and locally redistributed. Elements were leached and either transported away by the passage of the hydrothermal fluid or were partially incorporated into secondary phases such as chalcopyrite and pyrite (Fe, Cu, Zn, Co), or epidote (LREE) in the fault rock itself or into secondary phases such as plagioclase, prehnite and laumontite (Na, Sr) in the wall rocks. H_2O and other elements such as Ba, U were transported with the hydrothermal fluid into the system.

Fluid/rock ratios were estimated based on silica solubility in hydrothermal fluids and give a range of up to 450-900. Such high fluid-rock ratios have been reported previously from hydrothermal upflow zones in the upper ocean crust.

Calculated mass-changes were extrapolated to estimate global hydrothermal fluxes. It was assumed that one ridge-parallel lower crustal fault zone occurs per one cuboid of lower oceanic crust (1x1x4 km). A spreading rate of 5 km^2/y was assumed. Global fluxes were calculated for major elements and several key trace elements and were compared to hydrothermal fluxes resulting from pervasive background alteration throughout the whole ocean crust (Coggon et al., 2016; Staudigel, 2014). Calculated fluxes result in significant, previously undocumented fluxes of Si, Ti, Al, Fe, Mn, Mg, Ca, Cu, Zn, Sr and Cs in and out of the lower crust due to hydrothermal alteration related to this fault zone. This calculation further highlights the importance of lower crustal fault zones in constraining global fluxes resulting from hydrothermal alteration throughout the ocean crust.

6.2 Future work

The results of this thesis highlight three main possibilities for further work:

What are the chemical changes related to other described fluid-flow and fault zones observed in Wadi Gideah?

The calculated mass-changes and hydrothermal fluid fluxes of Chapter 5 show considerable mass-changes during intense hydrothermal alteration and previously unquantified elemental fluxes related to lower crustal faulting, extrapolated from one fault zone in Wadi Gideah. The question is whether similar calculations for the other observed fluid-flow and fault zones would indicate similar results. Furthermore, mass-changes from petrographically different zones could be expanded to global elemental fluxes, similar to what has been performed for the fault zone in Chapter 5. Expanding the global flux calculation to a wider range of fault zones and fluid-flow zones would further help to better constrain inputs to the global hydrothermal budget from highly altered zones in the lower oceanic crust

What are the chemical changes related to pervasive background alteration in the lower oceanic crust of the Samail ophiolite and how do they compare to chemical changes calculated for the fault zones in Wadi Gideah?

Calculated mass changes and elemental fluxes due to faulting in Chapter 5 have been compared to published estimates of the hydrothermal fluxes associated with pervasive “background” alteration of oceanic crust formed at different ages and different spreading rates than the crust

studied here. Consequently, there are discrepancies and errors associated with such a comparison (see discussion in Chapter 5.8.4), though these two studies are the only two published estimates of chemical changes associated with hydrothermal alteration in the oceanic crust. Therefore, it would be very usefuland valuable to calculate chemical changes and elemental fluxes due to background hydrothermal alteration in the lower oceanic crust. Wadi Gideah would be a suitable location to do such a study.

What is the role of lower crustal fluid-flow and fault zones in cooling the lower oceanic crust? Can time-integrated fluid-flux calculations be used to constrain the thermal effects of focussed fluid-flow in the lower crust of the Samail ophiolite?

Within this study, Sr-isotope compositions of zones of channelled fluid-flow such as faults and fluid-flow zones were documented down to the base of the crust. If it is assumed that these zones not only served for discharge of the hydrothermal fluid, but also for the recharge, time-integrated fluid-fluxes could be calculated, using for example the crack model of Bickle (1992). Calculated fluid-fluxes could be compared to estimated heat fluxes of the lower crust in the ophiolite and used to evaluate how much heat such zones extract and whether hydrothermal cooling of the lower oceanic crust via fault zones is plausible or not.

Appendix A

A.1 Microprobe data of primary and secondary minerals of Chapter 3

This is an electronic appendix containing all electron microprobe analysis in an excel file.

A.2 Whole rock and mineral separates major- and trace elements of samples presented in Chapter 3

This is an electronic appendix containing major- and trace element data of samples presented in Chapter 3.

Appendix B

B.1 Microprobe data of primary and secondary minerals of Chapter 4

This is an electronic appendix containing electron microprobe data of all primary and secondary minerals presented in Chapter 4.

B.2 Whole rock and mineral separates trace element data of samples presented in Chapter 4

B.3

This is an electronic appendix containing major- and trace element data of samples presented in Chapter 4.

B.4 Sample description of collected sheeted dyke samples Ibra area

This is an electronic appendix containing containing field and sample descriptions of sheeted dyke samples (P. Kelemen) presented in Chapter 4.

Appendix C

C.1 Additional Figures of Chapter 5

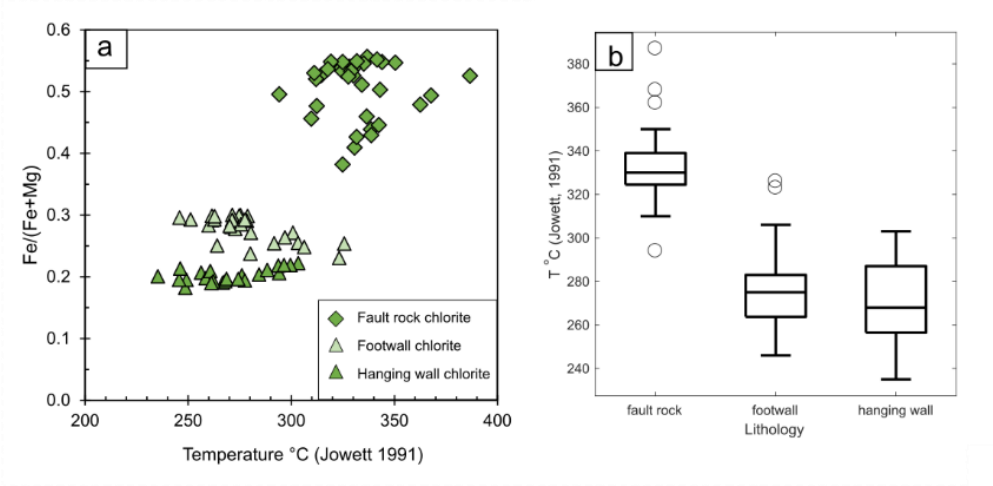

Figure C.1: Chlorite formation temperature calculated using the thermometer of Jowett (1991). (a) Calculated temperatures versus Fe/(Fe+Mg) concentration and (b) Boxplot showing median value of each lithology and the box representing the Q1 (25th percentile) and Q3 (75th percentile). Circles represent outliers.

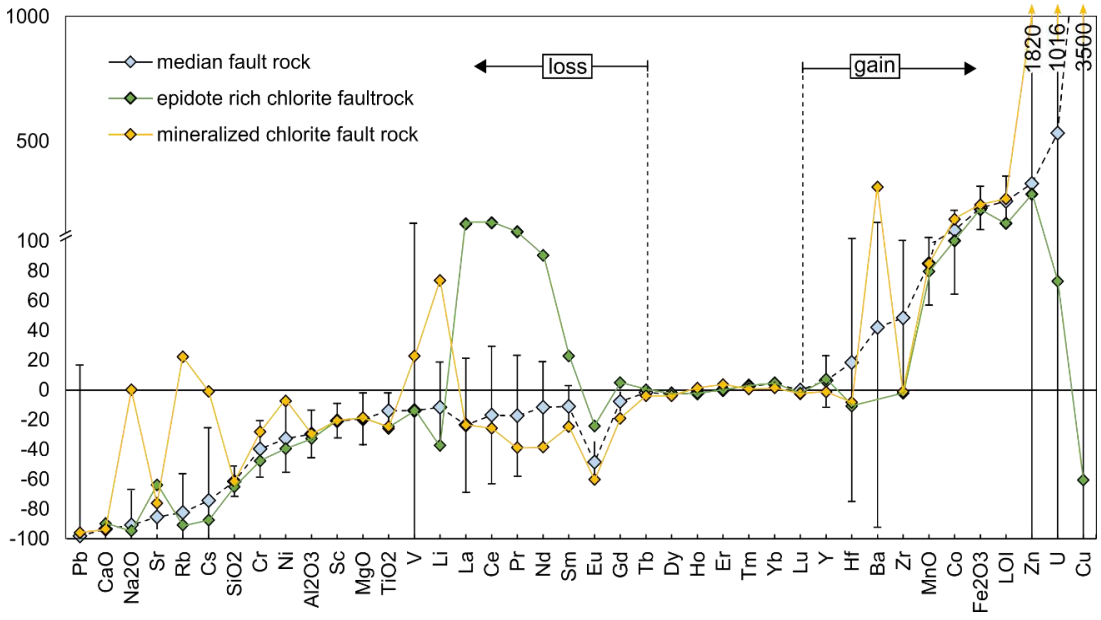

Figure C.2: Median major-and trace element gains and losses for chlorite rich fault rock compared to the epidote rich fault rock sample AD5 and mineralised fault rock sample OM15-3C. Elements are sorted by increasing mass gain (except for REEs). Error bars represent median absolute deviation (MAD) of median fault rock.

C.2 Composition of layered gabbro around fault zone in Chapter 5

Table C.1: Composition of W. Gideah rock samples / background gabbros (major elements in wt%, ICP-OES data; trace elements in µg/g, ICP-MS data)

Sample			**OM12-39**	**OM12-26**	**OM12-25**	**OM10-25**	**OM12-38**	**OM10-26**	**OM12-35**	**OM11-26**
Unit			**LG**	**LG**	**LG**	**LG**	**LG**	**LG**	**LG**	**LG**
UTM x			**655820**	**655385**	**655518**	**655711**	**655391**	**655427**	**655391**	**655407**
UTM y			**2532140**	**2532265**	**2532337**	**2532310**	**2532499**	**2532588**	**2532776**	**2532906**
h.a.m[1)]			**1304**	**1246**	**1212**	**1225**	**1136**	**1094**	**1006**	**945**
	method[2)]	**LOQ**								
SiO_2	calc		45.8	47.1	45.9	47.8	45.7	46.9	46.6	47.2
Al_2O_3	ICP-OES	0.20	17.9	19.4	20.1	14.7	18.1	17.1	18.2	17.6
Fe_2O_3T	ICP-OES	0.02	5.3	4	4.3	5.5	5.8	5.7	4.7	5.2
MnO	ICP-OES	0.001	0.09	0.07	0.07	0.11	0.1	0.1	0.09	0.09
MgO	ICP-OES	0.01	11.9	8.5	10	12.5	12	10.7	9.5	10.5
CaO	ICP-OES	0.10	15.6	17.7	16.4	17	15	16.6	16.2	16.5
Na_2O	ICP-OES	0.20	0.8	1.14	0.86	0.7	1.03	0.98	1.4	1
K_2O	ICP-OES	0.020	< 0.02	< 0.02	< 0.02	< 0.02	< 0.02	< 0.02	< 0.02	< 0.02
TiO_2	ICP-OES	0.020	0.19	0.24	0.17	0.25	0.2	0.24	0.21	0.24
P_2O_5	ICP-OES	0.080	< 0.08	< 0.08	< 0.08	< 0.08	< 0.08	< 0.08	< 0.08	< 0.08
LOI[3)]			2.44	1.9	2.2	1.48	2	1.78	3.09	1.7
Total	calc		100	100	100	100	100	100	100	100
Li	liq.-ICP-MS	0.5	0.951	0.483	0.817	1.06	0.816	1.064	0.826	0.479
Sc	liq.-ICP-MS	0.5	36.0	44.8	33.5	53.9	34.8	53.2	38.8	45.2
V	liq.-ICP-MS	0.5	100	125	91	149	98	148	115	140
Cr	liq.-ICP-MS	5	807	1070	476	750	757	469	589	621
Co	liq.-ICP-MS	0.2	41.4	24.1	33.1	41.9	45.3	44.5	30.6	39.2
Ni	liq.-ICP-MS	0.5	240	90	172	204	227	173	144	164
Cu	liq.-ICP-MS	1	131	69	90	151	108	200	109	155
Zn	liq.-ICP-MS	0.5	24.0	15.2	17.2	21.7	21.6	22.8	21.1	22.5
Rb	liq.-ICP-MS	0.2	0.057	0.045	0.084	< 0.2	0.080	0.092	0.082	0.065
Sr	liq.-ICP-MS	1	119	155	140	101	142	140	137	138
Y	LA-ICP-MS	0.01	3.83	4.40	3.10	5.56	3.74	4.55	4.25	4.79
Zr	LA-ICP-MS	0.015	2.84	3.40	2.95	4.06	3.02	3.79	3.03	4.22
Cs	liq.-ICP-MS	0.01	< 0.01	< 0.01	< 0.01	< 0.01	< 0.01	< 0.01	< 0.01	< 0.01
Ba	liq.-ICP-MS	1	2.134	2.537	3.284	2.03	2.213	2.210	1.925	2.408
La	liq.-ICP-MS	0.2	0.208	0.239	0.203	0.127	0.197	0.257	0.207	0.284
Ce	liq.-ICP-MS	0.5	0.606	0.724	0.564	0.622	0.579	0.738	0.644	0.811
Pr	liq.-ICP-MS	0.05	0.115	0.146	0.105	0.155	0.113	0.148	0.130	0.160
Nd	liq.-ICP-MS	0.1	0.777	0.969	0.687	1.06	0.772	0.999	0.899	1.049
Sm	liq.-ICP-MS	0.05	0.369	0.462	0.314	0.529	0.368	0.466	0.418	0.479
Eu	liq.-ICP-MS	0.01	0.247	0.297	0.222	0.286	0.236	0.290	0.295	0.294
Gd	liq.-ICP-MS	0.02	0.569	0.712	0.480	0.856	0.565	0.727	0.649	0.755

Tb	LA-ICP-MS	0.005	0.105	0.128	0.086	0.152	0.101	0.127	0.123	0.139
Dy	LA-ICP-MS	0.015	0.707	0.892	0.596	1.02	0.682	0.858	0.802	0.953
Ho	LA-ICP-MS	0.005	0.153	0.184	0.127	0.218	0.146	0.180	0.172	0.198
Er	LA-ICP-MS	0.015	0.414	0.500	0.338	0.608	0.394	0.482	0.463	0.547
Tm	LA-ICP-MS	0.005	0.059	0.070	0.049	0.090	0.056	0.067	0.066	0.078
Yb	LA-ICP-MS	0.015	0.370	0.457	0.310	0.536	0.336	0.430	0.391	0.491
Lu	LA-ICP-MS	0.005	0.053	0.065	0.046	0.074	0.049	0.061	0.060	0.071
Hf	LA-ICP-MS	0.015	0.123	0.166	0.114	0.180	0.133	0.168	0.140	0.189
Pb	liq.-ICP-MS	0.1	8.5	20.1	32.3	0.089	13.1	0.145	44.0	0.220
Th	LA-ICP-MS	0.005	< 0.005	< 0.005	0.010	< 0.005	< 0.005	< 0.005	< 0.005	< 0.005
U	liq.-ICP-MS	0.005	< 0.005	0.005	0.006	0.005	< 0.005	0.007	< 0.005	< 0.005

[1)] height above the Moho transition zone, calculated using a dip of 28°
[2)] SiO2 calculated to 100%, liq-ICP-MS by acid digestion see: Garbe-Schönberg, C. D. (1993), LA-ICP-MS on pressed poder tablets see: Garbe-Schönberg, D., & Müller, S. (2014)

[3)] LOI determined by loss-on-ignition experiment at 1000 °C

C.3 Electron microprobe analysis of primary and secondary minerals presented in Chapter 5

This is an electronic appendix containing all electron microprobe analysis of plagioclase, amphibole, epidote, chlorite, prehnite and laumontite

Bibliography

Aghaei, O., Nedimović, M.R., Carton, H., Carbotte, S.M., Canales, J.P., Mutter, J.C., 2014. Crustal 5.ness and Moho character of the fast-spreading East Pacific Rise from 9° 42′ N to 9° 57′ N from poststack-migrated 3-D MCS data. Geochemistry, Geophysics, Geosystems 15, 634–657.

Alabaster, T., Pearce, J.A., Malpas, J., 1982. The volcanic stratigraphy and petrogenesis of the Oman ophiolite complex. Contributions to Mineralogy and Petrology 81, 168–183.

Alt, J.C., 1998. Very low-grade hydrothermal metamorphism of basic igneous rocks. Low-Grade Metamorphism 169–201.

Alt, J.C., 1995. Subseafloor processes in mid-ocean ridge hydrothermal systems. Geophysical Monograph-American GEophysical Union 91, 85.

Alt, J.C., 1994. A sulfur isotopic profile through the Troodos ophiolite, Cyprus: primary composition and the effects of seawater hydrothermal alteration. Geochimica et cosmochimica acta 58, 1825–1840.

Alt, J.C., Kinoshita, H., Stokking, L.B., Others, A. 26, 1993. Proceedings of the Ocean Drilling Program, Vol. 148, Initial Reports, Costa Rica Rift. Ocean Drilling Program.

Alt, J.C., Laverne, C., Coggon, R.M., Teagle, D.A.H., Banerjee, N.R., Morgan, S., Smith-Duque, C.E., Harris, M., Galli, L., 2010. Subsurface structure of a submarine hydrothermal system in ocean crust formed at the East Pacific Rise, ODP/IODP Site 1256. Geochemistry, Geophysics, Geosystems 11, 1–28. doi:10.1029/2010GC003144

Alt, J.C., Teagle, D.A.H., 2000. Hydrothermal alteration and fluid fluxes in ophiolites and oceanic crust. Special Papers-Geological Society of America 273–282.

Apted, M.J., Liou, J.G., 1983. Phase relations among greenschist, epidote-amphibolite, and amphibolite in a basaltic system. American Journal of Science 283, 328–354.

Arnulf, A.F., Singh, S.C., Pye, J.W., 2014. Seismic evidence of a complex multi-lens melt reservoir beneath the 9° N Overlapping Spreading Center at the East Pacific Rise. Geophysical Research Letters 41, 6109–6115.

Augustin, N., Lackschewitz, K.S., Kuhn, T., Devey, C.W., 2008. Mineralogical and chemical mass changes in mafic and ultramafic rocks from the Logatchev hydrothermal field (MAR 15 N). Marine Geology 256, 18–29.

Bach, W., Bernhard, P.E., Hart, S.R., Blusztajn, J.S., 2003. Geochemistry of hydrothermally altered oceanic crust: DSDP/ODP Hole 504B-Implications for seawater-crust exchange budgets and Sr-and Pb-isotopic evolution of the mantle. Geochemistry, Geophysics, Geosystems 4, 40–55. doi:10.1029/2002GC000419

Barker, A.K., Coogan, L.A., Gillis, K.M., Hayman, N.W., Weis, D., 2010. Direct observation of a fossil high-temperature, fault-hosted, hydrothermal upflow zone in crust formed at the East Pacific Rise. Geology 38, 379–382.

Bédard, J.H., Sparks, R.S.J., Renner, R., Cheadle, M.J., Hallworth, M.A., 1988. Peridotite sills and metasomatic gabbros in the Eastern Layered Series of the Rhum complex. Journal of the Geological Society 145, 207–224.

Bednarz, U., Schmincke, H.U., 1989. Mass transfer during sub-seafloor alteration of the upper Troodos crust (Cyprus). Contributions to Mineralogy and Petrology 102, 93–101. doi:10.1007/BF01160193

Beermann, O., Garbe-Schönberg, D., Bach, W., Holzheid, A., 2017. Time-resolved interaction of seawater with gabbro: An experimental study of rare-earth element behavior up to 475° C, 100 MPa. Geochimica et Cosmochimica Acta 197, 167–192.

Bickle, M.J., 1992. Transport mechanisms by fluid-flow in metamorphic rocks; oxygen and strontium decoupling in the Trois Seigneurs Massif; a consequence of kinetic dispersion? American Journal of Science 292, 289–316.

Bickle, M.J., Teagle, D.A.H., 1992. Strontium alteration in the Troodos ophiolite: implications for fluid fluxes and geochemical transport in mid-ocean ridge hydrothermal systems. Earth and Planetary Science Letters 113, 219–237.

Bicknell, J.D., Sempere, J.-C., Macdonald, K.C., Fox, P.J., 1987. Tectonics of a fast spreading center: A Deep-Tow and Sea Beam survey on the East Pacific Rise at 19 30’ S. Marine Geophysical Researches 9, 25–45.

Bird, D.K., Schiffman, P., Elders, W.A., Williams, A.E., McDowell, S.D., 1984. Calc-silicate mineralization in active geothermal systems. Economic geology 79, 671–695.

Bird, D.K., Spieler, A.R., 2004. Epidote in geothermal systems. Reviews in Mineralogy and Geochemistry 56, 235–300.

Bird, P., 2003. An updated digital model of plate boundaries. Geochemistry, Geophysics, Geosystems 4.

Bloch, S., 1980. Some factors controlling the concentration of uranium in the world ocean. Geochimica et Cosmochimica Acta 44, 373–377.

Bohnenstiehl, D.R., Carbotte, S.M., 2001. Faulting patterns near 19 30' S on the East Pacific Rise: Fault formation and growth at a superfast spreading center. Geochemistry, Geophysics, Geosystems 2.

Bompard, N., 2018. An isotopic study of the chemical evolution of groundwater in the peridotite aquifers of the Oman-United Arab Emirates ophiolite. PhD thesis., University of Southampton.

Bosch, D., Jamais, M., Boudier, F., Nicolas, A., Dautria, J.M., Agrinier, P., 2004. Deep and high-temperature hydrothermal circulation in the Oman ophiolite - Petrological and isotopic evidence. Journal of Petrology 45, 1181–1208.

Boudier, F., Ceuleneer, G., Nicolas, A., 1988. Shear zones, thrusts and related magmatism in the Oman ophiolite: Initiation of thrusting on an oceanic ridge. Tectonophysics 151, 275–296. doi:10.1016/0040-1951(88)90249-1

Boudier, F., Nicolas, A., 2007. Comment on "dating the geologic history of Oman's Semail ophiolite: Insights from U-Pb geochronology" by C. J. Warren, R. R. Parrish, D. J. Waters and M. P. Searle. Contributions to Mineralogy and Petrology 154, 111–113. doi:10.1007/s00410-007-0189-5

Boudier, F., Nicolas, A., Ildefonse, B., 1996. Magma chambers in the Oman ophiolite: fed from the top and the bottom. Earth and Planetary Science Letters 144, 239–250.

Brabander, D.J., Giletti, B.J., 1995. Strontium diffusion kinetics in amphiboles and significance to thermal history determinations. Geochimica et Cosmochimica Acta 59, 2223–2238.

Browning, P., 1984. Cryptic variation within the cumulate sequence of the Oman ophiolite: magma chamber depth and petrological implications. Geological Society, London, Special Publications 13, 71–82.

Browning, P., 1982. The petrology, geochemistry and structure of the plutonic rocks of the Oman ophiolite.

Canales, J.P., Nedimović, M.R., Kent, G.M., Carbotte, S.M., Detrick, R.S., 2009. Seismic reflection images of a near-axis melt sill within the lower crust at the Juan de Fuca ridge. Nature 460, 89.

Cann, J., 1974. A model for oceanic crystal structure developed. Geophysical Journal International.

Cann, J.R., Strens, M.R., Rice, A., 1985. A simple magma-driven thermal balance model for the formation of volcanogenic massive sulphides. Earth and Planetary Science Letters 76, 123–134.

Cathelineau, M., 1988. Cation site occupancy in chlorites and illites as function of temperature. Clay minerals 23, 471–485.

Cathelineau, M., Nieva, D., 1985. A chlorite solid solution geothermometre. The Los Azufrez (Mexico) geothermal system. Contributions to Mineralogy and Petrology 91, 235–244.

Chan, L.H., Alt, J.C., Teagle, D.A.H., 2002. Lithium and lithium isotope profiles through the upper oceanic crust: A study of seawater-basalt exchange at ODP Sites 504B and 896A. Earth and Planetary Science Letters 201, 187–201. doi:10.1016/S0012-821X(02)00707-0

Chen, Y.J., 2001. Thermal effects of gabbro accretion from a deeper second melt lens at the fast spreading East Pacific Rise. Journal of Geophysical Research: Solid Earth 106, 8581–8588.

Childs, C., Manzocchi, T., Walsh, J.J., Bonson, C.G., Nicol, A., Schöpfer, M.P.J., 2009. A geometric model of fault zone and fault rock thickness variations. Journal of Structural Geology 31, 117–127.

Christeson, G.L., McIntosh, K.D., Karson, J.A., 2007. Inconsistent correlation of seismic layer 2a and lava layer thickness in oceanic crust. Nature 445, 418.

Cocker, J.D., Griffin, B.J., Muehlenbachs, K., 1982. Oxygen and carbon isotope evidence for seawater-hydrothermal alteration of the Macquarie Island ophiolite. Earth and Planetary Science Letters 61, 112–122.

Coggon, R.M., 2006. Hydrothermal alateration of the ocean crust: Insights from Macquarie Island and drilled in situ ocean crust. PhD thesis. University of Southampton.

Coggon, R.M., Teagle, D.A.H., Harris, M., Davidson, G.J., Alt, J.C., Brewer, T.S., 2016. Hydrothermal contributions to global biogeochemical cycles: Insights from the Macquarie Island ophiolite. Lithos 264, 329–347.

Coleman, R.G., 1981. Tectonic setting for ophiolite obduction in Oman. Journal of Geophysical Research: Solid Earth 86, 2497–2508.

Coogan, L.A., Dosso, S., 2012. An internally consistent, probabilistic, determination of ridge-axis hydrothermal fluxes from basalt-hosted systems. Earth and Planetary Science Letters 323–

324, 92–101. doi:10.1016/j.epsl.2012.01.017

Coogan, L.A., Gillis, K.M., MacLeod, C.J., Thompson, G.M., Hékinian, R., 2002a. Petrology and geochemistry of the lower ocean crust formed at the East Pacific Rise and exposed at Hess Deep: A synthesis and new results. Geochemistry, Geophysics, Geosystems 3, 1–30.

Coogan, L.A., Howard, K.A., Gillis, K.M., Bickle, M.J., Chapman, H., Boyce, A.J., Jenkin, G.R.T., Wilson, R.N., 2006. Chemical and thermal constraints on focussed fluid flow in the lower oceanic crust. American Journal of Science 306, 389–427.

Coogan, L.A., Jenkin, G.R.T., Wilson, R.N., 2002b. Constraining the cooling rate of the lower oceanic crust: a new approach applied to the Oman ophiolite. Earth and Planetary Science Letters 199, 127–146.

Coogan, L.A., Manning, C.E., Wilson, R.N., 2007. Oxygen isotope evidence for short-lived high-temperature fluid flow in the lower oceanic crust at fast-spreading ridges. Earth and Planetary Science Letters 260, 524–536.

Coogan, L.A., Wilson, R.N., Gillis, K.M., MacLeod, C.J., 2001. Near-solidus evolution of oceanic gabbros: insights from amphibole geochemistry. Geochimica et Cosmochimica Acta 65, 4339–4357.

Davatzes, N.C., Aydin, A., 2003. Overprinting faulting mechanisms in high porosity sandstones of SE Utah. Journal of Structural Geology 25, 1795–1813.

Davis, A.C., 2004. The hydrothermal contribution to the oceanic strontium budget: insights from the Oman ophiolite. PhD thesis University of Cambridge.

De Gramon, X., Le Métour, J., Villey, M., 1986. Geological Map of Samad (Scale 1:100,000, Sheet NF40-7c). Bureau de Recherches Geolgique et Minieres, ORLEANS-FRANCE.

Delaney, J.R., Mogk, D.W., Mottl, M., 1987. Quartz-cemented breccias from the Mid-Atlantic Ridge: Samples of a high-salinity hydrothermal upflow zone. Journal of Geophysical Research: Solid Earth 92, 9175–9192.

Detrick, R., Collins, J., Stephen, R., Swift, S., 1994. In situ evidence for the nature of the seismic layer 2/3 boundary in oceanic crust. Nature 370, 288.

Detrick, R.S., Buhl, P., Vera, E., Mutter, J., Orcutt, J., Madsen, J., Brocher, T., 1987. Multi-channel seismic imaging of a crustal magma chamber along the East Pacific Rise. Nature 326, 35–41.

Droop, T., R., G., 1987. A General Equation for Estimating Fe3+ Concentrations in Ferromagnesian

Silicates and Oxides from Microprobe Analyses, Using Stoichiometric Criteria. Mineralogical Magazine 51, 431–435. doi:10.1180/minmag.1987.051.361.10

Dunn, R.A., 2015. Crust and Lithospheric Structure-Seismic Structure of Mid-Ocean Ridges. Elsevier.

Dunn, R.A., Toomey, D.R., Solomon, S.C., 2000. Three-dimensional seismic structure and physical properties of the crust and shallow mantle beneath the East Pacific Rise at 9° 30'N. Journal of Geophysical Research: Solid Earth 105, 23537–23555.

Edwards, M.H., Fornari, D.J., Malinverno, A., Ryan, W.B.F., Madsen, J., 1991. The regional tectonic fabric of the East Pacific Rise from 12 50' N to 15 10' N. Journal of Geophysical Research: Solid Earth 96, 7995–8017.

Elderfield, H., Schultz, A., 1996. Mid-Ocean Ridge Hydrothermal Fluxes and the Chemical Composition of the Ocean. Annual Review of Earth and Planetary Sciences 24, 191–224. doi:10.1146/annurev.earth.24.1.191

Ernewein, M., Pflumio, C., Whitechurch, H., 1988. The death of an accretion zone as evidenced by the magmatic history of the Sumail ophiolite (Oman). Tectonophysics 151, 247–274.

Ernst, W.G., Liu, J., 1998. Experimental phase- equilibrium of Al- and Ti-contents of calcic amphibole in MORB- A semiquantitative thermobarometer. American Mineralogist 83, 952–969.

Faak, K., Coogan, L.A., Chakraborty, S., 2015. Near conductive cooling rates in the upper-plutonic section of crust formed at the East Pacific Rise. Earth and Planetary Science Letters 423, 36–47.

Faak, K., Gillis, K.M., 2016. Slow cooling of the lowermost oceanic crust at the fast-spreading East Pacific Rise. Geology 44, 115–118.

France, L., Ildefonse, B., Koepke, J., 2009. Interactions between magma and hydrothermal system in Oman ophiolite and in IODP Hole 1256D: Fossilization of a dynamic melt lens at fast spreading ridges. Geochemistry, Geophysics, Geosystems 10, 1–30. doi:10.1029/2009GC002652

Frey, M., Capitani, C. De, Liou, J.G., 1991. A new petrogenetic grid for low-grade metabasites. Journal of Metamorphic Geology 9, 497–509. doi:10.1111/j.1525-1314.1991.tb00542.x

Früh-Green, G.L., Plas, A., Dell'Angelo, L.N., 1996. Mineralogic and stable isotope record of

polyphase alteration of upper crustal gabbros of the East Pacific Rise (Hess Deep, Site 894), in: Proceedings-Ocean Drilling Program Scientific Results. National Science Foundation, pp. 235–254.

Garbe-Schönberg, C.D., 1993. Simultaneous determination of thirty-seven trace elements in twenty-eight international rock standards by ICP-MS. Geostandards Newsletter 17, 81–97.

Garbe-Schönberg, D., Müller, S., 2014. Nano-particulate pressed powder tablets for LA-ICP-MS. Journal of Analytical Atomic Spectrometry 29, 990–1000.

Gilbert, L.A., Salisbury, M.H., 2011. Oceanic crustal velocities from laboratory and logging measurements of Integrated Ocean Drilling Program Hole 1256D. Geochemistry, Geophysics, Geosystems 12.

Gillis, K.M., 2002. The rootzone of an ancient hydrothermal system exposed in the Troodos ophiolite, Cyprus. The Journal of geology 110, 57–74.

Gillis, K.M., Coogan, L.A., Pedersen, R., 2005. Strontium isotope constraints on fluid flow in the upper oceanic crust at the East Pacific Rise. Earth and Planetary Science Letters 232, 83–94.

Gillis, K.M., Ludden, J.N., Smith, A.D., 1992. Mobilization of REE during crustal aging in the Troodos Ophiolite, Cyprus. Chemical Geology 98, 71–86.

Gillis, K.M., Muehlenbachs, K., Stewart, M., Gleeson, T., Karson, J., 2001. Fluid flow patterns in fast spreading East Pacific Rise crust exposed at Hess Deep. Journal of Geophysical Research: Solid Earth 106, 26311–26329.

Gillis, K.M., Robinson, P.T., 1990. Patterns and processes of alteration in the lavas and dykes of the Troodos Ophiolite, Cyprus. Journal of Geophysical Research: Solid Earth 95, 21523–21548.

Gillis, K.M., Snow, J.E., Klaus, A., Abe, N., Adrião, Á.B., Akizawa, N., Ceuleneer, G., Cheadle, M.J., Faak, K., Falloon, T.J., Friedman, S.A., Godard, M., Guerin, G., Harigane, Y., Horst, A.J., Hoshide, T., Ildefonse, B., Jean, M.M., John, B.E., Koepke, J., MacHi, S., Maeda, J., Marks, N.E., McCaig, A.M., Meyer, R., Morris, A., Nozaka, T., Python, M., Saha, A., Wintsch, R.P., 2014. Primitive layered gabbros from fast-spreading lower oceanic crust. Nature 505, 204–207. doi:10.1038/nature12778

Gillis, K.M., Thompson, G., Kelley, D.S., 1993. A view of the lower crustal component of hydrothermal systems at the Mid-Atlantic Ridge. Journal of Geophysical Research: Solid Earth 98, 19597–19619.

Gnos, E., Peters, T., 1993. K-Ar ages of the metamorphic sole of the Semail Ophiolite: implications for ophiolite cooling history. Contributions to Mineralogy and Petrology 113, 325–332.

Godard, M., Dautria, J.M., Perrin, M., 2003. Geochemical variability of the Oman ophiolite lavas: Relationship with spatial distribution and paleomagnetic directions. Geochemistry, Geophysics, Geosystems 4. doi:10.1029/2002GC000452

Goldstein, J.I., Newbury, D.E., Echlin, P., Joy, D.C., Lyman, C.E., Lifshin, E., Sawyer, L., Michael, J.R., 2003. Quantitative X-ray analysis: the basics, in: Scanning Electron Microscopy and X-Ray Microanalysis. Springer, pp. 391–451.

Goodenough, K.M., Styles, M.T., Schofield, D., Thomas, R.J., Crowley, Q.C., Lilly, R.M., McKervey, J., Stephenson, D., Carney, J.N., 2013. Architecture of the Oman–UAE ophiolite: evidence for a multi-phase magmatic history, in: Lithosphere Dynamics and Sedimentary Basins: The Arabian Plate and Analogues. Springer, pp. 23–42.

Goodenough, K.M., Thomas, R.J., Styles, M.T., Schofield, D.I., MacLeod, C.J., 2014. Records of ocean growth and destruction in the Oman-UAE ophiolite. Elements 10, 109–114. doi:10.2113/gselements.10.2.109

Govindaraju, K., 1994. 1994 compilation of working values and sample description for 383 geostandards. Geostandards newsletter 18, 1–158.

Grant, J.A., 1986. The isocon diagram; a simple solution to Gresens equation for metasomatic alteration. Economic geology 81, 1976–1982.

Grapes, R.H., Hoskin, P.W.O., 2004. Epidote group minerals in low--medium pressure metamorphic terranes. Reviews in Mineralogy and Geochemistry 56, 301–345.

Gregory, R.T., Taylor, H.P., 1981. An oxygen isotope profile in a section of Cretaceous oceanic crust, Samail Ophiolite, Oman: Evidence for δ18O buffering of the oceans by deep (>5 km) seawater-hydrothermal circulation at mid-ocean ridges. Journal of Geophysical Research: Solid Earth 86, 2737–2755. doi:10.1029/JB086iB04p02737

Gresens, R.L., 1967. Composition - Volume Relationships of Metasomatism. Chemical Geology 2, 47–65.

Haase, K.M., Freund, S., Beier, C., Koepke, J., Erdmann, M., Hauff, F., 2016. Constraints on the magmatic evolution of the oceanic crust from plagiogranite intrusions in the Oman ophiolite. Contributions to Mineralogy and Petrology 171, 46.

Hacker, B.R., 1990. Simulation of the metamorphic and deformational history of the metamorphic sole of the Oman ophiolite. Journal of Geophysical Research: Solid Earth 95, 4895–4907.

Hacker, B.R., Mosenfelder, J.L., Gnos, E., 1996. Rapid emplacement of the Oman ophiolite: Thermal and geochronologic constraints. Tectonics 15, 1230–1247.

Han, S., Carbotte, S.M., Carton, H., Mutter, J.C., Aghaei, O., Nedimović, M.R., Canales, J.P., 2014. Architecture of on-and off-axis magma bodies at EPR 9° 37–40′ N and implications for oceanic crustal accretion. Earth and Planetary Science Letters 390, 31–44.

Harper, G.D., Bowman, J.R., Kuhns, R., 1988. A field, chemical, and stable isotope study of subseafloor metamorphism of the Josephine ophiolite, California-Oregon. Journal of Geophysical Research: Solid Earth 93, 4625–4656.

Harris, M., Coggon, R.M., Smith-Duque, C.E., Cooper, M.J., Milton, J.A., Teagle, D.A.H., 2015. Channelling of hydrothermal fluids during the accretion and evolution of the upper oceanic crust: Sr isotope evidence from ODP Hole 1256D. Earth and Planetary Science Letters 416, 56–66. doi:10.1016/j.epsl.2015.01.042

Hart, S.R., Staudigel, H., 1982. The control of alkalies and uranium in seawater by ocean crust alteration. Earth and Planetary Science Letters 58, 202–212. doi:10.1016/0012-821X(82)90194-7

Hasenclever, J., Theissen-Krah, S., Rüpke, L.H., Morgan, J.P., Iyer, K., Petersen, S., Devey, C.W., 2014. Hybrid shallow on-axis and deep off-axis hydrothermal circulation at fast-spreading ridges. Nature 508, 508–512. doi:10.1038/nature13174

Hayman, N.W., Karson, J.A., 2009. Crustal faults exposed in the Pito Deep Rift: Conduits for hydrothermal fluids on the southeast Pacific Rise. Geochemistry, Geophysics, Geosystems 10. doi:doi:10.1029/2008GC002319

Hayman, N.W., Karson, J.A., 2007. Faults and damage zones in fast-spread crust exposed on the north wall of the Hess Deep Rift: Conduits and seals in seafloor hydrothermal systems. Geochemistry, Geophysics, Geosystems 8. doi:10.1029/2007GC001623

Haymon, R.M., Koski, R.A., Abrams, M.J., 1989. Hydrothermal discharge zones beneath massive sulfide deposits mapped in the Oman ophiolite. Geology 17, 531–535.

Heft, K.L., Gillis, K.M., Pollock, M.A., Karson, J.A., Klein, E.M., 2008. Role of upwelling hydrothermal fluids in the development of alteration patterns at fast spreading ridges: Evidence from the sheeted dike complex at Pito Deep. Geochemistry, Geophysics,

Geosystems 9. doi:10.1029/2007GC001926

Henstock, T.J., Woods, A.W., White, R.S., 1993. The accretion of oceanic crust by episodic sill intrusion. Journal of Geophysical Research: Solid Earth 98, 4143–4161.

Hopson, C.A., Coleman, R.G., Gregory, R.T., Pallister, J.S., Bailey, E.H., 1981. Geologic section through the Samail Ophiolite and associated rocks along a Muscat-Ibra Transect, southeastern Oman Mountains. Journal of Geophysical Research 86, 2527. doi:10.1029/JB086iB04p02527

Hu, Z., Zhang, W., Liu, Y., Chen, H., Gaschnig, R.M., Zong, K., Li, M., 2013. Rapid bulk rock decomposition by ammonium fl uoride (NH 4 F) in open vessels at an elevated digestion temperature. Chemical Geology 355, 144–152.

Humphris, S.E., Alt, J.C., Teagle, D.A.H., Honnorez, J.J., 1998. Geochemical changes during hydrothermal alteration of basement in the stockwork beneath the active TAG hydrothermal mound, in: Proceedings Ocean Drilling Program Scientific Results. National Science Foundation, pp. 255–276.

Humphris, S.E., Thompson, G., 1978. Trace element mobility during hydrothermal alteration of oceanic basalts. Geochimica et Cosmochimica Acta 42, 127–136.

Imai, N., Terashima, S., Itoh, S., Ando, A., 1995. 1994 compilation values for GSJ reference samples,“Igneous rock series.” Geochemical Journal 29, 91–95.

Jarosewich, E., Nelen, J.A., NORBERG, J.A., 1980. Reference samples for electron microprobe analysis. Geostandards Newsletter 4, 43–47.

Jochum, K.P., Weis, U., Schwager, B., Stoll, B., Wilson, S.A., Haug, G.H., Andreae, M.O., Enzweiler, J., 2016. Reference values following ISO guidelines for frequently requested rock reference materials. Geostandards and Geoanalytical Research 40, 333–350.

Jowett, E.C., 1991. Fitting iron and magnesium into the hydrothermal chlorite geothermometer, in: GAC/MAC/SEG Joint Annual Meeting, Toronto, May 27-29, 1991, Program with Abstracts 16.

Juteau, T., Ernewein, M., Reuber, I., Whitechurch, H., Dahl, R., 1988. Duality of magmatism in the plutonic sequence of the Sumail Nappe, Oman. Tectonophysics 151, 107–135.

Kawahata, H., Nohara, M., Ishizuka, H., Hasebe, S., Chiba, H., 2001. Sr isotope geochemistry and hydrothermal alteration of the Oman ophiolite. Journal of Geophysical Research: Solid Earth

106, 11083–11099. doi:10.1029/2000JB900456

Kelemen, P.B., Koga, K., Shimizu, N., 1997. Geochemistry of gabbro sills in the crust-mantle transition zone of the Oman ophiolite: implications for the origin of the oceanic lower crust. Earth and Planetary Science Letters 146, 475–488. doi:10.1016/S0012-821X(96)00235-X

Kent, G.M., Harding, A.J., Orcutt, J.A., 1993. Distribution of magma beneath the East Pacific Rise between the Clipperton transform and the 9 17′ N Deval from forward modeling of common depth point data. Journal of Geophysical Research: Solid Earth 98, 13945–13969.

Klinkhammer, G.P., Elderfield, H., Edmond, J.M., Mitra, A., 1994. Geochemical implications of rare earth elements patterns in hydrothermal fluids from mid-ocean ridges. Geochimica et Cosmochimica Acta 58, 5105–5113.

Koepke, J., Berndt, J., Horn, I., Fahle, J., Wolff, P.E., 2014. Partial melting of oceanic gabbro triggered by migrating water-rich fluids: a prime example from the Oman Ophiolite. Geological Society, London, Special Publications 392, 195–212.

Koepke, J., Feig, S.T., Snow, J., 2005. Hydrous partial melting within the lower oceanic crust. Terra Nova 17, 286–291.

Koepke, J., France, L., Müller, T., Faure, F., Goetze, N., Dziony, W., Ildefonse, B., 2011. Gabbros from IODP Site 1256, equatorial Pacific: Insight into axial magma chamber processes at fast spreading ocean ridges. Geochemistry, Geophysics, Geosystems 12.

Koepke, J., Schoenborn, S., Oelze, M., Wittmann, H., Feig, S.T., Hellebrand, E., Boudier, F., Schoenberg, R., 2009. Petrogenesis of crustal wehrlites in the Oman ophiolite: Experiments and natural rocks. Geochemistry, Geophysics, Geosystems 10. doi:10.1029/2009GC002488

Korenaga, J., Kelemen, P.B., 1997. Origin of gabbro sills in the Moho transition zone of the Oman ophiolite: Implications for magma transport in the oceanic lower crust. Journal of Geophysical Research: Solid Earth 102, 27729–27749.

Kranidiotis, P., MacLean, W.H., 1987. Systematics of chlorite alteration at the Phelps Dodge massive sulfide deposit, Matagami, Quebec. Economic Geology 82, 1898–1911.

Lanphere, M.A., Coleman, R.G., Hopson, C.A., 1981. Sr isotopic tracer study of the Samail Ophiolite, Oman. Journal of Geophysical Research: Solid Earth 86, 2709–2720. doi:10.1029/JB086iB04p02709

Laverne, C., Vanko, D.A., Tartarotti, P., Alt, J.C., 1995. 15. Chemistry and geothermometry of

secondary minerals from the deep sheeted dike complex, Hole 504B1, in: Proceedings of the Ocean Drilling Program, Scientific Results. p. 140.

Leake, B.E., Woolley, A.R., Arps, C.E.S., Birch, W.D., Gilbert, M.C., Grice, J.D., Hawthorne, F.C., Kato, A., Kisch, H.J., Krivovichev, V.G., Linthouk, K., 1997. Report. Nomenclature of Amphiboles: Report of the Subcommittee on Amphiboles of the International Mineralogical Association Commission on New Minerals and Mineral Names. Mineralogical Magazine 61, 295–321.

Liou, J.G., Kim, H.S., Maruyama, S., 1983. Prehnite – Epidote Equilibria and their Petrologic Applications. Journal of Petrology 24, 321–342.

Liou, J.G., Kuniyoshi, S., Ito, K., 1974. Experimental studies of the phase relations between greenschist and amphibolite in a basaltic system. American Journal of Science 274, 613–632.

Liou, J.G., Maruyama, S., Cho, M., 1985. Phase equilibria and mineral parageneses of metabasites in low-grade metamorphism. Mineralogical Magazine 49, 352.

Lippard, S.J., Shelton, A.W., Gass, I.G., 1986. The Ophiolite of Northern Oman. Geological Society of London Memoir 11.

Lonsdale, P., 1988. Structural pattern of the Galapagos microplate and evolution of the Galapagos triple junctions. Journal of Geophysical Research: Solid Earth 93, 13551–13574.

Lowell, R.P., Van Cappellen, P., Germanovich, L.N., 1993. Silica precipitation in fractures and the evolution of permeability in hydrothermal upflow zones. Science 260, 192–194.

MacLean, W.H., 1990. Mass change calculations in altered rock series. Mineralium Deposita 25, 44–49.

MacLean, W.H., Barrett, T.J., 1993. Lithogeochemical techniques using immobile elements. Journal of geochemical exploration 48, 109–133.

MacLean, W.H., Kranidiotis, P., 1987. Immobile elements as monitors of mass transfer in hydrothermal alteration; Phelps Dodge massive sulfide deposit, Matagami, Quebec. Economic Geology 82, 951–962.

Maclennan, J., Hulme, T., Singh, S.C., 2004. Thermal models of oceanic crustal accretion: Linking geophysical, geological and petrological observations. Geochemistry, Geophysics, Geosystems 5. doi:10.1029/2003GC000605

MacLeod, C.J., Lissenberg, C.J., Bibby, L.E., 2013. “Moist MORB” axial magmatism in the Oman

ophiolite: The evidence against a mid-ocean ridge origin. Geology 41, 459–462.

MacLeod, C.J., Rothery, D.A., 1992. Ridge axial segmentation in the Oman ophiolite: evidence from along-strike variations in the sheeted dyke complex. Geological Society, London, Special Publications 60, 39–63.

MacLeod, C.J., Yaouancq, G., 2000. A fossil melt lens in the Oman ophiolite: Implications for magma chamber processes at fast spreading ridges. Earth and Planetary Science Letters 176, 357–373.

Manning, C.E., MacLeod, C.J., 1996. Fracture-controlled metamorphism of Hess Deep gabbros, site 894: Constraints on the roots of mid-ocean-ridge hydrothermal systems at fast-spreading centers. Proceedings of the Ocean Drilling Program, Scientific Results 147, 189–212. doi:10.2973/odp.proc.sr.147.011.1996

Manning, C.E., MacLeod, C.J., Weston, P.E., 2000. Lower-crustal cracking front at fast-spreading ridges: Evidence from the East Pacific Rise and the Oman ophiolite. Special Papers-Geological Society of America 261–272.

Manning, C.E., Weston, P.E., Mahon, K.I., 1996. Rapid high-temperature metamorphism of East Pacific Rise gabbros from Hess Deep. Earth and Planetary Science Letters 144, 123–132. doi:10.1016/0012-821X(96)00153-7

McArthur, J.M., Howarth, R.J., Bailey, T.R., 2001. Strontium isotope stratigraphy: LOWESS version 3: best fit to the marine Sr-isotope curve for 0-509 Ma and accompanying look-up table for deriving numerical age. The Journal of Geology 109, 155–170.

McCaig, A.M., Harris, M., 2012. Hydrothermal circulation and the dike-gabbro transition in the detachment mode of slow seafloor spreading. Geology 40, 367–370.

McCollom, T.M., Shock, E.L., 1998. Fluid-rock interactions in the lower oceanic crust: Thermodynamic models of hydrothermal alteration. Journal of Geophysical Research: Solid Earth 103, 547–575.

McCulloch, M.T., Gregory, R.T., Wasserburg, G.J., Taylor, H.P., 1981. Sm-Nd, Rb-Sr, and 18O/16O isotopic systematics in an oceanic crustal section: Evidence from the Samail Ophiolite. Journal of Geophysical Research: Solid Earth 86, 2721–2735.

McCulloch, M.T., Gregory, R.T., Wasserburg, G.J., Taylor, H.P.J., 1980. A Neodymium, Strontium, and Oxygen Isotopic Study of the cretaceous Samail ophiolite and implications for the petrogenesis and seawater-hydrothermal alteration of oceanic crust. Earth and Planetary 46,

201–211.

McDonough, W.F., Sun, S. -s., 1995. The composition of the Earth. Chemical Geology 120, 223–253.

McDowell, S.D., Elders, W.A., 1980. Authigenic layer silicate minerals in borehole Elmore 1, Salton Sea geothermal field, California, USA. Contributions to mineralogy and petrology 74, 293–310.

Mével, C., Cannat, M., 1991. Lithospheric Stretching and Hydrothermal Processes in Oceanic Gabbros from Slow-Spreading Ridges, in: Peters, T., Nicolas, A., Coleman, R.G. (Eds.), Ophiolite Genesis and Evolution of the Oceanic Lithosphere: Proceedings of the Ophiolite Conference, Held in Muscat, Oman, 7--18 January 1990. Springer Netherlands, Dordrecht, pp. 293–312.

Miller, D.J., Christensen, N.I., 1997. Seismic velocities of lower crustal and upper mantle rocks from the slow-spreading Mid-Atlantic Ridge, south of the Kane Transform Zone (MARK), in: Proceedings Ocean Drilling Program Scientific Results. National Science Foundation, pp. 437–456.

Miyashiro, A., 1973. The Troodos ophiolitic complex was probably formed in an island arc. Earth and Planetary Science Letters 19, 218–224.

Moody, J.B., Meyer, D., Jenkins, J.E., 1983. Experimental characterization of the greenschist/amphibolite boundary in mafic systems. American Journal of Science 283, 48–92.

Morgan, J.P., Chen, Y.J., 1993. The genesis of oceanic crust: Magma injection, hydrothermal circulation, and crustal flow. Journal of Geophysical Research: Solid Earth 98, 6283–6297.

Morton, J.L., Sleep, N.H., 1985. A mid-ocean ridge thermal model: Constraints on the volume of axial hydrothermal heat flux. Journal of Geophysical Research: Solid Earth 90, 11345–11353.

Mueller, S., Koepke, J., Garbe-Schoenberg, C.D., Müller, T., Mock, D., Strauss, H., Schuth, S., Ildefonse, B., 2017. A Reference Section through the Lower Fast-spreading Oceanic Crust in the Wadi Gideah (Sumail ophiolite, Sultanate Oman): Drill Sites GT1A and GT2A within the ICDP Oman Drilling Project, in: AGU Fall Meeting Abstracts.

Müller, R.D., Sdrolias, M., Gaina, C., Roest, W.R., 2008. Age, spreading rates, and spreading asymmetry of the world's ocean crust. Geochemistry, Geophysics, Geosystems 9.

Müller, T., 2016. A petrological and geochemical cross section of lower crust at the Wadi Gideah (Samail ophiolite): Implications for the crustal accretion at fast-spreading mid-ocean ridges (PhD thesis). Gottfried Wilhelm Leibniz Universität Hannover, Géosciences Montpellier Université Montpellier.

Müller, T., Koepke, J., Garbe-Schönberg, C.-D., Dietrich, M., Bauer, U., Wolff, P.E., 2017. Anatomy of a frozen axial melt lens from a fast-spreading paleo-ridge (Wadi Gideah, Oman ophiolite). Lithos 272, 31–45.

Nehlig, P., 1994. Fracture and Permeability Analysis in Magma-Hydrothermal Transition Zones in the Samail Ophiolite (Oman). Journal of Geophysical Research-Solid Earth 99, 589–601. doi:10.1029/93JB02569

Nehlig, P., Juteau, T., 1988a. Flow porosities, permeabilities and preliminary data on fluid inclusions and fossil thermal gradients in the crustal sequence of the Sumail ophiolite (Oman). Tectonophysics 151, 199–221. doi:10.1016/0040-1951(88)90246-6

Nehlig, P., Juteau, T., 1988b. Deep crustal seawater penetration and circulation at ocean ridges: Evidence from the Oman ophiolite. Marine Geology 84, 209–228.

Nehlig, P., Juteau, T., Bendel, V., Cotten, J., 1994. The root of oceanic hydrothermal systems: Constraints from the Semail ophiolite (Oman). Journal of Geophysical Research 99, 4703–4713. doi:10.1029/93JB02663

Nicolas, A., Boudier, F., Ildefonse, B., 1996. Variable crustal thickness in the Oman ophiolite: implication for oceanic crust. Journal of Geophysical Research: Solid Earth 101, 17941–17950.

Nicolas, A., Boudier, F., Ildefonse, B., Ball, E., 2000. Accretion of Oman and United Arab Emirates ophiolite--Discussion of a new structural map. Marine Geophysical Researches 21, 147–180.

Nicolas, A., Mainprice, D., Boudier, F., 2003. High-temperature seawater circulation throughout crust of oceanic ridges: A model derived from the Oman ophiolites. Journal of Geophysical Research 108, 2371.

Oeser, M., Strauss, H., Wolff, P.E., Koepke, J., Peters, M., Garbe-Schönberg, D., Dietrich, M., 2012. A profile of multiple sulfur isotopes through the Oman ophiolite. Chemical Geology 312, 27–46.

Pablo Canales, J., Detrick, R.S., Toomey, D.R., Wilcock, W.S.D., 2003. Segment-scale variations in the crustal structure of 150–300 kyr old fast spreading oceanic crust (East Pacific Rise, 8 15’

N–10 5′ N) from wide-angle seismic refraction profiles. Geophysical Journal International 152, 766–794.

Pallister, J.S., 1981. Structure of the sheeted dike complex of the Samail ophiolite near Ibra, Oman. Journal of Geophysical Research: Solid Earth 86, 2661–2672.

Pallister, J.S., Hopson, C.A., 1981. Samail Ophiolite plutonic suite: Field relations, phase variation, cryptic variation and layering, and a model of a spreading ridge magma chamber. Journal of Geophysical Research 86, 2593. doi:10.1029/JB086iB04p02593

Pallister, J.S., Knight, R.J., 1981. Rare-earth element geochemistry of the Samail Ophiolite near Ibra, Oman. Journal of Geophysical Research: Solid Earth 86, 2673–2697.

Palmer, M.R., Edmond, J.M., 1989a. Cesium and rubidium in submarine hydrothermal fluids: evidence for recycling of alkali elements. Earth and Planetary Science Letters 95, 8–14. doi:10.1016/0012-821X(89)90163-5

Palmer, M.R., Edmond, J.M., 1989b. The strontium isotope budget of the modern ocean. Earth and Planetary Science Letters 92, 11–26.

Party, R.S., Francheteau, J., Patriat, P., Segoufin, J., Armijo, R., Doucoure, M., Yelles-Chaouche, A., Zukin, J., Calmant, S., Naar, D.F., 1988. Pito and Orongo fracture zones: the northern and southern boundaries of the Easter microplate (southeast Pacific). Earth and Planetary Science Letters 89, 363–374.

Peacock, D.C.P., Nixon, C.W., Rotevatn, A., Sanderson, D.J., Zuluaga, L.F., 2016. Glossary of fault and other fracture networks. Journal of Structural Geology 92, 12–29.

Pearce, J.A., Alabaster, T., Shelton, A.W., Searle, M.P., 1981. The Oman ophiolite as a Cretaceous arc-basin complex: evidence and implications. Philosophical Transaction of the Royal Society London 300, 299–317.

Pearce, J.A., Lippard, S.J., Roberts, S., 1984. Characteristics and tectonic significance of supra-subduction zone ophiolites. Geological Society, London, Special Publications 16, 77–94.

Peters, T., El Amin, O., Blechschmid, I., Al-Busaidi, S., 2008. Geological Map Oman 1:50000, Sheet NF 40-8A1. Sultanate of Oman: Ministry of Commerce and Industry.

Peucker-Ehrenbrink, B., Hanghoj, K., Atwood, T., Kelemen, P.B., 2012. Rhenium-osmium isotope systematics and platinum group element concentrations in oceanic crust. Geology 40, 199–202. doi:10.1130/G32431.1

Pin, C., Briot, D., Bassin, C., Poitrasson, F., 1994. Concomitant separation of strontium and samarium-neodymium for isotopic analysis in silicate samples, based on specific extraction chromatography. Analytica Chimica Acta 298, 209–217.

Pollard, D.D., Aydin, A., 1988. Progress in understanding jointing over the past century. Geological Society of America Bulletin 100, 1181–1204.

Potts, P.J., Kane, J.S., 2005. International Association of Geoanalysts Certificate of Analysis: Certified Reference Material OU-6 (Penrhyn Slate). Geostandards and Geoanalytical Research 29, 233–236.

Price, N.J., 2016. Fault and joint development: in brittle and semi-brittle rock. Elsevier.

Python, M., Ceuleneer, G., 2003. Nature and distribution of dykes and related melt migration structures in the mantle section of the Oman ophiolite. Geochemistry, Geophysics, Geosystems 4.

Quick, J.E., Denlinger, R.P., 1993. Ductile deformation and the origin of layered gabbro in ophiolites. Journal of Geophysical Research: Solid Earth 98, 14015–14027.

Richards, H.G., Cann, J.R., Jensenius, J., 1989. Mineralogical zonation and metasomatism of the alteration pipes of Cyprus sulfide deposits. Economic Geology 84, 91–115.

Richardson, C.J., Cann, J.R., Richards, H.G., Cowan, J.G., 1987. Metal-depleted root zones of the Troodos ore-forming hydrothermal systems, Cyprus. Earth and Planetary Science Letters 84, 243–253.

Rioux, M., Bowring, S., Kelemen, P., Gordon, S., Dudás, F., Miller, R., 2012. Rapid crustal accretion and magma assimilation in the Oman-U.A.E. ophiolite: High precision U-Pb zircon geochronology of the gabbroic crust. Journal of Geophysical Research: Solid Earth 117, 1–12. doi:10.1029/2012JB009273

Rioux, M., Bowring, S., Kelemen, P., Gordon, S., Miller, R., Dudás, F., 2013. Tectonic development of the Samail ophiolite: High-precision U-Pb zircon geochronology and Sm-Nd isotopic constraints on crustal growth and emplacement. Journal of Geophysical Research: Solid Earth 118, 2085–2101.

Saccocia, P.J., Gillis, K.M., 1995. Hydrothermal upflow zones in the oceanic crust. Earth and Planetary Science Letters 136, 1–16.

Saccocia, P.J., Seyfried Jr, W.E., 1994. The solubility of chlorite solid solutions in 3.2 wt% NaCl

fluids from 300–400 C, 500 bars. Geochimica et Cosmochimica Acta 58, 567–585.

Schiffman, P., Fridleifsson, G.O., 1991. The smectite–chlorite transition in drillhole NJ-15, Nesjavellir geothermal field, Iceland: XRD, BSE and electron microprobe investigations. Journal of Metamorphic Geology 9, 679–696.

Schiffman, P., Smith, B.M., 1988. Petrology and oxygen isotope geochemistry of a fossil seawater hydrothermal system within the Solea Graben, northern Troodos Ophiolite, Cyprus. Journal of Geophysical Research: Solid Earth 93, 4612–4624.

Schiffman, P., Smith, B.M., Varga, R.J., Moores, E.M., 1987. Geometry, conditions and timing of off-axis hydrothermal metamorphism and ore-deposition in the Solea graben. Nature 325, 423.

Schumacher, J.C., 1997. Appendix 2: The estimation of the proportion of ferric iron in the electron-microprobe analysis of amphiboles. Canadian Mineralogist 35, 238–246.

Searle, M., Cox, J., 1999. Tectonic setting, origin, and obduction of the Oman ophiolite. Bulletin of the Geological Society of America 111, 104–122. doi:10.1130/0016-7606(1999)111<0104:TSOAOO>2.3.CO;2

Searle, M.P., 1980. The metamorphic sheet and underlying volcanic rocks beneath the Semail ophiolite in the northern Oman Mountains of Arabia. Open University.

Searle, M.P., Cox, J.O.N., 2002. Subduction zone metamorphism during formation and emplacement of the Semail ophiolite in the Oman Mountains. Geological Magazine 139, 241–255.

Searle, M.P., Malpas, J., 1982. Petrochemistry and origin of sub-ophiolitic metamorphic and related rocks in the Oman Mountains. Journal of the Geological Society 139, 235–248.

Seewald, J.S., Seyfried, W.E., 1990. The effect of temperature on metal mobility in subseafloor hydrothermal systems: constraints from basalt alteration experiments. Earth and Planetary Science Letters 101, 388–403. doi:10.1016/0012-821X(90)90168-W

Seyfried, W.E., Berndt, M.E., Seewald, J.S., 1988. Hydrothermal alteration processes at mid-ocean ridges; constraints from diabase alteration experiments, hot spring fluids and composition of the oceanic crust. The Canadian Mineralogist 26, 787–804.

Singh, S.C., Harding, A.J., Kent, G.M., Sinha, M.C., Combier, V., Bazin, S., Tong, C.H., Pye, J.W., Barton, P.J., Hobbs, R.W., 2006. Seismic reflection images of the Moho underlying melt sills

at the East Pacific Rise. Nature 442, 287.

Sinton, J.M., Detrick, R.S., 1992. Mid-ocean ridge magma chambers. Journal of Geophysical Research: Solid Earth 97, 197–216.

Sleep, N.H., 1991. Hydrothermal circulation, anhydrite precipitation, and thermal structure at ridge axes. Journal of Geophysical Research: Solid Earth 96, 2375–2387.

Spooner, E.T.C., Chapman, H.J., Smewing, J.D., 1977. Strontium isotopic contamination and oxidation during ocean floor hydrothermal metamorphism of the ophiolitic rocks of the Troodos Massif, Cyprus. Geochimica et Cosmochimica Acta 41, 873–890.

Stakes, D., Vanko, D.A., 1986. Multistage hydrothermal alteration of gabbroic rocks from the failed Mathematician Ridge. Earth and Planetary Science Letters 79, 75–92.

Staudigel, H., 2014. Chemical fluxes from hydrothermal alteration of the oceanic crust, in: Rudnick, R.L. (Ed.), Treatise on Geochemistry, 2nd Edition The Crust Vol. 4, Elsevier, Oxford. Elsevier, pp. 583–606.

Staudigel, H., Plank, T., White, B., Schmincke, H., 1996. Geochemical fluxes during seafloor alteration of the basaltic upper oceanic crust: DSDP Sites 417 and 418. Subduction: top to bottom 96, 19–38.

Strens, M.R., Cann, J.R., 1982. A model of hydrothermal circulation in fault zones at mid-ocean ridge crests. Geophysical Journal of the Royal Astronomical Society 71, 225–240.

Sun, C., Lissenberg, C.J., 2018. Formation of fast-spreading lower oceanic crust as revealed by a new Mg–REE coupled geospeedometer. Earth and Planetary Science Letters 487, 165–178.

Teagle, D., Ildefonse, B., Blum, P., 2010. Superfast Spreading Rate Crust 4 Integrated Ocean Drilling Program Expedition 335 Scientific Prospectus.

Teagle, D., Ildefonse, B., Blum, P., Scientists, & the E. 3354, 2012. Expedition 335 summary. Proceedings of the Integrated Ocean Drilling Program (Online), Proceedings of the Integrated Ocean Drilling Program; superfast spreading rate crust 4; Expedition 335 of the riserless drilling platform Puntarenas, Costa Rica, to Balboa, Panama; Site 1256, 13 April-3 June 2001 335, 110.

Teagle, D.A.H., Alt, J.C., 2004. Hydrothermal alteration of Basalts beneath the Bent Hill massive sulfide deposit, Middle Valley, Juan de Fuca Ridge. Economic Geology 99, 561–584. doi:10.2113/gsecongeo.99.3.561

Teagle, D.A.H., Alt, J.C., Bach, W., Halliday, A.N., Erzinger, J., 1996. Alteration of upper ocean crust in a ridge-flank hydrothermal upflow zone: mineral, chemical, and isotopic constraints from Hole 896A, in: Proceedings-Ocean Drilling Program, Scientific Results. National Science Foundation, pp. 119–150.

Teagle, D.A.H., Alt, J.C., Halliday, A., 1998. Tracing the chemical evolution of fluids during hydrothermal recharge: Constraints from anhydrite recovered in ODP Hole 504B. Earth and Planetary Science Letters 155, 167–182.

Teagle, D.A.H., Alt, J.C., Umino, S., Miyashita, S., Banerjee, N.R., Wilson, D.S., Scientists, E. 309/312, 2006. Superfast spreading rate crust 2 and 3. Proc. IODP 309, 312.

Teagle, D.A.H., Bickle, M.J., Alt, J.C., 2003. Recharge flux to ocean-ridge black smoker systems: a geochemical estimate from ODP Hole 504B. Earth and Planetary Science Letters 210, 81–89.

Theissen-Krah, S., Iyer, K., Rüpke, L.H., Morgan, J.P., 2011. Coupled mechanical and hydrothermal modeling of crustal accretion at intermediate to fast spreading ridges. Earth and Planetary Science Letters 311, 275–286. doi:https://doi.org/10.1016/j.epsl.2011.09.018

Theissen-Krah, S., Rüpke, L.H., Hasenclever, J., 2016. Modes of crustal accretion and their implications for hydrothermal circulation. Geophysical Research Letters 43, 1124–1131. doi:10.1002/2015GL067335

Tilton, G.R., Hopson, C.A., Wright, J.E., 1981. Uranium-lead isotopic ages of the Samail Ophiolite, Oman, with applications to Tethyan ocean ridge tectonics. Journal of Geophysical Research: Solid Earth 86, 2763–2775.

Toy, V.G., Sutherland, R., Townend, J., Allen, M.J., Becroft, L., Boles, A., Boulton, C., Carpenter, B., Cooper, A., Cox, S.C., Daube, C., Faulkner, D.R., Halfpenny, A., Kato, N., Keys, S., Kirilova, M., Kometani, Y., Little, T., Mariani, E., Melosh, B., Menzies, C.D., Morales, L., Morgan, C., Mori, H., Niemeijer, A., Norris, R., Prior, D., Sauer, K., Schleicher, A.M., Shigematsue, N., Teagle, D.A.H., Tobin, H., Valdez, R., Williams, J., Yeo, S., Baratin, L.-M., Barth, N., Benson, A., Boese, C., Célérier, B., Chamberlain, C.J., Conze, R., Coussens, J., Craw, L., Doan, M.-L., Eccles, J., Grieve, J., Grochowski, J., Gulley, A., Howarth, J., Jacobs, K., Janku-Capova, L., Jeppson, T., Langridge, R., Mallyon, D., Marx, R., Massiot, C., Mathewson, L., Moore, J., Nishikawa, O., Pooley, B., Pyne, A., Savage, M.K., Schmitt, D., Taylor-Offord, S., Upton, P., Weaver, K.C., Wiersberg, T., Zimmer, M., DFDP-2-Science Team, 2017. Bedrock geology of DFDP-2B, central Alpine Fault, New Zealand. New Zealand Journal of Geology and Geophysics 60, 497–518.

Vanko, D.A., 1986. High-chlorine amphiboles from oceanic rocks: product of highly saline hydrothermal fluids. Am. Mineral 71, 51–59.

VanTongeren, J.A., Kelemen, P.B., Hanghøj, K., 2008. Cooling rates in the lower crust of the Oman ophiolite: Ca in olivine, revisited. Earth and Planetary Science Letters 267, 69–82. doi:10.1016/j.epsl.2007.11.034

Velde, B., Hillier S, 1991. Octahedral occupancy and the chemical composition of diagenetic (low-temperature) chlorites. Clay Minerals 26, 149–168.

Vera, E.E., Mutter, J.C., Buhl, P., Orcutt, J.A., Harding, A.J., Kappus, M.E., Detrick, R.S., Brocher, T.M., 1990. The structure of 0-to 0.2-my-old oceanic crust at 9 N on the East Pacific Rise from expanded spread profiles. Journal of Geophysical Research: Solid Earth 95, 15529–15556.

Vogel, W., Kuipers, G., 1987. A pre-calibrated program for geological applications. Phillips New Developments in X-Ray Spectrometry 11, 2–8.

Von Damm, K.L., 1995. Controls on the chemistry and temporal variability of seafloor hydrothermal fluids. Seafloor hydrothermal systems: physical, chemical, biological, and geological interactions 222–247.

Von Damm, K.L., Bischoff, J.L., Rosenbauer, R.J., 1991. Quartz solubility in hydrothermal seawater; an experimental study and equation describing quartz solubility for up to 0.5 M NaCl solutions. American Journal of Science 291, 977–1007.

Von Damm, K.L., Lilley, M.D., Shanks Iii, W.C., Brockington, M., Bray, A.M., O'grady, K.M., Olson, E., Graham, A., Proskurowski, G., 2003. Extraordinary phase separation and segregation in vent fluids from the southern East Pacific Rise. Earth and Planetary Science Letters 206, 365–378.

Warren, C.J., Parrish, R.R., Searle, M.P., Waters, D.J., 2003. Dating the subduction of the Arabian continental margin beneath the Semail ophiolite, Oman. Geology 31, 889–892.

Warren, C.J., Parrish, R.R., Waters, D.J., Searle, M.P., 2005. Dating the geologic history of Oman's Semail ophiolite: Insights from U-Pb geochronology. Contributions to Mineralogy and Petrology 150, 403–422. doi:10.1007/s00410-005-0028-5

Warren, C.J., Searle, M.P., Parrish, R.R., Waters, D.J., 2007. Reply to Comment by F. Boudier and A. Nicolas on "dating the geologic history of Oman's Semail Ophiolite: Insights from U-Pb geochronology" by C.J. Warren, R.R. Parrish, M.P. Searle and D.J. Waters. Contributions to

Mineralogy and Petrology 154, 115–118. doi:10.1007/s00410-007-0182-z

Weinzierl, C.G., Regelous, M., Haase, K.M., Bach, W., Böhm, F., Garbe-Schönberg, D., Sun, Y.D., Joachimski, M.M., Krumm, S., 2018. Cretaceous seawater and hydrothermal fluid compositions recorded in abiogenic carbonates from the Troodos Ophiolite, Cyprus. Chemical Geology 494, 43–55.

Weyhenmeyer, C.E., 2000. Origin and evolution of groundwater in the alluvial aquifer of the Eastern Batinah Coastal Plain, Sultanate of Oman. PhD., University of Bern, Switzerland.

White, R.S., McKenzie, D., O'Nions, R.K., 1992. Oceanic crustal thickness from seismic measurements and rare earth element inversions. Journal of Geophysical Research: Solid Earth 97, 19683–19715.

White, S.M., Haymon, R.M., Fornari, D.J., Perfit, M.R., Macdonald, K.C., 2002. Correlation between volcanic and tectonic segmentation of fast-spreading ridges: Evidence from volcanic structures and lava flow morphology on the East Pacific Rise at 9–10 N. Journal of Geophysical Research: Solid Earth 107, EPM-7.

White, W.M., Hofmann, a. W., Puchelt, H., 1987. Isotope geochemistry of Pacific Mid-Ocean Ridge Basalt. Journal of Geophysical Research 92, 4881. doi:10.1029/JB092iB06p04881

Wilson, D.S., Teagle, D.A.H., Acton, G.D., ODP Leg 206 Scientific Party, 2003. An in situ section of upper oceanic crust formed by superfast seafloor spreading, in: Proceedings of the Ocean Drilling Program Initial Reports 206.

Wilson, D.S., Teagle, D.A.H., Alt, J.C., Banerjee, N.R., Umino, S., Miyashita, S., Acton, G.D., Anma, R., Barr, S.R., Belghoul, A., others, 2006. Drilling to gabbro in intact ocean crust. Science 312, 1016–1020.

Wolff, P.E., 2014. A petrological and geochemical cross section of lower crust at the Wadi Gideah (Samail ophiolite): Implications for the crustal accretion at fast- spreading mid-ocean ridges. Gottfried Wilhelm Leibniz Universität Hannover.

Xie, X., Byerly, G.R., Ferrell Jr, R.E., 1997. IIb trioctahedral chlorite from the Barberton greenstone belt: crystal structure and rock composition constraints with implications to geothermometry. Contributions to Mineralogy and Petrology 126, 275–291.

Xie, Z., Walther, J. V, 1993. Wollastonite+ quartz solubility in supercritical NaCl aqueous solutions. American journal of Science 293, 235.